2-13-2014

Modeling Moisture-Induced Damage in Asphalt Concrete

Mohammad Hossain

Mohammad Imran Hossain
Candidate

Civil Engineering
Department

This dissertation is approved, and it is acceptable in quality and form for publication:

Approved by the Dissertation Committee:

Dr. Rafiqul Alam Tarefder, Chairperson

Dr. Arup Kanti Maji

Dr. Tang-Tat Ng

Dr. Yu-Lin Shen

MODELING MOISTURE-INDUCED DAMAGE
IN
ASPHALT CONCRETE

by

MOHAMMAD IMRAN HOSSAIN

B.Sc. (Civil Engineering), Bangladesh University of Engineering and Technology, 2003
M.Engg. (Structural), Bangladesh University of Engineering and Technology, 2008
M.S. (Civil Engineering), The Ohio State University, 2009

DISSERTATION

Submitted in Partial Fulfillment of the
Requirements for the Degree of

Doctor of Philosophy
Engineering

The University of New Mexico
Albuquerque, New Mexico

December, 2013

DEDICATION

To

My Wife Samira Binte Kashem

and

My Son Keyaan Mohammad Hossain

ACKNOWLEDGEMENTS

I would first like to thank my advisor, Dr. Rafiqul Tarefder, for his insight and guidance throughout my Ph.D. journey. I would also like to express my gratitude to him for giving me the freedom to choose my career path. I really appreciate Dr. Tarefder's initiatives, supports, and encouragement on my career development in research beyond this Ph.D. dissertation. He is a true leader, mentor, and a lifelong advisor.

My special thanks go to my committee members: Dr. Arup Maji, Dr. Tang-Tat Ng, and Dr. Yu-Lin Shen. I appreciate their insight into the research process and helpful suggestions. I am very thankful to Dr. Alok Sutradhar at The Ohio State University for his encouragements during my entire career in the USA.

This research project is made possible through a National Science Foundation (NSF) research project funding. I like to express my gratitude to the New Mexico Department of Transportation (NMDOT) for their funding since I worked in several of their projects. A special thanks to Graduate and Professional Student Association (GPSA) at The University of New Mexico for funding my research through Student Research Grant.

I would like to acknowledge the professors and staff at The University of New Mexico. Dr. Walter Gerstle has been especially helpful on numerical modeling by giving valuable suggestions. Dr. John Stormont provided guidelines on some laboratory testing. Yolanda Sanchez, Josie Gibson, Missy Garoza, Rebekah Lucero, Candyce Torres, and Ambrose Martinez have been especially kind in taking care of administrative needs and always providing me with a laugh. A special thank goes to Hope McVeety for her endless efforts on editing my journal and conference papers. Kenny Martinez was really helpful

arranging laboratory supplies. Very special thanks to Stoney Haver at Mechanical Engineering machine shop for technical supports on laboratory equipments.

At The University of New Mexico, I would like to express my appreciation to my colleagues Hasan Faisal and Amina Mannan for their help at the nanoindentation and binder laboratory respectively. Special thanks go to undergraduate research assistants: Shahidul Faisal and Ivan Syed at the pavement laboratory for preparing laboratory samples. I am glad to have good friends at The University of New Mexico who always encourage me and support me at their best.

Last, but certainly not least, I am most grateful for my family. I have exceptional sister, brother-in-law, nephew and niece. Thank you for your kind word, encouragement, and supporting me. I would like to thank my parents for their unending support while they were alive. This effort and dissertation is a direct result of their commitment to being the best parents possible. Finally, this dissertation is dedicated to Samira Kashem and Keyaan Hossain. This research work would not be completed unless their encouragement and believe on me.

Modeling Moisture-Induced Damage in Asphalt Concrete

by

Mohammad Imran Hossain

B.Sc. (Civil Engineering), Bangladesh University of Engineering and Technology, 2003

M.Engg. (Structural), Bangladesh University of Engineering and Technology, 2008

M.S. (Civil Engineering), The Ohio State University, 2009

Ph.D. (Engineering), The University of New Mexico, 2013

ABSTRACT

Moisture damage in Asphalt Concrete (AC) is not new but an unsolved problem. For decades laboratory studies have been conducted on both loose and compacted mix to understand the effects of moisture on the AC damage. Adhesive and cohesive damages are the two major types of damages occur inside the AC. Adhesive damage is a separation between aggregate and coated mastic or matrix materials and cohesive damage is the degradation of strength of matrix materials within the AC samples. In this study, Finite Element Method (FEM) modeling technique is used to identify initiation and progression of adhesive and cohesive damage. In addition, the effects of moisture in the mastic materials (i.e. mixture of fines passing no. 200 sieve and asphalt binder) are

determined by laboratory investigations since mastic materials govern the mechanical properties of AC.

The asphalt mastic-aggregate interface damage is quantified using FEM and traction separation law. Model parameters are determined from laboratory pull-off and strength testing of mastic materials. The contact stress is significantly higher in dry conditioned mastic-aggregate interface than in the wet conditioned interface for all load magnitudes and patterns. Lower contact stresses are one of the reasons for higher mastic-aggregate interface damage under wet condition. That is, Lower contact stresses are responsible for de-bonding at the interface. It is shown that 6.8% (% perimeter) interface de-bonding occurs in dry sample. On the other hand, about 49.1% interface de-bonding occurs in wet conditioned sample. Adhesive damage is significantly higher under the wet condition, since interface region is the weakest considering the whole domain.

Cohesive damage is determined by maximum stress criteria, which indicates that a material is damaged when it reaches the maximum strength. Cohesive damage initiates at the top of matrix and then damage propagates towards the bottom of matrix and matrix-aggregate interface. Moisture causes 62.8% more damage in the matrix materials when considering only the matrix materials under the applied deformation region.

In addition, pull-off test and shear tests are conducted on the mastic film under different Relative Humidity (RH%) conditions. Mastic films show flexible behavior due to high RH% conditioning and brittle behavior due to low RH% conditioning in pull-off tests. Increase in elasticity at high RH% conditioning causes a decrease in viscosity in mastic films. Decrease in viscosity of mastic materials causes binding inefficiency between

aggregates due to lack of bonding forces. Damage causes due to binding inefficiency, which results in lack of bonding within asphalt binder and between asphalt binder and aggregates. To support this argument, nanoindentation tests are performed on the mastic materials. It is observed that, dry mastic follows linear Burgers and wet mastic follows Maxwell or modified Maxwell viscoelastic mechanical model. Wet mastic shows high viscous depth (i.e. low viscosity) compare to the dry mastic. In addition, Maxwell model does not show any retardation strain. Hence, it is proved that moisture takes away viscous effects from the AC and causes damage.

TABLE OF CONTENTS

LIST OF FIGURES

LIST OF TABLES

CHAPTER 1

INTRODUCTION

1.1 Problem Statement

Moisture damage in Asphalt Concrete (AC) is an unsolved problem. AC consists of asphalt binder, aggregate, and fines. The fines are defined as the material passing #200 sieve (0.075 mm). Asphalt binder creates a thin film or coating around the aggregate particles and fines. Indeed, the fines become trapped inside an asphalt binder film, which is also known as mastic. In this study, the mixture of asphalt binder and aggregates passing a #4 sieve (4.75 mm) and retained on a #200 sieve is called matrix. Thus AC can be defined as coarse aggregate (retain on #4 sieve) coated with mastic material and surrounded by matrix material. Characterization and modeling of moisture-induced damages in mastic and matrix are the main topics of discussion in this study.

Moisture-induced damage in asphalt concrete can be attributed to two primary mechanisms, namely, the loss of adhesion, and the loss of cohesion (Figure 1). Loss of adhesion, also called stripping, is caused by the breaking of the adhesive bonds between the aggregate surface and the mastic primarily due to the action of water (Tarefder and Zaman 2010). Loss of cohesion is caused by the softening or breaking of cohesive bonds within the matrix or mastic due to the action of water. The phenomena of adhesive and cohesive damage are shown schematically in Figure 1. Figure 1(a) shows a fresh sample of AC, which has not been subjected to any moisture-induced damage. Figure 1(b) shows loss of bonding within the matrix material (cohesive) and at mastic-aggregate or matrix-

aggregate interface (adhesive). Damages within the aggregate can be considered negligible and is not addressed in this study. The mechanisms of initiation (location and cause) and propagation (path, cause, and extent) of moisture-induced damages in matrix and mastic-aggregate interface are not known and therefore, addressed in this study through laboratory testing and Finite Element Method (FEM) modeling.

Damage within the mastic and/or at mastic-aggregate interfaces has been studied by several researchers (Scarpas 1997, Masad et al. 2001, Sadd et al. 2003, Kim and Little 2004). Lytton and his co-workers developed a phenomenological model that relates the compressive strength reduction in dry and wet conditions during cyclic loading to the work of adhesion, and the percentage of the aggregate surface area that has been exposed to water during testing (Cheng et al. 2002). Damage in mastic material due to diffusion of moisture under load and water flow has been thoroughly investigated (Kringos and Scarpas 2005, Kringos et al. 2007). Moisture-induced mastic-aggregate interface strength has been determined by pull-off tests (Kringos et al. 2008a). In addition, an empirical relation between moisture content and damages in mastic-aggregate interface has been developed (Kringos et al. 2008b, and 2008c). Caro et al. (2010a) focused on mastic film rupture due to moisture diffusion, dispersion, and desorption. It has been observed that fracture progresses through the mastic-aggregate interfaces due to long term diffusion action under loading conditions. Chang et al. (2003) determined the relationship between aggregate and asphalt surface characteristics under dry and wet conditions from surface energy point of view. It has been shown that moisture conditioned aggregate and asphalt binder has lower surface energy than unconditioned samples. Lower surface energy might cause moisture-induced damages in asphalt concrete. Tarefder et al. (2009) carried out

detailed investigations of crack growth through predefined notches in moisture conditioned asphalt concrete by laboratory testing. A semi-circular notched sample was loaded diametrically. It was shown that the crack propagates predominantly through the matrix materials and through the interface of matrix and aggregates upon moisture-conditioning. Also Tarefder and Arifuzzaman (2010) conducted nanoscale indentation testing on moisture conditioned mastic and aggregate for determining strength by considering contact mechanics. Significant reduction in hardness and Young's modulus of moisture conditioned mastic materials was observed. They also performed atomic force microscopy tests on moisture-induced asphalt binder using a chemically functionalized tip to understand moisture damage. They reported that moisture conditioned asphalt binders have less adhesive force than unconditioned binders. Moraes et al. (2011) studied bond strength between asphalt-aggregate interfaces under moist conditions using pull-off tests in the laboratory. Moisture induced asphalt binders showed adhesive failures due to pull-off force. Also moisture conditioned asphalt binders required less pull off forces. The pull-off test results ware verified using FEM modeling (Ban et al. 2011). Theories based on the principles of fracture mechanics have recently been employed to model and predict moisture-induced damage in asphalt concrete under indirect tensile loading (Birgisson et al. 2007). These studies suggest that a single parameter such as the ratio of indirect tensile strength of wet and dry sample is not sufficient to evaluate the complex interactions involved in moisture damage. Birgisson et al. (2007) used dissipated creep strain energy, tensile strength and stress to assess moisture induced damage.

None of the previous studies have identified the location and causes of adhesive and cohesive damage initiation, nor examined how damage progresses in the matrix and mastic-aggregate interfaces. In addition, it is not known what type of damage (cohesion or adhesion) caused easily due to mechanical action of water and loading. Specific measures and/or reinforcement can be done to prevent premature damages in AC if mechanisms of damage initiations and progressions within the mastic-aggregate interface and matrix materials can be identified.

A though laboratory test results provide a good assessment regarding moisture sensitivity of mastic and matrix materials, it is still difficult to understand initiation and progression of adhesive and cohesive damages in AC pavements through laboratory testing. Numerical modeling could overcome this limitation. FEM models based on damage mechanics are developed for such purpose in this study. Specifically, macro scale testing is conducted on mastic samples by applying static load under dry and wet conditions. Moisture damage is evaluated based on the laboratory test results (i.e. load, displacement, damage). A damage parameter in the model accounts for adhesive and/or cohesive damages due to mechanical action of water and loading. The simulation output, which is damage, is used for understanding the damage initiation and progression of moisture interactions with matrix and mastic-aggregate interfaces. Laboratory tests are conducted on mastic materials at different Relative Humidity (RH%) to determine the effects of vapor in the material. Laboratory test results are use for model validation. The following two hypotheses are proposed for this study.

1.2 Hypothesis

1.2.1 Hypothesis One

The mechanics of initiation and progression of moisture-induced adhesive and cohesive damage at the mastic-aggregate interface and inside the matrix are not known. It is hypothesized that adhesive and cohesive damage in mastic-aggregate interface can be studied by developing FEM models. Adhesive damage due to moisture can be identified by computing contact status between mastic-aggregate interfaces. Cohesive damage due to moisture can be identified by determining strength degradation of the matrix.

1.2.2 Hypothesis Two

Conventional indirect tensile tests only compare the strength between undamaged and moisture-induced damaged samples. It is unknown what moisture causes inside the material. It is hypothesized that causes of damage in mastic material due to moisture can be determined by conducting direct pull-off and shear tests at small scales, and nanoindentation tests. The change in material properties such as strength and displacement measured at different vapor concentration conditions can be used to identify the change that are caused by moisture in mastic material. This result can be validated by nanoindentation tests by developing viscoelastic mechanical models for mastic materials.

1.3 Dissertation Organization

The dissertation consists of eight chapters. Chapter 1 describes problem statements and hypotheses. Chapter 2 summarizes the literature review on material damage theories and laboratory tests of AC. Chapter 3 describes laboratory tests and FEM models conducted

for demining mastic-aggregate interface damage. Chapter 4 describes laboratory tests and FEM models conducted for determining damage in matrix material. Chapter 5 describes FEM models for determining matrix-aggregate interface damage. Chapter 6 describes laboratory tests to determine damage in mastic film. Chapter 7 describes nanoindentation tests on mastic materials for developing viscoelastic mechanical models. Finally, Chapter 8 summarizes conclusions of this study and provides recommendations for future study.

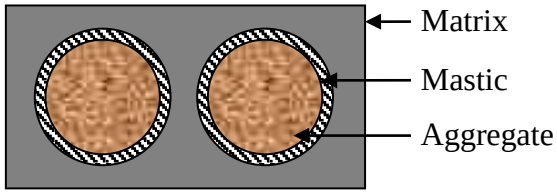

(a) No loss of bonding

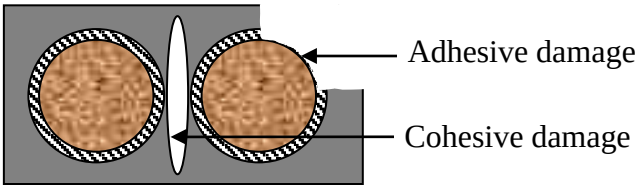

(b) Loss of bonding

Figure 1.1 Schematic of adhesive and cohesive damages in asphalt concrete

CHAPTER 2

LITERATURE REVIEW

2.1 General

This chapter describes available damage models for different materials such as ductile materials, fiber reinforced composite materials, and visco-elastic-plastic materials. Different methodologies for determining damages in Asphalt Concrete (AC) are described. The laboratory tests to predict moisture-induced damages in AC are summarized.

2.2 Introduction

Damages in materials have been studied for decades. According to Lemaitre and Desmorat (2005), Kachanov first introduces the term ψ and called it "continuity" as a field variable in the year of 1958. It has been mentioned that Kachanov used $D = (1-\psi)$ as an internal state variable where $0 \leq D \leq 1$. Later, the term D is considered as damages in materials due to applied load. It has also been mentioned that Robotnov first introduces the concept of effective stress in the year 1968. Robotnov noticed that load carrying capacity of a material reduces due to applied load. Though, basic developments of damage mechanics have been occurred in 1970.

According to Krajcinovic (1996, 2002), a solid is considered to be damaged if some of the bonds connecting parts of its microstructure are missing. Bonds between the molecules in a crystalline lattice may be ruptured, molecular chains in the polymers broken and the adhesion at the fiber-matrix interface lost. Also, a large number of micro-

cracks are randomly scattered over a large part of an impaired volume such that volumes loose partially the ability to transfer the momentum and fracture strength. Talreja (1994) refers damage as collectively to all entities of characteristic of objects in microscopic size, which are capable of changing their characteristic dimensions under the mechanical loading. In addition, Talreja (1994) added that, a damage entity is an individually identifiable change in the microstructural constitution of a solid which is brought about by an internal energy dissipative mechanism. Finally, damage is defines as a collection of all damage entities or, equivalently, as the set of all damage modes present in a body.

2.3 Damage in Ductile Materials

Materials show considerably larger plastic deformation before failure is known as ductile materials. For an example, steel is a ductile material. According to Bonora (1999), upon loading, microvoids are formed in ductile materials as a consequence of cracking or matrix debonding of the embedded brittle inclusions such as Carbides or Sulfides. Void nucleation as a particle is strongly dependent upon how the particle is bonded to the ductile matrix. If the bonding is weak, void will nucleate at low stresses and low strains and vice versa. Different criteria of ductile damages are presented below. The models are described and summarized from the ABAQUS (2009) manuals.

2.3.1 Porosity Model

The porosity model is also known as Gurson model. The Gurson model assumes that there is only one spherical void which is equivalent to the effective void distribution in the materials, in a ductile homogeneous and incompressible matrix. The material is

considered to be a rigid-perfectly plastic; the voided cell is under fully plastic and axi-symmetric deformation mode.

$$F = \left(\frac{\sigma_{eq}}{\sigma_y}\right)^2 + 2f\,cosh\left(\frac{3\sigma_m}{2\sigma_y}\right) - \left(1 + f^2\right) \tag{2.1}$$

where σ_{eq} = equivalent von Mises stress, calculated from the macroscopic Cauchy stress tensor σ_{ij} and its deviator s_{ij}. σ_m = hydrostatic part of $\sigma_{ij} = \left(\sigma_1 + \sigma_2 + \sigma_3\right)/3$ and σ_y = flow stress (current yield stress) of the matrix material, *f* is the porosity with is a ration of volume of void with total volume.

2.3.2 Continuum Damage Model

Continuum Damage Model (CDM) differs from the porosity-based models, because damage is one of the state variables, and its evolution is given by an equation function of the associated variables. In CDM, damage is the variables that are indirectly linked to the void growth process, in fact, in this framework it is not important in which way the single void is evolving of how many voids are coalescing while others are nucleating. Therefore, damage takes into account the progressive degradation of the material properties and the loss of performance in stiffness loss due to the irreversible processes associated with micro structural modification such as void formation and growth, micro cracking of brittle inclusions and their mutual interactions.

A physical definition of the damage variable can be given by considering that the presence of a damage state in the Reference Volume element (RVE) reduces the effective

resisting nominal area. Assuming, for simplicity, isotropic of the damage state, it is possible to write the following scalar expression:

$$D = 1 - \frac{A_{eff}}{A_0} \tag{2.2}$$

where, A_0 is the nominal section area of an RVE and A_{eff} the effective resisting section area reduced by damage. The definition of effective stress allows the damage variable D to be expressed as a function of the material stiffness reduction:

$$D = 1 - \frac{E_{eff}}{E_0} \tag{2.3}$$

The damage variable D is coupled with the plastic strain. Plasticity damage is related to the irreversible strain at the micro level and meso level. Damage phenomena are localized on the material micro scale and their effects remain confined until the complete failure of several RVEs occurs with the appearance of a macroscopic crack. Damage affects only stresses; the total strains are the same on both the macro scale and micro scale.

2.3.3 Johnson-Cook Damage Model

Johnson-Cook criteria is a special form of ductile damage where the equivalent plastic strain ε_D^{pl} is assumed to be the form of,

$$\varepsilon_D^{pl} = \left[d_1 + d_2 \, exp\left(-d_3 \eta\right) \right] \left[1 + d_4 \, ln\left(\frac{\dot{\varepsilon}^{pl}}{\dot{\varepsilon}_0} \right) \right] \left(1 + d_5 \bar{\theta} \right) \tag{2.4}$$

Where, d_1-d_5 is the failure parameter, $\dot{\varepsilon}_0$ is the reference strain rate and $\bar{\theta}$ is a non-dimensional temperature defined as,

$$\bar{\theta} = \begin{cases} 0 & for\ \theta < \theta_{transition} \\ \left(\theta - \theta_{transition}\right)/\left(\theta_{melt} - \theta_{transition}\right) & for\ \theta_{transition} \le 0 \le \theta_{melt} \\ 1 & for\ \theta > \theta_{melt} \end{cases} \tag{2.5}$$

where, θ is current temperature, θ_{melt} is melting temperature and $\theta_{transition}$ is the transition temperature is defined as one at or below which there is no temperature dependence on the expression of the damage strain ε_D^{pl}.

2.3.4 Shear Damage Model

The shear criterion is a phenomenological model for prediction the onset of damage due to shear band localization. The model assumes that the equivalent plastic strain at the onset of damage is ε_s^{pl} is a function of shear stress ration and strain rate.

$$\varepsilon_s^{pl}\left(\theta_s, \dot{\varepsilon}^{pl}\right) \tag{2.6}$$

here, the shear stress ratio θ_s can be expressed as,

$$\theta_s = \frac{\left(q + k_s p\right)}{\tau_{max}} \tag{2.7}$$

where, τ_{max} is the maximum shear stress, k_s is the material parameter.

2.3.5 Formation Limit Diagram Criterion

Necking instability is an important factor for sheet metal forming process. The size of the local neck region is typically the order of the thickness of the sheet and the local neck is rapidly leads to fracture. The conventional damage criteria are not applicable for necking instability modeling. The Forming Limit Diagram (FLD) is a useful concept to determine the amount of deformation that a material can withstand prior to the onset of necking instability. The maximum strains that a sheet material can sustain prior to the onset of necking are referred to as the forming limit strains. A FLD is a plot of the forming limit strains in the space of principal (in-plane) logarithmic strains. In the discussion that follows major and minor limit strains refer to the maximum and minimum values of the in-plane principal limit strains, respectively. The major limit strain is usually represented on the vertical axis and the minor strain on the horizontal axis, as illustrated in Figure 2.1. The line connecting the states at which deformation becomes unstable is referred to as the Forming Limit Curve (FLC). The FLC gives a sense of the formability of a sheet of material.

The damage initiation criterion for the FLD is given by the condition ω_{FLD}=1, where the variable ω_{FLD} is a function of the current deformation state and is defined as the ratio of the current major principal strain, ε_{major}, to the major limit strain on the FLC evaluated at the current values of the minor principal strain, ε_{minor}.

2.3.6 Forming Limit Stress Diagram Criterion

When strain-based FLCs are converted into stress-based FLCs, the resulting stress-based curves have been shown to be minimally affected by changes to the strain path; that is,

different strain-based FLCs, corresponding to different strain paths, are mapped onto a single stress-based FLC. This property makes Forming Limit Stress Diagrams (FLSDs) an attractive alternative to FLDs for the prediction of necking instability under arbitrary loading.

2.3.7 Marciniak Kuczynki Criterion

In Marciniak Kuczynki (M-K) analysis, virtual thickness imperfections are introduced as grooves simulating preexisting defects in an otherwise uniform sheet material. The deformation field is computed inside each groove as a result of the applied loading outside the groove. Necking is considered to occur when the ratio of the deformation in the groove relative to the nominal deformation (outside the groove) is greater than a critical value.

Figure 2.2 shows schematically the geometry of the groove considered for M-K analysis. In the figure, *a* denotes the nominal region in the shell element outside the imperfection, and *b* denotes the weak groove region. The initial thickness of the imperfection relative to the nominal thickness is given by the ratio $f_0 = t_0^b / t_0^a$, with the subscript *0* denoting quantities in the initial, strain-free state. The groove is oriented at a zero angle with respect to the 1-direction of the local material orientation.

The onset of necking instability is assumed to occur when the ratio of the rate of deformation inside a groove relative to the rate of deformation if no grooves are present is greater than a critical value.

2.4 Damage in Fiber Reinforced Composite Materials

The composite materials show different damage scenario than the conventional materials. Both the fiber and matrix shows damages. Damage is characterized by the degradation of material stiffness. Many such materials exhibit elastic-brittle behavior; that is, damage in these materials is initiated without significant plastic deformation. Consequently, plasticity can be neglected when modeling behavior of such materials. Four different modes of failure are considered for fiber reinforced composite materials:

1. Fiber rupture in tension
2. Fiber buckling and kinking in compression
3. Matrix cracking under transverse tension and shearing, and
4. Matrix crushing under transverse compression and shearing.

The response of the composite material is computed from

$$\sigma = C_d \varepsilon \tag{2.8}$$

Where, ε is the strain and C_d is the elasticity matrix, which reflects any damage and has the form:

$$C_d = \frac{1}{D}\begin{bmatrix} (1-d_f)E_1 & (1-d_f)(1-d_m)\upsilon_{21}E_1 & 0 \\ (1-d_f)(1-d_m)\upsilon_{12}E_2 & (1-d_m)E_2 & 0 \\ 0 & 0 & (1-d_s)GD \end{bmatrix} \tag{2.9}$$

where, $D=1-(1-d_f)(1-d_m)v_{12}v_{21}$, d_f reflects the current state of fiber damage, d_m reflects the current state of matrix damage, d_s reflects the current state of shear damage, E_1 is the

Young's modulus in the fiber direction, E_2 is the Young's modulus in the direction perpendicular to the fibers, G is the shear modulus, and v_{12} and v_{21} are Poisson's ratios.

2.4.1 Interface Damage

The failure of the fiber/matrix interface is the principal source of damage. This failure is determined by a local criterion which combines the normal and the shear stresses by a linear relation. Because the interfacial damage is distributed statically as a function of the spatial distribution of the microstructure, the local interface failure criterion must be written in a statistical form,

$$Pr\left(\sum\right) = 1 - exp\left(-\frac{\sigma + \beta\tau}{Ri}\right)^n \tag{2.10}$$

where, Pr denotes the interface failure probability relative to a given interfacial stress state σ and τ. σ and τ are the normal and the shear stress at the interface which are a function of the macroscopic stress, $\sum$, and of the fiber orientation. β is a coupling parameter and Ri denotes the interfacial strength and n is the statistical parameter. The knowledge of β, Ri and n denotes completely the statistical interface failure criterion. The three parameters of the interface criterion are numerically identified by using the micromechanical model to fit the experimental results.

2.4.2 Matrix Damage

The assumption is that the damage or failure of the specimen takes place by the coalescence of the micro-cracks initiated in the matrix from the broken particles. It is necessary to have knowledge of the stress and strain fields close to the broken particles in

order to elaborate a failure criterion. It has been observed that the damage occurs around the precipitates in the matrix including cavities growth.

2.5 Damage for Elastomers

The elastomer damage is described by Mullin effect. The Mullins effect material model is intended for modeling the phenomenon of stress softening, commonly observed in filled rubber elastomers as a result of damage associated with straining. When an elastomeric test specimen is subjected to simple tension from its virgin state, unloaded, and then reloaded, the stress required on reloading is less than that on the initial loading for stretches up to the maximum stretch achieved during the initial loading. This stress-softening phenomenon is known as the Mullins effect. Stress softening is interpreted as being due to damage at the microscopic level. As the material is loaded, damage occurs by the severing of bonds between filler particles and the rubber molecular chains. Different chain links break at different deformation levels, thereby leading to continuous damage with macroscopic deformation. An equivalent interpretation is that the energy required to cause the damage is not recoverable.

The stress-strain behavior of loading and unloading of an elastomer is shown in Figure 2.4. The primary loading path is *abb'* of a previously unstressed material with loading until an arbitrary point b' is reached. On unloading from b', the path *b'Ba* is followed. When the material is loaded again, the softened path is retraced as *aBb'*. If further loading is then applied, the path *b'cc'* is followed, where *b'cc'* is a continuation of the primary loading path *abb'cc'* (which is the path that would be followed if there was no unloading). If loading is now stopped at *c'*, the path *c'Ca* is followed on unloading and

then retraced back to *c'* on reloading. If no further loading beyond *c'* is applied, the curve *cCc'* represents the subsequent material response, which is then elastic. For loading beyond c', the primary path is again followed and the pattern described is repeated. This is an ideal representation of Mullins effect.

2.6 Asphalt Concrete Pavement Damage Models

AC pavement is consists of asphalt, coarse aggregates, fine aggregates, fines and air voids. Asphalt is used as a bonding agent in asphalt concrete. Both coarse, fine aggregates and fines are necessary for good bonding and appropriate compaction in the asphalt concrete. Asphalt is heated up to appropriate temperature before mixing with hot course and fine aggregates. AC pavement experiences dynamic load from traffic. The load is taken care by the interlocking force of aggregates and adhesive/cohesive forces of aggregate and asphalt. AC pavement also experiences environmental load in addition to traffic load. The environmental load comes from different sources of water/ice, oxidation and temperature. The sources of water could be rainfall, seepage flow, capillary flow etc. Water passes through the asphalt film by diffusion process and get into contact with aggregates. Aggregates then absorb water until it becomes saturated. Aggregates and asphalt get weak upon presence of water due to chemical reaction between aggregate minerals and asphalt functionalize groups. Contentious interaction with moisture weakens both asphalt and aggregates. The result is damages in cohesive and adhesive interactions. Progressive damage causes failure. The damages between the asphalt-aggregate interfaces occur in micro scale level and progress to macro scale level. The strength of pavements decreases and continuous degradation of materials cause ultimate failure of pavements.

Pavement damage models are primarily described with constitutive models. There are two different models have been described in the literature. The models are,

1. Visco-elastic-plastic modeling of asphalt concrete
2. Unified disturbed state constitutive modeling of asphalt concrete

The models described the asphalt's behavior with temperature and loading conditions. Until now no constitutive model is available for predicting moisture-induced damages.

2.6.1 Constitutive Model of Asphalt

According to Wang (2011) the constitutive equations are actually a set of phenomenological relationships between cause and effect such as stress and strain. For the case of asphalt, the relationship of stress and strains are not straight forward due to its viscous properties. Two common behaviors are observed in viscoelastic asphalt materials, one is creep and other is stress relaxation. Creep is time dependent strain function under a constant stress. For a certain temperature, under constant stress the strain increases with time. On the other hand the stress relaxation is the time dependent stress under a constant strain. For a certain temperature, under constant strain the stress decreases with time. The stress-strain relationship for viscoelastic material can represents as,

$$\sigma(t) = \int_{-\infty}^{t} C\left(t - t'\right) \frac{\partial \varepsilon\left(t'\right)}{\partial t'} dt' \tag{2.11}$$

where $\sigma(t)$ is stress with is a function of time, C is relaxation modulus, t is time variable, t' is reference time variable and $\varepsilon\left(t'\right)$ is strain function of time.

2.6.2 Visco-Elastic-Plastic Continuum Damage Model

Kim (2009) described the Visco-Elastic-Plastic Continuum Damage (VEPCD) model. The model is divided into two parts; viscoelastic and viscoplastic. The damage is based on micro cracking due to strain caused by cyclic loading. Also the model can be calibrated with Time-Temperature Superposition (TTS) principle with growing damage to describe the effect of temperature in viscous materials.

The viscoelastic part of the damage can be presented as,

$$\varepsilon_{ve} = E_R \int_0^{\xi} D(\xi - \tau) \frac{d\left(\frac{\sigma}{C(S)}\right)}{d\tau} d\tau \tag{2.12}$$

where E_R is the reference modulus, which is a constant and has the same dimension as the relaxation modulus *E(t). C(S)* indicates that *C* is a function of single damage parameter *S*. The damage is due to accumulation of elastic strains into the materials for a long time. *D* is the creep compliance, τ is integration variable and ξ is time.

The viscoplastic part of the damage model can represent as,

$$\varepsilon_{vp} = \left(\frac{p+1}{Y}\right)^{1/(p+1)} \left(\int_0^{\xi} \sigma^q d\xi\right)^{1/(p+1)} \tag{2.13}$$

here *p, q* and *Y* are the model coefficients.

2.6.3 Disturb State Constitute Model

Desai (2007) described the unified Disturbed State Constitutive (DSC) model for pavement structures. The DSC model is based on the idea that the behavior of a deforming material can be expressed in terms of the behavior of the Relative Intact (RI) or continuum part and the micro cracked part called the Fully Adjusted (FA) part. During the deformation, the transformation of RI to FA occurs due to microstructural changes caused by relative motions as translation, rotation and interpolation of the particles and softening or healing at the micro level. The simple expression of the DSC model is,

$$d\underline{\sigma}^{a} = \underline{C}^{D} d\underline{\varepsilon} \tag{2.14}$$

where $\underline{\sigma^{a}}$ and $\underline{\varepsilon}$ is the stress and strain vectors, respectively, *a* is observed RI responses, $\underline{C^{D}}$ is constitutive matrix, *D* is disturbance and assumed as scalar. If there is no damage (i.e. *D=0*), then the equation rewrite as,

$$d\underline{\sigma}^{i} = \underline{C}^{i} d\underline{\varepsilon}^{i} \tag{2.15}$$

where $\underline{C^{i}}$ represents elastic, elastic-plastic, or visco-elastic-plastic responses. The parameter *D* can be computed using the following equation,

$$D = D_{u}\left(1 - e^{-A\xi_{D}^{Z}}\right) \tag{2.16}$$

where, *A*, ξ_{D}, and *Z* are the disturbance parameters. ξ_{D} is the deviatoric strain component.

$$\xi_{D} = \int \left(dE_{ij}^{p} . dE_{ij}^{p}\right)^{1/2} \tag{2.17}$$

where dE_{ij}^{p} is deviatoric plastic strain.

2.6.4 Surface Energy Based Damage Model

Cheng et al. (2003) developed an adhesion failure model based on surface energy theory and moisture diffusion model based on results from Universal Sorption Device (USD) testing. Adhesive strength is influenced by surface energies of asphalt and aggregate, surface texture of aggregate, and the presence of water.

The surface energy in an asphalt aggregate system is primarily composed on a nonpolar component and an acid-base component.

$$\Gamma = \Gamma^{LW} + \Gamma^{AB} \tag{2.18}$$

where Γ is the surface energy of asphalt or aggregate, Γ^{LW} is the Lifshitz-van der Walls component of surface energy, Γ^{AB} is the acid-base component of surface energy. The surface energy of adhesion between two different materials can be expressed as,

$$\Delta G_{ij}^{a} = \Delta G_{ij}^{aLW} + \Delta G_{ij}^{aAB} \tag{2.19}$$

where ΔG_{ij}^{aLW} is the non polar part of the surface energy of adhesion and can be expressed as,

$$\Delta G_{ij}^{aLW} = 2\sqrt{\Gamma_i^{LW}\Gamma_j^{LW}} \tag{2.20}$$

$$\Delta G_{ij}^{aAB} = 2\sqrt{\Gamma_i^{+}\Gamma_j^{-}} + 2\sqrt{\Gamma_i^{-}\Gamma_j^{+}} \tag{2.21}$$

where Γ^+ is the Lewis acid component, Γ^- is the Lewis base component. The subscripts *i* and *j* represent the asphalt and aggregate, respectively.

For general case, the surface energy of adhesion for two different materials in contact within a third medium can be expressed as,

$$\begin{aligned}\Delta G^a_{123} &= \Gamma_{13} + \Gamma_{23} - \Gamma_{12} \\ &= 2\Gamma_3^{LW} + 2\sqrt{\Gamma_1^{LW}\Gamma_2^{LW}} - 2\sqrt{\Gamma_1^{LW}\Gamma_3^{LW}} + 4\sqrt{\Gamma_3^+\Gamma_3^-} - 2\sqrt{\Gamma_3^+}\left(\sqrt{\Gamma_1^-} + \sqrt{\Gamma_2^-}\right) \\ &\quad -2\sqrt{\Gamma_3^-}\left(\sqrt{\Gamma_1^+} + \sqrt{\Gamma_2^+}\right) + 2\sqrt{\Gamma_1^+\Gamma_2^-} + 2\sqrt{\Gamma_1^-\Gamma_3^+}\end{aligned} \tag{2.22}$$

where, subscripts *1*, *2*, and *3* can be represent as asphalt, aggregate and water respectively.

2.6.5 Moisture Diffusion Model

Diffusion is the flow at a molecular level under the influence of an appropriate property gradient. The steady-state form of Fick's first law states the relationship between the flux of moisture and the concentration gradient. Fick's first law can be expressed as,

$$F = -D\left(\frac{\partial c}{\partial x}\right) \tag{2.23}$$

where *F* is the flux of moisture (kg/m^2 sec), with is the rate of transfer per unit area of section, $\frac{\partial c}{\partial x}$ is the gradient of concentration *c*, *D* is the coefficient of proportionality and the negative sign indicates that the flux occurs in the direction of decreasing *c*.

Crank (1975) derived a diffusion equation for a sheet of material or membrane as described below.

$$\frac{M_t}{M_\infty} = 1 - \frac{8}{\pi^2}\sum_{m=0}^{\infty}\frac{1}{(2m+1)^2}\, e^{\left(\frac{D(2m+1)^2\pi^2 t}{h^2}\right)} \tag{2.24}$$

where M_t is the total amount of vapor absorbed by the sample at time t, M_∞ is the equilibrium sorption attained when the sorption curve reach a constant value, and h is the sample thickness.

Kringos et al. (2008b and 2008c) mentioned that the assumption of the equation is the sheet of mastic is immediately placed in the vapor and that each surface attains a concentration value corresponding to the equilibrium moisture capacity M_∞ for the vapor pressure existing and remain constant afterward. In $Mt/M\infty=0.5$, which is called "half time" of the sorption process then the previous equation turns to,

$$D = 0.049\frac{1}{\left(\frac{t_{0.5}}{h^2}\right)} \tag{2.25}$$

The moisture diffusion model is based on adsorption and absorption of water in asphalt film. The term adsorption means to gather (a gas or liquid) on a surface in condensed layer. On the other hand absorption means to incorporate. In the first stage both adsorption at the asphalt surface and absorption within the asphalt occur simultaneously. In the second stage, adsorption on the surface of the asphalt comes to equilibrium but absorption continues and eventually becomes constant. The second stage can be expressed by,

$$w = w_{100}\left(1 - e^{\frac{-3Dt}{l^2}}\right) + C \tag{2.26}$$

where W is the measured water mass, W_{100} is the maximum absorption of asphalt film, C is the absorption constant at the vapor pressure level at which the measurement are made, l is the layer thickness. The first stage can be expressed by,

$$w = w_{100}\left(1 - e^{\frac{-3Dt}{l^2}}\right) + w_a\left(1 - e^{-\alpha t}\right) \tag{2.27}$$

2.7 Finite Element Method Model

The Finite Element Method (FEM) is a numerical method for solving problems of engineering and physics. The usefulness of this method is limited to structural analysis, heat transfer, fluid flow, mass transport and electromagnetic potential. This method is very useful for complicated geometry, loading and material properties where the conventional analytical solution is limited (Logan, 2007). The fundamental of FEM is to measure force/moment due to displacement/ rotation in a body specifically in a node of an element or vice-versa. A structure is divided into small pieces and analyze individually and then integrated to get the resultant for the whole structure. To get more accurate results the number of elements is increased. Figure 2.5 shows a element with a force P_i at the corner node. The response in terms of stress or strain due to applied load can be determined by FEM model.

The basic principle of FEM is based on the potential energy that is stored to a structure. The potential energy is decreases due to application of external forces, decrease in body

forces (i.e. gravitational forces and electromagnetic forces) and surface traction force. According to Ugural (1991), the work done by external forces in producing deformation is stored within the body as "Strain energy". For perfectly elastic body no dissipation of the energy occurs, and all the stored energy is recovered upon unloading. Let an element is subject to a slowly increasing normal stress σ_x. The element is assumed to be initially free of stress. The cross sectional dimension is *dy.dz*. The force acting on the cross sectional force is σ_x*.dy.dz*, elongates the element as amount of ε_x*.dx*, where ε_x is the x-direction strain. In the case of linear elastic material, $\sigma_x = E.\varepsilon_x$. The average force acting on the element during the straining is *1/2 σx.dy.dz*. Thus the strain energy *U* corresponding to the work done by this force, *1/2 σx.dy.dz.*ε_x*.dx*, is expressed as,

$$dU = \frac{1}{2}\sigma_x \varepsilon_x \left(dxdydz\right) = \frac{1}{2}\sigma_x \varepsilon_x dV \tag{2.28}$$

where *dV* is the volume of the element. The strain energy per unit volume, *dU/dV*, is referred to as the "strain energy density", designated U_0. So,

$$U_0 = \frac{1}{2}\sigma_x \varepsilon_x = \frac{\sigma_x^2}{2E} \tag{2.29}$$

The quantity represents the area under stress-strain curve up to proportional limit.

The work equivalent finite element model with applied force can be expressed as,

$$\Pi_p = \iiint \frac{1}{2}\lfloor \varepsilon \rfloor \{\sigma\} d_{vol} - \iiint \lfloor u \rfloor \{B\} d_{vol} - \lfloor d_i \rfloor P_i - \iint \lfloor u \rfloor \{T\} d_{sur} \tag{2.30}$$

where, ε is the strain vector, σ is the stress vector, u is the displacement vector, B is the body force, d_i is the displacement at node i, P_i is the applied external force at node i and T is the traction force over the surface. After discretization,

$$\Pi_p = \frac{1}{2}\lfloor d_i \rfloor \iiint [b]^T [E][b] d_{vol} \{d_i\} - \lfloor d_i \rfloor \iiint [N]^T \{b\} d_{vol} - \lfloor d_i \rfloor P_i - \iint [N]^T \{T_i\} d_{sur} \tag{2.31}$$

where b is the differential matrix of shape function, E is the stiffness matrix, N is the shape function matrix and the subscript T is the transpose of matrix. The dictionary explanation of "traction" is the adhesive friction of body on some surface or attraction power or influence. If the traction force between the aggregate surface and asphalt for both dry and wet condition could measure, then FEM model can be generated using commercially available software called ABAQUS. Moreover the damage between the interaction surfaces can be evaluated.

2.7.1 Traction-Separation Damage Model

This law is applicable for cohesive elements. This law assumes that the traction-separation behavior is linear up to the initiation and evolution of damage. The elastic behavior is written in terms of an elastic constitutive matrix that relates the nominal stresses to the nominal stains across the interface. The nominal stresses are the force components divided by the original area at each integration point. On the other hand, the nominal strains are the separations divided by the original thickness at each integration point.

The nominal traction stress vector, t, consists of three components t_n, $t_{s,}$ and t_t. Three corresponding separations are denoted by δ_n, δ_s, and δ_t. T_0 is the original thickness of the cohesive element. The nominal strain can be defined as,

$$\varepsilon_n = \frac{\delta_n}{T_0};\ \varepsilon_s = \frac{\delta_s}{T_0};\ \varepsilon_t = \frac{\delta_t}{T_0} \tag{2.32}$$

The elastic behavior can then be written as,

$$t = \begin{Bmatrix} t_n \\ t_s \\ t_t \end{Bmatrix} = \begin{bmatrix} K_{nn} & K_{ns} & K_{nt} \\ K_{ns} & K_{ss} & K_{st} \\ K_{nt} & K_{st} & K_{tt} \end{bmatrix} \begin{Bmatrix} \varepsilon_n \\ \varepsilon_s \\ \varepsilon_t \end{Bmatrix} = K\varepsilon \tag{2.33}$$

The elasticity matrix provides fully coupled behavior between all components of the traction vector and separation vector. The uncoupled behavior can be found by taking zero for the off-diagonal terms.

2.7.1.1 Damage Initiation

As the name implies, damage initiation refers to the beginning of degradation of the response of a material point. The process of degradation begins when the stresses and/or strains satisfy certain damage initiation criteria that you specify. Several damage initiation criteria are available and are discussed below. Each damage initiation criterion also has an output variable associated with it to indicate whether the criterion is met. A value of 1 or higher indicates that the initiation criterion has been met.

In the discussion below, t_n^0, t_s^0, and t_t^0 represent the peak values of the nominal stress when the deformation is either purely normal to the interface or purely in the first or the

second shear direction, respectively. Likewise, ε_n^0, ε_s^0, and ε_t^0 represent the peak values of the nominal strain when the deformation is either purely normal to the interface or purely in the first or the second shear direction, respectively.

2.7.1.2 Maximum Nominal Stress Damage Initiation Criterion

Damage is assumed to initiate when the maximum nominal stress ratio reaches a value of one. This criterion can be represented as,

$$max\left\{\frac{\langle t_n \rangle}{t_n^0}, \frac{t_s}{t_s^0}, \frac{t_t}{t_t^0}\right\} = 1 \tag{2.34}$$

The symbol ⟨ ⟩ represents the Macaulay bracket with the usual interpretation. The Macaulay brackets are used to signify that a pure compressive deformation or stress state does not initiate damage.

2.7.1.3 Maximum Nominal Strain Damage Initiation Criterion

Damage is assumed to initiate when the maximum nominal strain ratio reaches a value of one. This criterion can be represented as,

$$max\left\{\frac{\langle \varepsilon_n \rangle}{\varepsilon_n^0}, \frac{\varepsilon_s}{\varepsilon_s^0}, \frac{\varepsilon_t}{\varepsilon_t^0}\right\} = 1 \tag{2.35}$$

2.7.1.4 Quadratic Nominal Stress Damage Initiation Criterion

Damage is assumed to initiate when a quadratic interaction function involving the nominal stress ratios reaches a value of one. This criterion can be represented as,

$$\left\{\frac{\langle t_n \rangle}{t_n^0}\right\}^2 + \left\{\frac{t_s}{t_s^0}\right\}^2 + \left\{\frac{t_t}{t_t^0}\right\}^2 = 1 \tag{2.36}$$

2.7.1.5 Quadratic Nominal Strain Damage Initiation Criterion

Damage is assumed to initiate when a quadratic interaction function involving the nominal strain ratios reaches a value of one. This criterion can be represented as,

$$\left\{\frac{\langle \varepsilon_n \rangle}{\varepsilon_n^0}\right\}^2 + \left\{\frac{\varepsilon_s}{\varepsilon_s^0}\right\}^2 + \left\{\frac{\varepsilon_t}{\varepsilon_t^0}\right\}^2 = 1 \tag{2.37}$$

2.8 Moisture Damage Tests and Methods

Several test methods are available to quantify moisture damages into asphalt concrete. Moisture damage tests are classified based on two major categories, qualitative tests and quantitative tests. The first test done on loose mix was about in 1920 and on compacted mix in about 1950 (Solaimanian et al., 2003).

2.8.1 Loose Mix Test

The following table gives short descriptions of available loose mix test,

Name of the test	Short description	Scope of the test
Methyne blue test	Find harmful clay and dust available into fine aggregate. Fine aggregates are immersed into Methyne blue and the color change of Methyne blue is recorder. The resulting color indicates the presence of harmful clay into the fine aggregate.	If the aggregate has montmorillonite-type clay then a good bonding between asphalt and aggregates cannot be achieved.

Name of the test	Short description	Scope of the test
Film stripping test	Loose mix of asphalt-aggregate is heated up to 60 °C for 15 to 18 hours. The sample is then cooled and place into 175 ml of distilled water. The sample is then rotate with a speed of 35 rpm for 15 min.	The sample is then checked under florescent light to determine the stripping area of aggregate.
Static immersion test	Loose mix is cured for 2 hr. at 60 °C and then cooled at room temperature. The mix is then put into 600 ml of distilled water for 16 to 18 hours.	The amount of stripping is observed and measured with establish criteria.
Dynamic immersion test	Similar to static immersion test with the curing time of 4 hr.	Since the immersion time is increased the stripping also increased.
Chemical immersion test	The stone aggregate mixed with asphalt are immersed with different concentration of Sodium Carbonate (Na_2CO_3). The concentration of Sodium Carbonate is recorded when the stripping of aggregate reaches such an extent that the film on aggregate does not exists, only specks or droplets are visible. The number of concentration is known as Riedel and Weber (R&W) number, ranges from 0 to 9.	The zero concentration means distilled water and 1 concentration means 0.41 gm of Sodium Carbonate into 1 L of water. The concentration of Sodium Carbonate increases in double for every number of R&W increment.
Surface reaction test	A gas will produce by a reaction with calcareous or siliceous minerals of aggregate with acid. The pressure created by the produced gas is proportional to the exposed surface area of stripped aggregate.	The aggregate coated with asphalt stripped by some means. Different amount of stripping on surface will give different pressure value.
Quick bottle test	This test is done to check the amount of antistripping agent used in the plant mix. Kerosene or Naphtha is used as a solvent of asphalt concrete. Ottawa sand is heated for 140 °F and the mixed with asphalt blend and shake for 30 sec.	Asphalt sand mixture is qualitatively checked for coating of asphalt on sand grain.
Boiling water test	The test is done with asphalt aggregate loose mix with boiled in water for 10 min.	Visual observation of stripping is done after the mix is cooled at room temperature.

Name of the test	Short description	Scope of the test
Rolling bottle method	Aggregate coated with asphalt are placed in jar of water and rotated to achieve agitation.	Periodically visual inspection of agitation is made.
Net adsorption	Asphalt is absorbed onto aggregate from a toluene solution, the amount of asphalt remain in solution is measured and the amount of asphalt absorbed by the aggregate is determined. Then water is added into the solution and asphalt agitated from aggregate surface.	The asphalt present in the solution is measured and remaining asphalt onto the aggregate is determined. The amount of asphalt remaining on the surface of aggregate is net adsorption of asphalt.
Surface energy	The surface free energy for aggregate is measured by universal sorption devise. Also the surface free energy of asphalt is measured by Wilhelmy plate device by measuring the dynamic contact angle between asphalt and liquid solvent.	The cohesive strength of asphalt itself is depends on the surface free energy of asphalt and the adhesive strength is depends on the surface free energy of asphalt and aggregates.
Pneumatic pull-off test	The tensile and bonding strength of binder applied on glass surface as a function of time while exposed into water. A 66Kpa/sec pulling force is applied onto 200 microns thick asphalt at 25 °C.	The higher the soaking time the less pulling force is required to detach the asphalt from the glass plate.

2.8.2 Compacted Mix Test

The following table gives short descriptions of available compacted mix test,

Name of the test	Short description	Scope of the test
Moisture vapor sensitivity	Specimens are prepared in stainless steel mold by kneading compactor. The compacted surface of each specimen is covered with aluminum seal cap. The edges are sealed to secure leak between the mold and cap. The sample is then placed in to 60 °C temperature water for 75	After conditioning the sample is tested in Hveem stabilometer.

	hours.	
Name of the test	**Short description**	**Scope of the test**
Immersion compression	One group of dry and one group of wet sample are used. The wet samples are immersed for 4 days at 120°F. A quick test can be done by immersing for 24 hr at 140 °F.	Compressive strength test is done for specific deformation rate and temperature. The average strength of conditioned sample with dry sample is used as an indicator of moisture sensitivity in the mix.
Marshall immersion	Similar to the previous test procedure, the conditioning is done.	Instead of compressive strength test, Marshall Stability test is used.
Freeze thaw pedestal test	Aggregate passing #20 (0.85 mm) and retained on #35 (0.5 mm) are selected for this test to minimize the variation of aggregate size in standard mix. The mix is prepared at 150 °C with 5% asphalt content. The specimen size is 41 mm in diameter and 19 mm thick. The sample is submerged for 3 days at room temperature into distilled water. Then the sample goes under thermal cycles of 15 hr into -12 °C and then 9 hr at 49 °C until it shows cracks.	The test stopped until the crack is shown.
Original Lottman indirect tensile test	One group of dry and one group of wet sample are prepared. The size of the sample is 4" in diameter and 2.5" thick. The conditioning is done initially for vacuum saturation with 26 in mercury vacuum for 30 min followed by 30 min at atmospheric pressure. The accelerated freeze–thaw saturation is done by putting sample into water bath for 0 °F for 15 hr followed by 140 °F for 24 hr. thermal cyclic conditioning can also be done.	After conditioning the sample is tested for tensile resilient modulus or indirect tensile test at 55 °F with 0.065"/min loading rate or 73 °F with 0.150"/min loading rate. The sensitivity of moisture is measured by determining the strength ratio of wet and dry.
Modified Lottman indirect tensile test	The first difference between the original and modified Lottman test is the vacuum saturation is continued until the saturation level reached to	Higher loading rate and temperature is selected for doing the test in Marshall stability tester.

	70% to 80% range. The second difference is the loading rate and the testing temperature. The modified test requires 0.065"/min loading rate for 55 °F or 2"/min loading rate for 77 °F.	
Tunicliff-Root	This test is comparable with modified Lottman test except, curing of loose mixture at 60 °C for 16 hr is eliminated.	
ECS with resilient modulus	This test incorporates temperature, moisture saturation and dynamic loading into compacted sample. In addition the effect of pour water pressure can be determined under dynamic loading. 102±4 mm diameter and 102±4 mm thick sample with 7.5%±0.5% air void containing sample are prepared. Air permeability is done by 68 kpa vacuum pressure inside the environmental conditioning chamber. Resilient Modulus (M_R) tests then done with haversine wave loading with loading period 0.1 sec and rest period 0.9 sec. After measuring the M_R, the sample is then saturated with pulling deaired distilled water through sample. The saturated sample's M_R is determined at 60°C.	If the ratio of conditioned sample M_R is less than 70% of unconditioned sample M_R then the sample is moisture susceptible. This test took longer time for conditioning but it can simulate field conditions.
Asphalt pavement analyzer/ Humburg wheel-tracking device	The test measures combining effects of rutting and moisture sensitivity under wheel pressure. Four cubical or beam shape sample are used. Two wheels pass back and forth for 20,000 times or 20 mm of deformation is recorded on the sample. The results are plotted with cycles number as independent variable and deformation as dependent variable.	Three stages of deformation are classified. The pre-compaction stage is up to 1000 cycle, creep slope is the number of repetition to create 1 mm of rut depth, and the stripping slope is represented by the line after sudden change in the deformation. The intersection of creep slope and stripping slope is known as stripping inflation point.

Name of the test	Short description	Scope of the test
Environmental conditioning system/ Simple performance tests	Environmental conditioning system test can be tied up with Dynamic Modulus test, flow number test and flow time test. Dynamic modulus test is done with sinusoidal compression loading under five standard temperatures (i.e. –10 °C, 4.4 °C, 21.1 °C, 37.8 °C) and six standard frequencies (0.1, 0.5, 1.0, 5, 10, and 25 Hz).	If the sample can be moisture conditioned by ECS then dynamic modulus test can be done and field condition can be simulated.
Moisture induced stress testing (MIST)	With a pressurized chamber water is pushed and pulled through a compacted asphalt sample creating pore pressure buildup and hydraulic scouring.	Indirect tensile test or simple performance test can be performed on the MIST conditioned sample.

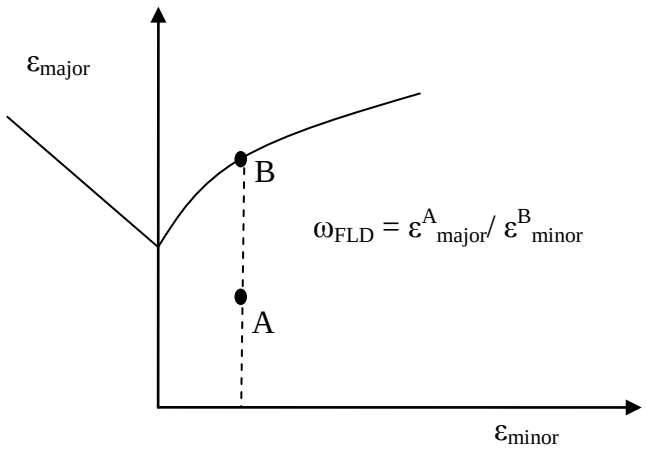

Figure 2.1 Forming Limit Diagram (FLD)

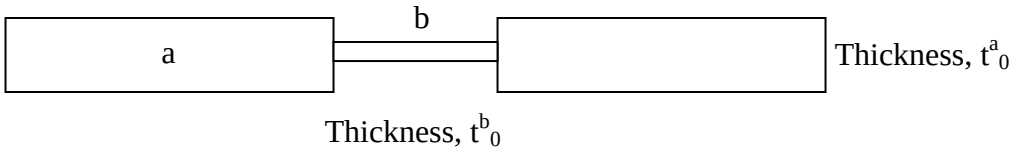

Figure 2.2 Imperfection model for M-K analysis

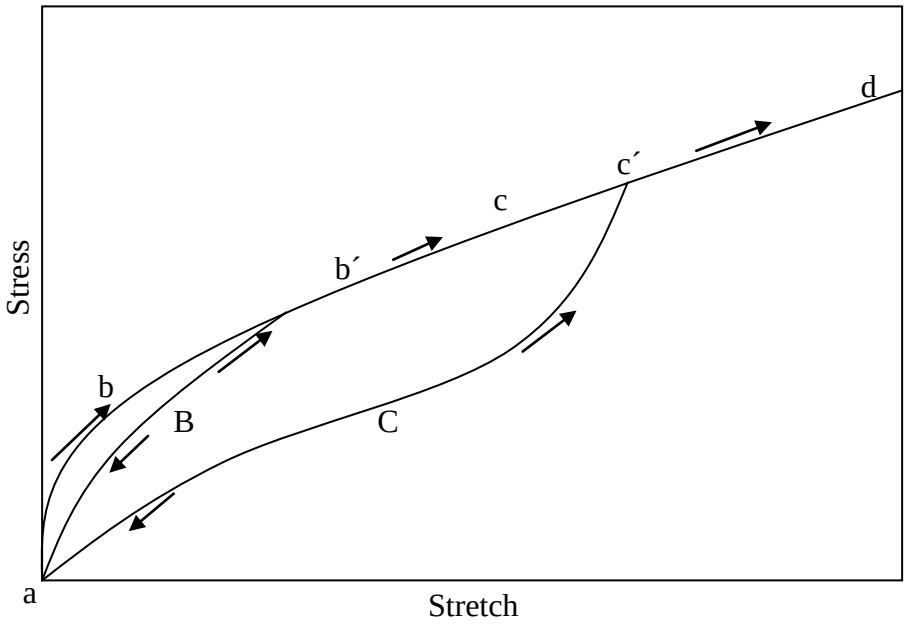

Figure 2.3 Generalized Mullin effect

Figure 2.4 A finite element with an applied force at a single node

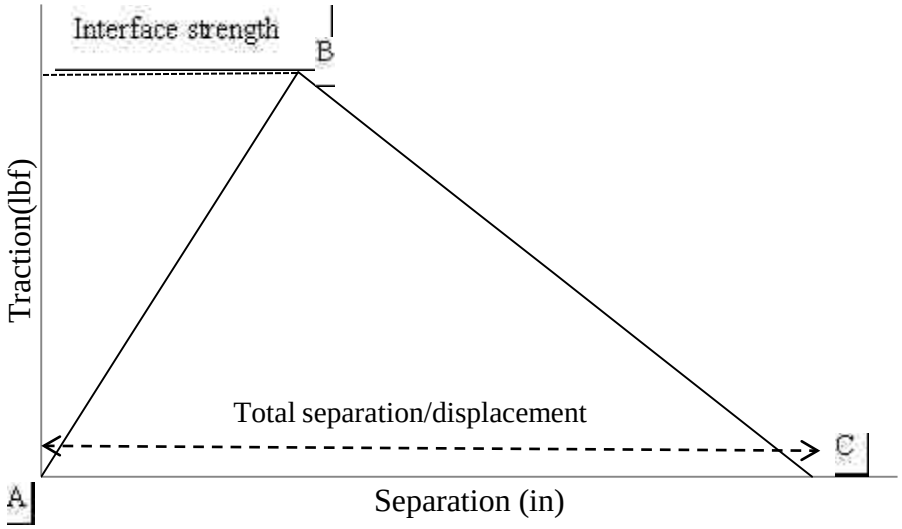

Figure 2.5 Graphical representation of traction-separation model

CHAPTER 3

DAMAGE AT MASTIC-AGGREGATE INTERFACE

3.1 General

This chapter deals with the adhesive damage at mastic aggregate interface. Adhesive damage is defined as the separation at the interface of two materials. This chapter has been published in the peer-reviewed journal name *International Journal of Pavement Engineering* with the title "Quantifying Moisture Damage at Mastic-Aggregate Interface". A copy of the journal is given in the Appendix A.

3.2 Introduction

Adhesion damage is the separation between the aggregate and asphalt binder at the interface locations. Adhesion failure is also known as stripping or de-bonding. On the other hand, cohesive damage is stiffness degradation within the asphalt materials (Mohamed 1993; Hao and Hachiya 2003, Tarefder and Yousefi 2012). When aggregate is mixed with hot asphalt, asphalt binder makes a coating around the aggregate surface. The coating is made up of asphalt combined with fine particles. The combination of asphalt and fine particles that passes through #200 sieves is called mastic. Figure 3.1 shows generalized phenomena of adhesive and cohesive damages in asphalt. Figure 3.1(a) shows aggregate coated with mastic. Figure 3.1(b) shows mastic coating on some portion is worn out, which resembles cohesive damage. Figure 3.1(b) also shows that there is no mastic at some aggregate surface locations, which resembles adhesive damage. The

weakening of mastic-aggregate interfaces (i.e., adhesive damage) under dry and wet conditions is modeled in this study.

In the past, a number of researchers have studied asphalt damage using FEM. Most of the FEM study consider a pavement section and subjected to traffic loading condition (Kim et al. 2008, Desai 2009). However, very few of them address how damage initiates in the asphalt components such as matrix, mastic and aggregate interface. For example, Kim et al. (2009) developed visco-elastic-plastic continuum damages under tension and compression loading of asphalt concrete. However, their model is unable to differentiate the adhesive and cohesive damages at mastic-aggregate interfaces and within the material itself. Desai (2001) has developed a Disturbed State Concept (DSC) model to predict damage in asphalt concrete. Though DSC was used to quantify damage as a disturbance, DSC model has never been used to predict the degradation stiffness at mastic-aggregate interface. Recently, Kringos et al. (2008c) and Kringos and Scarpas (2008) have conducted FEM study considering mastic-aggregate interface. These studies determined moisture damage due to diffusion through mastic and aggregates. Mainly stress variations within the materials due to selected diffusion rate of moisture are observed in their studies; however, they are not directly related to the quantification of damages at mastic-aggregate interface.

3.3 Concept of Damage

Different definitions of damages have been introduced based on constitutive behavior of materials. According to Krajcinovic (1996), a material is said to be damaged if (i) some of the bonds connecting the parts of its microstructure are missing, (ii) the bond between

the molecules within the materials is ruptured, (iii) the molecular chain in a polymer is broken, or (iv) the adhesion between two materials is lost. The classical damage models are based on micro voids extension and coalescences concepts, which are also known as porosity based models (Bonora 1999). The continuum damage models are based on reduction in strength due to breakdown of molecules or changes in molecular structures.

The degradation of strength at the interfaces of mastic and aggregate is the primary indication of moisture damages in asphalt (Tarefder and Yousefi 2012, Tarefder and Arifuzzaman 2011, Caro et al. 2010a, Kringos et al. 2008a, Bhasin et al. 2006). This phenomenon is characterized using traction-separation damage law in this study. For a mastic-aggregate assembly, the traction forces are generated by the physical-chemical interaction between the mastic and aggregate. Generally the interaction strength is smaller than the material strength itself. Interactions between two materials could fail even before the material fails by degradation of its own stiffness due to various reasons like loading magnitudes. On the other hand, separation is the opening between the two surfaces which are previously in contact with each other.

To facilitate an easier understanding of traction-separation damage law, the Authors have created a schematic plot in Figure 3.2. The two surfaces layers in Figure 3.2 can be considered to be attached to each other with some glue-like material. If a normal force is applied on the surface, a traction force develops between the interfaces of these two surfaces. The developed traction force is resisted by the interlocking of two surfaces generated from the glue-like material. As the magnitude of the applied normal force increases, the two surfaces tend to separate from each other due to increased traction force. Under the increment of traction force, the separation between the two surfaces

increases until the force reached its ultimate strength at point B. The slope of line AB, as shown in Figure 3.2, is known as the interface stiffness and termed as *K*. After point B, the separation between the two surfaces increases as the load carrying capacity decreases. Point B is known as damage initiation phenomenon, which means there is a separation between the two surfaces that will not recover. Beyond point B to point C, the phenomenon is known as damage evolution or progression. At the damage progression region, the separation between two surfaces increases, eventually leading to a surface failure.

The following linear traction-separation law has been used in this study:

$$t = k\delta \tag{3.1}$$

$$\begin{Bmatrix} t_1 \\ t_2 \\ t_3 \end{Bmatrix} = \begin{bmatrix} K_{11} & K_{12} & K_{13} \\ K_{21} & K_{22} & K_{23} \\ K_{31} & K_{32} & K_{33} \end{bmatrix} \begin{Bmatrix} \delta_1 \\ \delta_2 \\ \delta_3 \end{Bmatrix} \tag{3.2}$$

In Eq. (3.2), t_1, t_2 and t_3 are the three components of force on a surface in three orthogonal directions, *K*'s are the stiffness coefficients and δ_1, δ_2 and δ_3 are three deformation components due to the respective forces and. The diagonal terms are for three orthogonal directions, and the off-diagonal terms are for coupled directions. In this study, only 2D idealization is made, and therefore the off-diagonal components are not considered. The FEM model is developed considering stiffness in two directions: one is normal to the surface and the other is along the surface. The resulting the equation of the traction-separation is shown in Eq. (3.3) below:

$$\begin{Bmatrix} t_1 \\ t_2 \\ 0 \end{Bmatrix} = \begin{bmatrix} \delta K_{11} & 0 & 0 \\ \partial 0 & K_{22} & 0 \\ 0 & 0 & 0 \end{bmatrix} \begin{Bmatrix} {}_1 \\ {}_2 \\ 0 \end{Bmatrix} \tag{3.3}$$

Damage can be initiated either normal to the surface or along the tangential direct of the surface. The ratio between the interface strength and load is measured along the normal to the surface and tangential direction (i.e., shear direction) of the surface. The maximum ratio indicates the damage initiation at a particular direction and it is presented in Eq. (3.4).

$$max\left\{\frac{t_1}{t_1^0}, \frac{t_2}{t_2^0}\right\} = 1 \tag{3.4}$$

where t_1^0 and t_2^0 are the interface strength for normal and shear directions. Here t_1 and t_2 are the resulting forces due to applied load in the respective directions. When the ratio becomes one, the bond state between the two interfaces breaks down and a gap occurs between them, which can be predicted by FEM. The maximum ratio cannot be greater than one.

3.4 Determining Model Parameters by Laboratory Testing

3.4.1 Determining Rheological Properties of Mastic

Laboratory tests are performed to determine dynamic shear modulus of mastic material and converted to dynamic elastic modulus using following Eq. (3.5). The converted dynamic elastic modulus is used as elastic parameters in ABAQUS for the material property of mastic coating over aggregate.

$$|E^*| = 2.5|G^*| \tag{3.5}$$

DSR is used to calculate the complex shear modulus (G^*) values for mastic. The dynamic shear modulus can be expressed as $|G^*|$. The dynamic modulus presents the magnitude that is the length of complex modulus. A rectangular shape mould is used for preparing the sample. Total 3.6 samples are prepared; 3 samples are tested under dry condition and 3 samples are tested for wet condition. The average theoretical maximum specific (G_{mm}) gravity for the sample is 2.319 and the percent air voids of the samples are 11.5±1.0. The wet condition is prepared following AASHTO T-283. The laboratory test is done at 22 °C and 1 Hz frequency. A strain rate of 0.007% is applied on the rectangular shape sample. The modulus values, which are given in Table 3.1. The modulus value is taken as average of three test results under dry and wet conditions. The elastic modulus of aggregate is taken from other studies and described later.

3.4.2 Determining Damage Model Parameters

Laboratory aggregate pull-off tests under both dry and wet conditions are done to measure the stiffness of mastic-aggregate interfaces. Pictures taken in the laboratory are shown in 3.3. For tensile pull-off test, a coated aggregate is cut into half and the flat face is exposed and the other end is embedded into mastic up to the half of the aggregate. The wet and dry mastic samples are compacted to a target void ratio of 4 ±0.5% for both tension and shear tests. The wet condition is prepared following AASHTO T283 method before conducting the pull-off test. The flat end is fixed with the loading frame with glue and the bottom of the mastic material container is also fixed with the base. The sample is

then load in tension at a rate of 1.27 mm/min (0.05 in/min). Two samples are prepared; one sample kept dry and other is wet conditioned before test.

Aggregate pull-off tests are also performed under direct shear load. The mastic material samples are prepared in similar fashion except the materials are prepared in the shear box of direct shear testing equipment. The hot mastic material are compacted in two lifts into the bottom half of the shear box. Just before the final compaction of the top layer, a coated and fractured face of the hot aggregate is pressed onto the surface of the top lift and the compaction to the required volume is then completed to ensure proper contact between the aggregate and the mastic. One sample is left in a dry condition and the other is conditioned following AASTHTO T283 standard. The top of the shear box is placed on the bottom of the shear box and the apparatus is placed into the direct shear machine. The set screws in the shear box are removed and the height of the top of the shear box is raised so that no mastic material impedes the shearing of the aggregate. The sample is then load in shear at a rate of 1.27 mm/min (0.05 in/min).

The load-displacement graphs due to aggregate pull-off in tension under dry and wet conditions are shown in Figure 3.4. As expected, the tensile strength of aggregate pull-off is higher under dry conditions than under wet conditions. The load-displacement curves due to shear pull-off under dry and wet conditions are shown in Figure 3.5. Under wet conditions, the initial load-displacement curve has lower values and then it increases rapidly. Also the ultimate load under wet condition is higher than the dry condition. Unlike tension pull-off test, the aggregate is not glued to the loading frame for shear pull-off tests. For this reason the load-displacement curve shows wavy and discontinuous phenomena under dry and wet condition. The stiffness of mastic-aggregate interface due

to tension and shear is determined by measuring the slope of the curve before peak load, also known as secant modulus. The secant modulus is determined by measuring the slope of tangent connecting origin with 50% of maximum strength. The tangent lines for determining secant modulus are shown in Figure 3.4 and 3.5 graphs. The measured sustained loads and stiffness for both tension and shear under both dry and wet conditions are given in Table 3.2. Both tensile and shear interface stiffness under dry conditions are higher than under wet conditions.

3.4.3 Interface Modeling Techniques

Two methods are available in ABAQUS for surface damage simulations, cohesive element approach and cohesive surface approach. For cohesive element approach, the stiffness degradations of materials are considered. On the other hand, for cohesive surface approach, the stiffness degradation of surfaces is considered. For cohesive element approach, the stress-strain distribution and the modulus of material and fracture energy, which is the area under the stress-strain curve, are the essential requirements. For cohesive surface approach, the modulus of materials is necessary, but the strength and stiffness of the interfaces are essential for damage simulations. Also, the separation between the two surfaces is required to simulate the damage evolutions. For example, if two metal plates are lap joined by adhesive materials like glue and the damages of that adhesive material needs to be investigated, the proper way of simulation is to model the adhesive material with cohesive elements. For this particular research there is no additional adhesive material between mastic and aggregate. Mastic works as adhesive material on aggregates and the purpose of simulation is not determining the damages of mastic. The damages at interface are the point of interest. In addition, the laboratory tests

are conducted to predict the surface damages of mastic and aggregate rather than damages of the mastic itself. For this reason, the surface damage approach is considered for this research.

3.5 FEM Model Development

ABAQUS/CAE version 6.9-EF1 (2009) is employed for conducting FEM analysis. Only one spherical shape aggregate is considered in this model. The radius of the aggregate is 19.05 mm (0.75 in). A 0.254 mm (0.01 in ≈ 300 μm) mastic thickness is considered. Previously, Kringos et al. (2008b) considered a 300 μm of mastic thickness in his model. The inner side of mastic and outer side of aggregate is restrained in both horizontal and vertical directions at four points to overcome the rigid body movements. It is assuming that there is no damage occurred inside the aggregate. Generalized shape, boundary conditions and loading state are shown in Figure 3.6. A portion of the finite element model that is simulated is shown in Figure 3.6. The finite element model shows a combination of both triangular and rectangular elements. The model is generated as a two-dimensional continuum homogeneous structure. The model is developed with plane stress continuum three- and four-noded linear quadrilaterals elements. The mastic and aggregate is considered as elastic materials. The elasticity of mastic is assigned according to Table 3.1 with Poisson's ratio of 0.30 under dry and wet conditions. Kringos et al. (2007) considered 0.30 Poisson's ratio of mastic in her FEM models. The elasticity value of aggregate is assumed as 48.3 GPa (7,000,000 psi) with Poisson's ratio of 0.20, which is a common value for gravel. The damage evolution is assumed as linear and an elastic displacement value has been given for controlling the damage initiations. The damage stabilization is given as 1E-05, which is a very small value required for analysis purpose.

Real pavement experiences cyclic tire pressure which comes from traffic. The monotonically increasing static loading condition does not show the actual degradation of materials. For this reason, the FEM is simulated with three different patterns loads. The loading pattern resembles one cycle of dynamic tire pressure. The three different load patterns are shown in Figure 3.7. The load patterns are named triangle, sawtooth and rectangle. The triangular pattern represents a very high speed car, the sawtooth pattern represents a moderate to low speed car and the rectangular pattern represents a car that is stationary for awhile and suddenly moves from its stationary position, also known as a stop and go situation. Several studies are done with cyclic loading on asphalt concrete pavements (Zaghloul and White 1993; Blab and Harvey 2002; Saad et al. 2005). Three different types of load magnitudes are used in this study. Three displacement loads of value 0.00508 mm (0.0002 in), 0.0508 mm (0.002 in) and 0.508 mm (0.02 in) are applied as peak amplitude. Huang (2004) showed that in two-layer pavement systems with 0.483 MPa (70 psi) dual tire loads applied over 152.4 mm (6 in) asphalt concrete of 689.48MPa (100,000 psi) elastic modulus, the maximum vertical deflection is 0.6858 mm (0.027 in) under one tire at the bottom of the asphalt concrete. The assumption of maximum vertical deformation load of 0.508 mm (0.02 in) seems appropriate for these simulations.

3.6 Results and Discussions

3.6.1 Contact Stresses at the Interface

Contact stresses are generated at the surface between the mastic and aggregate. At every element of the surface, the resulting stresses are divided into normal and shear contact stresses. The contour of contact stresses along the surface can be shown using FEM.

Variations of contact stresses under dry and wet conditions are investigated for different load patterns. The rectangular pattern causes higher normal and shear contact stresses under both dry and wet conditions. For the case of the rectangular pattern, the load is applied with its maximum amplitude for a longer time than triangular and sawtooth patterns. The normal and shear contact stresses due to rectangle pattern load under dry and wet conditions are shown in Figure 3.8. The locations of maximum positive and negative normal contact stresses are shown in Figs. 3.8(a) and (b). The locations of maximum positive and negative shear contact stresses are shown in Figs. 3.8(c) and (d). For normal contact stress, positive value represents tensile stress and negative value represents compressive stress. In the case of shear stress, counter-clockwise from element center is positive. Higher intensity of normal contact stresses is close to the supports and loading point. Maximum tensile contact stresses are located at the two right and left support conditions. For shear contact stresses, the positive and negative stresses are on either side of the support. The locations of maximum shear contact stresses are not the same for dry and wet conditions. Figure 3.9 represents the variations of the maximum positive contact stresses for 0.00508 mm (0.0002 in) vertical deformation under dry and wet conditions for all load patterns. From Figure 3.9, it could be observed that for all load patterns, dry conditions give both higher normal and shear contact stresses than wet conditions. The presence of moisture in mastic develops reasonably lower normal contact stresses and significantly lower shear contact stresses at the interface locations. Low contact stresses at the interfaces could be one of the reasons for having higher adhesive damages at moist mastic-aggregate interfaces. It should be noticed that the shear strength under wet condition is higher than the dry condition but secant modulus or interface

stiffness is higher under dry condition than wet condition. For this reason, interface contact stress affected due to stiffness of interface rather strength of interface.

3.6.2 Effects of Loading

The contact stress variations due to three load patterns and two load magnitudes are compared and presented. Normal and shear contact stresses for 0.0508 mm (0.002 in) and 0.508 mm (0.02 in) deformation load under dry and wet conditions are presented in Figure 3.10. Contact stress variations for 0.00508 mm (0.0002 in) vertical deformation load have been presented in Figure 3.9. There are no significant differences of normal and shear contact stresses under dry and wet conditions for triangular and sawtooth patterns load due to incremental deformations from 0.00508 mm (0.0002 in) to 0.0508 mm (0.002 in) and 0.508 mm (0.02 in). The major differences have been observed while vertical deformation increases from 0.0508 mm (0.002 in) to 0.508 mm (0.02 in) under rectangular pattern load. For rectangular pattern load, while vertical deformation increases from 0.0508 mm (0.002 in) to 0.508 mm (0.02 in), the normal contact stresses increase about 61% under dry conditions and approximately 90% under wet conditions. In addition, while comparing the shear contact stresses due to vertical deformation increments from 0.0508 mm (0.002 in) to 0.508 mm (0.02 in) for the rectangular pattern load, the shear contact stresses under both dry and wet conditions increases about 163% and 537% respectively. Normal contact stresses under dry conditions are two to four times higher than the wet conditions for all three load patterns. Shear contact stresses under dry conditions are around two to five times higher than wet conditions. Wet conditions show higher adhesive damages than dry conditions due to lower contact stresses for all three load patterns.

3.6.3 Resistance to Moisture Induced Damage

According to AASHTO T283 (2007) standard, the ratio of strength of wet and dry samples is a common measure for resistance of compacted asphalt mixtures to moisture induced damages. The ratio is known as tensile strength ratio (TRS). Indirect tensile strength is developed within the sample by applying direct compression load. The standard indicates that the lower the ratio, the higher the damages in the samples. In other words, the lower the ratio, the sample has a lower resistance to moisture. Laboratory investigations for wet condition samples are completed following AASHTO T283 standard. In these mastic-aggregate interface damage simulation models, from Figure 3.8, it has been observed that under vertical deformation load the maximum contact tensile stresses are developed at the left and right supports. This resembles the T283 standard's indirect tension development in the samples. In addition, the loading phenomenon is similar to the T283 standard. The contact stress ratios under wet and dry conditions are given in Table 3.3. The variations of the ratios are also plotted in Figure 3.11 for normal contact stresses and shear contact stresses. It can be observed that the maximum ratio under normal contact stress is 0.39 for 0.0508 mm (0.0002 in) deformation load and for triangular load pattern. For rectangle pattern load, the minimum ratio under normal contact stress is 0.24 for 0.508 mm (0.002 in) deformation load. Similar to normal contact stress, decrease in ratio is also observed for shear contact stresses under all pattern loads. Shear contact stress ration is smaller than normal contact stress ratio except for rectangular pattern load for 0.508 mm (0.02 in) deformation. The general trend is, normal and shear contact stress ratio is decreased for deformation load increment except rectangular pattern. The ratio might influence by higher deformation load, but rectangular

pattern exhibited significantly higher adhesive damages under both dry and wet conditions. The inverse relation explained in AASHTO T283 standard is not observed only in the rectangular pattern load under 0.508 mm (0.02 in) deformation.

3.6.4 Damage Analysis

3.6.4.1 Location of Maximum Damage

Damage is also termed as scalar degradation of stiffness, which is a dimensionless quantity, and varies from zero to one. Zero represents no degradation of stiffness and one represents complete degradation of stiffness. The location between zero and one is sensitive to damages and will become damaged upon increment of loading. The location of damages can be identified by observing the contour images of damage initiation criteria. For rectangular pattern loads, the damage initiation criteria have been plotted in Figure 3.12, 0.0508 mm (0.002 in) deformation loads under dry and wet conditions. Damage initiates near the location of applied boundary conditions and progresses along the surfaces. Initially, there are thirteen locations where the maximum damages occur under wet conditions and eight damaged locations under dry condition. Wet conditions show higher damage locations than dry conditions. The higher the deformation load, the higher the damage locations on the interfaces.

3.6.4.2 Progression of damages

The contour plot for surface damages due to 0.0508 mm (0.002 in) deformation loads under dry and wet conditions for three different load patterns are shown in Figure 3.13. There are no significant differences found in surface damage contours between 0.00508

mm (0.0002 in) and 0.508 mm (0.002 in) deformation loads under both dry and wet conditions. According to Figure 3.13, the wet conditions show a considerable amount of damage near the supports for rectangular load pattern. The stiffness degradations are about 0.4, 0.4 and 0.9 for triangular, sawtooth, and rectangular pattern loads respectively under dry conditions. The maximum surface damage value is 1.0, which is calculated from the ratio of surface strength and applied load at the node or element. For this reason, under dry conditions for all three load patterns, the surface damage has not reached its limiting value, or, there is still some stiffness left to the nodes under dry conditions. It should be noticed that initiation of damages are near the supports, which means the damage initiation is based on boundary locations for this analysis. The extent of the surface damage under wet conditions is more than under dry conditions. Under wet conditions, eight damage initiation points show stiffness degradation of 1.0, which means there is no stiffness left in those particular nodes or elements. Under wet conditions, damage has been initiated for low (0.002 in) vertical deformation loads. Damage contours between triangular and sawtooth under wet conditions does not clearly differentiate, but it can differentiate between sawtooth and rectangle pattern loads.

The contour plot for surface damages due to 0.508 mm (0.02 in) deformation loading under dry and wet conditions for three different load patterns are shown in Figure 3.14. Damage contour shows clear differences in dry and wet conditions for all three load patterns in Figure 3.14. Under both dry and wet conditions for all three loading patterns, several locations of interfaces are exposed to damages. For triangular load patterns under dry conditions, two new locations and under wet conditions, three new locations are exposed to damages. For sawtooth load patterns under dry conditions, three new locations

and under wet conditions four new locations are exposed to damages. For rectangular load patterns under wet conditions, the upper portion of the interfaces shows as entirely damaged. Under dry conditions for rectangle load patterns, the upper portion shows nearly complete damage. The extent of damage increased for all previously exposed eight locations. The upper portion of interfaces shows more surface damage than the lower portion of the interfaces for all load patterns.

The numerical values of damages under dry and wet conditions due to three different deformation load magnitudes for a particular nodal point are shown in Figure 3.15. Node 22 is chosen and the position of the node is also shown in Figure 3.15. This node is very critical since it is near the support and more sensitive to damages. Also node 22 shows clear progression of damages under different load pattern and magnitudes. Under dry conditions and three different load patterns, the variations of damages are shown. As the deformation increases, the slope of the curve becomes steeper. Also damage magnitude increases as loading time and magnitude increases. Similar phenomena observed under wet conditions. For higher load magnitudes, the wet interfaces initiate damage earlier than dry interfaces.

3.6.5 Interface-De-Bonding due to Damage

3.6.5.1 Contact Interface Status

The bond state under dry and wet conditions for rectangular load pattern due to 0.0508 mm (0.002 in) deformation loading are shown in Figure 3.16. The contour value 1.0 means bonded and 0.0 means de-bonded between the two surfaces. For 0.0508 mm (0.002 in) deformation loads under dry conditions, there is no de-bonded region. On the

other hand, under wet conditions, some particular locations show de-bonding between mastic and aggregate. The locations where the de-bonding occurs have surface damage values equal to 1.0. If we compare Figs. 3.13 and 3.16, under dry conditions, the surface damages do not exceed 1.0 indicating the interfaces of mastic and aggregate are bonded. The similar scenario is also observed for 0.0508 mm (0.0002 in) deformation loading and similar loading patterns. It is clear that bondage between mastic and aggregate depends on the interface damages and the phenomena are critical under wet conditions.

The bond state under dry and wet conditions for three different load patterns due to 0.508 mm (0.02 in) deformation loading are shown in Figure 3.17. As the deformation increases from 0.0508 mm (0.002 in) to 0.508 mm (0.02 in), the bonding status under dry conditions changes and under wet conditions becomes worse. Figure 3.17 shows that under dry conditions, we have initiation of de-bonding that begins from the upper portion of the interfaces. Under wet condition, the rectangular pattern load shows severe bond damages. For triangular load pattern under dry conditions, there are three de-bonded locations and under wet conditions there are nine de-bonded locations. Similar numbers of damaged locations are observed for sawtooth load patterns under dry and wet conditions. For rectangle load pattern under both dry and wet conditions there are three and twelve de-bonded locations respectively. The de-bonding locations are dominated at the upper portion of the surfaces. It has been previously observed that the damage locations are also extended over the upper portion of the interfaces.

3.6.5.2 Quantification of de-bonded surfaces

The bond status can be explained by determining the contact perimeter between mastic and aggregate. Before loading, the bonded contact perimeter is measured as 119.63 mm (4.71 in). The contact perimeter, after applying the deformation load, can be computed for rectangular pattern and is shown in Figure 3.18. Under dry conditions and for 0.00508 mm (0.0002 in) and 0.0508 mm (0.002 in) deformation loading, the contact area is intact or no de-bonding is found, but for 0.508 mm (0.02 in) deformation loading, about 6.8% of the perimeter has lost contact. On the other hand, under wet conditions due to 0.00508 mm (0.0002 in) deformation there is no de-bonding observed but due to 0.0508 mm (0.002 in) deformation, about 44.92% and for 0.508 mm (0.02 in) deformation about 49.1% of perimeter has lost contact. Significant amount of de-bonded interface observed under wet conditions than dry conditions.

3.7 Conclusions

The asphalt mastic-aggregate interfaces are simulated and interface damage is quantified using FEM and traction separation law, readily available in ABAQUS. Model parameters are determined from laboratory pull-off and strength testing of mastic materials. Model geometry is defined by a two dimensionally idealized aggregate particle surrounded by mastic materials to represent adhesive damage. Moisture damage is quantified through contact stress, load magnitude to damage initiation, and de-bonding. The findings of this study are summarized below.

1. The contact stress is significantly higher in dry conditioned mastic-aggregate interface than in the wet conditioned interface for all load magnitudes and

patterns. Lower contact stresses are one of the reasons for higher mastic-aggregate interface damage under wet condition.

2. It is shown that damage initiates and progresses mostly on the upper half of the mastic-aggregate interfaces. In wet conditioned samples, surface damage initiates at 0.00508 mm (0.002 in) deformation, whereas damage initiates at 0.508 mm (0.02 in) deformation in dry condition. Stiffer dry mastic material carries higher applied deformation and shows lower mastic-aggregate interface damage. Softer mastic material is unable to carry smaller applied deformation and exposed to higher interface damage.

3. De-bonding in wet sample is significantly higher than that in dry sample. About 6.8% (% perimeter) interface de-bonding occurs in dry sample. On the other hand, about 49.1% interface de-bonding occurs in wet conditioned sample. Lower contact stresses are responsible for higher de-bonding. De-bonding between mastic and aggregate is one of the main reasons for premature permanent failure of AC pavement under wet condition.

Table 3.1 Dynamic shear and elastic modulus of mastic

	Dry	Wet
$\|G^*\|$	2.0 MPa (290,075 psi)	0.74 MPa (108,778 psi)
$\|E^*\|$	5.0 MPa (725,188 psi)	1.87 MPa (271,945 psi)

Table 3.2 Ultimate strength and interface stiffness under dry and wet conditions

	Ultimate strength in tension	Ultimate strength in shear	Interface stiffness in tension (K_{11})	Interface stiffness in shear (K_{22})
Dry	391.67 N (88.05 lbf)	302.50 N (68.00 lbf)	3706.71 N/mm (21,165.87 lbf/in)	2991.33 N/mm (17,080.96 lbf/in)
Wet	167.21 N (37.59 lbf)	489.30 N (110.00 lbf)	1947.64 N/mm (11,121.30 lbf/in)	690.06 N/mm (3,940.35 lbf/in)

Table 3.3 Ratio of wet and dry contact stresses

Load pattern	Deformation magnitudes	Wet/Dry	
		Normal	Shear
Triangular	0.0002"	0.39	0.24
	0.002"	0.37	0.23
	0.02"	0.31	0.23
Sawtooth	0.0002"	0.38	0.23
	0.002"	0.37	0.23
	0.02"	0.29	0.24
Rectangular	0.0002"	0.38	0.23
	0.002"	0.24	0.21
	0.02"	0.28	0.52

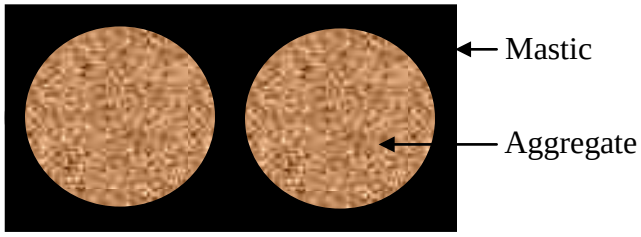

(a) No loss of bonding

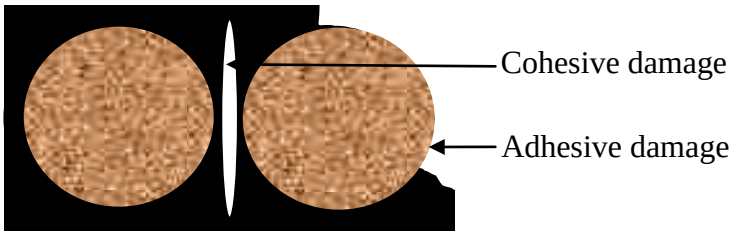

(b) Loss of bonding

Figure 3.1 Schematic of adhesive and cohesive damages in aggregates and mastic

.

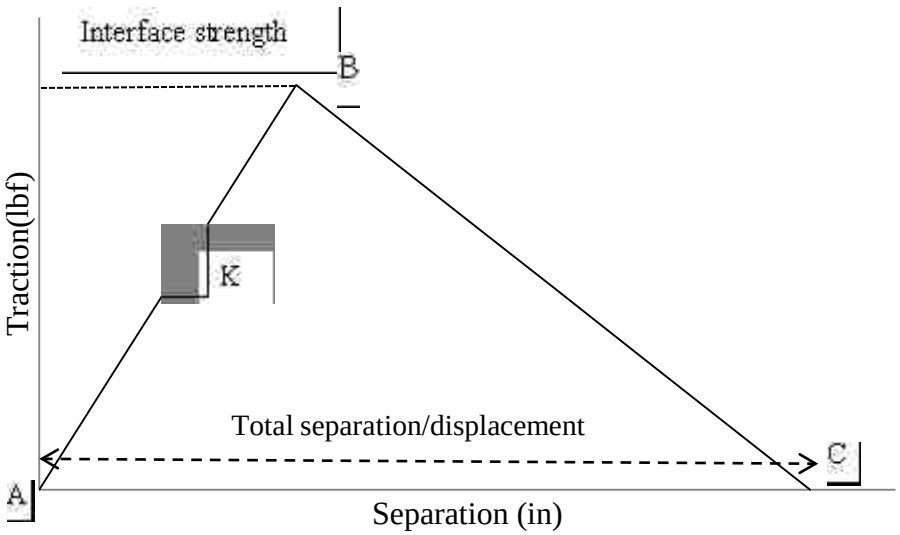

Figure 3.2 Schematic of traction-separation damage law

(a) Aggregate pull-off due to tension

(b) Aggregate pull-off due to shear

Figure 3.3 Laboratory measurement of interface strength

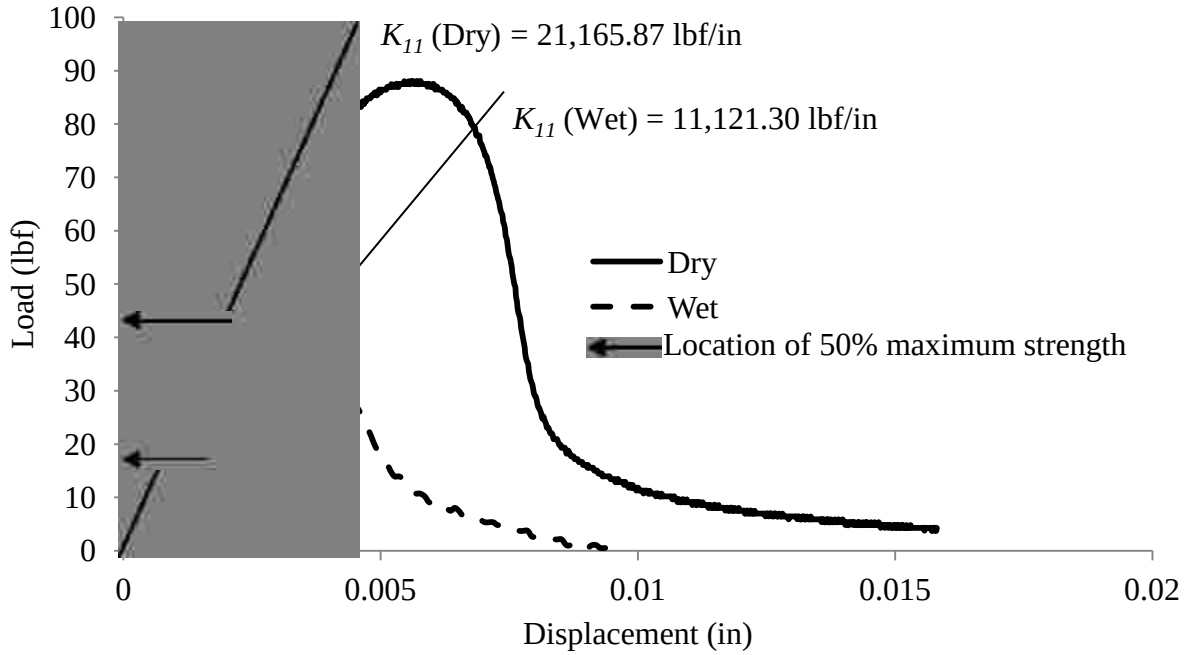

Figure 3.4 Load vs. displacement curve in tension with secant modulus

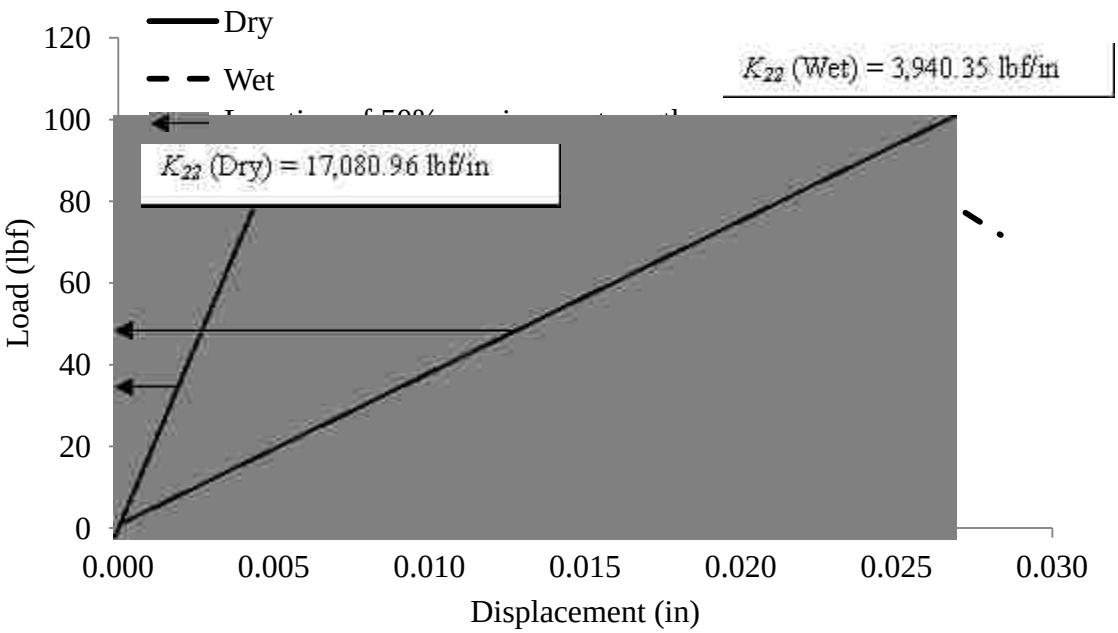

Figure 3.5 Load vs. displacement curve in shear with secant modulus

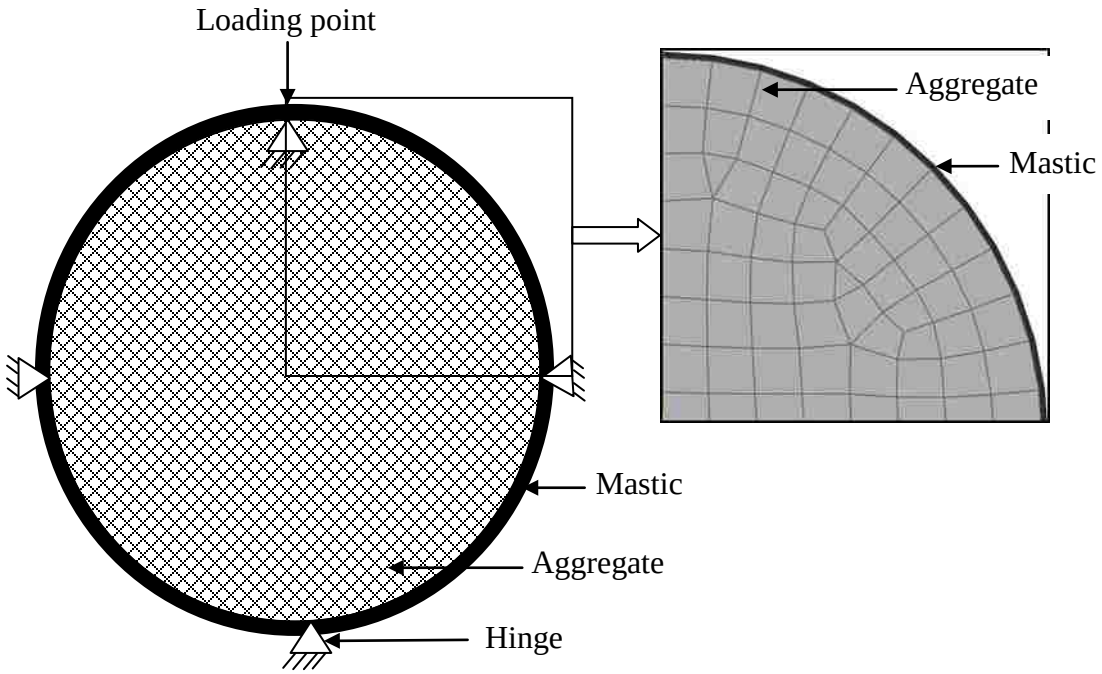

Figure 3.6 A generalized diagram of aggregate and mastic with boundary conditions, loading, and a portion of finite element model

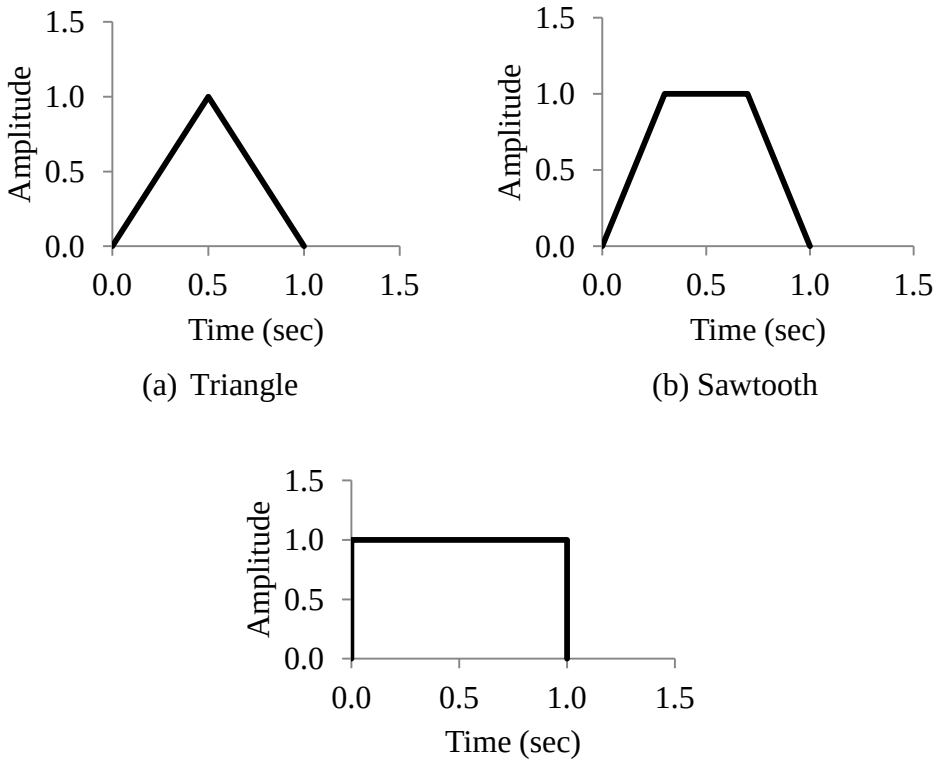

Figure 3.7 The load patterns (a) Triangle, (b) Sawtooth, and (c) Rectangle

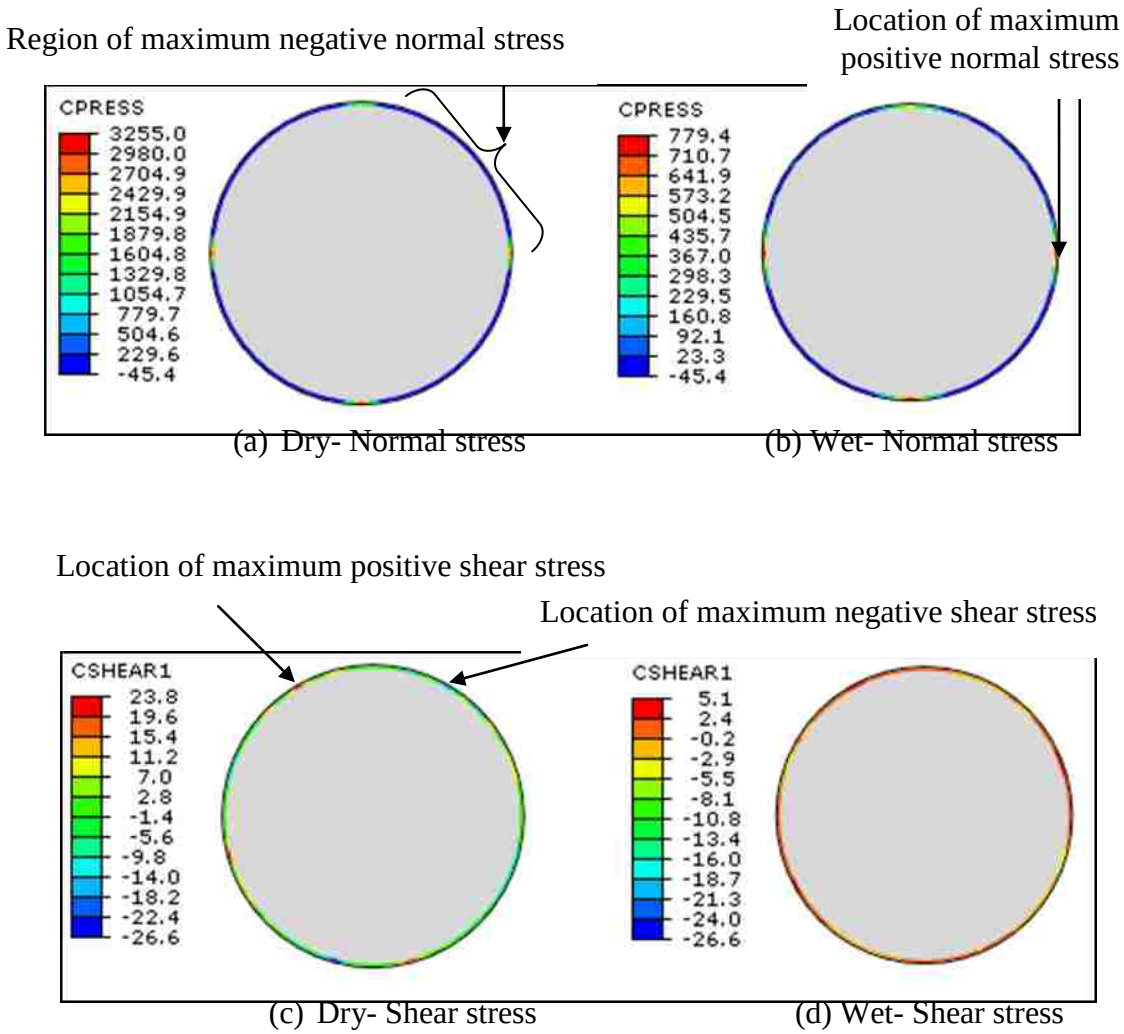

Figure 3.8 Contact stresses due to 0.0508 mm (0.002 in) vertical deformation under rectangular load (CPRESS means Contact Pressure and CSHEAR1 means Contact Shear at direction 1)

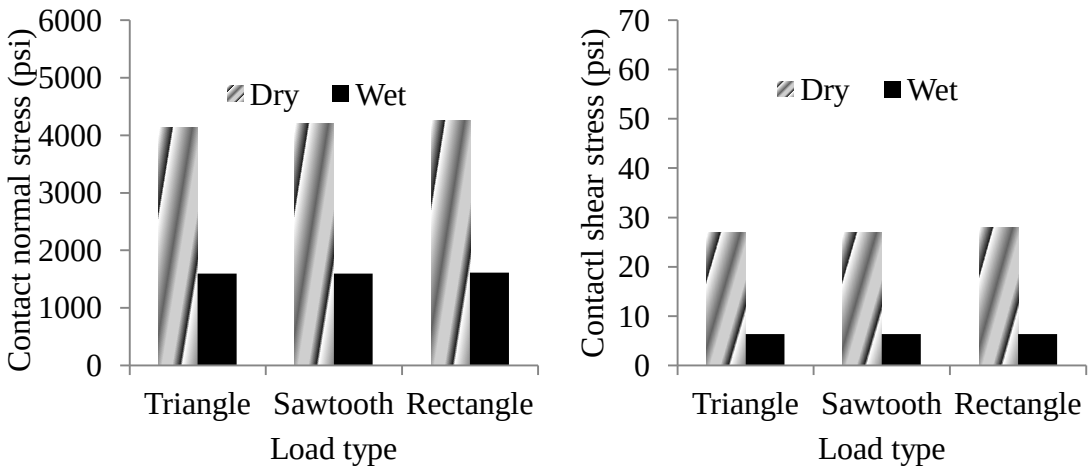

(a) Normal stress (b) Shear stress

Figure 3.9 Contact stresses due to 0.00508 mm (0.0002 in) vertical deformation for three load patterns

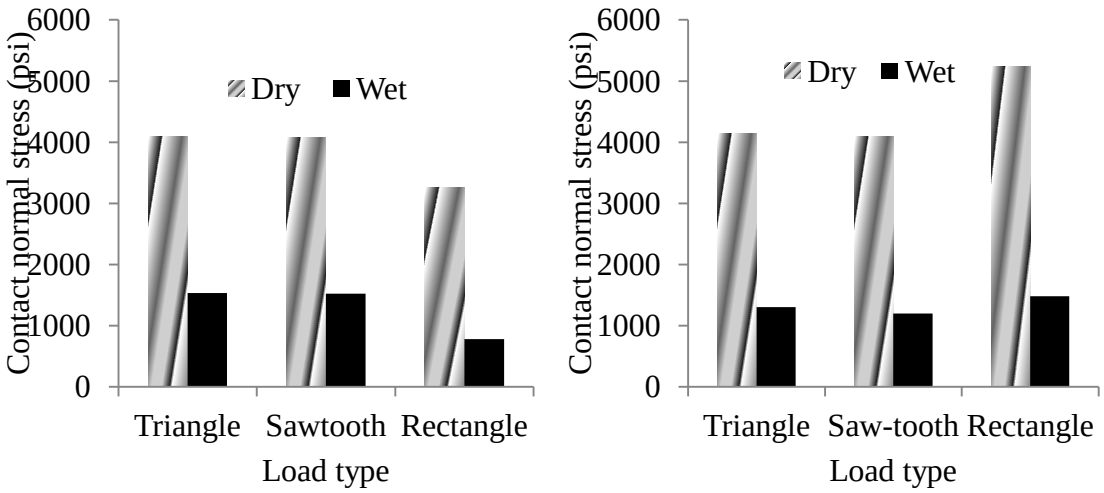

(a) Normal stress-0.002 in deformation (b) Normal stress- 0.02 in deformation

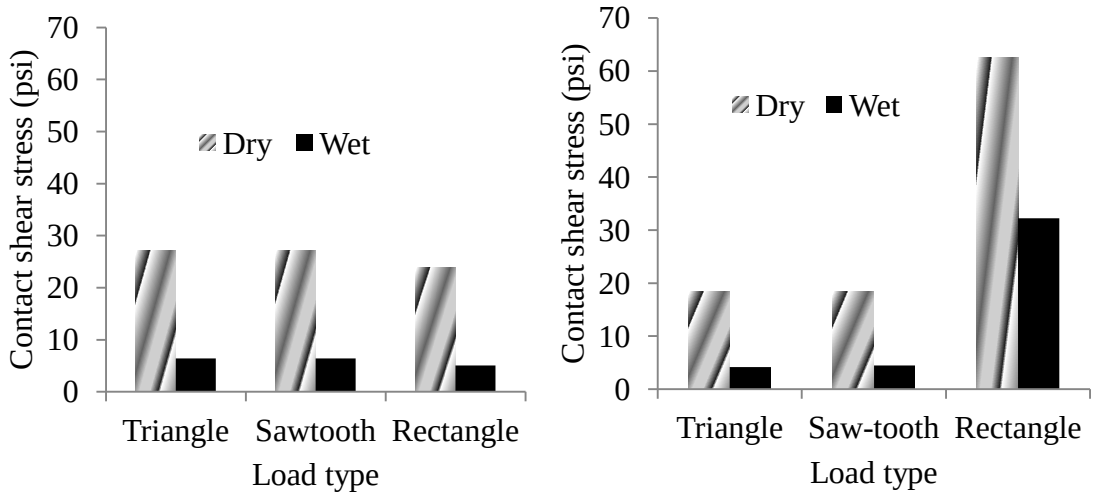

(c) Shear stress-0.002 in deformation (d) Shear stress-0.02 in deformation

Figure 3.10 Contact stresses due to vertical deformation loading for three load patterns

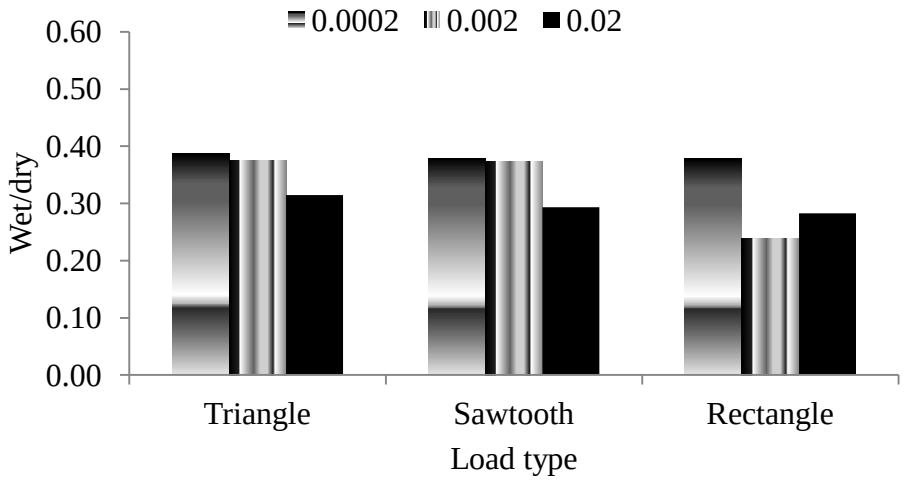

(a) Normal contact

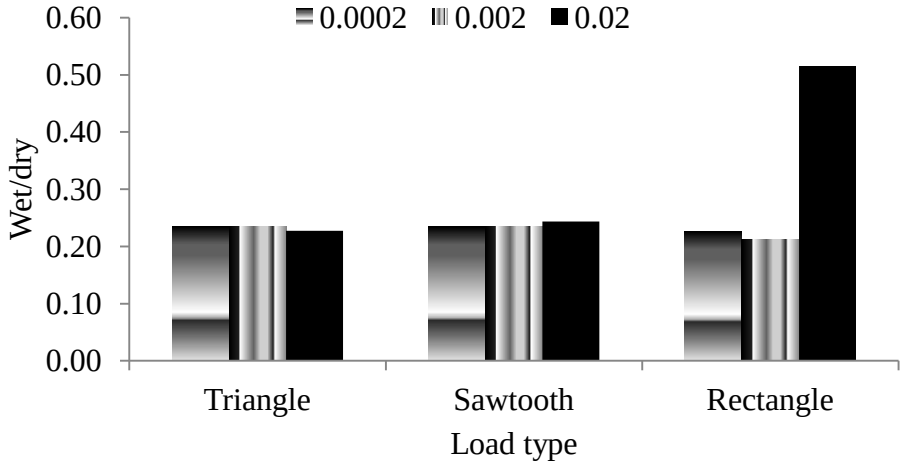

(b) Shear contact

Figure 3.11 Ratio of wet and dry contact stresses

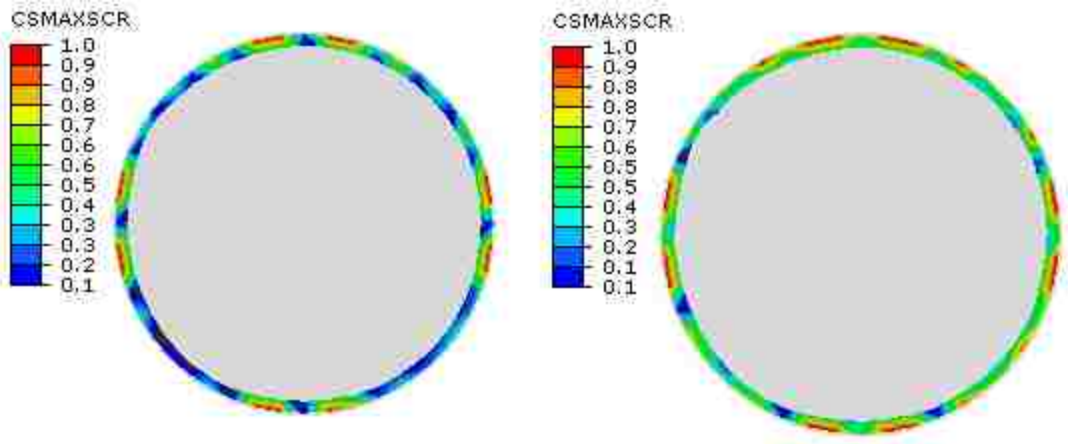

(a) Dry

(b) Wet

Figure 3.12 Damage locations due to 0.0508 mm (0.002 in) vertical deformation under rectangular load (CSMAXSCR is Maximum Traction Damage Initiation Criteria for Cohesive Surfaces)

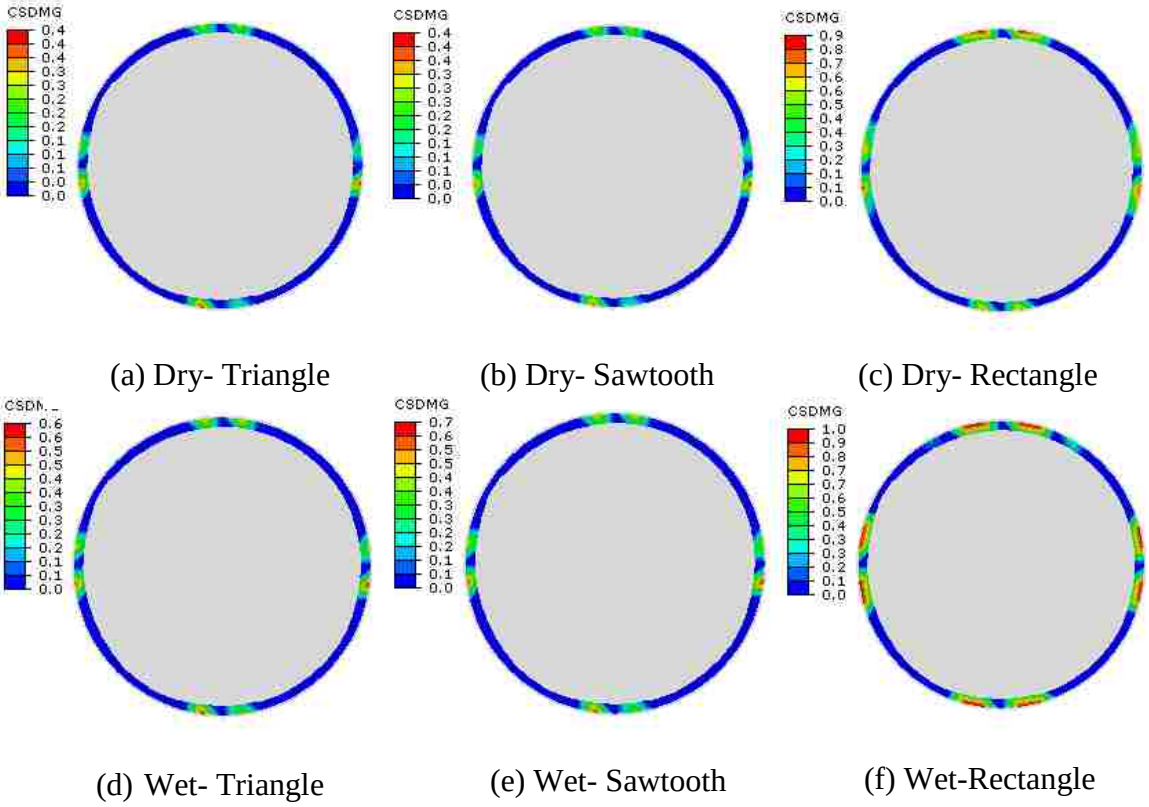

(a) Dry- Triangle (b) Dry- Sawtooth (c) Dry- Rectangle

(d) Wet- Triangle (e) Wet- Sawtooth (f) Wet-Rectangle

Figure 3.13 Contour of surface damages due to 0.0508 mm (0.002 in) vertical deformation load (CSDMG is Scalar Stiffness Degradation for Cohesive Surfaces)

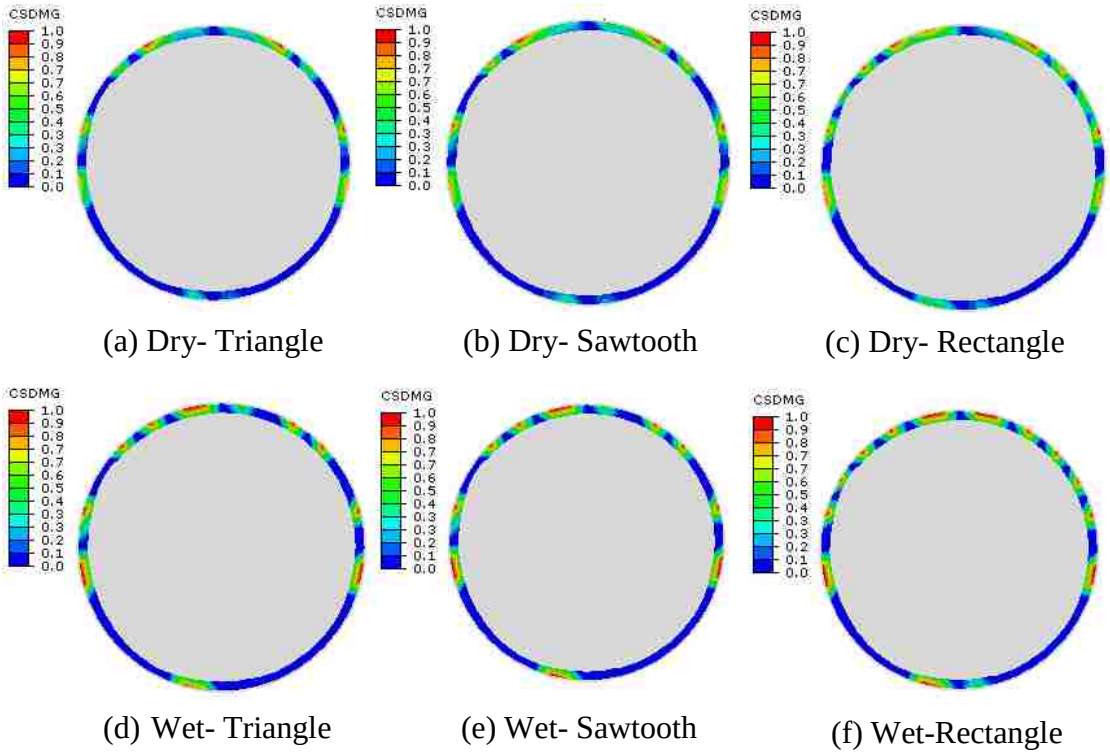

(a) Dry- Triangle (b) Dry- Sawtooth (c) Dry- Rectangle

(d) Wet- Triangle (e) Wet- Sawtooth (f) Wet-Rectangle

Figure 3.14 Contour of surface damages due to 0.508 mm (0.02 in) vertical deformation load (CSDMG is Scalar Stiffness Degradation for Cohesive Surfaces)

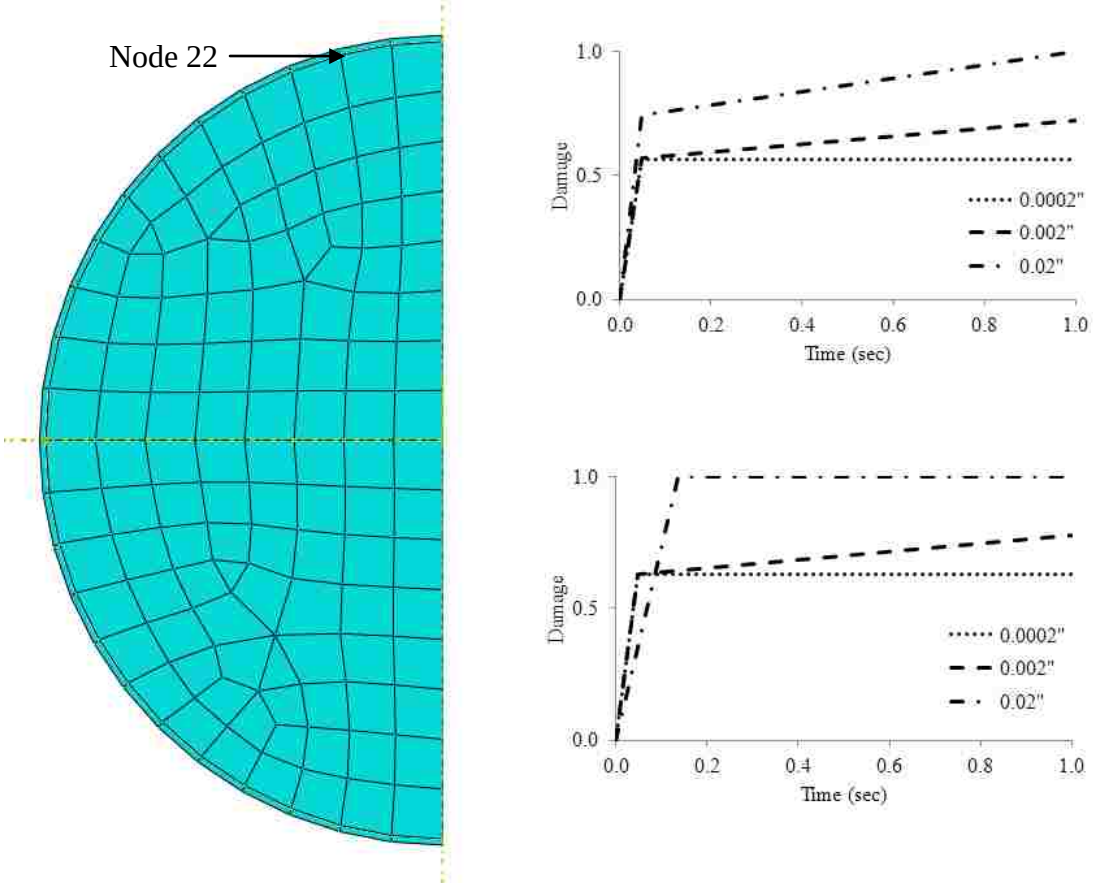

Figure 3.15 Damages at node 22 due to vertical deformation load

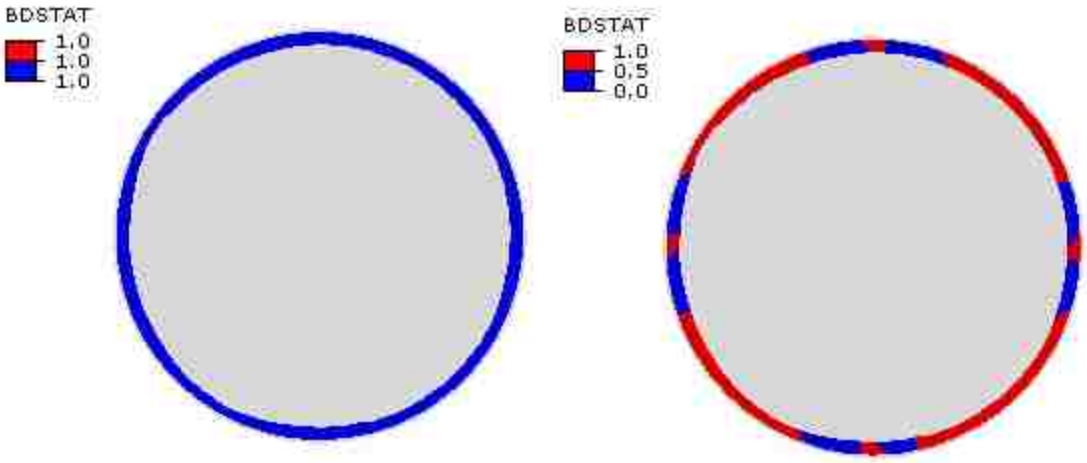

(a) Dry- Rectangle

(b) Wet-Rectangle

Figure 3.16 Interface bonding due to 0.0508 mm (0.002 in) vertical deformation load (BDSTAT is Bond State)

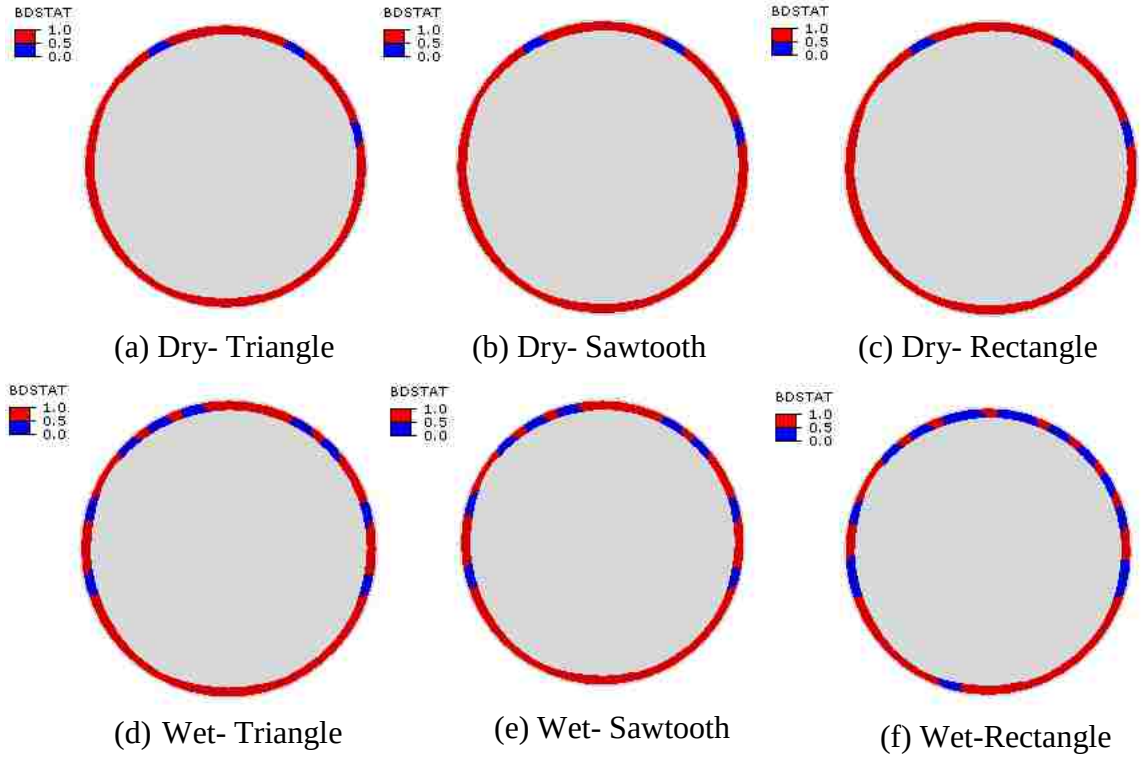

(a) Dry- Triangle (b) Dry- Sawtooth (c) Dry- Rectangle

(d) Wet- Triangle (e) Wet- Sawtooth (f) Wet-Rectangle

Figure 3.17 Interface bonding due to 0.508 mm (0.02 in) vertical deformation load (BDSTAT is Bond State)

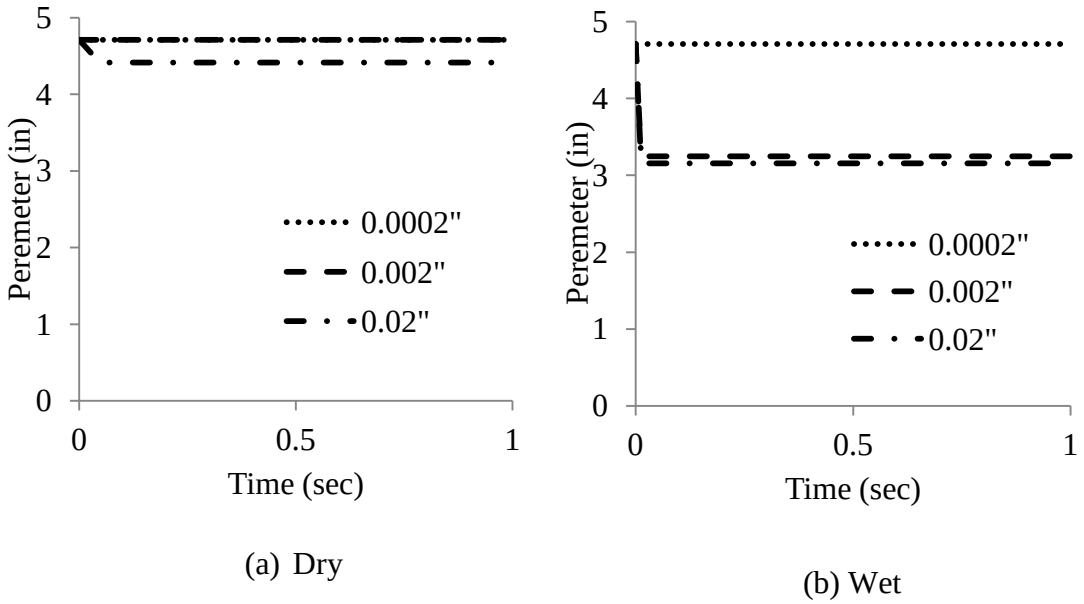

Figure 3.18 Contact perimeters between mastic and aggregate under rectangular load

CHAPTER 4

DAMAGE IN MATRIX MATERIALS

4.1 General

This chapter describes both cohesive and adhesive damage in matrix materials. Cohesive damage is defined as the strength degradation in the matrix materials. On the other hand, adhesive damage is defined as the strength degradation of matrix materials near the matrix-aggregate interface. This chapter is published in the peer-reviewed journal name *Construction and Building Materials* titled "Identifying damage in asphalt matrix materials surrounding an aggregate particle". A copy of the published article is given in the Appendix B.

4.2 Introduction

Asphalt Concrete (AC) can be defined as asphalt coated coarse aggregate particles surrounded by mastic and matrix materials. Mastic is a mixture of fines (materials passing #200 sieve) and asphalt binders. Matrix is a mixture of asphalt binder with fine aggregates passing through a #4 (4.75 mm) sieve and retained on a #200 sieve (Abu Al-Rub et al. 2010; Kringos et al. 2008a; Shah 2003). Damage due to moisture in AC occurs mostly in the mastic or matrix or interface of the materials (Tarefder et al. 2009). Most researchers agree that damage due to moisture inside an aggregate particle is limited. Rather, most of the moisture damage occurs in mastic and matrix materials. This study focuses only on the matrix damage due to moisture.

Cohesive and adhesive damages are two major reasons of AC damage (Cheng et al. 2003; Khalid and Monney 2009; Kutay et al. 2007; Spinel 2009; Wasiuddin et al. 2011). The phenomena of adhesive and cohesive damage are shown schematically in Figure 4.1. Figure 4.1(a) shows a fresh sample of AC, which has not been subjected to any damage. Figure 4.1(b) shows loss of bonding within the asphalt binder or mastic or matrix (cohesive) and at the matrix-aggregate or mastic-aggregate interface (adhesive). Few studies have been considered in the past to understand the evolution and progression of matrix damage under dry and wet conditions (Abu Al-Rub et al. 2010; Kringos et al. 2008a; Kringos et al. 2008b).

Damage initiates at molecular scale but it is clearly visible at meso scale, a full scale pavement. Although the previous studies show the severity of damage due to moisture condition but this study is done to understand how damage initiates in matrix materials (cohesive damage) and then move towards matrix aggregate interface (adhesive damage) and quantify this damage for a small scale considering variability of AC. It is believed that, the understanding of damage in small scale will help to improve the mix design procedure, select appropriate construction materials, application of additives, better material design to prevent damage and many more. In this study, damage in a system of aggregate coated by matrix, considered as small scale AC, is studied. Total damage is characterized as cohesive and adhesive damage as described in Figure 1. To identify initiation and location of damage, the damage is evaluated using damage evaluation criteria defined by maximum nominal stress criteria. Maximum stress criteria is defined as, damage initiates within a material when it reaches to maximum strength under loading condition (Allix and Hild 2002; Inman et al. 2005; Saanouni 2001; Suaris et al. 1990).

4.3 Objectives

The objectives of this research work are:

1. Identify damage and categorize it into the adhesive and cohesive damages in matrix material of AC under dry and wet conditions.
2. Evaluate the effects of moisture in adhesive and cohesive damage initiation and propagation.
3. Quantification of adhesive and cohesive damages in the matrix materials.

4.4 Methodology

Maximum stress criteria are used to determine adhesive and cohesive damage by applying Finite Element Method (FEM) modeling. Commercial software ABAQUS is used as a tool of FEM. Laboratory tests are performed on matrix material under dry and wet conditions to determine the FEM damage model inputs. The initiation and progression of the adhesive and cohesive damages of matrix coated an aggregate particles are evaluated and quantified considering two different matrix thicknesses, two deformation magnitudes representing tire pressure on AC, and three deformation intensity patterns representing deformation application time of tire pressure on AC.

4.5 Damage Modeling in AC

Concept of damage mechanics has been introduced in early 1920 but a major breakthrough has been occurred in late 1950 by L. M. Kachanov (Lemaitre 1996). Damages in material due to environmental degradation such as presence of moisture and damages in concrete materials due to non-homogeneous material has been introduced

(Kachanov 1986). It has been mentioned that geo-materials and polymers changes their mechanical properties under the influence of environment even in the absence of stress. Also concrete like materials have weak mechanical resistant due to non-homogeneity.

Damage in AC has been studied for decades. In early 1990, damages in viscoelastic materials in terms of accumulated viscous strain has been described (Lemaitre and Desmorat 2005). Later on, viscoelastic damage model has been applied on AC (Park et al. 1996). This model has been modified and a Visco-Elastic-Plastic Continuum Damage (VEPCD) model has been developed to study initiation and accumulation of micro-cracking due to material damage and to study damage progression (Y. Richard Kim 2009). FEM has been implemented using VEPCD and simulation of damage growth due to accumulation of viscous strain under fatigue loading has been performed (Y. Richard Kim et al. 2008). According to authors knowledge, VEPCD does not identified cohesive and adhesive damages in AC. Desai defined disturbance as a damage to measure the translation, rotation and micro-structural changes within AC materials (Y. Richard Kim 2009). Desai's Disturb State Constitutive (DSC) model has not been used to characterize stiffness degradation of matrix or disturbance in mastic or matrix due to moisture.

Several finite element method (FEM) based damage models have been developed to characterize linear viscoelastic and visco-elastic-plastic materials (Abu Al-Rub, Darabi, et al. 2011; Abu Al-Rub, You, et al. 2011; You et al. 2012). Most of the models used VEPCD or modified VEPCD with user defined constitutive equation implemented in FEM model for full scale pavement or cylindrical core specimens. Damage due to accumulation of viscoelastic and viscoplastic strain has been shown for different temperature under loading conditions. Also, maximum stress criteria has been

implemented as cohesive zone modeling for predicting multi-scale damage model by FEM (Kim et al. 2012). An aggregate surrounded by asphalt have considered as small scale and a full scale AC pavement consists of several aggregates has been considered as large scale model. Average stress and strain in the FEM models have computed and compared for both undamaged and damaged conditions. Cohesive zone model has also been implemented by FEM for cylindrical AC sample (Kim et al. 2005). Only stress and strain relationships have been computed for different strain rates.

Many studies have been done to identify damages under dry and wet conditions in AC (Ban et al. 2011; Bhasin et al. 2006; Birgisson et al. 2003; Fromm 1974; Kringos et al. 2008a; Spinel 2009; Tarefder and Arifuzzaman 2010). Most of the studies evaluate damages in AC by laboratory measurements. Even though both laboratory investigations and FEM model studies have agreed with the concept of adhesive and cohesive damages but very few of them able to identified and evaluated those damages into FEM models. Most of the studies emphasized on the total damages of AC. Also, none of them has able to include and evaluate both adhesive and cohesive damages in a single FEM model. In addition, very few studies conducted FEM analysis under both dry and wet conditions. Initiation, progression, and quantification of the adhesive and cohesive damages using maximum stress criteria in matrix under wet and dry conditions have not been performed yet.

4.6 Damage Law for Cohesive Elements

Cohesive element damage law is used in this study to define matrix damage. Cohesive law is defined by a monotonically increasing traction-separation load up to a critical point

followed by a monotonically decreasing load or softening curve (Lucas et al. 2007). The critical point or highest point or load is known as the damage initiation point. The elastic behavior is defined by an elastic constitutive matrix that relates to the nominal stress and nominal stain in the interface elements. Nominal stress is defined by the force component divided by the element area at each integration point. Nominal strain is the separation divided by the original thickness at each integration point. The nominal stress vector, σ, consists of three traction components σ_n acting to the pure normal direction, σ_s acting toward the first shear direction and σ_t acting toward second shear direction. The stress tensor σ can be express in terms of stiffness E and strain ε

$$\sigma = \begin{Bmatrix} \sigma_n \\ \sigma_s \\ \sigma_t \end{Bmatrix} = \begin{bmatrix} E_{nn} & E_{ns} & E_{nt} \\ E_{ns} & E_{ss} & E_{st} \\ E_{nt} & E_{st} & E_{tt} \end{bmatrix} \begin{Bmatrix} \varepsilon_n \\ \varepsilon_s \\ \varepsilon_t \end{Bmatrix} = E\varepsilon \tag{4.1}$$

where E_{nn} is the stiffness in the pure normal mode, E_{ss} is the stiffness in the first shear direction and E_{tt} is the stiffness in the second shear direction.

4.6.1 Damage Initiation Criteria

Damage is assumed to initiate when the maximum nominal stress ratio reaches a value of one. The maximum nominal stress ratio is defined by Eq. (4.2) below

$$max\left\{\frac{\langle \sigma_n \rangle}{\sigma_n^0}, \frac{\sigma_s}{\sigma_s^0}, \frac{\sigma_t}{\sigma_t^0}\right\} = 1 \tag{4.2}$$

where σ_n^0 is the nominal strength toward the normal direction, σ_s^0 is the nominal shear strength toward the first direction and σ_t^0 is the nominal shear strength toward the

second direction measured in the laboratory. In this study, only compressive strength and shear strength to the first direction of the matrix are measured in the laboratory. Also, two dimensional FEM model is considered for identifying damage. For this reason the second shear strength parameter is not required and Eq. (4.3) becomes,

$$max\left\{\frac{\langle\sigma_n\rangle}{\sigma_n^0},\frac{\sigma_s}{\sigma_s^0}\right\}=1 \tag{4.3}$$

The tests are done under both dry and wet conditions. The symbol ⟨ ⟩ is known as Macaulay bracket. Macaulay brackets are used to signify that a pure compressive deformation or stress state does not initiate damage. It should be noted that, maximum strain ratio can also be computed by Eq. (4.4), which is similar to Eq. (4.2). The maximum strain ratio can be expressed as,

$$max\left\{\frac{\langle\varepsilon_n\rangle}{\varepsilon_n^0},\frac{\varepsilon_s}{\varepsilon_s^0},\frac{\varepsilon_t}{\varepsilon_t^0}\right\}=1 \tag{4.4}$$

where ε_n^0 is the maximum nominal compressive strain of matrix, ε_s^0 is the maximum nominal shear strain toward the first direction and ε_t^0 is the maximum nominal shear strain toward the second direction measured in the laboratory. This equation is not used for this study.

4.7 Materials and Methods

4.7.1 Sample Preparation

Asphalt mix is collected from a local plant in cooperation with the New Mexico Department of Transportation (NMDOT). The loose mix is separated by sieving. Loose mix passing through number 16 sieve (1.19 mm) and retained on number 200 sieve (0.074 mm) is collected as matrix material. Cylindrical samples of height 69.85 mm (2.75 in.) and 35.31 mm (1.39 in.) diameter are compacted to a target void ratio of 4.0 ± 0.5%. For wet conditioning, samples are soaked before testing for 48-hours under water at room temperature and subjected to a vacuum pressure of 30 mm Hg for half an hour.

4.7.2 Compression and Shear Tests

Three dry and three wet cylindrical matrix samples are uniaxially loaded to failure under strain-controlled mode (Hossain and Tarefder 2013; Hossain and Tarefder 2013a). Figure 4.2(a) shows the testing configuration of the matrix sample under compression. A loading rate of 1.27 mm/min (0.5 in/min) is used. Also three dry and three wet samples are compacted in a shear box and subjected to shear failure with a loading rate of 1.27 mm/min as shown in Figure 4.2(b). Average of three samples' results from compression and shear tests are summarized in Table 4.1. Stiffness E-value is determined by measuring the slope of secant modulus. Secant modulus is defined as slope connecting origin to 50% of maximum strength of material (Santi et al. 2000). Several studies used and recommended secant modulus to calculate elastic modulus of asphalt concrete (Degrieck and Van Paepegem 2001; Voyiadjis and Allen 1996; Wang 2011). Ultimate strength of matrix obtained from compression and shear tests are also listed in Table 4.1

(Hossain and Tarefder 2013; Hossain and Tarefder 2013a). It can be seen that E-values of dry sample are higher than those of wet samples, which is expected. But there is an exception; E-value of wet sample under compression is found to be smaller than the E-value in shear. In a previous study, it has been observed that, aggregate surface roughness increases after moisture conditioning (Kasthurirangan Gopalakrishnan, Broj Birgisson, Peter Taylor 2011). This increased surface roughness might cause the material stiffer than the dry material. Unlike compressive test, the shear test is confined into shear box and might causes additional stiffness.

4.8 FEM Model Development

The FEM model is developed using ABAQUS/CAE 6.9-EF1, commercially available software. A two-dimensional idealization of a spherical aggregate surrounded by a layer of matrix material is considered. Obviously, it can be argued that the spherical aggregate is not a true representation of aggregate particles reside in an AC. Similar argument can be made on the size of the aggregate particle. Also other studies use spherical shape aggregate to predict moisture-induced damage (Kringos et al. 2008a; Kringos et al. 2008b). The fact is the shape and size of aggregate particle varies a lot in asphalt concrete. Therefore a study that would consider the effects of the size and shape on the outcomes, that is asphalt cohesion and adhesion, can itself be complex but doable. For simplicity, the model considered for this study is one quarter of a spherical coarse aggregate surrounded by a layer of matrix material, as shown in Figure 4.3. This suffices the purpose of this study. The radius of the aggregate is assumed to be 19.05 mm (0.75 in.) based on the nominal maximum size (25.4 mm or 1.0 in.) of the mix aggregate collect from the plant. Since matrix thickness varies in asphalt concrete, two thicknesses of

matrix layers (0.508 and 1.27 mm) are considered. The size of the selected fine aggregate is ranges from 1.19 mm to 0.074 mm. The thickness of matrix is chosen such that the fine aggregates itself have sufficiently coated with asphalt binder to make a homogeneous matrix material.

Though AC has been considered to be visco-elastic-plastic material, matrix is assumed to behave elastically following the behavior observed in other studies. It has been mentioned that AC behaves elastically at low temperature and visco-elastically at high temperature (Zhu et al. 2010). Also the stiffness of binder is close to stiffness of filler at lower temperature (Shashidhar and Shenoy 2002). In addition, the phase angle and rut factor for wet AC material is small comparing to dry AC material and wet AC material considered behaves elastically (Tarefder, Yousefi, et al. 2010). E-value of limestone aggregate is well established in literature, therefore laboratory tests are not conducted on aggregate. The E-value of aggregate used in this study is 48.26 GPa (7,000,000 psi) and the Poisson's ratio is 0.20 (Roque et al. 2009).

The loading and the shape of the FEM model are symmetrical to the vertical axis. The model is restrained for vertical and horizontal movement at the bottom, but only horizontal movement is restrained on the sides. Four noded linear quadrilateral cohesive elements are used to define the matrix. Linear elements are used since quadratic elements are not available for assigning axi-symmetric cohesive element in ABAQUS. Three and four noded linear quadrilateral plane stress elements are used to define the aggregate. Combinations of both three and four noded elements are required due to the spherical shape of the aggregate. In ABAQUS, maximum stress criteria required maximum stress in both vertical and shear directions according to Eq. (4.2). Since the model is two-

dimensional, data from one shear direction is sufficient as per Eq. (4.3). The interface between matrix and aggregate is defined as cohesive interaction. The bottom of matrix surface and top of aggregate surface are selected to make an interface. FEM model should have interface interaction behavior while model consists of two different materials and in contact.

In the FEM model, instead of applying a load, a specified deformation is applied and stresses are calculated using Eq. (4.1) and used to determine damage according to the Eq. (4.3). Deformation magnitudes of 0.72 mm (0.0285 in.) and 1.45 mm (0.057 in.) are applied on the FEM model. The magnitude of the deformation is calculated based on a standard duel tandem wheel on a pavement. It has been observed that a dual tandem wheel of total 889.64 KN (200,000 lb) load produces a 1.45 mm (0.057 in.) deformation in a 203.02 mm (8 in.) thick AC. Therefore 1.45 mm value of the deformation is considered. Also, half of this 1.45 mm is considered. The selected deformation is the extreme deformation that a pavement can experience since the weight of the dual tandem is for the landing gear of an aircraft. Also an aggregate coated with matrix material located at the top surface of pavement might experiences that amount of deformation. This deformation is considered to observe the extreme scenario of damage in AC. The deformation load is applied on 10.16 mm (0.4 in.) length of matrix. Usually, Indirect tensile strength of asphalt concrete wheel is determined by subjecting an asphalt concrete sample diametrically though a 20.32 mm-25.4 mm (0.8-1.0 in.) loading strip. Since the model is axi-symmetric, deformation load is applied over 10.16 mm (0.4 in.) length.

Traffic load on the roadway pavement is dynamic and cyclic. The shape of the dynamic load varies and really depends on the tire foot-print and speed of the vehicle. For

example, dynamic modulus of asphalt concrete is determined using sinusoidal loading for using in the new mechanistic-empirical pavement design procedure. In this study the FEM is simulated using three deformations intensity shapes or patterns namely, triangle, sawtooth and rectangle (Hossain and Tarefder 2013b). In each case, only one cycle of dynamic deformation is applied. These three deformation patterns are shown in Figure 4.4. In this study the deformation intensity pattern used to see how damage initiates and progressed into matrix while the deformation applied with highest intensity for a very short time (i.e. triangular patter) or the deformation applied with highest intensity for the entire analysis period (i.e. rectangular patter) and in between of those two (i.e. sawtooth pattern).

The deformation is applied on the FEM model by following three load intensity patterns shown in Figure 4.4 and according to the function described in Table 4.2. According to Table 4.2, *i* stands for intensity magnitude and *t* stands for time in second. For an example, for triangular pattern, at *t*=0, 0.072 mm deformation multiply with intensity magnitude *i*=0, so total zero deformation is applied at *t*=0; then at *t*=0.05, 0.072 mm deformation multiply with intensity magnitude *i*=1.0, so total 0.072 mm deformation is applied at *t*=0.5; then at *t*=0.10, 0.072 mm deformation multiply with intensity magnitude *i*=0, so total zero deformation is applied at end of the cycle. If the time increment and corresponding magnitude in the cycle is needed for the ABAQUS solver then it calculated automatically by linear interpolation.

The analysis matrix is shown in Table 4.3. Total twenty-four FEM simulations are run according to Table 4.3.

4.9 Results and Discussions

The damage locations near the top surface of the matrix and/or in between the top surface and matrix-aggregate interface are named as cohesive damage. The damage locations at the bottom of matrix and/or near the matrix-aggregate interface are named as adhesive damage. The matrix layer with a thickness of 0.508 mm (0.02 in.) is termed as thin matrix and 1.27 mm (0.05 in.) is termed as thick matrix in the subsequent sections.

4.9.1 Damage Magnitudes

Damage magnitudes are identified using Maximum Stress Criteria (MAXSCRT) contours. MAXSCRT contour is a plot of the ratio of stress computed by the FEM model due to applied deformation over ultimate stress or strength measured in the laboratory as described in Eq. (4.3). Upon applied deformation and using Eq. (4.1), for each integration point of an element, the normal and shear stresses are calculated; the calculated normal and shear stresses are normalized by using Eq. (4.3) for two dimensional FEM model; the maximum normalized value between the two ratios are the critical normalized value and showed as MAXSCRT value in the contour diagram. MAXSCRT is a unit less value since it is a ratio of two stresses. The maximum value of MAXSCRT is 1.0. When MAXSCRT value is 1.0 for an element than that particular element is known as damaged element for the whole domain. When MAXSCRT value is less than 1.0 for an element, the element is not damaged yet but will or might damaged upon increase of load magnitude or increase of duration of load or decrease in material thickness. The two deformations are used to see the changes in damage initiation and progression due to increase of deformation magnitudes; three load patterns are used to see the changes in

damage initiation and progression due to changes of duration of applied deformation; thin and thick matrix are used to see the change in damage magnitude due to change in thickness.

According to Table 4.1, the E-value for normal direction is higher for dry samples than wet samples, so, for same deformation and using Eq. (4.1), the normal stress under dry condition is higher than wet condition. On the other hand, the maximum normal stress is also significantly higher under dry condition than wet condition, so, the normalized value calculated using Eq. (4.2) for dry condition might lower than wet condition. If E-value for shear directions are considered, the dry sample has lower E-value than wet sample, so, for the same deformation or strain and using Eq. (4.1), the shear stress is lower under dry condition than wet condition. Furthermore, the maximum shear stress is significantly higher under dry condition than wet condition, so, the normalized value calculated using Eq. (4.2) for dry condition might lower than wet condition. While comparing the normalized normal and shear stresses under dry or wet condition, ABAQUS solver picks the highest value between two and shows as MAXSCRT value for that particular condition.

In addition to deformation value, the duration of applied deformation is also important for progression of damage. Maximum deformation is applied for a specified time step. For triangular pattern, deformation increases over time and the maximum deformation applied for almost zero second or instantaneously, for sawtooth pattern, maximum deformation applied for 0.04 sec and for rectangular pattern, maximum deformation applied for almost 0.0999998 sec. Damage inside the material is higher when deformation is applied for longer time. The reason behind, when damage initiates due to

applied deformation in some elements (i.e. MAXSCRT value is 1.0), that element does not carry any stress for the rest of the analysis period. For this reason, stress carrying capacity increase for adjacent elements and their MAXSCRT value increases over time and damaged if normalized value exceeds 1.0 and the process continues until the end of analysis period. It is expected that rectangular pattern shows higher damage locations than sawtooth or triangular pattern since the applied deformation is applied for longer time period.

Moreover, thickness of matrix on aggregate might help prevent damage inside the matrix material. Thicker matrix provides higher stress carrying capacity since more area of matrix is taking stresses. Thick matrix will carry higher deformation and distribute stresses evenly into the larger area to reduce damage than thin matrix.

The maximum MAXSCRT values for the whole model of wet and dry samples are plotted in Figure 4.5 for three intensity patterns for 0.72 mm (0.0285 in.) and 1.45 mm (0.057 in.) applied deformation on thin and thick matrix. Maximum MAXSCRT values are taken from the contour plots. Comparing Figure 4.5(a) and 4.5(b), and Figure 4.5(c) and 5(d), it can be seen that MAXSCRT values for thick matrix is lower than thin matrix for triangular and sawtooth pattern. Rectangular pattern shows highest MAXSCRT value for both thin and thick matrix in all cases. Indeed, thicker matrix is less damaged than thinner matrix for both dry and wet conditions and proved that thicker matrix sustain more deformation than thinner matrix. On the other hand comparing Figure 4.5(a) and 4.5(c), and 5(b) and 5(d), it can be seen that maximum MAXSCRT value increases due to increase of applied deformation. Also wet samples show higher maximum MAXSCRT value than dry samples and prove that wet samples are more damage prone than dry

samples. Reasons for showing higher MAXSCRT value under wet condition comparing to dry condition is explained in the following sections. Also maximum MAXSCRT value increases when load intensity pattern changes from triangular to sawtooth to rectangle. This supports the argument that, duration of applied deformation influences damage in the matrix and more damaged locations are exposed inside the matrix material.

In Figure 4.5 (a), the maximum MAXSCRT value is about 0.68 under dry conditions and 0.73 under the wet conditions for the triangle pattern. Since for the triangular loading, the MAXSCRT value is less than 1.0, so no element is damaged. The MAXSCRT value in some elements reaches the maximum value of 1.0 under both dry and wet conditions for sawtooth and rectangular patterns. So for both sawtooth and rectangular patterns there are damaged elements. According to Figure 4.5(b), the maximum MAXSCRT value is about 0.06 under the dry condition and 0.09 under the wet condition for triangular pattern; the maximum MAXSCRT value is about 0.11 under dry condition and 0.15 under wet condition for sawtooth pattern. In Figure 4.5(c), the maximum value of MAXSCRT is 1.0 for all three load patterns; means, both dry and wet samples shows damages. In Figure 4.5(d), the maximum value of MAXSCRT is about 0.13 under dry condition and about 0.18 under wet condition is about 0.18 for the triangular pattern; the maximum MAXSCRT value is about 0.21 under the dry condition and 0.30 under the wet condition for sawtooth load pattern; the maximum value reaches to 1.0 for rectangular pattern under both dry and wet conditions.

4.9.2 Damage Contours

The advantage of the FEM model is the contour plots of the output variables. Figure 4.6 and 4.7 are plotted for MAXSCRT to identify the distribution of damages in matrix material for the 1.45 mm (0.057 in.) deformation and for the thin and thick matrix respectively. Contour plots for the 1.45 mm (0.057 in.) deformation are presented because according to Figure 4.5, 1.45 mm (0.057 in.) deformation shows higher damage in the matrix material. One zoomed in section is shown for each loading pattern so that the contour of damage can be seen clearly. The color of contours ranges from blue to red; blue means small damage and red means large damage. Comparing Figure 4.6 with Figure 4.7, there are more red color regions for thin matrix than thick matrix, since thin matrix have higher damaged locations than thick matrix. Most importantly both adhesive and cohesive damages are occurred in dry and wet conditioned samples for thin matrix but mostly cohesive damage observed for thick matrix. Surely, thick matrix is stronger than thin matrix and carries more deformation before damage.

It is difficult to quantify damages in matrix and identified it to adhesive and cohesive damage under the triangular pattern for thin matrix by only observing and comparing the Figure 4.6(a) and 4.6(b). Similar scenario is also true for Figure 4.6(c) and 4.6(d) under the sawtooth pattern for thin matrix. For the rectangular pattern, cohesive damage at the top of matrix and adhesive damage at the bottom of matrix and near the interface are clearly shown in the Figure 4.6(e) and 4.6(f) for the thin matrix. Both dry and wet samples show cohesive and adhesive damages but wet sample shows more damage at the bottom of the matrix. Damage initiates under the deformation loading zone and at the top of the matrix. Most of the elements at the top of matrix damaged just after applying deformation. After initiating damage at the top of the matrix, it progresses towards the

bottom of the matrix and near the interface region since interface region is weakest in the whole domain. Damage progressed towards the bottom of the matrix and continues progression until every element near interface region exposed to damage; when no element is capable of taking any stress at the interface region, than the damage progressed to the second bottom layer since those elements are the weaker in the domain. It is clear that matrix material near interface region is the weakest and prone to damage under both dry and wet conditions for the thin matrix. In addition, the strength and stiffness under dry condition is higher than under wet condition; for this reason, dry condition sustain more deformation and carry more stress than wet condition at the bottom of the matrix and shows less damage. The elements near to the left side boundary conditions do not show significant damages because according to Eq. (4.3) pure compressive stress will not cause any damage in the matrix. Indeed those elements are under pure compressive stress.

Figure 4.7 presents MAXSCRT for 0.057 in. deformation load for the thick matrix. According to Figure 4.7 (a) to 4.7(b) the maximum MAXSCRT value is 0.13 and 0.18 for the triangular pattern under the dry and wet conditions respectively. In Figure 4.7(c) and (d), the maximum MAXSCRT value is 0.21 and 0.30 for the sawtooth pattern under the dry and wet conditions respectively. The MAXSCRT value less than 1.0 means no element exposed to damage but will damage with changes in deformation duration time or higher deformation magnitude. Figure 4.7(e) and 4.7(f) shows the maximum MAXSCRT value 1.0 for the top elements, means cohesive damage occurred for the rectangular pattern. It should be noticed that the minimum value of MAXSCRT are showing zero but this is not zero rather very small; the values are showing zero since the

MAXSCRT values are rounded up to two decimal points. The Triangular and sawtooth patterns do not show damage but they definitely shows the path of the stress flow from top the surface to the bottom surface of matrix. This stress flow and path from the top to bottom of matrix is not clearly visible for thin matrix as shown in Figure 4.6. Damage progresses from the top of matrix layer to the bottom of matrix layer following the stress path as show in Figure 4.7(a) to 7(d). The locations of the maximum MAXSCRT for both triangular and sawtooth patterns are on the surface and near 10.16 mm (0.4 in.) from the left support. The region shows the stress concentration at the top of the matrix and perpendicular stress path from the top of the matrix to the bottom of the matrix. This location is important because for both thin and thick matrix the path is similar. For thin matrix, when the cohesive damage occurred at the top of the matrix than this perpendicular path at the end of the loading zone is followed to initiate and progress of the adhesive damage at the bottom of the matrix. For the rectangular pattern in the Figure 4.7(e) and (f), this path is not present, since the cohesive damage initiates and dominates at the top of the matrix for entire duration. This stress concentration path is more visible when the deformation is ramped up like triangular and sawtooth pattern but not for rectangular pattern when the deformation jumps to maximum intensity in a very short time. Stress distributed evenly when load increase gradually with step time like the triangular or the sawtooth pattern.

4.9.3 Damage Initiation, Distribution, and Progression

The Cohesive and the adhesive damage variations at the top of the matrix and at the bottom of the matrix are not clearly differentiable in the contour diagrams as presented in the Figure 4.6 and 4.7. For this reason, the variations of MAXSCRT magnitude are

presented in Figure 4.8 for the triangular and the rectangular patterns under dry and wet conditions for the 0.72 mm (0.0285 in.) deformation and for thin matrix. Figure 4.9 presents the MAXSCRT variation for thick matrix under dry and conditions. The x-axis is the distance measured from the left side boundary conditions on the top and the bottom of the matrix perimeter. The x-axis is taken up to 10.13 mm (0.4 in), because the applied deformation is up to 10.13 mm (0.40 in.) on the top of the matrix. Also, from the contour diagrams, it is observed that damage initiates at about 10.13 mm (0.4 in.) distance on the perimeter. The y-axis presents the MAXSCRT values for the corresponding elements. Only triangular and rectangular patterns are selected, since triangular pattern shows MAXSCRT value less than 1.0 and rectangular pattern shows highest number of elements exposed to damage for both thin and thick matrix. The first elements at both top and bottom locations are not considered in the graphs, since the elements are horizontally restrained only at the left side and it is assumed that these elements might influenced by boundary conditions and will not provide accurate MAXSCRT values.

According to the Figure 4.8(a) and (b), it is observed that MAXSCRT value increases gradually for the triangular pattern and abruptly for the rectangular pattern while distance increases. This phenomenon proves that, cohesive damage initiates rapidly while deformation magnitudes increases abruptly. The significance of Figure 4.8(a) is, under both dry and wet conditions, elements at the bottom location shows higher MAXSCRT value than top location. This means, cohesive damage initiates at the top of the matrix but interface of the two materials influences the initiation and propagation of adhesive damage at the bottom of the matrix elements. Clearly, interface between the two materials influences to initiate adhesive damage at the bottom of the matrix and interface

is the weakest region in the whole domain. According to Figure 4.8(b), for the rectangular pattern, MAXSCRT at the bottom of the matrix is higher under wet conditions than dry conditions. Again, lower stiffness and strength causes higher damage under wet condition than dry condition. Also more elements at the bottom of the matrix reach to the MAXSCRT value 1.0 under wet conditions than dry conditions but all the elements at the top of the matrix reach to MAXSCRT value 1.0 under dry conditions. However this scenario is not true for the thick matrix as explained in the next sections.

The MAXSCRT value is low at both top and bottom of the matrix according to Figure 4.9(a). Cohesive damage at top of the matrix under the wet condition is higher than the dry condition. The scale of the MAXSCRT is kept same for both cases to see the magnitude variations for triangular and rectangular patterns. As seen on Figure 4.9(b), more locations are exposed to cohesive damage under wet condition than dry condition. MAXSCRT value at the bottom of the matrix is very low so the adhesive damage is not initiated yet. Clearly thick matrix helps to prevent adhesive damage but not cohesive damage for both lower and higher deformations. This also proves that cohesive damage initiates and progresses due to applied deformation magnitudes and intensity patterns but adhesive damage initiates and progresses due to weak interface between the two elements. Also, the wet condition shows higher cohesive and adhesive damages due to lower stiffness and strength comparing dry condition.

4.9.4 Strength Degradation of Damaged Elements

It is defined that, when the MAXSCRT value reaches to 1.0 for an element, that element is considered as damaged and unable to carry any stress upon deformation. This

phenomenon is called Strength Degradation (SDEG) for that particular element. The SDEG of a material is a scalar value varies from zero to one but only clearly visible in the FEM model when the value is one. Progression of damage can also be clearly observed by plotting SDEG of the matrix material. Figure 4.10 shows the SDEG value for the rectangular pattern load under dry and wet conditions. The major similarity between the MAXSCRT contour and the SDEG contour is that, SDEG contour only shows 1.0 where MAXSCRT value is also 1.0. The SDEG contour helps to differentiate and identify cohesive and adhesive damages clearly and later on based on SDEG contour, quantifications of the adhesive and cohesive damages are performed. Explanations of initiation and progression of damage are given in the previous sections.

In Figure 4.10 the SDEG are presented for thin matrix and for both 0.72 mm (0.0285 in.) and 1.45 mm (0.057 in.) deformation load. The red color indicates strength degradation in the matrix elements and the blue color indicates no degradation of strength in the matrix elements. Cohesive damage observed for the 0.72 mm (0.0285 in.) deformation load under the dry condition as shown in the Figure 4.10(a). Both cohesive and adhesive damages observed for the 0.72 mm (0.0285 in.) deformation load under the wet condition as shown in the Figure 4.10(b). Both cohesive and adhesive damages observed for the 1.45 mm deformation load under dry and wet conditions, but cohesive damage is significantly higher under wet condition as shown in Figure 4.10(d). Dry sample shows cohesive damage under 0.72 mm (0.0285 in.) deformation but exposed to both cohesive and adhesive damage under 1.45 mm (0.057 in.) deformation. Wet sample shows both cohesive and adhesive damage under 0.72 mm (0.0285 in.) deformation but adhesive damage extends under 1.45 mm (0.057 in.) deformation.

Figure 4.11 shows SDEG for the thick matrix for the rectangular pattern and for both 0.72 mm (0.0285 in.) and 1.45 mm (0.057 in.) deformation load. Damage due to the rectangle intensity pattern is presented because MAXSCRT value due to the triangular and sawtooth patterns are relatively small. One zoomed in section at damaged location is presented for each condition to visualize the SDEG contour plots more clearly. Damage initiation and propagation is observed in the thick matrix. The SDEG value ranges from 0.0 to 1.0 for all cases. It is observed that damage initiations are similar between thin and thick matrix. Maximum cohesive damage is observed at the surface of matrix and at the end of loading zone for both dry and wet conditions and for two different deformation magnitudes. Thick matrix shows cohesive damage and no adhesive damage is observed for any intensity pattern and deformation, since thicker matrix sustains more deformation than thinner matrix and transfer less stresses to the weaker interface region. It is also observed that damage is more under the wet conditions than the dry conditions since wet matrix has lower strength and stiffness than dry matrix. In addition, cohesive damage propagates on top of both dry and wet conditions as deformation increases from 0.72 mm (0.0285 in.) to 1.45 mm (0.057 in.). More elements at the top of the matrix reached to MAXSCRT value 1.0 when deformation value increases.

4.9.5 Quantifying Damaged Area in Thin and Thick Matrix

The MAXSCRT contour provides locations of damaged and undamaged matrix elements; the SDEG contour provides specific location of damaged matrix. In order to measure severity of damage under the dry and the wet condition it is necessary to quantify damage and separate it into the adhesive and cohesive damages. The damaged areas are quantified by measuring the matrix area that is exposed to cohesive and adhesive damages. The

SDEG contour plots are selected to quantify adhesive and cohesive damages. The area of single element for both thin and thick matrix is 0.065 square mm (0.0001 square in.). Number of damaged elements are counted and multiplied by the area of the element to determine damaged area. Total undamaged area of thin matrix is 15.48 square mm (0.024 square in.) and thick matrix is 39.35 square mm (0.061 square in.). It can be noted that thin matrix is divided into 4 equal layers of which top three layers are used in the cohesive damage calculations and the bottom single layer that interfaces with aggregate surface is considered for the adhesive damaged area calculation. The percentages of damaged to undamaged areas are calculated. It is observed that cohesive damage initiate at the top layer of matrix and then progress at the bottom of matrix and initiates adhesive damage and keep progressing from the bottom of matrix as cohesive damage into the matrix.

A summary of adhesive and cohesive damaged matrix area are given in Table 4.4. According to the table total 13.3% of the matrix area is damaged under dry condition; among this 12.47% area shows cohesive damage and 0.83% dry matrix area shows adhesive damage. 29.6% of the matrix area is damaged under wet condition; among this 19.18% area shows cohesive damage and 10.42% area shows adhesive damage. When deformation increases from 0.72 mm (0.0285 in.) to 1.45 mm (0.057 in.), then total 29.60% of matrix area is damaged under dry condition; among this 15.85% area shows cohesive damage and 13.75% area shows adhesive damage. On the other hand, total 46.15% of matrix area damaged under wet conditions; among that 30.30% area shows cohesive damage but 16.67% area shows adhesive damage. Thick matrix shows significantly low cohesive damage than thin matrix and no adhesive damaged area is

observed. Total 4.1% area is cohesive damaged under dry condition, while 4.8% is damaged under wet condition. When deformation increases, 5.6% of matrix area shows cohesive damage comparing to 6.1% area under wet condition. Adhesive damage increases significantly under the dry and wet conditions while deformation increases from 0.72 mm (0.0285 in.) to 1.45 mm (0.057 in.). For thin matrix and higher deformation, both adhesive and cohesive damages seem vulnerable; on the other hand, cohesive damage is sensitive to both lower magnitude loads.

4.10 Conclusions

1. Top surface of the matrix showed cohesive damage and cohesive damage is higher under wet condition than dry condition. Matrix material near the interface region shows adhesive damage and adhesive damage is higher under wet condition than dry condition. Adhesive damage is the driving factor for pavement degradation and measure needs to be taken to reduce adhesive damage as well as cohesive damage in AC.
2. Upon deformation, cohesive damage initiates at the top of matrix and then damage propagates towards the bottom of matrix and matrix-aggregate interface and initiates adhesive damage. Adhesive damage is significantly higher under the wet condition and for the rectangular pattern. This finding also supports the previous conclusion regarding adhesive damage, which is critical for ultimate degradation of AC.
3. Interface region is weakest considering the whole domain. The weakest interface is also a reason for higher adhesive damage in AC. The commonly used additives

used to prevent moisture damage in AC, such as lime, are needed to evaluate more to strengthen the interface between aggregate and matrix material.

4. Only cohesive damage is observed in thick matrix but both cohesive and adhesive damages are observed in thin matrix. Higher matrix thickness improved deformation carrying capacity and transferred less stresses to the interface, so no adhesive damage near interface. In general, interface between the two materials need to be improved to reduce the adhesive damage and improve the overall performance of AC. An optimum asphalt content should be determined that will reduce adhesive damage at the interface by providing thicker matrix coating on coarse aggregate. Also pre-coated aggregate might reduce adhesive damage and more studies are required in this area.

5. The worst damage scenario observed for thin matrix with 1.27 mm (0.057 in.) deformation; about 16.67% and 30.30% matrix exhibits adhesive and cohesive damages respectively under wet condition. On the other hand, 13.75% and 15.85% matrix material exhibits adhesive and cohesive damages respectively under dry condition.

Table 4.1 Laboratory test results under dry and wet conditions

	Test type	Ultimate strength	E-value
Dry	Compression	2.61 MPa (379 psi)	192.72 MPa (27,952 psi)
	Shear	0.81 MPa (118 psi)	147.64 MPa (21,413 psi)
Wet	Compression	2.02 MPa (293 psi)	129.44 MPa (18,773 psi)
	Shear	0.56 MPa (81 psi)	139.10 MPa (20,174 psi)

Table 4.2 Deformation intensity patterns and functions specify in ABAQUS

Triangle	Sawtooth	Rectangle
$i = 0$ at $t = 0$	$i = 0$ at $t = 0$	$i = 0$ at $t = 0$
$i = 1.0$ at $t = 0.05$	$i = 1.0$ at $t = 0.03$	$i = 1.0$ at $t = 0.0000001$
$i = 0$ at $t = 0.10$	$i = 1.0$ at $t = 0.07$	$i = 1.0$ at $t = 0.0999999$
	$i = 0$ at $t = 0.10$	$i = 0$ at $t = 0.10$

Table 4.3 FEM model analysis matrix

Condition	Matrix Thickness	Deformation Intensity Pattern	Deformation value
Dry	0.508 mm (0.02 in.)	Triangle	0.72 mm (0.0285 in.)
		Sawtooth	
Wet	1.27 mm (0.05 in.)	Rectangle	1.45 mm (0.057 in.)

Table 4.4 Adhesive and cohesive damaged matrix area for rectangular intensity pattern load

Deformation magnitude	Damage type	Thin matrix		Thick matrix	
		Dry	Wet	Dry	Wet
0.508 mm (0.0285 in.)	Cohesive damage	12.47%	19.18%	4.1%	4.8%
	Adhesive damage	0.83%	10.42%	-	-
1.27 mm (0.057 in.)	Cohesive damage	15.85%	30.30%	5.6%	6.1%
	Adhesive damage	13.75%	16.67%	-	-

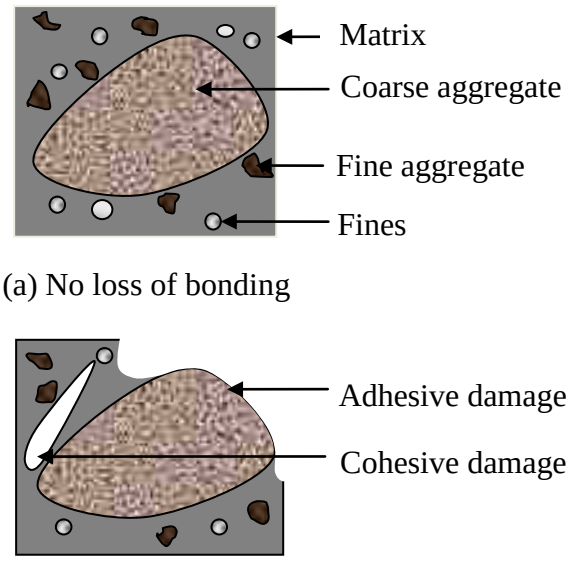

Figure 4.1 Schematic of adhesive and cohesive damage in AC

(a) Sample under compression test

(b) Direct shear test setup

Figure 4.2 Compression and shear tests on matrix

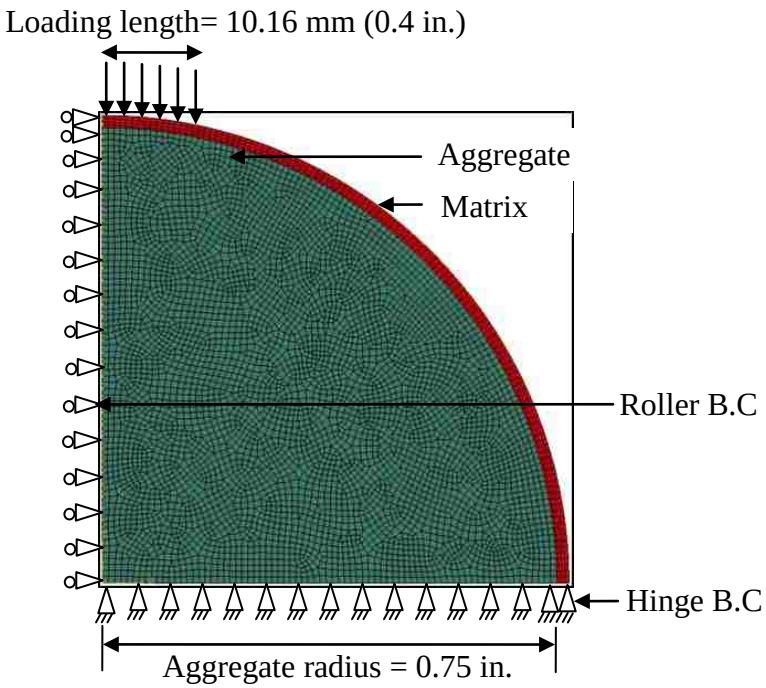

Figure 4.3 Aggregate-matrix FEM model geometry

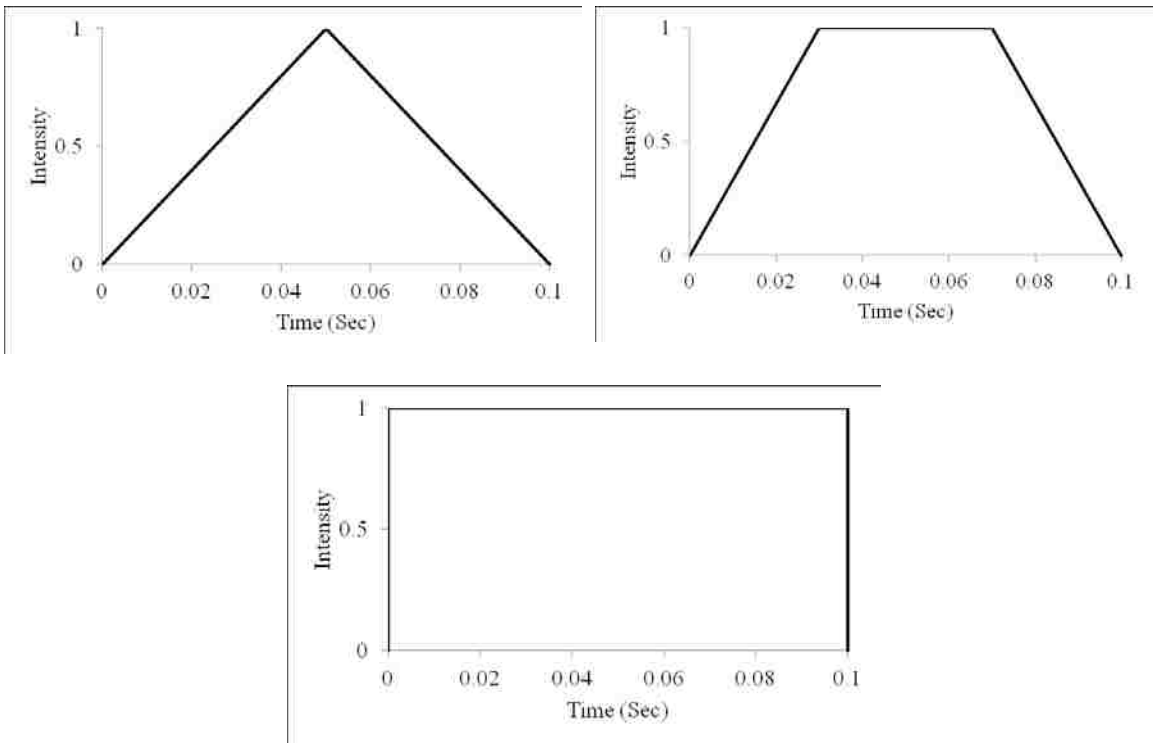

Figure 4.4 Deformation intensity patterns used for FEM modeling

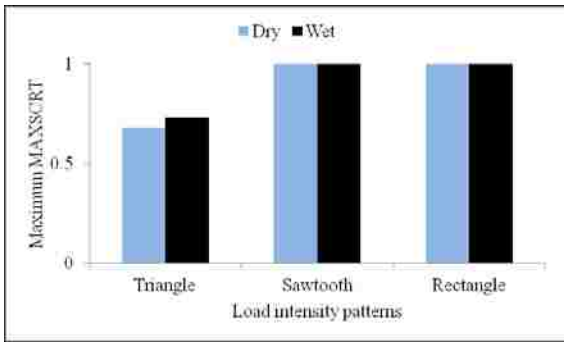

(a) Thin matrix

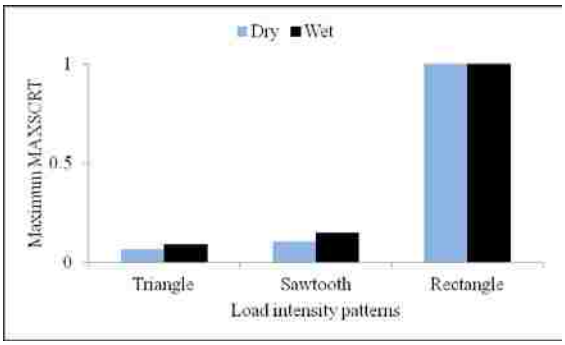

(b) Thick matrix

(i) 0.72 mm (0.0285 in.) deformation

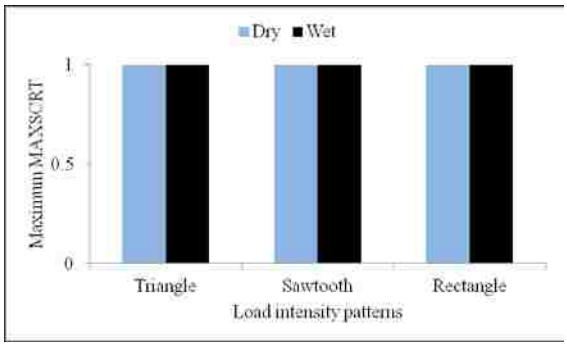

(c) Thin matrix

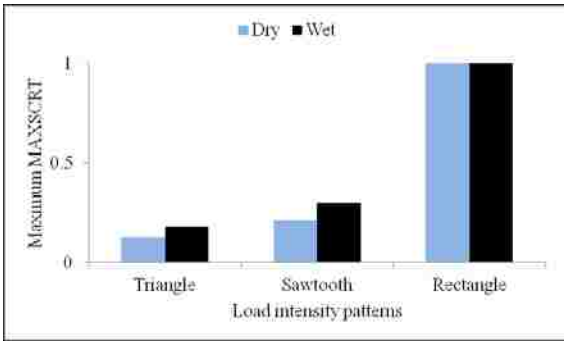

(d) Thick matrix

(ii) 1.45 mm (0.057 in.) deformation

Figure 4.5 Maximum values of Maximum Stress Criteria (MAXSCRT) for three intensity patterns under dry and wet conditions for thin and thick matrix

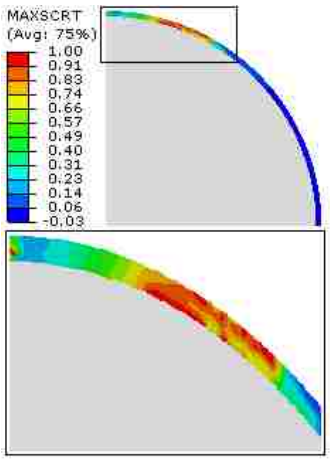

(a) Dry-Triangle

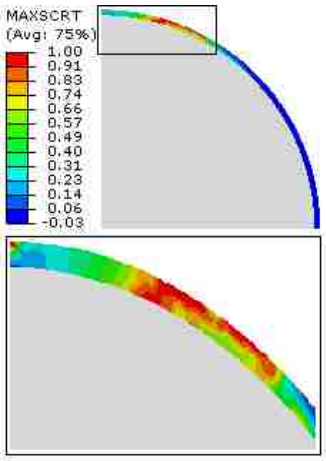

(b) Wet-Triangle

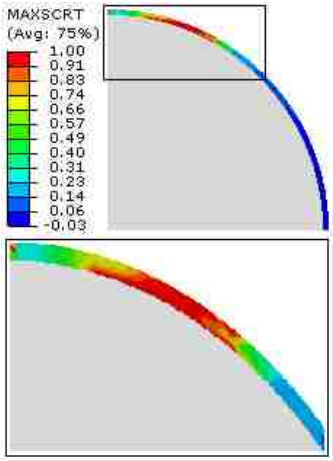

(c) Dry-Sawtooth

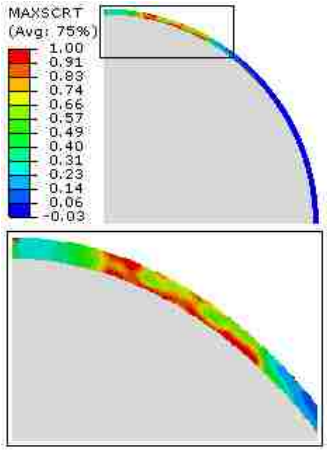

(d) Wet-Sawtooth

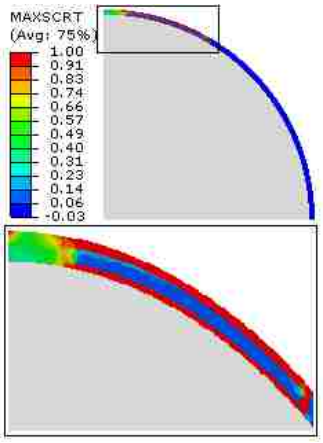

(e) Dry-Rectangle

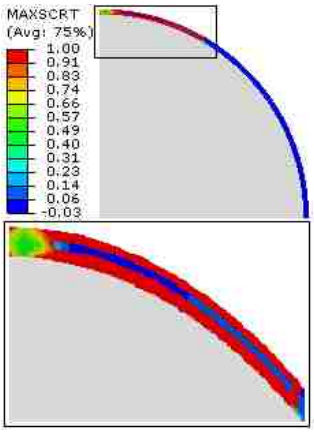

(f) Wet-Rectangle

Figure 4.6 Maximum Stress Criteria (MAXSCRT) under dry and wet conditions for 1.45 mm (0.057 in.) deformation and for thin matrix

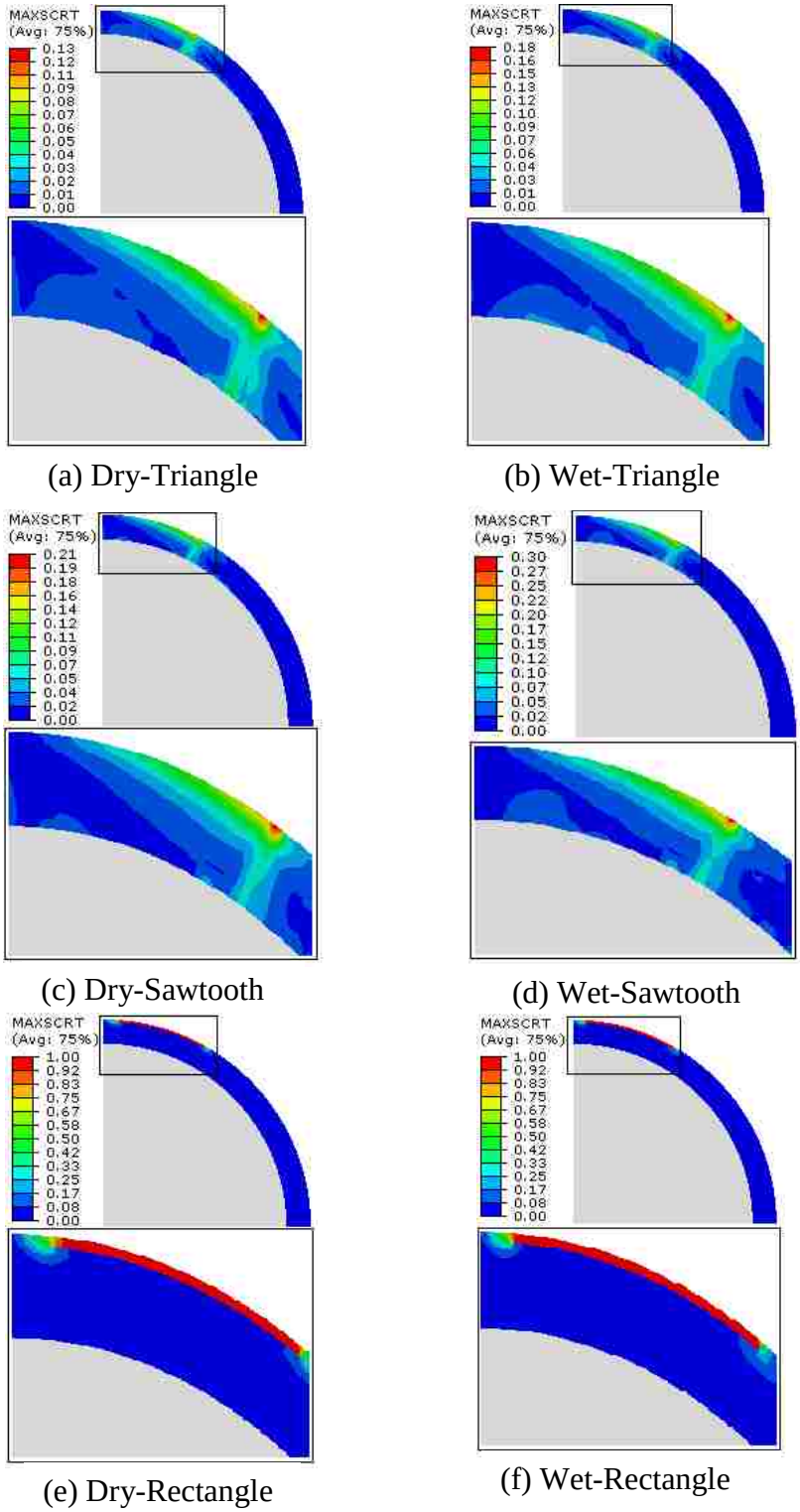

(a) Dry-Triangle

(b) Wet-Triangle

(c) Dry-Sawtooth

(d) Wet-Sawtooth

(e) Dry-Rectangle

(f) Wet-Rectangle

Figure 4.7 Maximum Stress Criteria (MAXSCRT) under dry and wet conditions for 1.45 mm (0.057 in.) deformation and for thick matrix

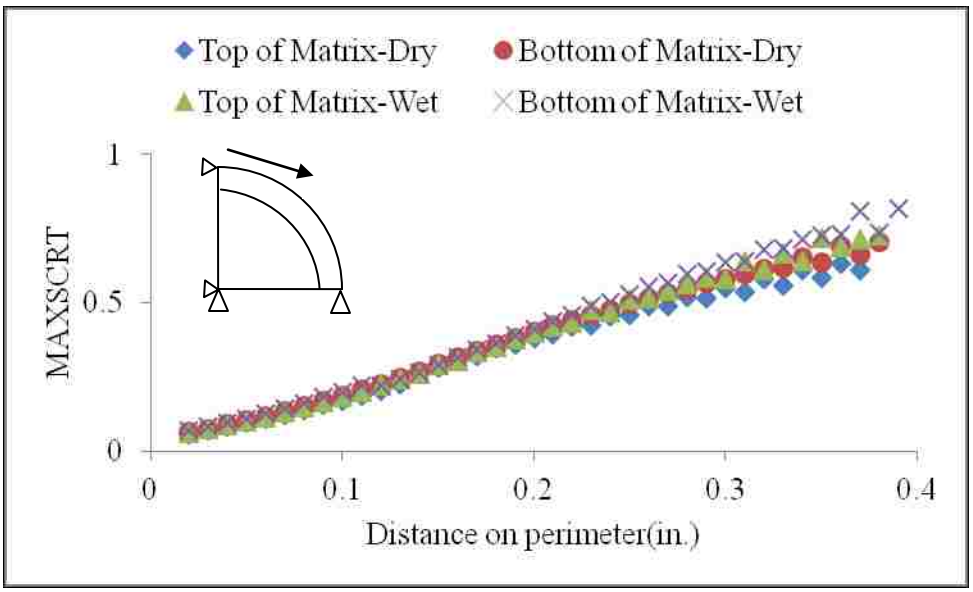

(a) Triangular pattern

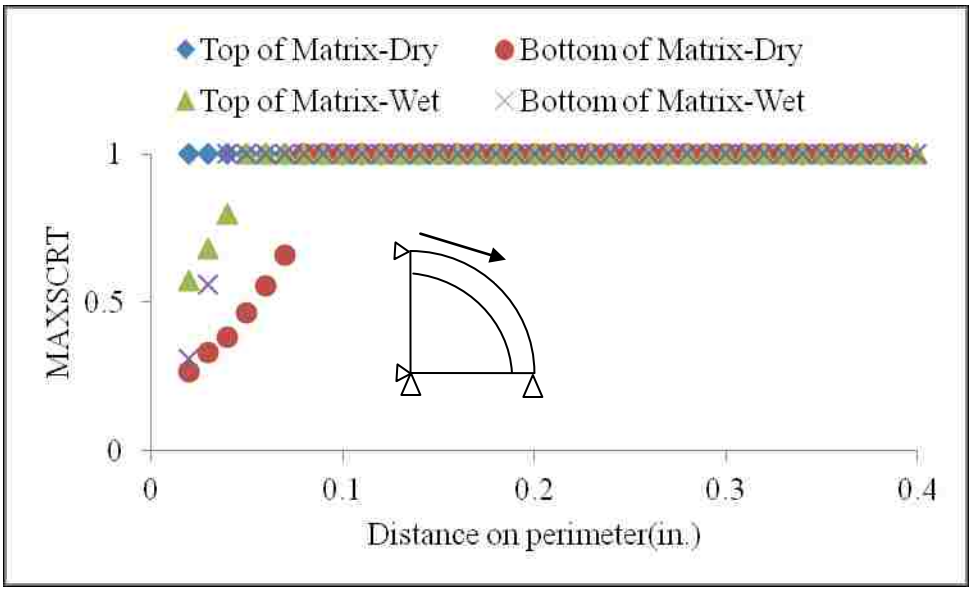

(b) Rectangular pattern

Figure 4.8 Maximum Stress Criteria (MAXSCRT) in the matrix measured from the left side boundary conditions for the 0.72 mm (0.0285 in.) deformation and for the thin matrix

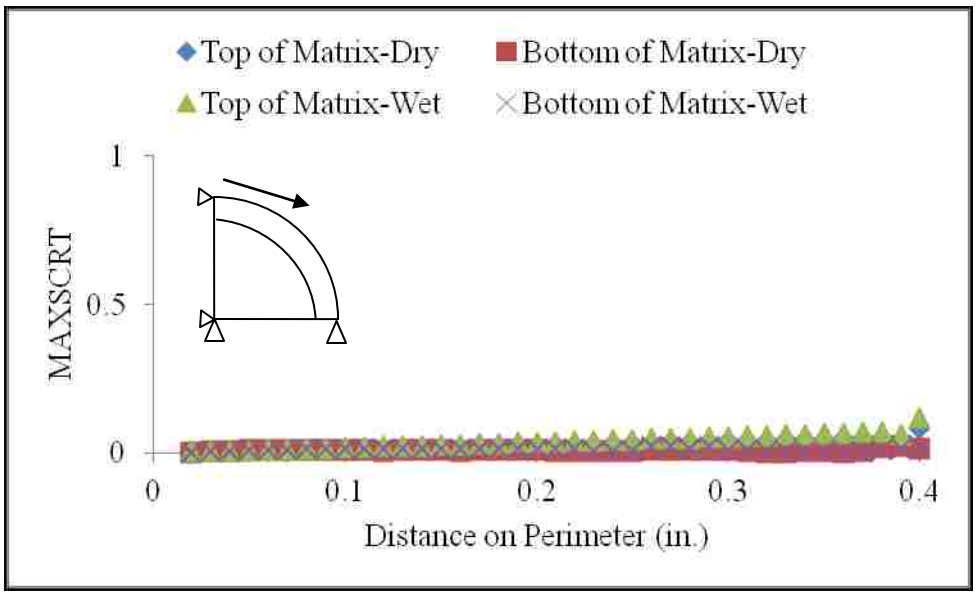

(a) Triangular pattern

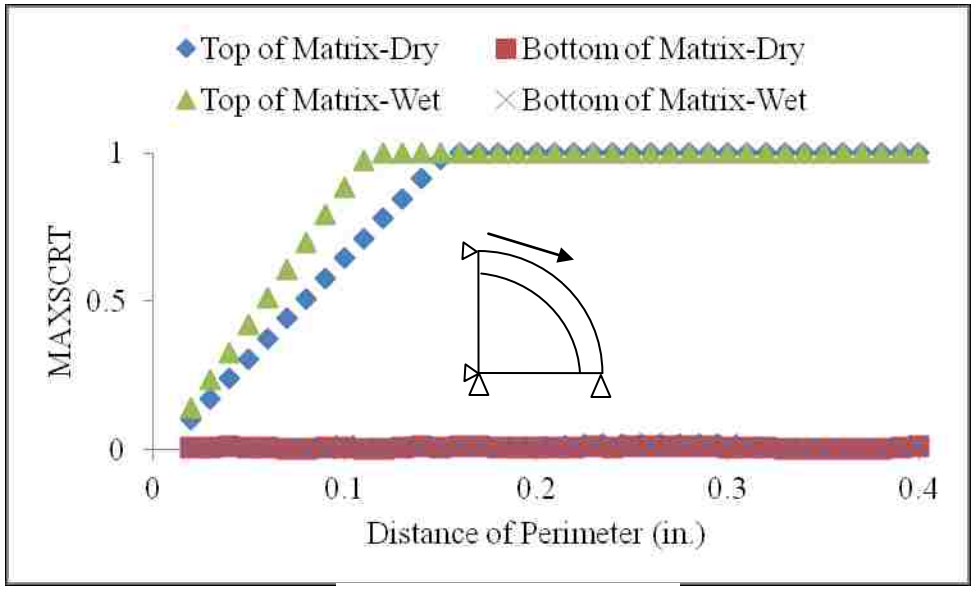

(b) Rectangular pattern

Figure 4.9 Maximum Stress Criteria (MAXSCRT) in the matrix measured from the left side boundary conditions for the 0.72 mm (0.0285 in.) deformation and for the thick matrix

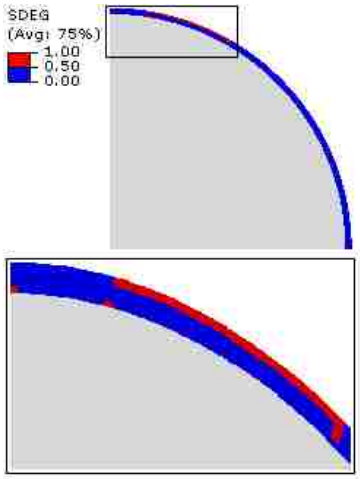

(a) Dry-Rectangle

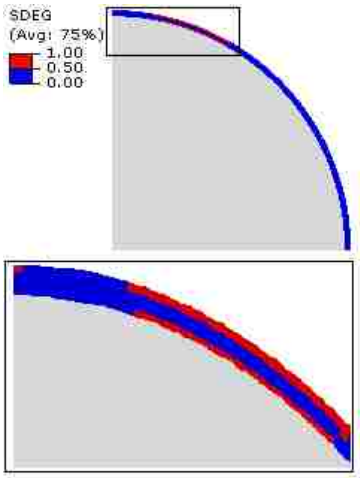

(b) Wet-Rectangle

(i) 0.72 mm (0.0285 in.) Deformation

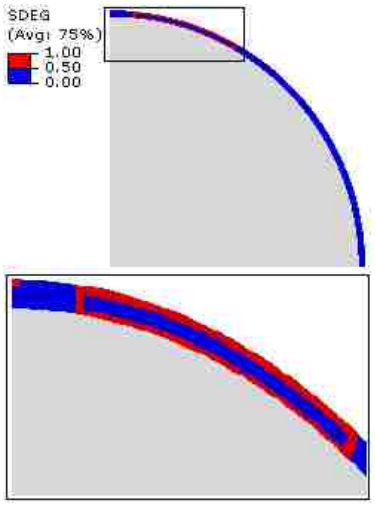

(c) Dry-Rectangle

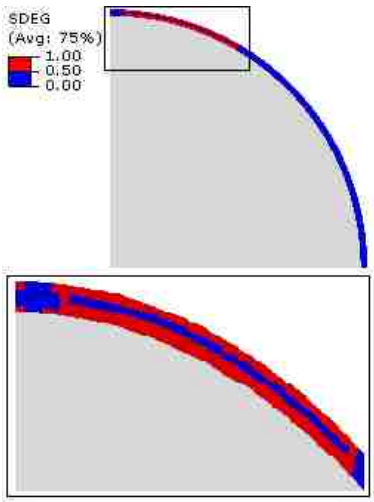

(d) Wet-Rectangle

(ii) 1.45 mm (0.057 in.) Deformation

Figure 4.10 Strength degradation (SDEG) of matrix under dry and wet conditions for 1.45 mm (0.057 in.) deformation and for thin matrix

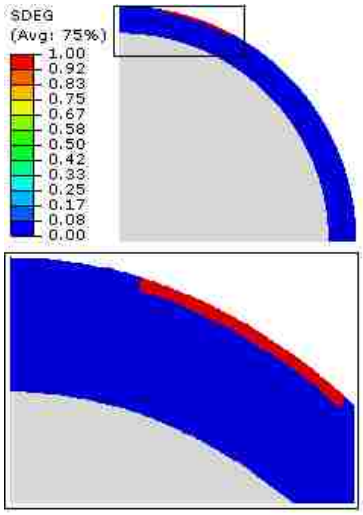

(a) Dry-Rectangle

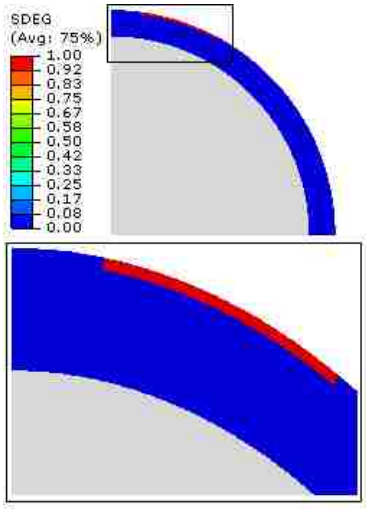

(b) Wet-Rectangle

(i) 0.0285 in. Deformation load

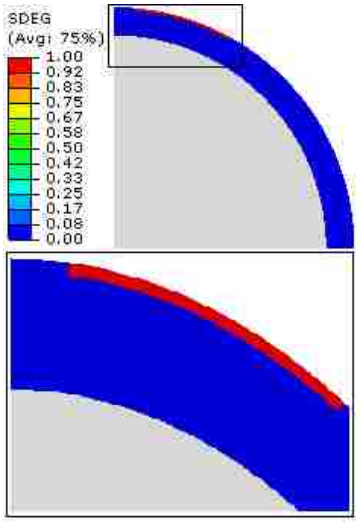

(c) Dry-Rectangle

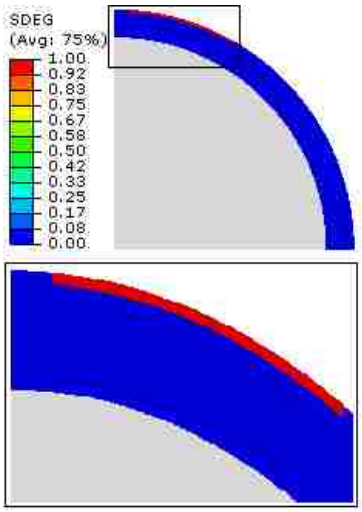

(d) Wet-Rectangle

(ii) 0.057 in. Deformation load

Figure 4.11 Strength Degradation (SDEG) in the thick matrix under dry and wet conditions

CHAPTER 5

DAMAGE AT MATRIX-AGGREGATE INTERFACE

5.1 General

This chapter describes the coupled cohesive and adhesive damage in matrix materials and matrix-aggregate interface, respectively, and effects of moist aggregate in the AC.

5.2 Introduction

Asphalt concrete (AC) is a geological composite material consisting of coarse aggregate, fine aggregate, fines and asphalt binder. In general, coarse aggregate is defined as aggregate retained on a #4 (4.75 mm) sieve, fine aggregate is defined as aggregate passing through a #4 sieve and retained on a #200 (0.075 mm) sieve, and fines are defined as aggregate passing through a #200 sieve. A mixture of asphalt binder with fine aggregate and fines are known as matrix materials (Caro et al. 2010b; Degrieck and Van Paepegem 2001; Fakhari Tehrani et al. 2013). Matrix materials make a coating on coarse aggregate while mixing and compacting with coarse aggregate. This study focuses on the behavior of AC for unconditioned (dry) and moisture-induced (wet) conditions.

Moisture-induced damage in AC has been studied for decades (Birgisson et al. 2003; Fromm 1974; Graf 1986; Kim et al. 2004; Mohamed 1993). Moisture gets into the AC pavement when rainwater gets through pavement cracks or due to capillary action from the bottom of the subbase resulting from a high ground water table or seepage flow. Moisture diffuses through the matrix materials and infiltrates into the matrix-aggregate interface and saturates the aggregates. It has been well established by the researchers that

moisture causes damage in AC. Damage due to moisture in AC occurs mostly in the matrix or interface of the materials (Tarefder et al. 2009). Most researchers agree that damage due to moisture inside an aggregate particle is limited. Rather, most of the moisture damage occurs in the matrix materials. This study focuses only on the effects of moisture in the matrix materials and the matrix-aggregate interface.

Damage in AC can be categorized into damage in the matrix materials and damage at the matrix-aggregate interface. In this study, damage in the matrix materials are expressed as cohesive damage and damage at the matrix-aggregate interface is expressed as adhesive damage (Cheng et al. 2003; Khalid and Monney 2009; Kutay et al. 2007; Spinel 2009; Wasiuddin et al. 2011). The phenomena of adhesive and cohesive damage are shown schematically in Figure 5.1. Figure 5.1(a) shows a fresh dry sample of AC that has not been subjected to any damage: coarse aggregate surrounded by matrix materials. Figure 5.1(b) shows moisture diffusing from the top of the sample through matrix materials, but the coarse aggregate is not saturated yet. Figure 5.1(c) shows moisture diffusing into the coarse aggregate saturating the aggregate and matrix materials. Figure 5.1(d) shows cohesive and adhesive damage due to the moisture diffusion. Cohesive damage is due to softening of the matrix materials by action of the moisture inside the matrix materials and adhesive damage due to the loss of bonding by the action of water at the matrix-aggregate interface.

Few studies have been considered in the past to understand the evolution and progression of matrix damage under dry and wet conditions (Abu Al-Rub et al. 2010; Kringos et al. 2008a; Kringos et al. 2008b). Both dry and wet AC show adhesive and cohesive damage, but it is expected that wet AC will show higher adhesive and cohesive damage due to the

chemical and physical action of water in the matrix materials and matrix-aggregate interface. Conventional laboratory tests on large scale AC samples show the differences in strength in wet AC from dry AC (Azari 2010; Nadkarni et al. 2009; Shah 2003; West et al. 2004). In addition, atomic and nanoscale tests show promising results to evaluate moisture-conditioned asphalt binder and AC samples respectively (Tarefder and Arifuzzaman 2010). However, the mechanical actions of moisture inside the material and at the interface of two materials are not well understood. Most of the previously mentioned studies are limited to cylindrical shape samples or full-scale pavement sections or models to understand the damage caused by moisture. It is also necessary to understand damage behavior at the small scale since damage initiates at the small scale and can be observed clearly at the large scale. In addition, proper precautions can be taken to reduce moisture-induced damage if small-scale behavior is understood. This study is carried out on small-scale AC samples to understand the mechanical action of moisture inside the matrix material and at the matrix-aggregate interface.

5.3 Objectives

The objective of this study is:

1. To understand and investigate the mechanical action of moisture in matrix materials and at the interface of two different materials such as the matrix materials and the aggregate.

An aggregate coated with matrix materials representing a small-scale mechanical model of AC, compared to the large-scale laboratory specimen, is selected since the small-scale AC sample will provide a more in depth view of the mechanical action of moisture. In

this study, plotting the stress-strain relationship of undamaged and moisture-induced damaged materials, quantifying the amount of damage caused in the matrix materials, and quantifying the permanent strain in the matrix materials determine the matrix material damage behaviors. The matrix-aggregate interface damage behaviors are determined by measuring the interface contact status in terms of contact stress, contact opening and contact displacement. The effect of moisture in the matrix materials and at the matrix-aggregate interface is determined by computing results under dry and wet conditions and comparing results from the dry condition.

5.4 Previous Studies on Damage Computation in AC

The concept of damage mechanics is introduced in the early 1920s, but a major breakthrough occurred in the late 1950s by L. M. Kachanov (Lemaitre 1996). Damages in material due to environmental degradation such as the presence of moisture and damage in concrete materials due to non-homogeneous material is introduced (Kachanov 1986). It is also mentioned that geo-materials and polymers change their mechanical properties under the influence of the environment even in the absence of stress. Further, concrete-like materials have weak mechanical resistant due to non-homogeneity.

Damage in AC has been studied for decades. In early 1990, damages in viscoelastic materials in terms of accumulated viscous strain is described (Lemaitre and Desmorat 2005). Initially, this visco-elastic damage model is widely applied on fiber reinforced composite materials (Voyiadjis and Allen 1996; Voyiadjis et al. 1998). Later on, the visco-elastic damage model is applied to AC (Park et al. 1996). Y. Richard Kim (2009) modified the viscoelastic damage model and developed a Visco-Elastic-Plastic

Continuum Damage (VEPCD) model to study initiation and accumulation of micro-cracking due to material damage and to study damage progression. Finite element method modeling (FEM) is implemented using VEPCD and simulation of damage growth due to accumulation of viscous strain under fatigue loading is performed (Y. Richard Kim et al. 2008). According to the author's knowledge, the VEPCD model is applied on the full scale AC pavement model but not on the small-scale AC such as only one aggregate coated with matrix material. Moreover, VEPCD provided damage as a bulk measurement and is not separated into cohesive and adhesive damage. Desai et al. defined disturbance as a damage to measure the translation, rotation and micro-structural changes within AC materials (Y. Richard Kim 2009). Desai's Disturb State Constitutive (DSC) model has not been used to characterize stiffness degradation of matrix or disturbance in matrix due to moisture.

Several FEM based damage models are developed to characterize linear viscoelastic and visco-elastic-plastic materials (Abu Al-Rub, Darabi, et al. 2011; Abu Al-Rub, You, et al. 2011; You et al. 2012). Most of the models used VEPCD or modified VEPCD with a user defined constitutive equation implemented in FEM model for full-scale pavement or cylindrical core specimens. Damage due to accumulation of viscoelastic and viscoplastic strain showed different temperatures under loading conditions. The average stress-strain relationship of the models compared with the different strain rates.

Many studies are done to identify damages under dry and wet conditions in AC (Ban et al. 2011; Bhasin et al. 2006; Birgisson et al. 2003; Fromm 1974; Kringos et al. 2008a; Spinel 2009; Tarefder and Arifuzzaman 2010). Most of the studies evaluate damages in AC by laboratory measurements. Even though both laboratory investigations and FEM

model studies agreed with the concept of adhesive and cohesive damages, very few of them identified and evaluated those damages in FEM models. Most of the studies emphasized the total damages of AC similar to the VEPCD model. Also, none of the studies included and evaluated both adhesive and cohesive damages in a single FEM model. In addition, very few studies conducted FEM analysis under both dry and wet conditions.

5.5 Methodology

FEM modeling technique is used to determine the behavior of AC under dry and wet conditions. ABAQUS, which is commercially available FEM software, is used as a FEM tool. An FEM model is developed considering an aggregate coated with matrix materials. The damage model and material model parameters for matrix materials are determined by laboratory investigations under dry and wet conditions. Also, the damage model parameters for the matrix-aggregate interface are determined from laboratory tests under dry and wet conditions. In addition, the material model parameters of aggregate under dry and wet conditions are collected from other studies. Three FEM models are simulated by considering dry matrix coated on dry aggregate, wet matrix coated on dry aggregate, and wet matrix coated on wet aggregate. The dry matrix-aggregate interface is considered to be in between the dry matrix and dry aggregate, the wet matrix-aggregate interface is considered to be in between both the wet matrix and dry aggregate, and the wet matrix and wet aggregate simulations. It is assumed that no damages occur in the aggregate, but the wet aggregate might influence the damage at the matrix-aggregate interface.

The limitations of this study are considered to be a spherical shaped coarse aggregate coated with matrix materials. Obviously, it can be argued that the spherical aggregate is not a true representation of aggregate particles that reside in an AC. Similar argument can be made on the size of the aggregate particle. The fact is the shape and size of the aggregate particle varies a great deal in AC. Therefore, a study that would consider the effects of the size and shape on the outcomes of the asphalt cohesion and adhesion can itself be complex but doable. A very thin matrix layer is considered on the aggregate and the layer behavior is assumed as elastic. Matrix material shows elastic behavior at low temperature and viscoelastic behavior at high temperature. A static deformation is considered as an input load on the matrix materials even though AC pavement experiences cyclic load from tire pressure. The use of cyclic load would be practical if the strain growth in the viscoelastic material is considered. Since matrix materials are modeled as elastic material, cyclic load application will not show any effect on the materials.

5.6 Introduction to Damage Models

5.6.1 Damage Model for Matrix Materials

The maximum stress criteria damage model is used to define cohesive damage in matrix materials. The model is defined by a monotonically increasing stress-strain up to a critical point followed by a monotonically decreasing softening curve (Lucas et al. 2007). Figure 5.2 shows a linear stress-strain behavior up to the maximum strength (i.e. line AB) of material with linear softening part (i.e. line BC). The material is considered damaged while the stress value is reached at point B from point A. This stress-strain relationship

for computing damage in a material is known as maximum stress criteria. Maximum stress criteria has been implemented as cohesive zone modeling for predicting the multi-scale damage model by FEM (Kim et al. 2012). An aggregate coated by asphalt considered as small-scale and a large-scale AC pavement consisting of several aggregates. Average stress and strain in the FEM models have computed and compared for both undamaged and damaged conditions. In this model, damage is not considered due to moisture as it is mentioned earlier, damage can occur under dry condition, also. The cohesive zone model has also been implemented by FEM for cylindrical AC sample (Kim et al. 2005). Only stress and strain relationships have been computed for different strain rates.

An elastic constitutive matrix that relates to the nominal stress and nominal stain in the elements defines the elastic behavior. The stress tensor σ can be expressed in terms of stiffness E and ε,

$$\sigma_i = E_{ij}\varepsilon_j \tag{5.1}$$

The nominal stress vector consists of three stress components: σ_n acting to the pure normal direction, σ_s acting toward the first shear direction and σ_t acting toward the second shear direction. The modulus matrix consists of nine diagonal components: E_{nn} is the stiffness in the pure normal mode, E_{ss} is the stiffness in the first shear direction and E_{tt} is the stiffness in the second shear direction. Damage is assumed to initiate when the maximum nominal stress ratio reaches a value of one and is expressed in maximum stress criteria

$$max\left\{\frac{\langle\sigma_n\rangle}{\sigma_n^0},\frac{\sigma_s}{\sigma_s^0},\frac{\sigma_t}{\sigma_t^0}\right\}=1 \tag{5.2}$$

where σ_n^0 is the nominal strength toward the normal direction of the matrix, σ_s^0 is the nominal shear strength toward the first direction and σ_t^0 is the nominal shear strength toward the second direction measured in the laboratory. The symbol ⟨ ⟩ is known as Macaulay bracket, which signifies that a pure compressive stress state does not initiate damage.

5.6.2 Damage Model for Matrix-Aggregate Interface

Similar to the cohesive damage model, the adhesive damage model can be presented in terms of load and displacement since adhesive damage occurs at the surface, which is the interface of the matrix and aggregate in this study. Figure 5.2 also presents in terms of force and displacement instead of stress and strain. The force-displacement is also known as the traction-separation law. Traction-separation is used widely for damage prediction in fiber-reinforced composite materials (Saanouni 2001; Vallejo and Tarefder 2011; Voyiadjis et al. 1998). The adhesive damage model is presented in terms of load-displacement relationship,

$$t_i = K_{ij}\delta_j \tag{5.3}$$

Three components of traction such as t_1, t_2 and t_3 are the surface in three orthogonal directions, K's are the stiffness coefficients and δ_1, δ_2 and δ_3 are three deformation components due to the respective forces. The ratio between the interface strength and

load is measured along the normal to the surface and tangential direction (i.e. shear direction) of the surface. Traction-separation criteria is shown as

$$max\left\{\frac{\langle t_1 \rangle}{t_1^0}, \frac{t_2}{t_2^0}, \frac{t_3}{t_3^0}\right\} = 1 \tag{5.4}$$

where t_1^0, t_2^0 and t_3^0 are the interface strength for normal and shear directions.

In this study, only compressive strength and shear strength to the first direction of the matrix materials and tensile strength and shear strength to the first direction for the interface are measured in the laboratory. When the wheel load is applied on AC pavement, it experiences compressive stress in the matrix materials and slip occurs at the matrix-aggregate interface. For this reason, compressive tests are done for matrix materials and tensile pull-off tests are done on the matrix-aggregate interface.

5.6.3 Contact Modeling Techniques in ABAQUS

Interface modeling is necessary while two materials with different material properties are in contact, therefore, the interface modeling is also known as contact modeling in ABAQUS. In this study, the matrix materials are coated on aggregate and surface-based contact modeling is used to create an interface between them. The inner surface of matrix materials and outer surface of aggregate are created as surface, and then the two surfaces are joined together and act as an integrated surface. The joined surfaces behave as a cohesive surface. The damage model for the cohesive surface is assigned according to Eq. (5.3). The integrated surface is de-bonded while the damage occurs at the interface. The intentions of this study are to evaluate the de-bonded phenomena at the interface of

the matrix materials and aggregate. For this reason, the surface based interface modeling technique is selected. It should be noted that, when de-bonding occurs at the interface, the inner surface of the matrix materials and outer surface of the aggregate separate from each other. Before separation, the nodes belong to the matrix materials and the aggregate overlapped each other and no new node is created at the damaged surface.

5.7 Laboratory Investigations

5.7.1 Test on Matrix Materials

Laboratory tests are conducted to determine inputs of FEM model. A Superpave mix (SP-B) is collected from a local plant in cooperation with the New Mexico Department of Transportation (NMDOT). To separate the matrix from the SP-B mix, the loose mix is heated at 151 °C. Once heated, the mix is agitated on a flat surface by hand until the mix cooled to room temperature (23 °C). The mix is then shaken over a customary U.S. sieve of size designation #10 (2.0 mm) sieve. All of the loose mix retained on the #16 (1.19 mm) sieve and retained on the #200 (0.075 mm) sieve is collected as matrix material.

Cylindrical samples are molded inside a Harvard miniature mold. These samples are compacted to a target void ratio of 4.0 ± 0.5%. The void ratio is calculated by the mass of the matrix material needed to fill the mold volume of 68334.06 mm^3 (4.17 in^3) using a maximum specific gravity of 38.673 g/in^3 and 4.0 ± 0.5% air voids. The matrix material is heated in an oven at 590 °F for one hour and then compacted in the cylindrical mold in three lifts. Immediately after compaction, samples are extruded from the mold and allowed to cool to room temperature. Next, the samples are sliced using a lab saw at both ends to 69.85 mm (2.75 in) length so as to eliminate excessive voids at the ends of the

sample. For wet conditioning, samples are soaked for 48-hours under water at room temperature and at a pressure of 30 mm Hg.

Both compressive and shear strength tests are performed on the matrix materials. The bottom of the matrix sample is attached to the Universal Testing Machine (UTM). The crosshead is then raised so that the top post came into contact with the loading frame. Test data is recorded until the sample failed. Shear test is also performed for the matrix. A loading rate of 1.27 mm/min (0.5 in/min) is used for both tension and shear tests. The results for the compression and shear test are summarized in Table 5.1. The results are averaged for three dry and wet samples. E-values are determined by measuring the slope of the secant modulus (Santi et al. 2000). The secant modulus is defined as the slope connecting the origin to 50% of the maximum strength of the material. The secant modulus is used as the Elastic modulus in the FEM modeling. The test results are shown in Table 5.1.

5.7.2 Test on Matrix-Aggregate Interface

Laboratory aggregate pull-off tests under both dry and wet conditions are done to measure the stiffness of matrix-aggregate interfaces. For tensile pull-off test, a coated aggregate is cut in half and the flat face is exposed to air and the other coated end is embedded in the matrix up to the half of the aggregate. The wet and dry matrix samples are compacted to a target void ratio of 4 ±0.5% for both tension and shear tests. The wet condition is prepared following AASHTO T283 (2007) method before conducting the pull-off test. The flat end is fixed with the loading frame with glue and the bottom of the matrix material container is also fixed with the base. The sample is then load in tension at

a rate of 1.27 mm/min (0.05 in/min). Two samples are prepared; one sample is kept dry and the other is wet conditioned before the test.

Aggregate pull-off tests are also performed under direct shear load. The matrix material samples are prepared in similar fashion except the materials are prepared in the shear box of the direct shear testing equipment. The hot matrix material is compacted in two lifts into the bottom half of the shear box. Just before the final compaction of the top layer, a coated and fractured face of hot aggregate is pressed onto the surface of the top lift and compaction to the required volume is then completed to ensure proper contact between the aggregate and the matrix. Three samples are left in a dry condition and the other three are wet conditioned following AASTHTO T283 standard (2007). The top of the shear box is placed on the bottom of the shear box and the apparatus is placed into the direct shear machine. The set screws in the shear box are removed and the height of the top of the shear box is raised so that no matrix material impeded the shearing of the aggregate. The sample is then loaded in shear displacement at a rate of 1.27 mm/min (0.05 in/min).

The average tensile and shear strength of three dry samples and three samples are calculated and presented in Table 5.2. The tensile and shear strength of the aggregate pull-off is higher under dry conditions than under wet conditions. The K-values of mastic-aggregate interface due to tension and shear is determined by measuring the slope of the curve before the peak load, also known as the secant modulus. The average K-value of three samples under dry and wet conditions is presented in Table 5.2.

The elastic modulus of dry and wet aggregate is collected from the previous study. Aggregate modulus under dry and wet condition has been measured by nanoindentation

tests (Tarefder & Arifuzzaman, 2010). Aggregate elastic modulus is taken as 87,061 MPa and 5,721 MPa under dry and wet condition respectively.

5.8 FEM Model Development

The FEM model is developed using ABAQUS/CAE 6.9-EF1, commercially available software. A two-dimensional idealization of a spherical aggregate with a radius of 19.05 mm (0.75 in) and coated with matrix materials with a thickness of 0.508 mm (0.02 in) is considered as shown in Figure 5.3. For simplicity, one quarter of a spherical coarse aggregate surrounded by a layer of matrix material is the model considered for this study. The interface layer between the matrix materials and the aggregate is schematically drawn in the Figure 5.3(b). Though AC is considered to be visco-elastic-plastic material, matrix is assumed to behave elastically since the matrix thickness in this study is very small compared to the diameter of the coarse aggregate. The loading and the shape of the FEM model are symmetrical to the vertical axis. Hinge boundary condition (BC) is used at the bottom and roller BC is used at the left side of the model. Four noded linear quadrilateral cohesive elements are used to define the matrix materials. Linear elements are used since quadratic elements are not available for assigning a cohesive element. Three and four noded linear quadrilateral plane stress elements are used to define the aggregate. Combinations of both three and four noded elements are required due to the spherical shape of the aggregate.

In the FEM model, instead of applying a load, a specified deformation is applied. Deformation magnitudes 1.45 mm (0.057 in) are applied on the FEM model. The magnitude of the deformation is calculated based on a standard duel tandem wheel on a

pavement. It has been observed that a dual tandem wheel of total 889.64 KN (200,000 lb) load produces a 1.45 mm (0.057 in) deformation in a 203.02 mm (8 in) thick AC pavement (Huang 2004). Therefore 1.45 mm (0.057 in) deformation is considered. The 1.45 mm (0.057 in) deformation is applied statically with a time step of 0.01 sec. The maximum time step is considered as 1.0E-5. It is observed that a lower time step provides good results. The deformation load is applied in ABAQUS on 10.16 mm (0.4 in) length of matrix. Usually, indirect tensile strength of AC is determined by subjecting diametrically though a 20.32 mm-25.4 mm (0.8-1.0 in) loading strip by AASHTO T283 (2007). Since the model is symmetric, deformation load is applied over 10.16 mm (0.4 in) length.

5.9 Results and Discussions

5.9.1 Matrix Damage Contour

Damage in matrix materials can be observed by plotting maximum stress criteria (MAXSCRT) contour. Figure 5.4 presents the MAXSCRT contour under dry and wet conditions. Figure 5.4(a) shows the FEM model with the applied deformation expressed by the downward arrow on the FEM model. The arrows at the top of the model represent the applied deformation and are placed on the perimeter of the model up to 10.16 mm (0.40 in), exactly as it is placed in the FEM model. Damage is observed under the applied deformation zone. Figure 5.4(b) is the zoomed section of the damaged location for dry matrix and Figure 5.4(c) is the zoomed section of the damaged location for wet matrix. The MAXSCRT contour color ranges from blue to red and the maximum magnitude is 1.0 for the red color. The matrix materials are damaged when the MAXSCRT value is

1.0. The matrix materials are not damaged if the MAXSCRT value is less than 1.0. It should be noted that the blue color shows zero magnitude, but the value is very small and shows zero because the magnitude is rounded for two decimal digits.

According to Figure 5.4(b) and 5.4(c), it is clear that wet matrix materials show higher damage than dry matrix materials. Damage is higher at the end of the applied deformation zone than at the top of the model and near the left BC. MAXSCRT value is the maximum value computed from the ratio of normal and shear stress. For understanding more about MAXSCRT contour, the normal and shear stress distribution at the top of the matrix materials are presented in Figure 5.5. Figure 5.5(a) and 5.5(b) shows the maximum normal stress and shear stress at the top of model for dry and wet matrix materials. The x-axis is the distance on the perimeter of the top of the matrix materials measured from the top left corner of the applied deformation region. The stress values are plotted up to the end of the loading region because damage is observed up to the end of loading region. It should be noted that normal stress is decreasing and shear stress is increasing as distance on the perimeter is increasing. This is due to the spherical shape of the model. The maximum normal stress is 1.857 MPa and the maximum shear stress is 0.814 MPa for dry matrix materials. The maximum normal stress is 1.488 MPa and the maximum shear stress is 0.558 MPa for wet matrix materials. It should be noted that shear stress shows constant maximum magnitude and normal stress drops significantly while shear stress reaches its maximum values. The locations where shear stress shows a constant maximum are the damaged locations and the wet matrix shows a longer damaged location than the dry matrix. It can be concluded that the matrix material

coating spherical aggregate is exposed to damage due to shear stress rather normal stress and the damage is higher for wet matrix materials.

5.9.2 Effects of Moisture in Matrix Materials

Wet matrix shows higher damages then dry matrix as seen in the MAXSCRT contours. The contour plot gives a good comparison between dry and wet matrix. For understanding more about the influence of moisture in the matrix materials, the MAXSCRT values for each layer of matrix materials are measured and plotted in Figure 5.6. The thickness of the matrix layer is 0.508 mm (0.02 in) and divided into four layers, each with a thickness of 0.127 mm (5E-3 in). The MAXSCRT value for each element under the deformation zone is measured from the model and plotted for dry and wet conditions. It should be noted that the 2nd and 3rd layers show higher MAXSCRT values than the 1st top layer at the beginning and mid region. This could be due to the stress concentration at the 2nd and 3rd row of the thin matrix materials. All three layers from the top show a MAXSCRT value of 1.0 for some locations and are recognized as the damaged location as shown in Figure 5.6(a) and 5.6(b). The damaged length is 1.99 mm for dry matrix and 3.24 mm for wet matrix. About 0.758 square mm of dry matrix and about 1.234 square mm of wet matrix are exposed to damage. Moisture causes 62.80% more damage in matrix materials considering only the region under the applied deformation.

5.9.3 Behavior of Matrix Materials

Both dry and wet matrix materials are damaged under the applied deformation, but the wet matrix shows higher damage then the dry matrix due to lower strength and stiffness.

Figure 5.7 presents a zoomed section of the damaged matrix materials. The damaged region is divided into three sub-regions; region 1 shows no damage for dry and wet matrix, region 2 shows no damage for dry matrix but damage for wet matrix, and region 3 shows damage for both dry and wet matrix. A detailed stress-strain relationship is done on the elements of the three regions in the above-mentioned sections.

It is observed that shear stress increases and normal stress decreases as the distance on the perimeter increases. Also, damage occurs when shear stress reaches its capacity. For this reason, normal stress-strain distribution is plotted for undamaged or region 1 matrix materials, shear stress-strain distribution is plotted for damaged wet matrix materials or region 2 and 3, and shear stress-strain distribution is plotted for damaged dry matrix materials or region 3. Figure 5.8 shows normal and shear stress-strain distribution on an element located at region 1. All diagrams show the expected linear relationship, though the wet matrix shows a lower stiffness values then the dry condition. According to Figure 5.8(a), the maximum normal stress for the dry matrix is 1.7013 MPa and the corresponding normal strain is 8.83E-3 mm/mm; the maximum normal stress for wet matrix is 1.4488 MPa and the corresponding normal strain is 1.12E-2 mm/mm. The calculated E-values from these plotted stress-strain relationships are 192.67 MPa and 129.36 MPa for dry and wet matrix respectively. Similarly, according to Figure 5.8(b), the maximum shear stress for dry matrix is 0.06079 MPa and the corresponding shear strain is 4.12E-4 mm/mm. The maximum shear stress under wet condition is 0.06143 MPa and the corresponding shear strain is 4.42E-4 mm/mm. The calculated E-values from these plotted stress-strain relationships are 147.55 MPa and 138.98 MPa under dry

and wet conditions respectively. The calculated E-values closely matched with the E-values measured in the laboratory and given in Table 5.1.

Figure 5.9 shows the shear stress-strain distribution on an element located at region 2. The dry matrix in region 2 is undamaged, but the wet matrix is damaged and damage is observed for shear stress only. Figure 5.9(a) is an element located near the upper portion of region 2 and closer to region 1. Figure 5.9(b) is an element located near the lower portion of region 2 and closer to region 3. The stress strain relationship is linear for the dry matrix since no damage occurred at region 2. The maximum stresses for the dry matrix are 0.7540 MPa in Figure 5.9(a) and 0.7956 in Figure 5.9(b). All the maximum stress values are smaller than the maximum shear strength of 0.81 MPa for the dry matrix. For this reason no damage is observed under the dry condition for region 2.

On the other hand, the wet matrix shows damage after the shear stress reaches 0.5574 MPa in Figure 5.9(a) and 0.5578 MPa in Figure 5.9(b). According to Table 5.1, 0.56 MPa is the maximum shear strength of the matrix under wet condition. The softening part of the stress-strain returns to zero as damage progresses after the peak stress under the wet condition. For Figure 5.9(b), at the end of softening curve, there is a remaining shear strain, which represents permanent shear strain in the matrix materials. The remaining strain is defined in this case as strain magnitude when the stress is zero. The magnitude of the strain is 18.99E-3 mm measured from the damage initiation point to the tail of the damage progression, also shown with an arrow in Figure 5.9(b). The magnitude of the remaining strain is 8.8E-3 mm according to Figure 5.9(b). The significance of this remaining shear strain is that the, lower portion of region 2 has higher damages than the upper portion. It can be said that permanent shear strain increases when the distance on

the perimeter increases from the left BC. Indeed, presence of moisture causes permanent shear strain for damaged matrix materials and the amount of permanent shear strain is higher for wet matrix than that of dry matrix. The stress-strain relationship for the damaged dry matrix is explained in the following section.

Figure 5.10 presents the stress-strain relationship of the damaged section for both dry and wet matrix. Figure 5.10(a) is plotted for an element located near the upper region of 3 and near the lower region of 2 and Figure 5.10(b) is plotted for an element located near the lower region of 3. Both the dry and wet matrix show damages in region 3, but the wet matrix shows higher damage since permanent shear strain is higher for wet matrix than dry matrix. The maximum shear stresses under the dry condition are 0.8099 MPa in Figure 5.10(a) and 0.8130 MPa in Figure 5.10(b). The shear strength for the dry matrix is 0.81 MPa as mentioned in Table 5.1. It should be noted that the tail of the softening curve under wet condition in Figure 5.10(a) and Figure 5.10(b) is extending when compared to Figure 5.9(b). This means a more permanent shear strain is growing in this region for wet matrix. The permanent strain for wet matrix is 29.20E-3 mm as measured from Figure 5.10(a). The permanent strain for wet matrix is 32.5E-3 mm and dry matrix is 4.10E-3 mm as measured from Figure 5.10(b). The permanent strain is approximately 693% higher under wet matrix when compared with the dry matrix in Figure 5.10(b).

5.9.4 Matrix-Aggregate Interface Damage Contour

Damage in the matrix-aggregate interface can be observed by plotting the cohesive surface maximum stress criteria (CSMAXSCR) contour. Figure 5.11 presents the CSMAXSCR contour under dry and wet conditions. The CSMAXSCR contour color

ranges from blue to red and the maximum magnitude is 1.0 for the red color. The interface is damaged when the CSMAXSCR value is 1.0; the interface is not damaged if the CSMAXSCR value is less than 1.0. It should be noted that the blue color shows zero magnitude, but the value it is very small and shows zero because the magnitude is rounded for two decimal digits. The arrows at the top of the model are the applied deformation and placed on the perimeter of the model up to 0.40 in, exactly as it placed in the FEM model. The CSMAXSCR value showing in Figure 5.11(b) and 11(c) is for dry and wet matrix with dry aggregate respectively. Influence of wet aggregate at the matrix-aggregate interface is explained in the later sections. According to Figure 5.11(b) and 11(c), the wet interface shows higher damage than dry interface. The damage variations for the wet interface compared to the dry interface is difficult to observe since interface contour shown in Figure 5.11 is very thin. For this reason the interface stresses are presented in the following sections and explained.

5.9.5 Effects of Moisture at Matrix-Aggregate Interface

Contact normal and shear stresses are presented in Figure 5.12 for dry and wet matrix materials with dry aggregate. The perimeter is measured on the matrix-aggregate interface from the left BC. According to Figure 5.12(a), contact normal stresses are decreasing while the distance on the perimeter increases for both dry and wet matrix. Contact normal stress drops to zero at the end of the loading zone and continues to show negative magnitudes. The negative contact stress means compression, so at the end of the loading zone the interface has compressive contact stress.

On the other hand, shear contact stress increases while the distance on the perimeter increases and then drops to zero and continues as zero up to the end of the applied deformation zone. The zero shear contact state means no contact between the matrix and aggregate, so the region is damaged. When deformation is applied on the model, the interface shear contact stress increases and reaches to its maximum allowable contact stress and initiates damage by separating the two surfaces. While the two surfaces separate from each other, no shear stress is present on the surface, but normal stress is present due to applied deformation. The no contact region length is higher for wet matrix than dry matrix. About 6.46 mm and 5.5 mm of the interface lost contact for wet and dry matrix respectively. About 17.45% more of the matrix-aggregate interface lost contact for wet matrix when compared with the dry matrix.

5.9.6 Effects of Moist Aggregate at Matrix-Aggregate Interface

It is observed that interface damage occurred due to loss in contact between the two surfaces. Moisture infiltrates through the matrix-aggregate interface and saturates the aggregates and this might influence the contact stresses. Figure 5.13 is presented for contact shear stress for the dry and wet interfaces with dry and wet aggregate. The interface with dry and wet aggregate almost overlaps with each other. For this reason a zoomed in section is drawn for the peak location. It is observed that the contact shear stress shifts more to the right side for wet aggregate scenario than for the dry aggregate. The maximum contact shear stress for dry aggregate is 0.1616 MPa and for wet aggregate is 0.1592 MPa. The maximum shear stress for dry aggregate is 1.51% higher than wet aggregate. Damage initiates for wet aggregate is almost at the same location where it is

for dry aggregate. Significant differences are not observed for wet aggregate when comparing to dry aggregate.

5.9.7 Matrix-Aggregate Interface Contact Status

Matrix and aggregate surface separates from each other at the interface damaged location. This separation can be measured by plotting the contact opening between the two surfaces. Figure 5.14 presents the contact opening at the damaged locations for dry and wet matrix with a schematic diagram of the contact opening. It is observed that the contact opening is higher for wet matrix than dry matrix up to some distance and then dry matrix shows a significantly higher opening than wet matrix. The location where dry matrix shows higher opening than wet matrix falls under region 3. The maximum contact opening for dry matrix is 9.38E-15 mm and for wet matrix is 1.50E-15 mm at region 3. The contact opening at region 3 is approximately 525% higher for dry matrix than for wet matrix. Higher stiffness of dry matrix materials rebound more than less stiffness or wet matrix materials when separation occurs. The maximum contact opening for dry matrix is 5.54E-16 mm and for wet matrix is 1.04E-15 mm in region 2. The contact opening for wet matrix is about 88% higher than dry matrix. This suggests that contact separation is more vulnerable for dry matrix than wet matrix due to higher strength of matrix materials.

When matrix materials and aggregate surfaces separate, it not only shows an opening but also shows the relative displacement from each other. Figure 5.15 shows the relative displacement of surfaces for dry and wet matrix. Wet matrix shows lower relative displacement than dry matrix. The maximum relative displacement for dry matrix is

8.67E-5 mm and for wet matrix is 6.37E-5 at region 3. Dry matrix relative displacement is approximately 36% higher than wet matrix. It should be noted that magnitude of the contact opening is significantly lower than magnitude of the surface relative displacement. Matrix materials try to slip more at the interface then separate from each other since vertical load is applied on the spherical perimeter. The higher relative displacement for dry matrix is also due to the higher strength and stiffness of dry matrix compared to the wet matrix. The rebound effect causes higher displacement for dry matrix compared wet matrix.

5.10 Conclusions

This study is conducted to understand and evaluate the behavior of AC under dry and wet conditions. AC is made of aggregate coated with matrix materials. FEM modeling is used to simulate behavior considering damage in the matrix materials and the matrix-aggregate interface for dry matrix with dry aggregate, wet matrix with dry aggregate and wet matrix with wet aggregate. The FEM model results are summarized below.

1. Damage occurred in the matrix materials coated on spherical aggregate due to shear stress reached its capacity before normal stress reached its capacity. Slipping occurred at the end of the loading zone since vertical deformation is applied on the spherical shape model. In addition, shear stress is lower for wet matrix compared to dry matrix. Eventually, moisture caused higher damage in the wet matrix materials. Moisture caused 62.80% more damage in the matrix materials when considering only the matrix materials under the applied deformation region.

2. Permanent shear strain is higher for wet matrix than dry matrix at the damaged locations. Permanent strain is defined as strain magnitudes at zero stress after damage occurred in the matrix materials. In certain locations, the permanent shear-strain is approximately 693% higher for wet matrix when compared with dry matrix.

3. Damage occurred at the matrix-aggregate interface due to shear contact stress when it reached its capacity and interfacial de-bonding occurred at the damaged locations. Interface de-bonding is higher for wet matrix than dry matrix with dry aggregate. Moisture caused 17.45% more de-bonding at the interface region compared to dry matrix.

4. Moist aggregate does not influence significantly at the matrix-aggregate interface. De-bonding region is same for dry aggregate comparing wet aggregate with wet matrix. The maximum shear contact stress is 1.51% higher for wet aggregate comparing dry aggregate.

5. Matrix materials slide horizontally (i.e. relative displacement) and move vertically (i.e. contact opening) after de-bonding occurs. Magnitude of the surface relative to displacement is higher compared to the magnitude of contact opening. The vertically applied load prevented vertical contact opening and the couple effect of sliding and vertically applied load influenced relative displacement at the damaged locations. A strong rebound effect of dry matrix is the cause for the higher relative displacement and contact opening at the damaged locations.

Table 5.1 Cohesive damage model parameters

	Test type	Ultimate strength	E-value
Dry	Compression	2.61 MPa (379 psi)	192.72 MPa (27,952 psi)
	Shear	0.81 MPa (118 psi)	147.64 MPa (21,413 psi)
Wet	Compression	2.02 MPa (293 psi)	129.44 MPa (18,773 psi)
	Shear	0.56 MPa (81 psi)	139.10 MPa (20,174 psi)

Table 5.2 Adhesive damage model parameters

	Test type	Ultimate strength	K-value
Dry	Tension	391.44 N (88 lbf)	3,706.42 N/mm (21,163 lbf/in)
	Shear	280.24 N (63 lbf)	3,150.00 N/mm (17,987 lbf/in)
Wet	Tension	244.65 N (55 lbf)	2,858.25 N/mm (16,321 lbf/in)
	Shear	124.55 N (28 lbf)	1,912.39 N/mm (10,920 lbf/in)

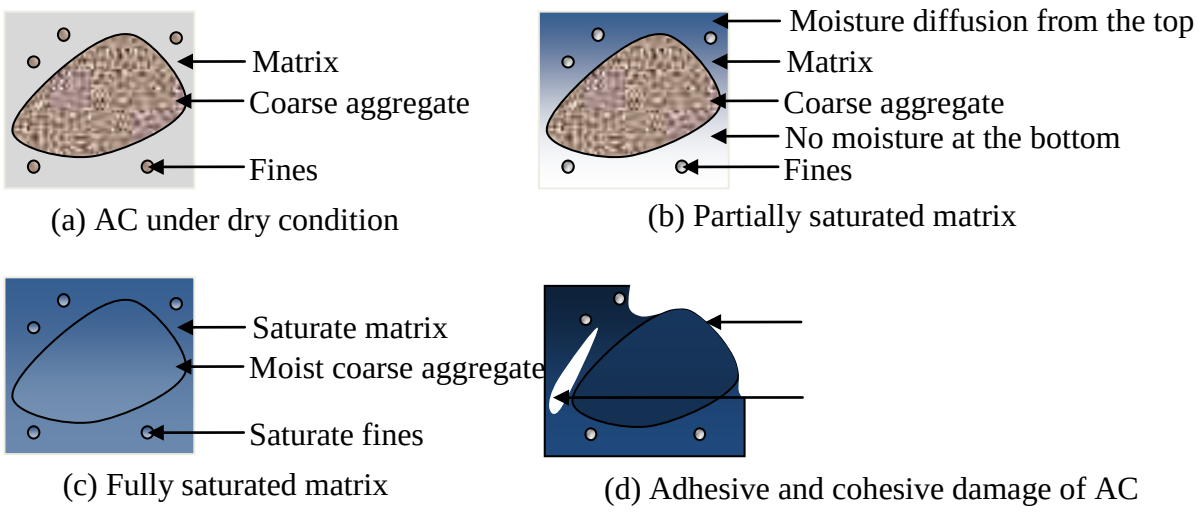

Figure 5.1 Schematic of moisture flow in AC that causes adhesive and cohesive damage

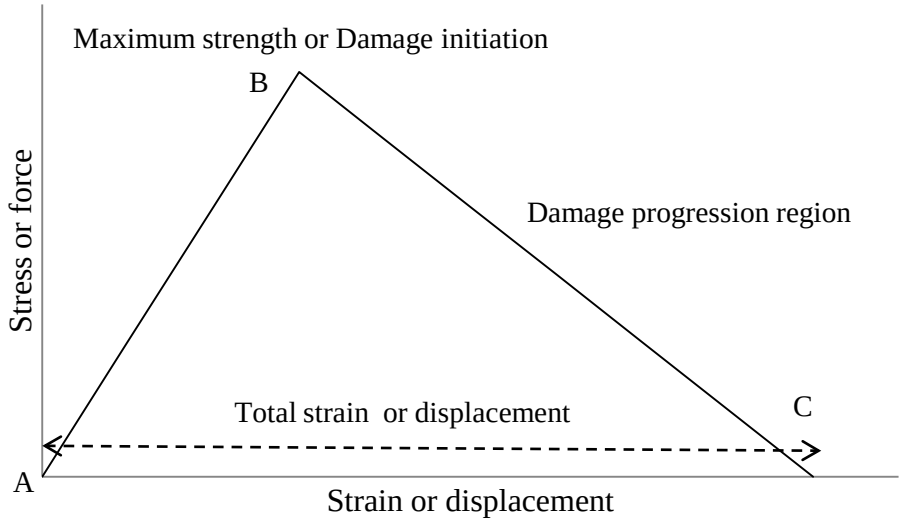

Figure 5.2 Linear stress-strain or force-displacement relationship for computing damage

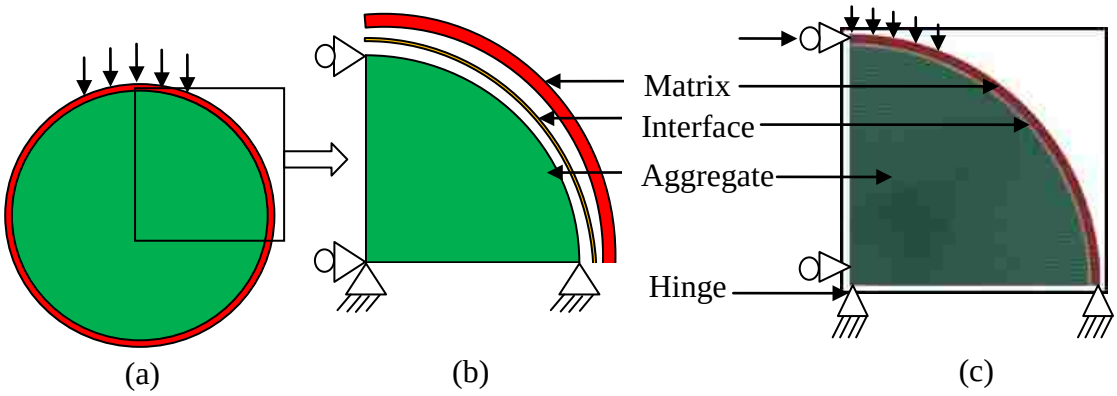

Figure 5.3 Schematic of aggregate coated by (a) matrix materials, (b) separately shown matrix materials, interface, and aggregate, and (c) FEM model with mesh, BC and loading condition

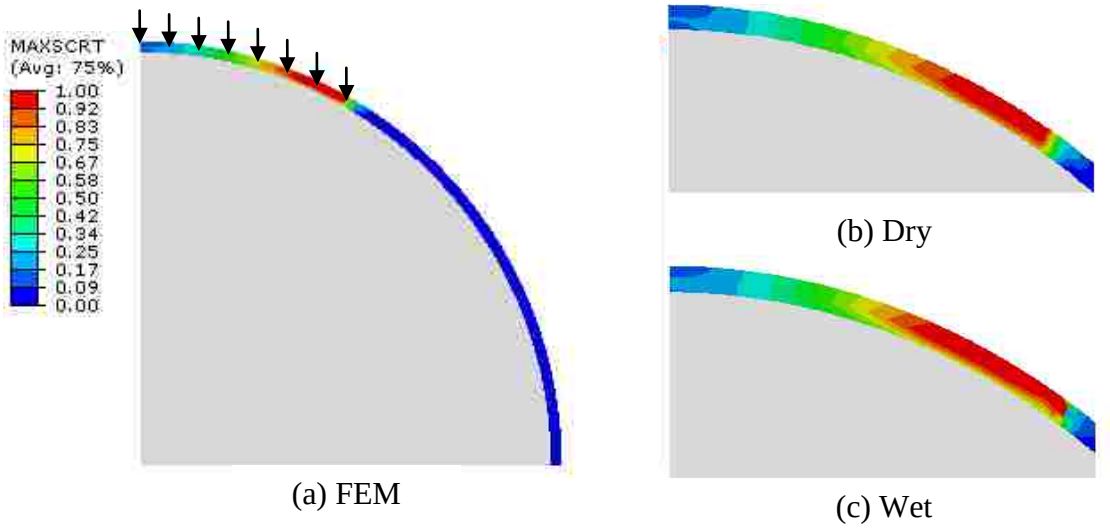

(a) FEM

(b) Dry

(c) Wet

Figure 5.4 Maximum stress criteria (MAXSCRT) contour of matrix materials under dry and wet conditions

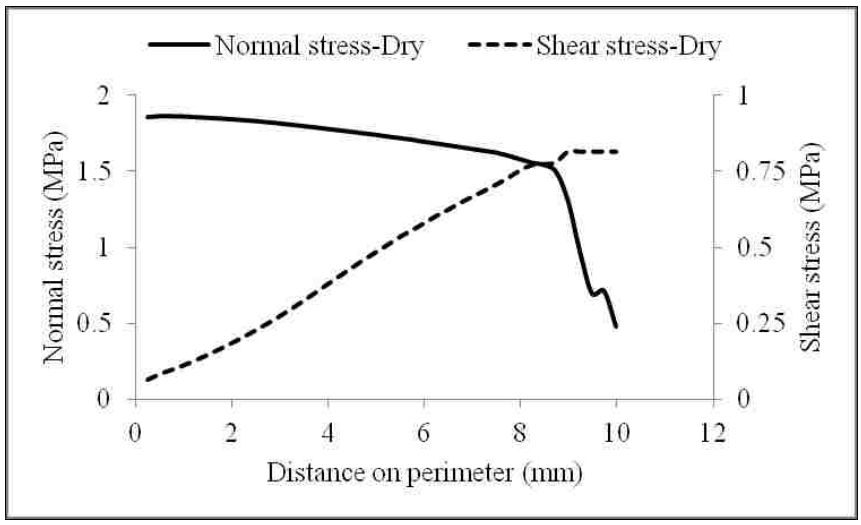

(a) Dry

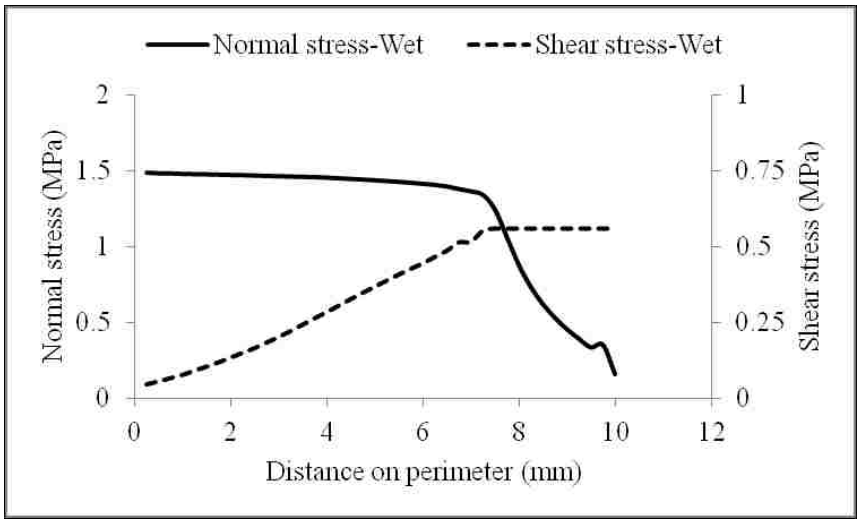

(b) Wet

Figure 5.5 Maximum stresses at the top of the model for dry and wet matrix materials

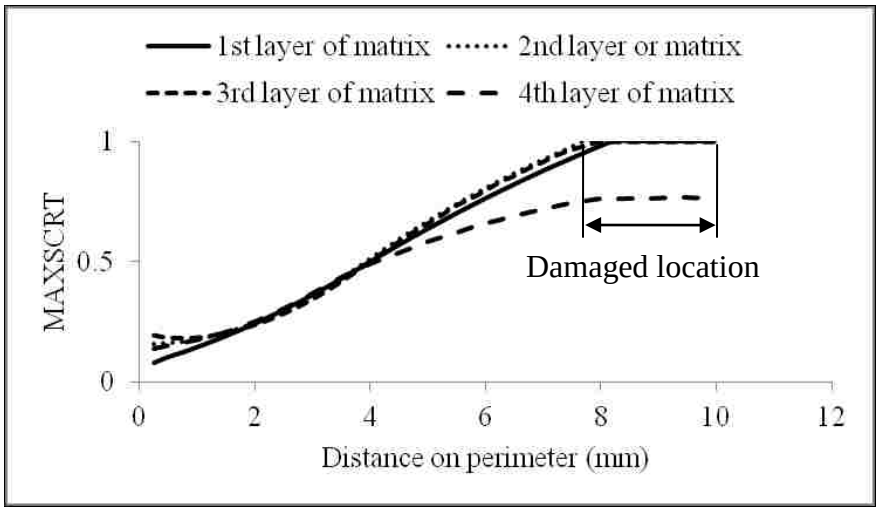

(a) Dry

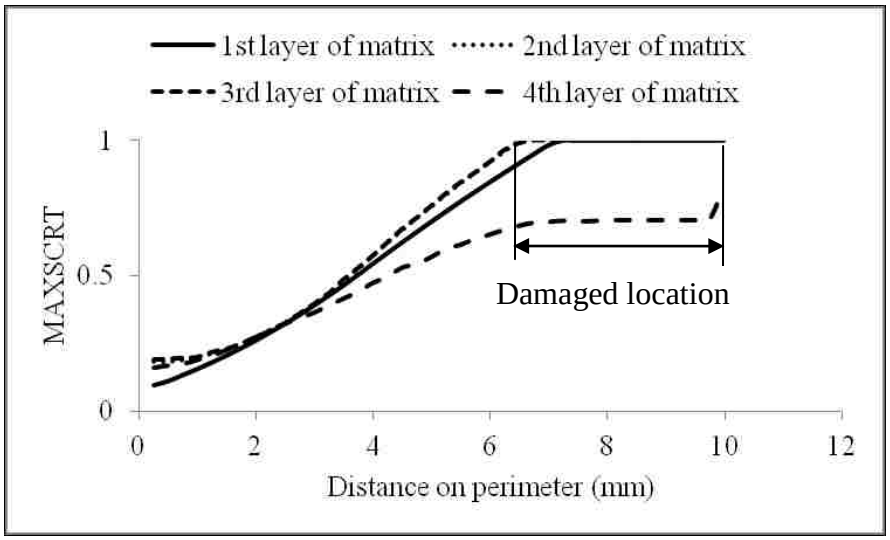

(a) Wet

Figure 5.6 Maximum stress criteria (MAXSCRT) distribution in different layer of matrix materials under dry and wet conditions.

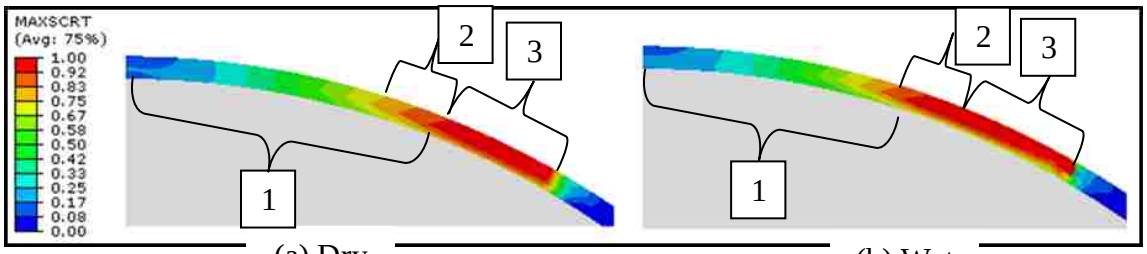

(a) Dry (b) Wet

Figure 5.7 Maximum stress criteria (MAXSCRT) for dry and wet matrix materials under the applied deformation zone

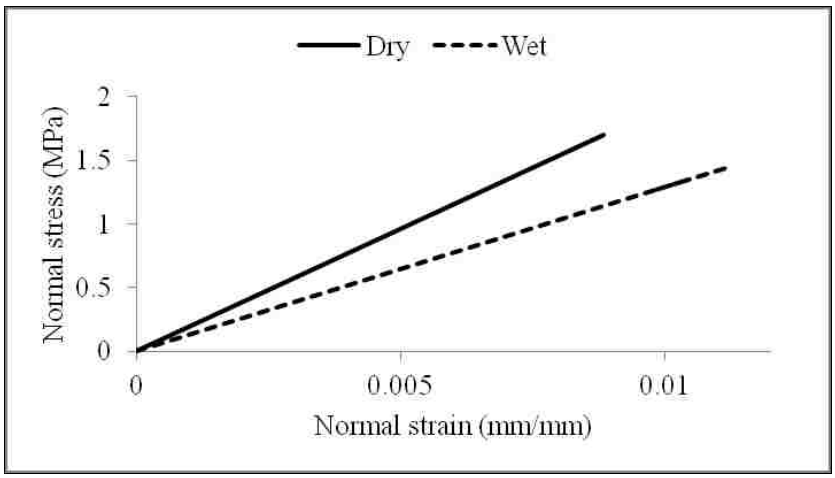

(a) Normal stress-strain

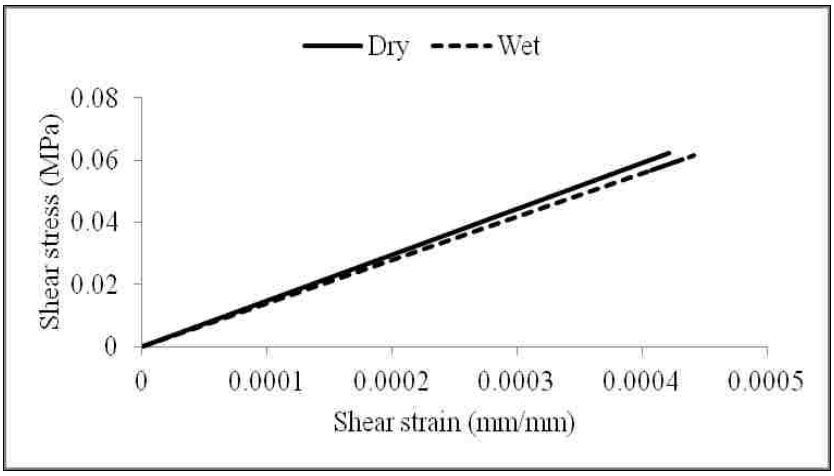

(b) Shear stress-strain

Figure 5.8 Stress-strain relationships of undamaged matrix materials

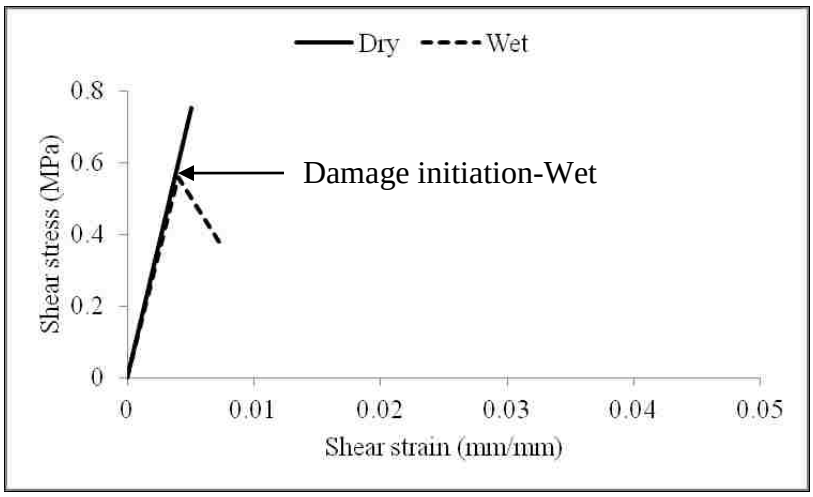

(a) Damage initiation under wet condition

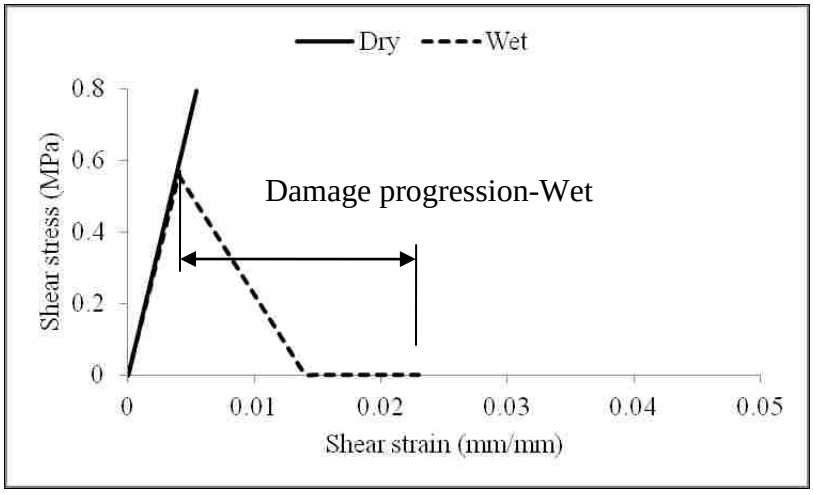

(b) Damage progression under wet condition

Figure 5.9 Shear stress-strain relationships of damaged matrix materials under dry and wet condition

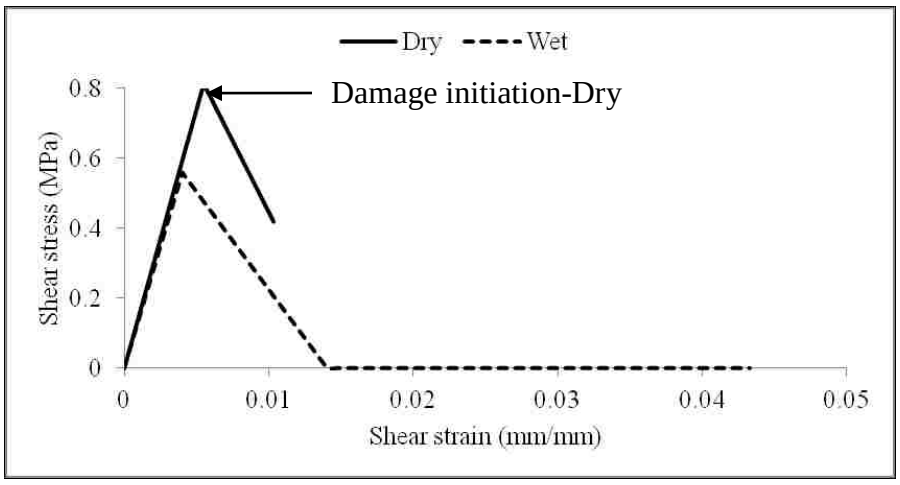

(a) Damage initiation under dry condition and damage progression under wet condition

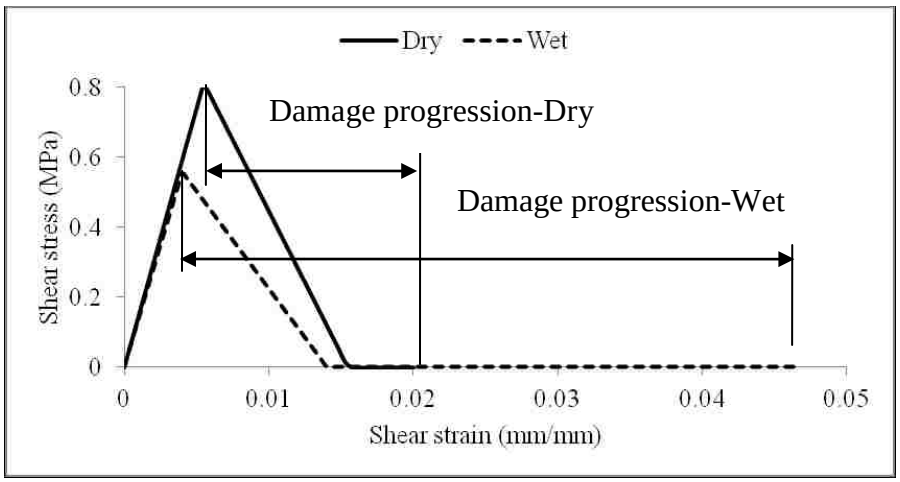

(b) Damage progression under dry and wet conditions

Figure 5.10 Shear stress-strain relationship of damaged matrix materials under dry and wet conditions

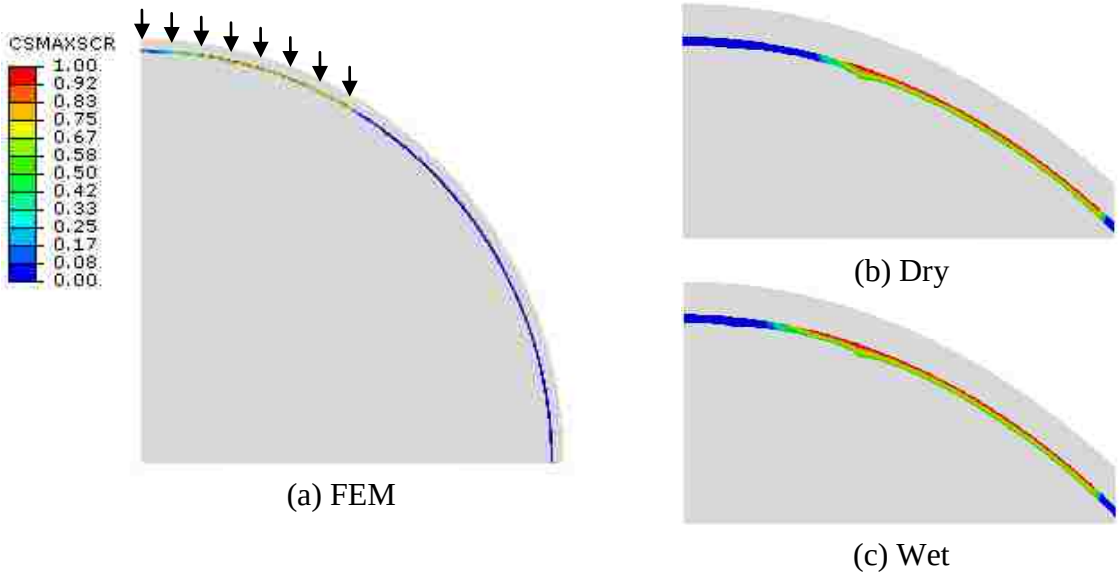

(a) FEM

(b) Dry

(c) Wet

Figure 5.11 Cohesive surface maximum stress criteria (CSMAXSCR) at the matrix-aggregate interface for dry and wet matrix with dry aggregate

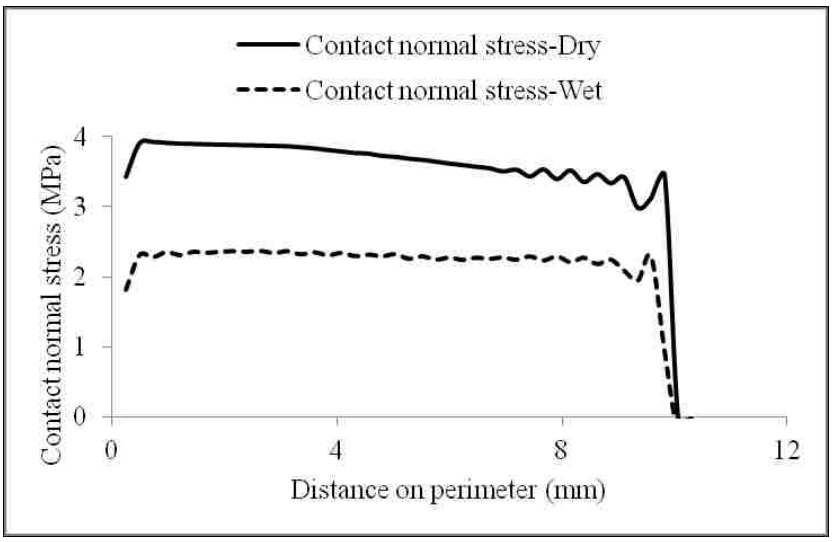

(a) Contact normal stress

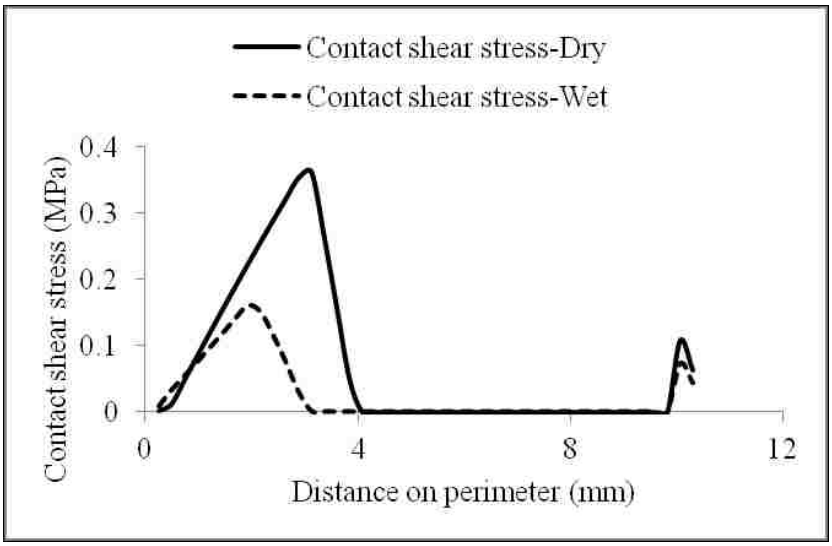

(b) Contact shear stress

Figure 5.12 Contact stresses for dry and wet matrix with dry aggregate

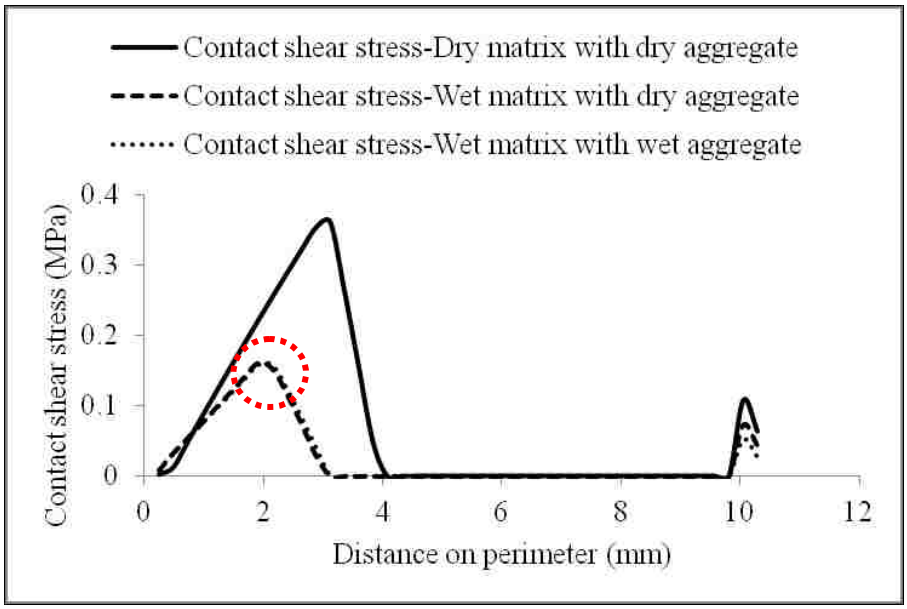

(a) Contact shear stress

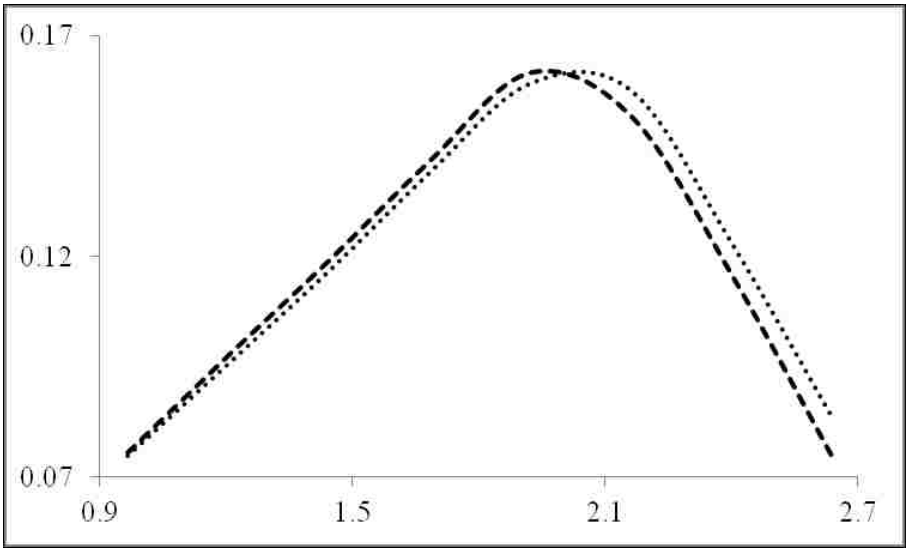

(b) Zoomed in selected section

Figure 5.13 Contact shear stress under dry and wet conditions with wet aggregate

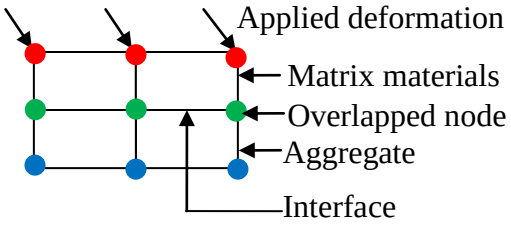

(a) Contact between matrix materials and aggregate

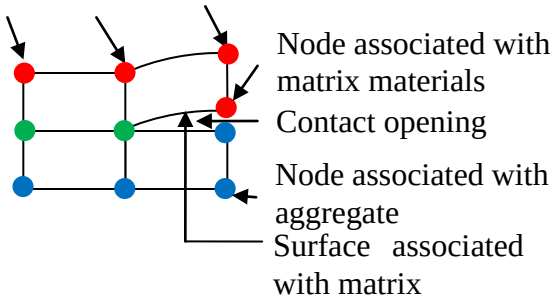

(b) Contact opening between matrix materials and aggregate

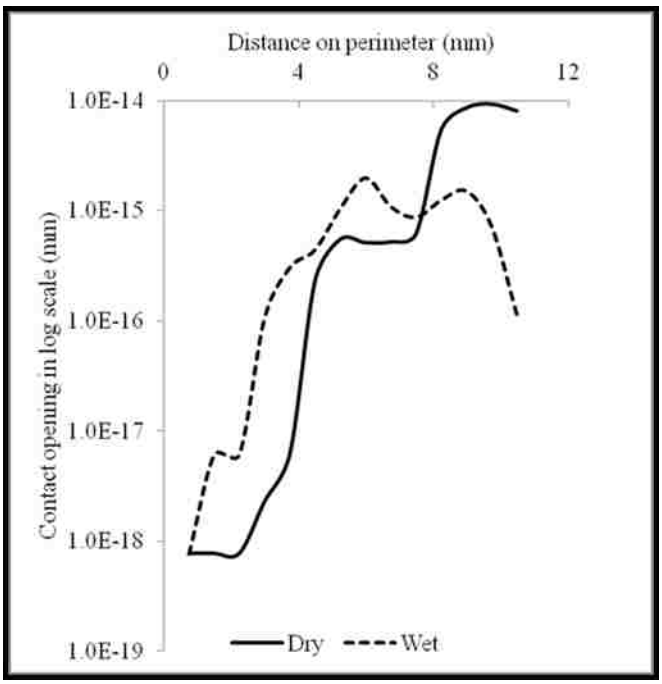

(c) Contact opening profile

Figure 5.14 Contact opening under dry and wet conditions

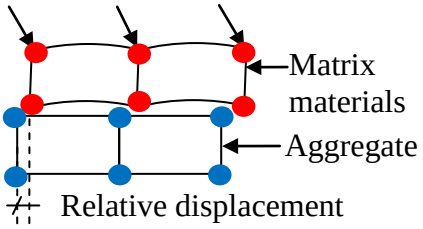

(a) Contact displacement between matrix materials and aggregate

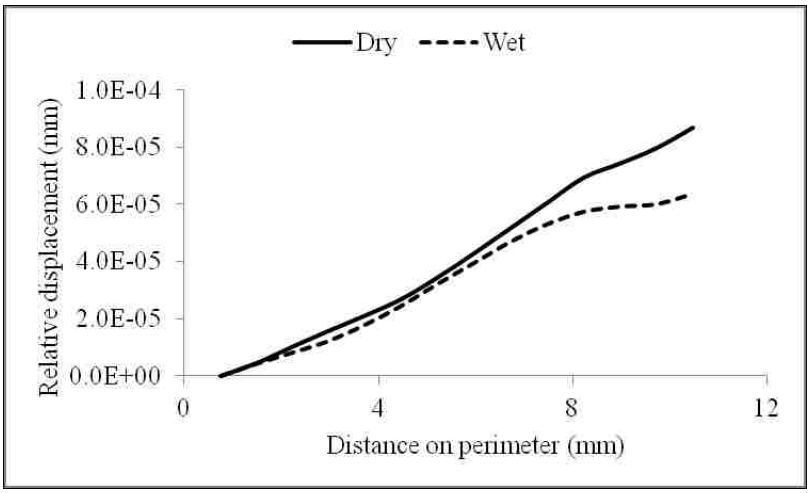

(b) Contact displacement profile

Figure 5.15 Relative displacement of contact surfaces under dry and wet conditions

CHAPTER 6

DAMAGE OF MASTIC FILMS

6.1 General

This chapter describes the effects of vapor in mastic films. The vapor concentration is measured at different level of humidity conditions and the normal and shear strength of mastic films are measured.

6.2 Introduction

The mixture of fines (mineral size smaller than 0.075 mm) and asphalt binder is known as asphalt mastic or mastic materials (Hossain and Tarefder 2013b; Kim and Little 2004; Kringos et al. 2008a). The mixture of asphalt binder with fine aggregates (aggregate size ranges from smaller than 4.75 mm to larger than 0.075 mm) is known as matrix materials (Tarefder, Yousefi, et al. 2010). Two damage mechanisms named as adhesive and cohesive damage in mastic have been recognized by researchers (Cheng et al. 2003; Tarefder and Arifuzzaman 2010). Adhesive damage is the separation between aggregate or mastic materials and cohesive damage is the strength degradation within the mastic or matrix materials. It has been observed that both adhesive and cohesive damage increases due to moisture or humidity (Abu Al-Rub et al. 2010; Azari 2010; Kringos et al. 2008b). It has also been noticed that the interface between the aggregate and mastic is the weakest region and more prone to initiate damage(Caro et al. 2010a; Copeland 2007). Damage accumulates and causes fatigue cracking and other distress in the mastic and/or Asphalt

Concrete (AC). This study determines mastic strength under different humidity conditions.

Figure 6.1 represents a schematic diagram of mastic damage and failure of AC. Figure 6.1(a) shows a mastic film binding two hypothetical spherical shape aggregates. Under vertical tire pressure and traction force, the aggregates tend to pull-off from each other horizontally and vertically, as shown in Figure 6.1(b). As pull-off force increases, damage occurs inside the mastic film and/or at the mastic-aggregate interface. Figure 6.1(c) shows damage initiates within the mastic film and propagated through the mastic-aggregate interfaces. This study focuses on whether such mastic damage is affected by the presence of water vapor.

Currently, a considerable amount of research is going on to define mechanical properties such as dynamic shear modulus, fracture strength, and cohesive strength of mastic materials to understand damage in AC (Hossain and Tarefder 2013b; Kim and Little 2004; Kim et al. 2005; Kringos et al. 2008a; Tong et al. 2013). Mastic-aggregate interface strength is determined using ASTM D 4541 (*ASTM Designation No. D4541-09 Standard Test Method for Pull-Off Strength of Coatings Using Portable Adhesion Testers* 2009) known as pull-off strength of coating using portable adhesion tester, well known as Pneumatic Adhesion Tension Testing Instrument (PATTI) test (Ban et al. 2011; Copeland 2007). In the PATTI test, the substrate is aggregate and the aggregate is coated with mastic materials, a pull-off force is applied to the mastic materials. The pull-off strength required to separate mastic film from the aggregate surface is recorded and the failure surface is qualitatively analyzed. If more than 50% of the aggregate surface is exposed, then the failure is adhesive, otherwise the failure is cohesive. The limitation of the PATTI

test is the pull-off stud is not an aggregate; it is made of steel or ceramic plate attached to a steel head. As a result, when the mastic film separates from the substrate aggregate, the other side of the film is attached with stud materials. In addition, the PATTI test is unable to measure shear pull-off strength. Though binder strength in between two aggregates are determined using modified Dynamic Shear Rheometer (DSR) test (Moraes et al. 2011). Very few studies have been conducted to understand the normal pull-off strength of mastic using mastic in between two aggregates. Also, the fracture tests that have been done to simulate cohesive zone fracture modeling using Finite Element Method (FEM), have mastic materials in between polystyrene sheets (Kim et al. 2005). In their study, the fracture strength of mastic materials is measured by applying normal pull-off forces from two ends of polystyrene sheet.

Moisture causes damage in AC. In the following sections moisture and water are used interchangeably. Moisture gets into AC by diffusion of water. Physical-chemical-mechanical actions occur while moisture gets into AC. Physical action consists of diffusion of moisture; chemical action consists of chemical affinity between aggregate and binder in the presence of moisture; and mechanical action consists of friction between aggregate surfaces with mastic materials in the presence of moisture. In addition to moisture, water vapor can diffuse in AC. Continuous vapor diffusion occurs from air inside AC even though the weather is dry. Also, water vapor comes from beneath the pavement due to the capillary rise of water and suction of vapor from the base or subgrade (Tong et al. 2013). In recent studies, water vapor conditioning is used to condition mastic materials (Arambula et al. 2010; Tong et al. 2013). The Relative Humidity (RH) measures the amount of water vapor in the air at any given time, which is

usually less than that required to saturate the air. Previous studies condition mastic samples either at 0% RH or 100% RH. In this study, mastic materials are conditioned from a range of 20% RH to 80% RH. The normal and shear pull-off strength of mastic films are measured in different RH% levels.

6.3 Objectives and Methodology

The specific objectives of this study are to:

1. Determine the normal and shear pull-off strength of mastic films at different RH conditions.
2. Express damage of mastic films in terms of bond strength degradation due to diffusion of water vapor caused by different RH conditions.

T3 Texture analyzer, manufactured by Brookfield, is used to measure normal and shear pull-off strength of the mastic materials. The mastic materials are placed in between two aggregates and normal or shear pull-off force is applied to one aggregate keeping the other aggregate fixed. The force-displacement curve is plotted for mastic films at different RH% conditioning. In addition to that, a relationship to mastic films bond strength at different RH% conditioning is developed.

6.4 Theory of Diffusion of Water Vapor and Relative Humidity

When a mastic sample is subjected to water vapor, vapor transport depends on vapor concentration (Lu and Likos 2004). Flick's first law captures the quantitative description of steady vapor flux q_v, as shown in Eq. (6.1).

$$q_v = -D_v \nabla \rho_v \tag{6.1}$$

where D_v is the diffusion coefficient for water vapor transport, and ρ_v is the vapor density or absolute RH of the pore water vapor. The vapor diffusion coefficient for transport porous materials is generally smaller than that for transport in free air due to limited pore space and tortuous flow path available for vapor movement in porous media. The vapor density can be measure by the Eq. (6.2):

$$\rho_v = \frac{w_v u_v}{RT} \tag{6.2}$$

where T is temperature, R is universal gas constant, u_v is vapor pressure, w_v is molecular mass of vapor. Vapor pressure can be determined by deducting dry air pressure from the total air pressure. It should be noted that vapor pressure increases with increase in temperature keeping the same RH.

RH is defined as the ratio of the absolute humidity (i.e. ρ_v), in equilibrium with any solution to the absolute humidity in equilibrium with free water (i.e. $\rho_{v,abs}$) at the same temperature, as shown in Eq. (6.3). In this study, RH is measured through a humidity and temperature recorder from Measurement Computing.

$$RH = \frac{\rho_v}{\rho_{v,sat}} \tag{6.3}$$

Two methods are available for controlling humidity in the laboratory, one is isotropic humidity control and the other is two-pressure humidity control. In this study, isotropic humidity control is used. In isotropic humidity control, salt is allowed to come to

thermodynamic equilibrium in small sealed containers. In isothermal control, the RH in the headspace above the solution approaches a fixed, reproducible value that depends on the salt concentration. Osmotic desiccators are used for controlling RH in this manner.

6.5 Past Studies on Measuring Mastic-Aggregate Interface Bond Strength Measurement

Copeland (Copeland 2007) developed a relation between pull-off strength with moisture concentration through PATTI tests and numerical simulation. In her test, the substrate is an aggregate plate, which is emerged into a water bath. The pull-off stud is fixed with one end of the ceramic plate and the other end is coated with mastic materials. The mastic materials with the pull-off stud and ceramic plate are placed on the aggregate substrate. Moisture is diffused into the aggregate substrate, and then thorough the mastic materials. The pull-off test is performed as a function of diffusion time and a relation between the mastic strength degradation with time to moisture diffusion is developed. In addition, a relationship between moisture content with time to moisture diffusion at the mastic-aggregate interface is developed through FEM modeling. By combining the two relationships from the laboratory and FEM models, an equation is developed that relates moisture with the Pull-Off Tensile Strength (POTS):

$$POTS = e^{(0.30-3.76\sqrt{\theta})} \tag{6.4}$$

where θ is the amount of moisture. This relationship assumes that no loss of bond strength at zero moisture content.

Ban et al. (Ban et al. 2011) developed a relationship of moisture concentration with the pull-off strength ratio of wet to dry conditioned AC samples. Like Copeland (Copeland 2007), they used PATTI test to measure the normal pull-off strength of binder modified with different additives and the FEM diffusion model to measure moisture concentration at the interface of the binder and aggregate substrate. The equation is as follows:

$$\frac{\tau_{wet}^{0}}{\tau_{dry}^{0}} = exp\left[-k\left(\frac{\phi}{\phi_{sat}}\right)^{n}\right] \tag{6.5}$$

where τ_{dry}^{0} is the cohesive zone tensile strength at the unconditioned (dry) stage, τ_{wet}^{0} is the tensile strength at a certain level of moisture conditioning (wet), φ is the degree of saturation at a certain level of moisture conditioning, φ_{sat} is the degree of saturation at the fully saturated level, and k and n are the model parameters, k represents the bond strength remaining at the complete level of moisture saturation, n represents the shape of the degradation rate. To the authors' knowledge, no study has been done to measure the shear pull-off strength of mastic materials subjected to vapor diffusion.

6.6 Laboratory Tests

6.6.1 Creating Laboratory Relative Humidity Controlling Chambers

In this study, the laboratory humidity controlling chamber is developed following ASTM E104 standard (*ASTM Designation No. E104-02 Standard Practice for Maintaining Constant Relative Humidity by Means of Aqueous Solutions* 2012). According to the standard, an aqueous solution of salts is able to create a constant RH in an enclosed chamber considering the temperature does not vary significantly in the chamber. Three

salts such as Potassium Acetate (CH_3COOK), Potassium Carbonate (K_2CO_3), and Sodium Chloride (NaCl) are selected to make the aqueous solutions. The salts are selected such that they cover the low to high RH range. The RH of Potassium Acetate solution varies from 23.4% to 21.6% with the temperature range of 10 °C to 25 °C respectively. RH of the Potassium Carbonate solution varies from 43.1% to 43.2% with the temperature range of 5 °C to 25 °C respectively. RH of the Sodium Chloride solution varies from 75.7% to 73.9% with the temperature range of 5 °C to 80 °C. Three vacuum desiccators are used to control RH with three different salts as discussed above. The salts are mixed with distilled water in desiccators at room temperature. The salts are mixed with water such that free water is visible after complete mixing.

The laboratory temperature and RH are recorded in fifteen-minute intervals for five continuous days with a temperature and RH recorder. The variations of the laboratory temperature and RH are shown in Figure 6.2. It can be observed that the laboratory temperature is fairly constant during the day since the laboratory temperature is centrally controlled. The temperature varies from 22 °C to 21 °C, but the initial temperature is recorded at 25 °C, but it dropped to 22 °C within an hour.

Three desiccators are conditioned with three salts. The RH values are recorded inside the desiccators and are shown in Figure 6.2. It is observed that the RH for Potassium Acetate decreases over time and becomes constant within approximately two and half days. The RH for Potassium Carbonate increases for approximately one day and then decreases over time and becomes constant within approximately two days. The RH for Sodium Chloride increases over time and becomes constant after three days. Potassium Acetate gives constant RH value of 25% after five days; Potassium Carbonate gives a constant

RH value of 49% after five days; and Sodium Chloride gives a constant RH value of 71% after five days. After five days the temperature inside the desiccators are recorded as 21 °C. According to ASTM E104 (*ASTM Designation No. E104-02 Standard Practice for Maintaining Constant Relative Humidity by Means of Aqueous Solutions* 2012), at 21 °C, the approximate RH value for Sodium Chloride would be 75%, for Potassium Acetate RH would be 22%, and for Potassium Carbonate RH would be 43%. The values mentioned in the standard are close to the values measured in the enclosed desiccators. In the standard, it does not mention how long it will take to reach the above-mentioned RH% for different salts.

6.6.2 Preparing Laboratory Samples

Performance grade (PG) binder, PG 58-28 is mixed with fines passing through a #200 sieve to make mastic materials. Both binder and fines are heated at 160 °C before mixing. About 40% of the fines by weight of binder are mixed. 40% of the fines are selected due to the fact that too many fines would not stick to the aggregate and too few fines would show significant binder effects rather than mastic effects.

Rock samples of varying sizes from 150 mm to 200 mm diameter are collected from a local aggregate supplier as seen in Figure 6.3(a). The rocks are then cut into square shaped pieces of approximately 25.0±2.0 mm using a laboratory saw. Thickness of the rock square is kept to 5.0±1.0 mm. The rock squares are washed to remove dust and then heated inside an oven for thirty minutes at 160 °C for water drying. Before using the rock squares, they are kept at room temperature for two hours. Two rock squares are used to make a sandwich sample of mastic. One rock is covered with duct tape with an opening

of 5 mm^2 at the middle. The aggregate square covered with duct tape is show in Figure 6.3(b). A ruler is shown to check the dimension of the opening. Prepared mastic materials are put on the opening and pressed gently on the aggregate slice. Then the duct tape is removed carefully from the aggregate face. A 5 mm square mastic sample as shown in Figure 6.3(c). Another aggregate is placed on the top of mastic as show in Figure 6.3(d). The top aggregate slice is offset about 5±1 mm for the shear test sample as show in Figure 6.3(e). The offset is necessary to set up the sample on the base of the loading frame with glue. The 5 mm^2 mastic film is selected by considering varying shape and size of aggregates in the AC and the random placing of aggregate in the AC mix. It is assuming that the contact area between two aggregates with mastic materials in between them will not exceed 5 mm^2.

6.6.3 Conditioning of Samples

The desiccators are placed in a vacuum chamber. Salt solution is prepared inside the desiccators. The base is put inside the desiccators with a clear distance of 25 mm from the top of the solution to avoid spilling the samples. As soon as the salt solution is prepared, the sandwich samples are laid on top of the base and a RH and a temperature monitoring unit is attached to the inside wall of the desiccators. A conditioning picture is shown in Figure 6.3(f). The monitoring unit automatically records the chamber temperature and humidity and stored it. After completing the test the data is downloaded into computer. The room temperature is set at 21 °C. Each desiccator is kept for five days for conditioning the samples.

6.6.4 Determine Strength of Asphalt Mastic Films

The strengths of the mastic film under tension and shear pull-off force are measured as shown in Figure 6.4. Figure 6.4(a) shows the loading frame, which is a T3 Texture Analyzer. A computer with software controlled the loading frame. Both compressive and tensile test can be performed with the loading frame. Figure 6.4(b) and (c) show schematic diagrams of tension and shear tests respectively. Figure 6.5 (a) and (b) shows the test arrangement of normal and shear pull-off test. For the tension test, one aggregate is attached with the loading frame and another aggregate is attached with the base. Both the base and loading frame are attached with glue to the aggregate. Prior to each test, the loading frame and the base are cleaned with Acetone to remove any dust and clean glue residue from the previous test. It is noticed that improper placement of glue or presence of residual glue from previous tests caused failure at the interface of both the base and aggregate or loading frame and aggregate. The sandwich sample is set with the loading frame and the base as soon as it came out from the desiccators. The sample mass is measured in four significant digits before and after vapor conducting to see if the change in water mass is due to conditioning. A steady state deformation of 0.10 mm/sec. rate is applied to the loading frame for both tension pull-off and shear pull-off tests. The force and distance data are recorded.

6.7 Results and Discussions

6.7.1 Thickness of Mastic Films

Figure 6.6(a) shows the average thickness of mastic for both normal and shear tests. The average thicknesses of mastic are 0.210 mm, 0.202 mm and 0.193 mm, which are tested

with Potassium Acetate (25% RH), Potassium Carbonate (49% RH), and Sodium Chloride (71% RH) solutions respectively. Average thickness of the mastic films under 25% RH conditioning is 8.79% thicker than films subjected to 71% RH conditioning. Mastic film under 49% RH conditioning is 4.71% thicker than those with 71% RH conditioning. Differences in thickness are due to variation of applied pressure on the mastic materials while sandwiching between the two aggregates.

6.7.2 Absorption of Water Vapor

The amount of vapor absorbed by the mastic films is measured by taking the mass of samples before and after conditioning. It should be noted that vapor will diffuse through both mastic films and aggregate slices. It is observed that the sample mass after conditioning is less than the sample mass before conditioning for Potassium Acetate (25% RH) conditioning. This phenomenon indicates that Potassium Acetate absorb vapor from the fines of mastic materials and also from the aggregate slices. This is known as vapor desorption. Even though the aggregate slices are kept in the oven for thirty minutes at 160 °C but kept for two hours at the laboratory temperature and humidity condition after the oven dry, water vapor might have been inside the aggregate slices or it might absorb vapor from the air during the process of cooling. The percentages of vapor absorbed and desorbed by the mastic materials are shown in Figure 6.6(b). Mastic materials absorbed vapor from both Potassium Carbonate (49% RH) and Sodium Carbonate (71% RH) solutions. Mastic film absorbed 0.34% vapor by its mastic materials volume under Sodium Chloride (71% RH) conditioning. It absorbed 0.27% vapor under Potassium Carbonate (49% RH) conditioning and desorbed 0.09% vapor under Potassium Acetate (25% RH) conditioning.

6.7.3 Normal Pull-off Strength of Mastic Films

Normal pull-off strength of the mastic films is measured by applying tensile force on one aggregate while keeping the other aggregate fixed on the base. In the following sections the terms elasticity and flexibility or ductility is used interchangeably. Three normal pull-off tests are performed on each RH conditioning. Figure 6.7(a) shows the force-displacement relationship of mastic films under 25% RH. All three force-displacement curves show a straight increase in load and then show mastic film elongation followed by ultimate strength and failure strength. The "yield" strength is measured where the load-displacement curve turns from the straight line to curvature. The maximum load or the ultimate strength of mastic films is determined. Figure 6.7(b) and (c) shows force-displacement curves for mastic films under 49% RH and 71% RH respectively. The ultimate strength of mastic films for all three curves under 25% RH conditioning are higher than under 49% RH and 71% RH conditioning. At low RH, brittle failure is observed. At 49% RH conditioning, the load-displacement curve looks like an elastic-perfectly plastic material. The mastic film fails suddenly for all three tests at 49% RH. On the other hand, 71% RH conditioning shows more elongation or stretching and then ultimate strength followed by failure. The average deformation at failure in 71% RH conditioning is higher than those in 25% and 49% RH conditionings. This means that higher RH conditioning makes mastic film more flexible or ductile. The elastic behavior of mastic materials at moisture-induced condition is supported by a previous study conducted on mastic and matrix materials through DSR tests (Tarefder, Yousefi, et al. 2010).

6.7.4 Shear Pull-off Strength of Mastic Films

Figure 6.8 shows the shear force variations in mastic films. Unlike normal-pull strength, shear pull-off strength increases with increase in percent RH conditioning. Figure 6.8(a) shows shear force-displacement relationship for 25% RH conditioning. Shear force increases with increase in shear displacement and after ultimate shear strength; the displacement continues and decreases slowly. The high shear elongation or displacement is due to the viscous nature of the mastic films. Even though mastic film fails, the failure surfaces stick together until they completely tear away from each other.

This increase in shear force can be explained from the findings of previous studies. An Atomic Force Microscope (AFM) image shows that the wet binder has rough surfaces due to vapor absorption and an increase in volume (Tarefder and Zaman 2010). In addition, nanoindentation tests show that wet aggregates have rough surfaces due to vapor absorption and increase in volume (Kasthurirangan Gopalakrishnan, Broj Birgisson, Peter Taylor 2011). When shear force is applied on one aggregate keeping the other aggregate fixed and mastic materials in between, the mastic materials roughen and increase in volume due to vapor absorption, thus additional shear pull-off force is required to overcome this rough surface. For this reason, the shear pull-off force is higher under high RH conditioning than low RH conditioning. In addition, it is observed in the normal pull-off test that the mastic material becomes more elastic at high RH conditioning. This elasticity of mastic materials causes higher shear forces to fail in mastic materials. The explanation can be given by the vector plot in Figure 6.9. *E1* and *V1* are elastic and viscous strength, respectively, before vapor conditioning. *E2* and *V2* are the elastic and viscous strength, respectively, after vapor conditioning. *S1* and *S2* are

the shear strength before and after vapor conditioning. From the figure, it is observed that shear pull-off strength increases with an increase in elasticity and with a decrease in viscosity. Even if the viscosity does not decrease, elasticity increases and therefore shear strength increases.

6.7.5 Determining Bond Strength

The average yield strength and ultimate strength for three tests and for all three RH conditioning values are plotted in Figure 6.10 and 6.11. Figure 6.10(a) and (b) shows the normal yield and normal ultimate strength variations with RH%. Both normal yield and ultimate strengths decrease with an increase in RH%. The points are fitted with exponential equations. The R-square value for the normal yield strength is 0.9088 and for the normal ultimate strength is 0.7529.

Figure 6.11(a) and (b) shows the shear yield and shear ultimate strength variations with RH%. Both shear yield strength and ultimate strength increase with an increase in RH%. The R-square value for shear yield strength is 0.8952 and for shear ultimate strength is 0.9214. The increase in shear strength is rapid compared to the decrease in normal strength.

The strength ratio with the degree of vapor saturation is plotted in Figure 6.12. The strength ratio is the ratio of strength at arbitrary RH% with respect to 0% RH. The degree of vapor saturation is the ratio of arbitrary RH% with respect to 100% RH. Only ultimate strength is considered for the plotting strength ratio with the degree of vapor saturation. The strength ratio is calculated by using Eq. (6.6), which is a modified version of Eq. (6.5) for vapor conditioning.

$$\frac{\tau^0_{RH\%}}{\tau^0_{RH\,0\%}} = exp\left[\pm k\left(\frac{\phi_{RH\%}}{\phi_{RH\,100\%}}\right)\right] \tag{6.6}$$

The *n* in Eq. (6.5) is assumed to be 1.0 since only one type of mastic materials is used without any additives. The negative sign is applicable to normal pull-off strength and the positive sign is applicable to shear pull-off strength. The normal pull-off strength decreases, but shear pull-off strength increases with an increase in vapor saturation. Less than 50% normal strength is remaining in mastic films at 100% vapor saturation. The increase in shear strength indicates an increase in elasticity and decrease in viscosity of mastic materials, which may reduce binding capability of mastic materials and causes more damage.

6.8 Conclusions

The following conclusions are drawn from the above discussions.

1. Normal pull-off – Mastic films show flexible behavior at high RH% conditioning and brittle behavior at low RH% conditioning while normal pull-off strength is measured.
2. Shear pull-off – The flexible nature of mastic films at high RH% influences shear pull-off strength by showing higher shear pull-off strength.
3. Relative humidity – Mastic materials can be vapor conditioned with aqueous solutions. Lower RH% will absorb vapor from the aggregates and fines if vapor is present inside the aggregates and fines before put into conditioning.
4. Strength degradation – Increase in elasticity at high RH% conditioning causes a decrease in viscosity in mastic films. Decrease in viscosity of mastic materials

might cause binding inefficiency between aggregates. Binding inefficiency causes additional damage in AC.

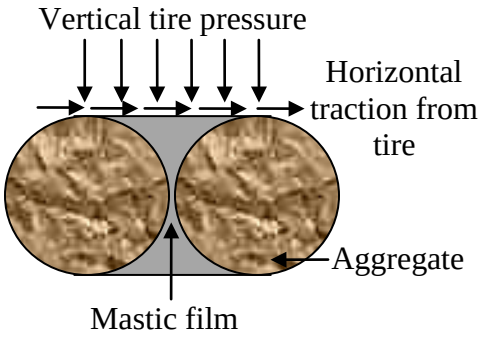

(a) Aggregate and mastic in undamaged AC

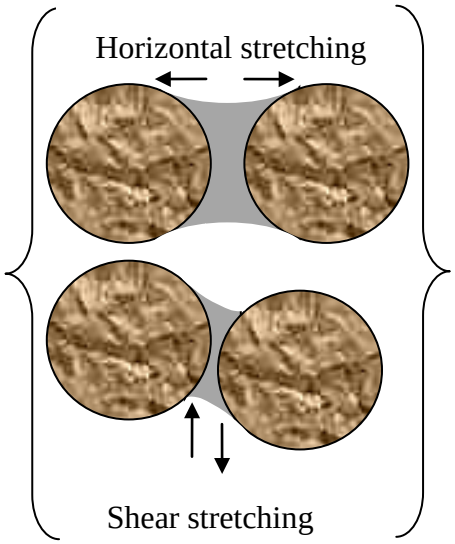

(b) Horizontal and shear pull-off actions

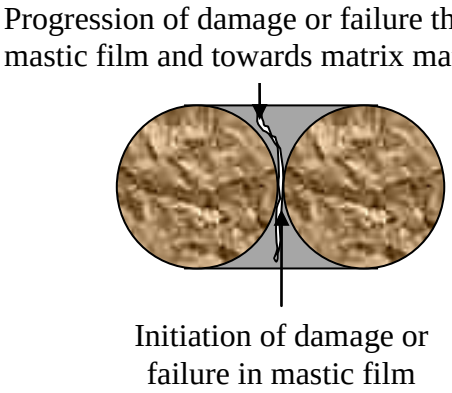

(c) Aggregate and mastic in damaged AC

Figure 6.1 Schematically aggregate and mastic film in undamaged and damaged AC

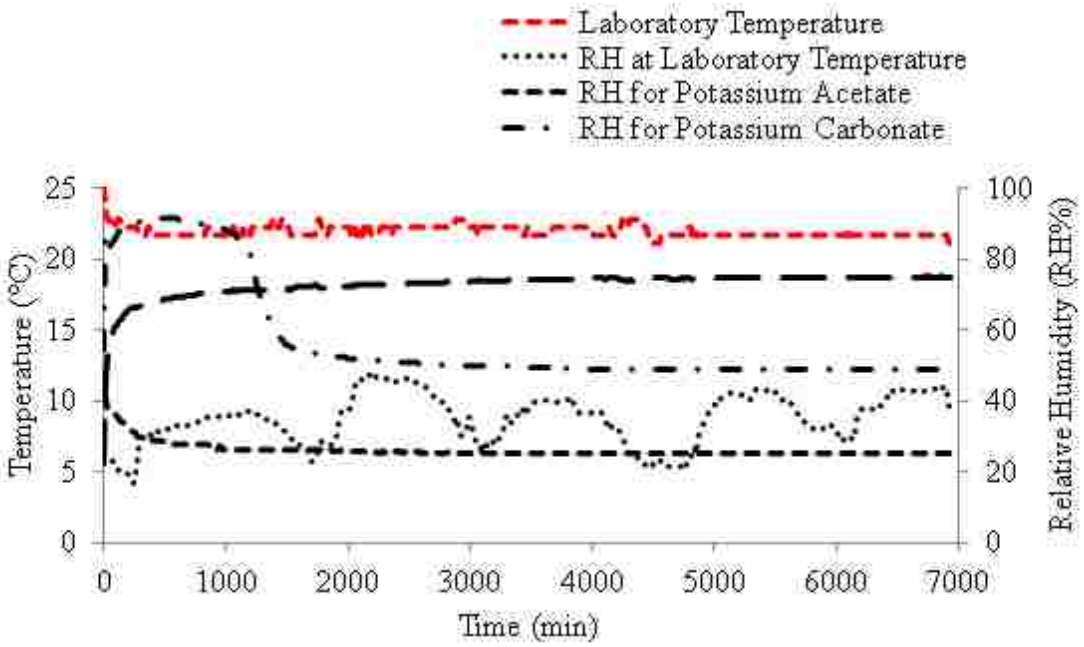

Figure 6.2 Variations of temperature and RH inside the laboratory and the desiccators

(a) Rock samples

(b) Aggregate covered with duct tape

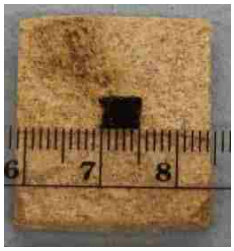

(c) Mastic on aggregate

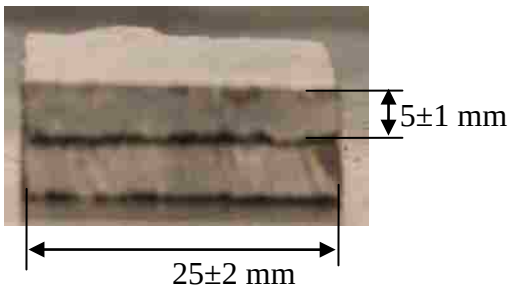

(d) Normal test sample

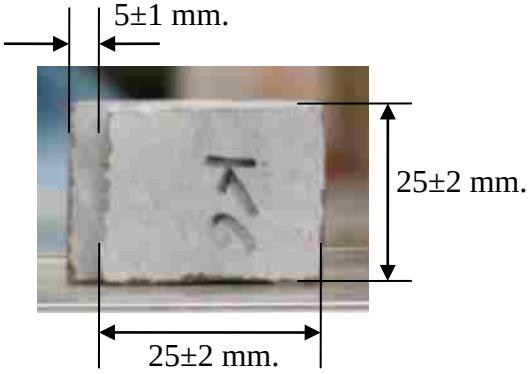

(e) Shear test sample

(f) Conditioning of samples

Figure 6.3 Procedure for making laboratory samples and conditioning

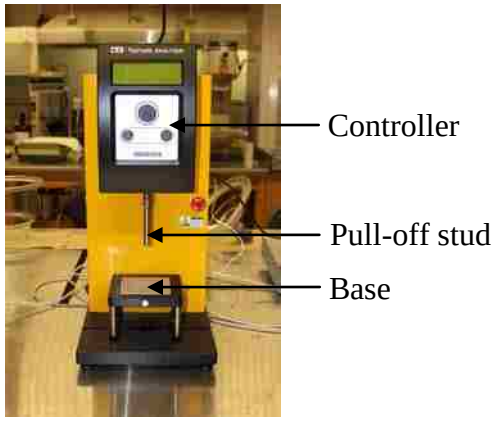

(a) T3 Texture Analyzer

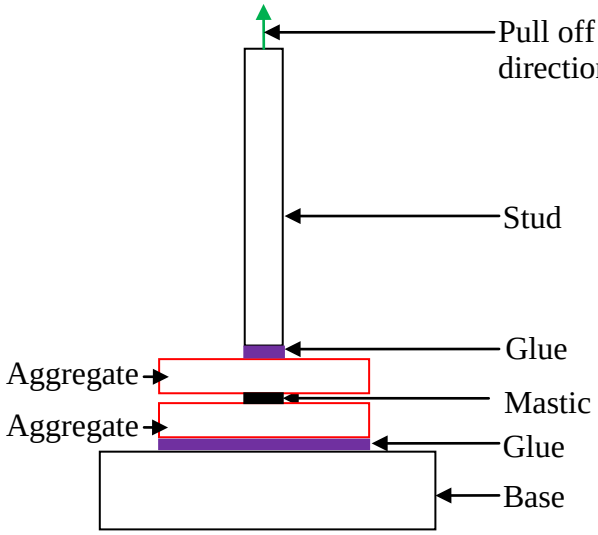

(b) Test setup for tensile pull-off test

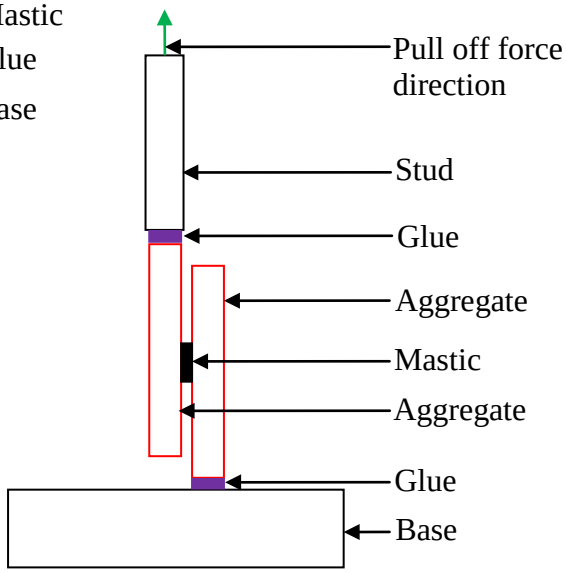

(c) Test setup for shear pull-off test

Figure 6.4 T3 Texture analyzer with schematic diagram of measuring normal and shear strength of mastic materials

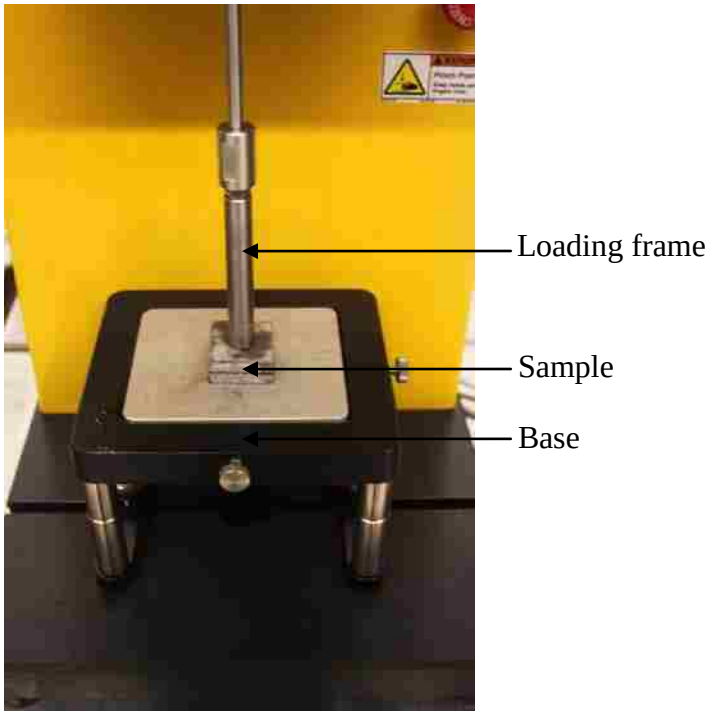

(a) Normal pull-off test on mastic film

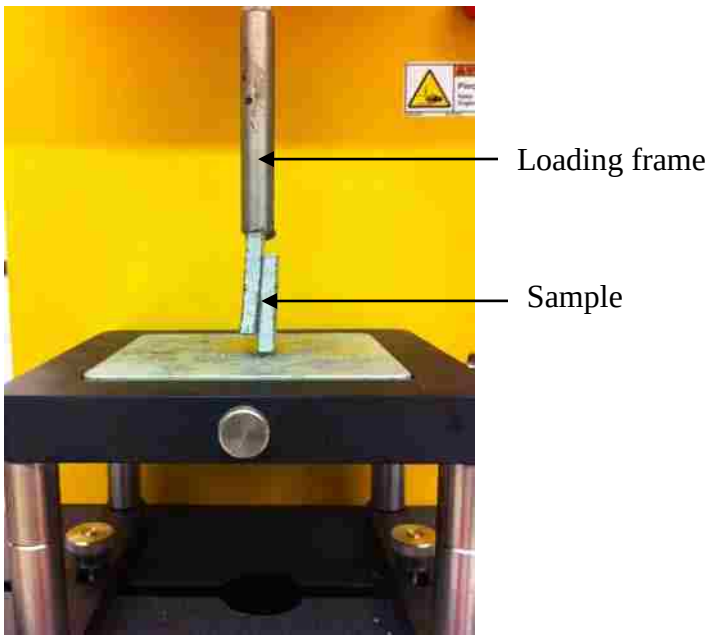

(b) Shear pull-off test on mastic film

Figure 6.5 Normal and shear pull-off tests on mastic film

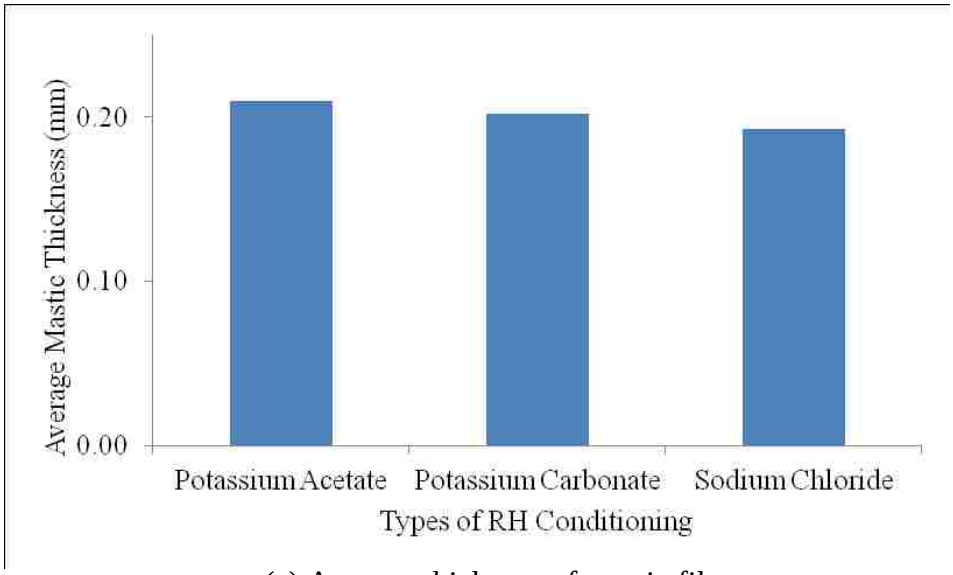

(a) Average thickness of mastic films

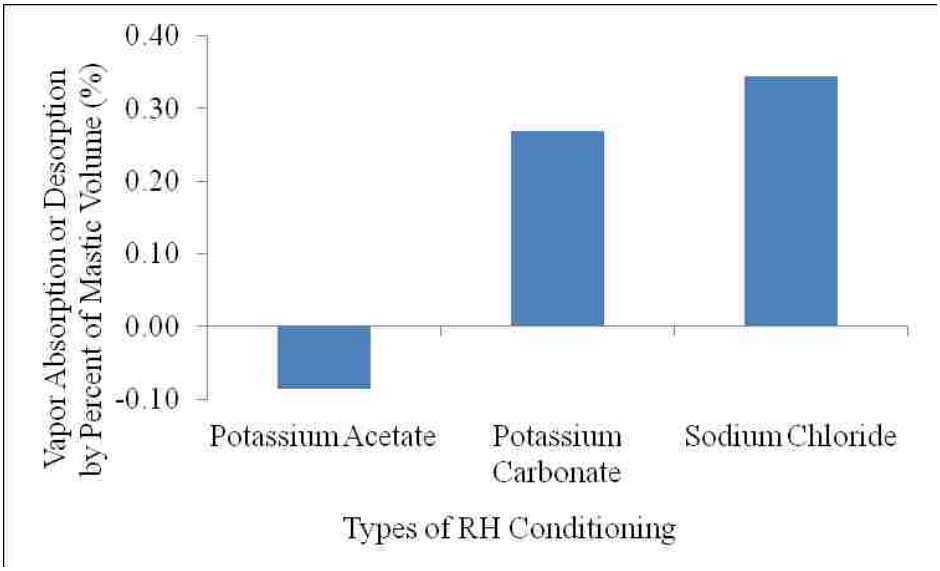

(b) Vapor absorption/desorption by mastic films

Figure 6.6 Status of mastic film

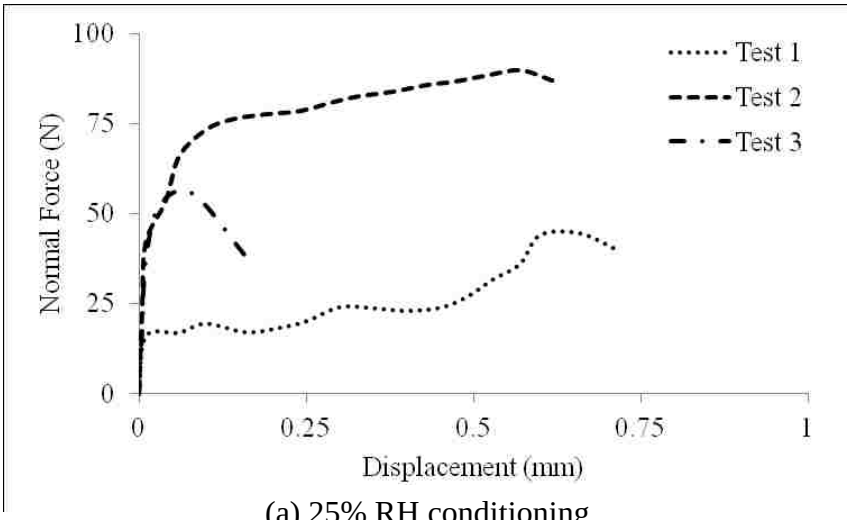

(a) 25% RH conditioning

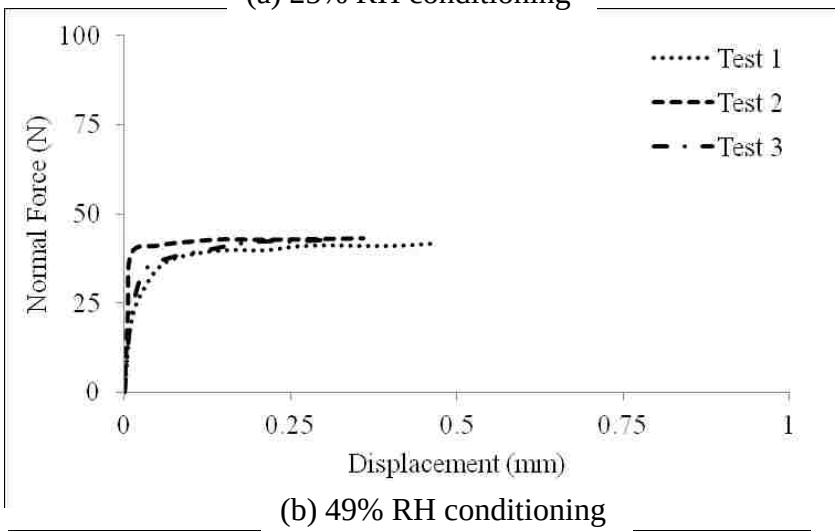

(b) 49% RH conditioning

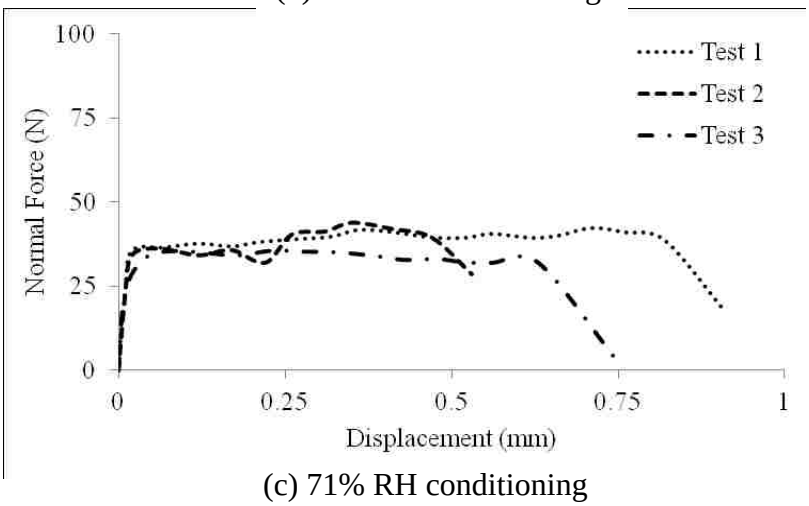

(c) 71% RH conditioning

Figure 6.7 Normal force-displacement curves of mastic films under three RH% conditioning

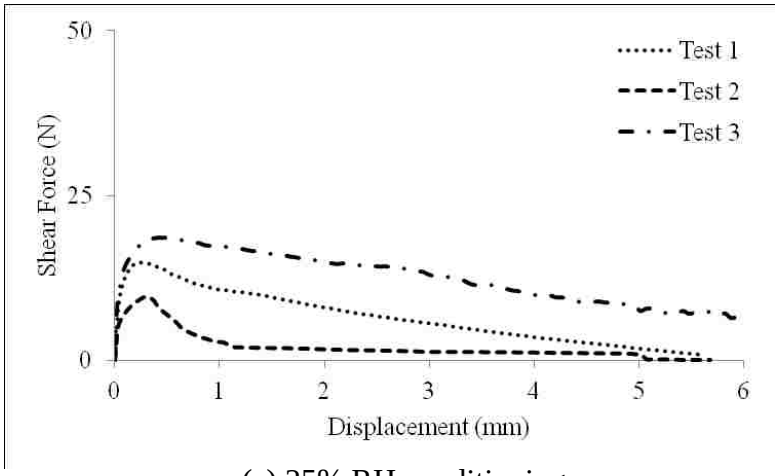

(a) 25% RH conditioning

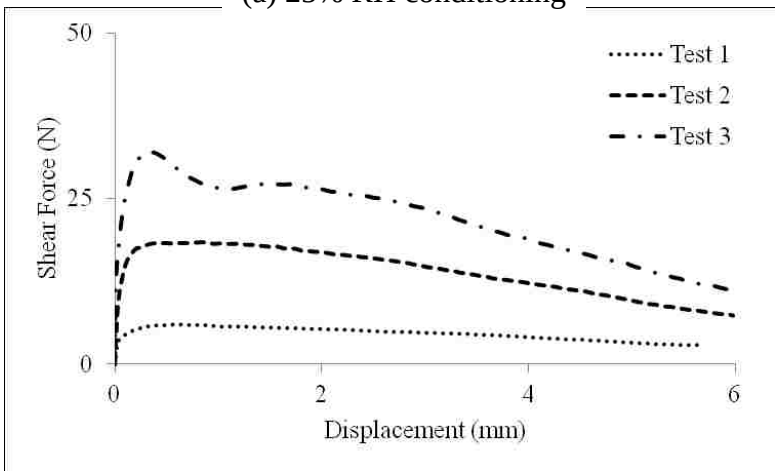

(b) 49% RH conditioning

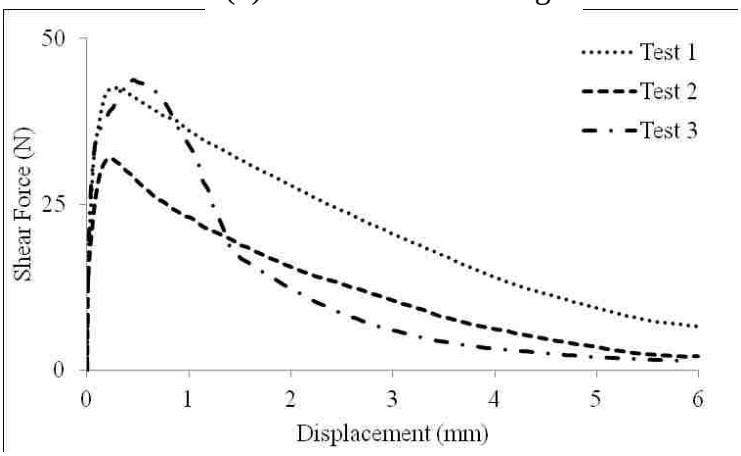

(c) 71% RH conditioning

Figure 6.8 Shear force-displacement curves of mastic films under three RH% conditionings

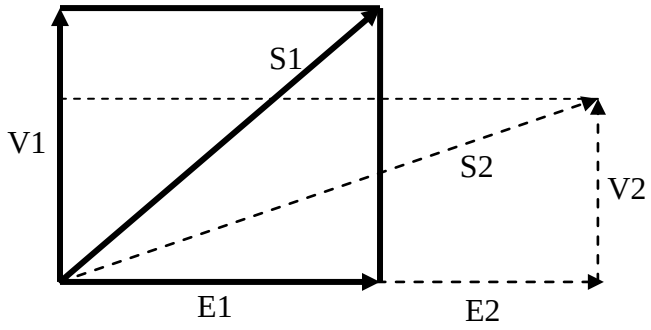

Figure 6.9 Schematic of elastic and viscous forces

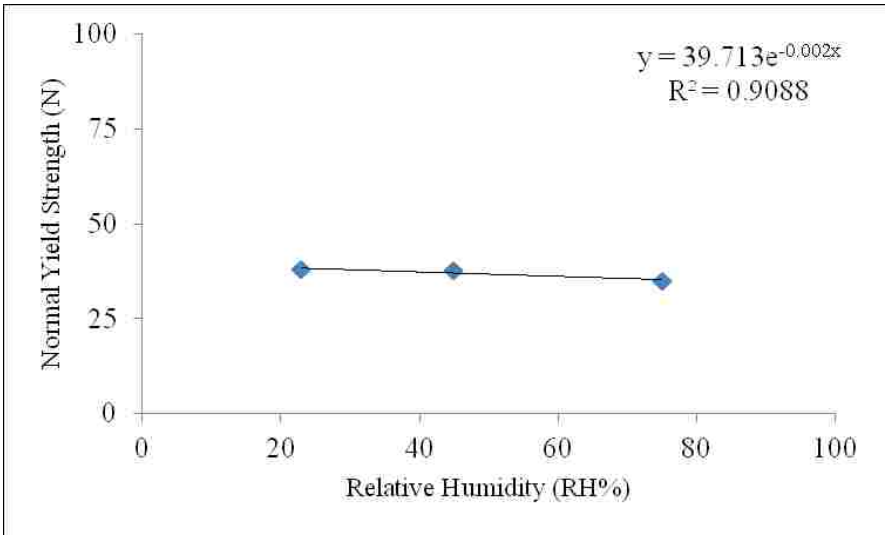

(a) Normal yield strength

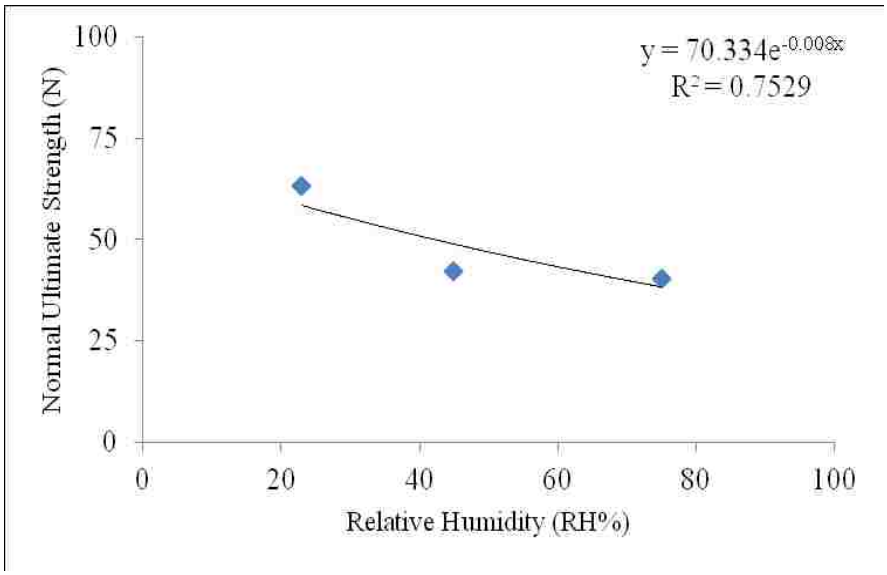

(b) Normal ultimate strength

Figure 6.10 Variations of normal strength of mastic films due to three RH% conditionings

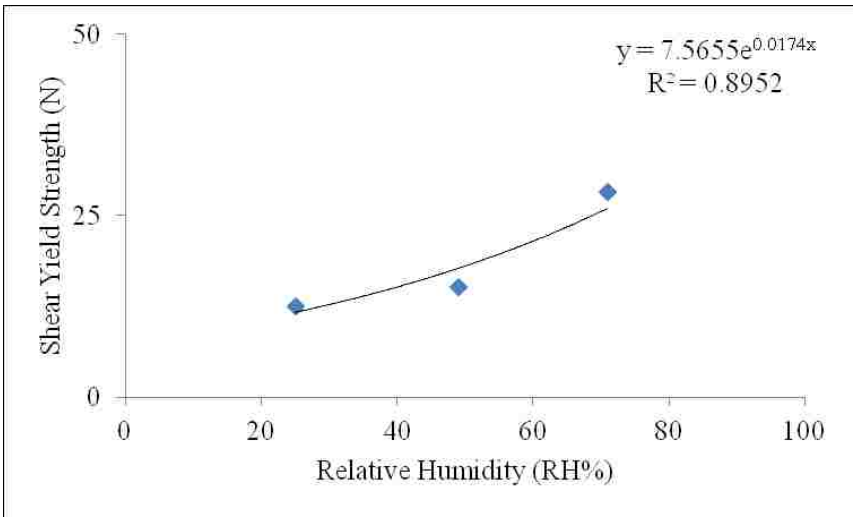

(a) Shear yield strength

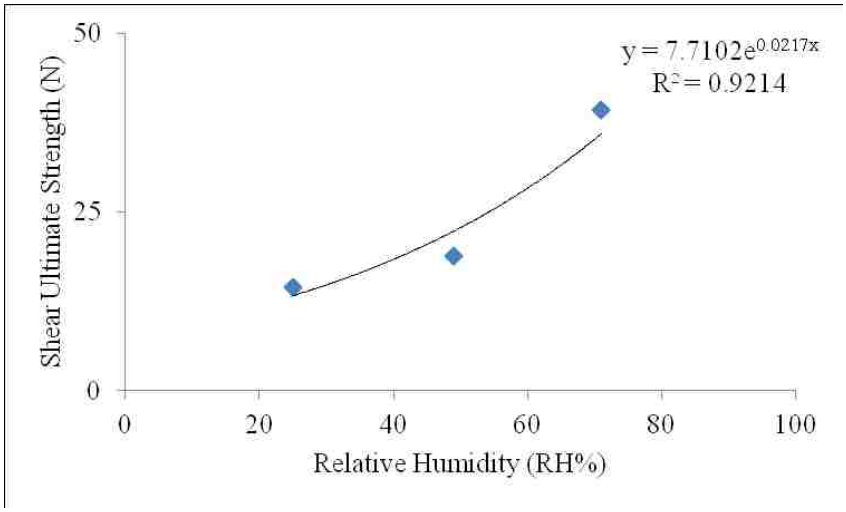

(b) Shear ultimate strength

Figure 6.11 Variations of shear strength of mastic films due to three RH% conditionings

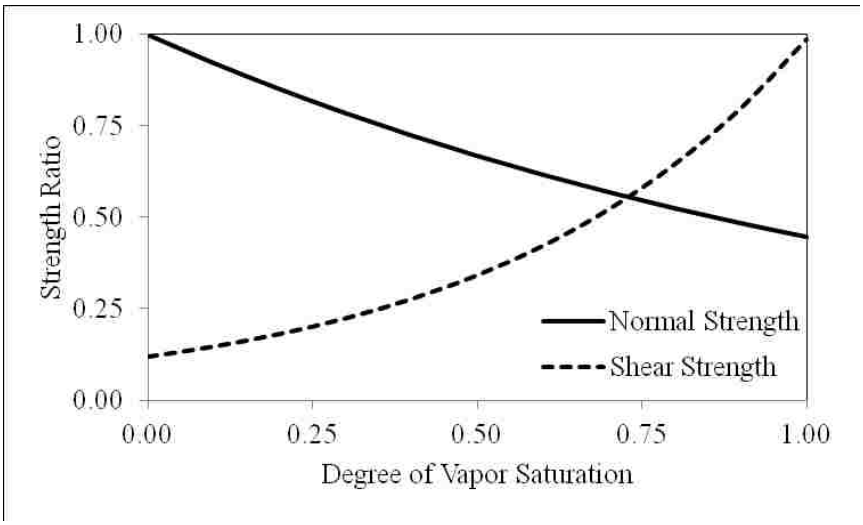

Figure 6.12 Variations of strength with degree of vapor saturations

CHAPTER 7

NANOINDENTATION ON MASTIC MATERIALS

7.1 General

This chapter describes nanoindentation tests on mastic materials for developing viscoelastic mechanical models for dry and wet mastic materials.

7.2 Introduction

Several laboratory testing protocols are available to evaluate and characterize asphalt concrete (AC) mix. Laboratory tests are performed on both compacted and loose AC mix. Also there are several laboratory tests available to determine moisture sensitivity of AC mix for both compacted and loose mix (Spinel 2009). In recent years, many researchers are conducting tests by nanoindentation on asphalt mixture components such as asphalt binder and aggregates to understand materials behavior at micron scale (Allen et al. 2013; Ossa et al. 2005; Schilde and Kwade 2012). In a nanoindentation test, an indenter is used to indent a sample surface and the movement of the indenter is measured with an increasing load or deformation (Oliver and Pharr 1992). It is a very powerful technique to measure hardness and Young's modulus of a material. Very few studies have been done on the AC mix such as on mastic and matrix materials using nanoindentation techniques (Tarefder, Zaman, et al. 2010). In addition, very limited studies have been done to evaluate effects of moisture in AC by nanoindentation (Kasthurirangan Gopalakrishnan, Broj Birgisson, Peter Taylor 2011). Though extensive research have been done on elastic-plastic and composite materials using this novel approach (Hodzic et al. 2001; Kurapati

2008; Minster and Micka 2012; Schuh 2006). In addition, biomedical engineers used nanoindentation test to measure mechanical properties of organ and components of human body such as strength of bones and muscles (Gupta et al. 2011; Wu et al. 2012). In this study, nanoindentation test is done on mastic phase of AC.

Mastic materials or asphalt mastic is defined as mixture of asphalt binder with fines passing through # 200 sieve (0.075 mm) (Kim and Little 2004; Kringos et al. 2008a). On the other hand, matrix materials are mixture of asphalt binder with fine aggregate passing through a # 4 sieve and retained on a # 200 sieve (Mohammad I. Hossain and Tarefder 2013b). When aggregates are heated and mixed with hot asphalt binder to produce AC, coarse aggregates are coated with mastic materials and surrounded by matrix materials. It is challenging to do nanoindentation tests on the asphalt binder since the binder stick at the tip of indenter at the ambient temperature (Tarefder, Zaman, et al. 2010). Despite this challenge, successful indentation tests have been performed on the aged asphalt binder (Tarefder and Faisal 2013a; Tarefder and Faisal 2013b). Also, nanoindentation using Atomic Force Microscope (AFM) probe has been used to measure relaxation modulus of aged and unaged binder (Allen et al. 2013). This study is done to understand the viscoelastic behavior of mastic materials at the ambient temperature using nanoindentation tests. In addition, the effects of moisture in the viscoelastic behavior of mastic materials are also evaluated.

Asphalt mastic is a well known viscoelastic materials. Several studies have been done to understand the behavior of mastic materials (Dai and You 2007; Kim and Little 2004; Kringos et al. 2008a). Researchers conducted both laboratory tests and numerical modeling to characterize the mastic materials. Mechanical properties of mastic materials

are required while researchers focus on the small-scale behavior of AC, such as, two aggregates, coated with mastic materials, are joined with each other and forces are acting on them (Hossain and Tarefder 2013a). Faults such as damage and cracks initiated at small-scale and visible at macro-scale. For an example, in AC pavements, a crack initiated at the mastic-aggregate interface and propagated through mastic materials and visible while it reaches at the surface of pavements (Caro et al. 2010b). Understanding small-scale behavior of AC will help researchers to broaden their knowledge about macro-scale behavior of AC. For these reason, it is indeed very important to understand the mechanical behavior of mastic materials, especially at environmentally induced conditions such as moisture, to conduct small-scale computational research. It has been observed that moisture causes change in viscoelastic behavior of AC (Caro et al. 2008; Gubler et al. 2005; Nadkarni et al. 2009). Dynamic modulus tests have been performed to see the change in dynamic modulus after moisture conditioned at high temperature in addition with the cyclic water pressure. The results show significant decrease in dynamic modulus after moisture conditioning.

Several mechanical models are available to describe the viscoelastic materials using arrangement of springs and dashpots. Spring represents the elastic effects and dashpot represents viscous effects in the materials. The mechanical properties of spring and dashpot can be determined from the laboratory tests and using numerical methods those properties can be converted to the Proney series data to apply with the numerical modeling. Viscoelastic response of AC can be determined from dynamic modulus tests (Y. Richard Kim 2009). On the other hand the viscoelastic response of mastic materials can be determined form dynamic shear modulus test (Kim and Little 2004). Both

dynamic modulus and dynamic shear modulus tests can be performed in low to high temperature range under different frequencies. The mechanical models developed from laboratory tests are then used in numerical modeling such as Finite Element Method (FEM) modeling (Kim et al. 2005; Kringos et al. 2008a). Generally, for moisture-induced FEM modeling, diffusion of moisture that follows Flick's law is used along with the viscoelastic mechanical model. In some previous study, it has been observed that, the components of mechanical model, such as dashpots and springs have different properties while comparing with virgin and aged binder of AC (Tarefder and Faisal 2013a; Tarefder and Faisal 2013b). It is hypothesized that, the viscoelastic mechanical models will be different for virgin and moisture-induced conditions. Very limited studies have been done to determine effects of moisture in mastic materials and no study has been done using nanoindentation to determine the mechanical model for mastic materials for both virgin and moisture-induced conditions.

7.3 Objectives and Methodology

The objectives of this study are:

1. Perform nanoindentation tests on dry and wet mastic materials at the ambient temperature to understand the viscoelastic behavior.
2. Develop a viscoelastic mechanical model for dry and wet mastic materials from the nanoindentation creep data.

Two fulfill the objectives; AC samples are made by mixing fine aggregates and fines with asphalt binder. Laboratory nanoindentation tests are performed only on the mastic phase of AC. To understand the viscoelastic behavior, a creep indentation is applied following

loading and before unloading an indenter from the mastic materials. From the creep indentation data, non-linear least square method is followed to develop viscoelastic mechanical model by fitting the laboratory data with the selected model.

7.4 Background on Nanoindentation Tests

Nanoindentation tests have been using for decades but this is comparatively new testing procedure for AC. Both load control and displacement control indentation tests can be performed. The force involved is usually in the millinewton (mN) range and the indentations are measured in nanometer (nm). The indenter is usually very hard (i.e. diamond) of definite tip shape such as pyramid or spherical. The penetration depth together with the known geometry of the indenter tip provides an indirect measure of the indentation area at full load. The Young's modulus and the hardness of the tip are known and using this known value the Young's modulus and harness of materials with unknown property are determined. Figure 7.1 shows schematics of conventional nanoindentation test. Figure 7.1(a) shows the depths measure during loading and unloading of the indenter and Figure 7.1(b) shows the typical load-displacement curve. A sitting load is typically applied initially to facilitate contact between the tip and sample surface. Next, the load is increased gradually from point A to B. The tip is unloaded at the maximum load point B. The unloading path is assumed to be elastic for most of the elastic-plastic material. The unloading curve does not come back to point A due to plastic deformation in the elastic-plastic materials. The slope of the unloading curve at point B is usually equal to the slope of the loading curve at point A. The surface profile as shown in Figure 7.1(a) is a function of the penetration depth during loading and unloading. It should be noted that

mastic materials is a visco-elastic-plastic material. To overcome the viscous effect into the unloading part, a creep load is applied at the maximum load after point B.

As it mentioned earlier, nanoindentation is mostly applied to measure Young's modulus and hardness of materials. The Oliver-Pharr method is the most widely used method for determining stiffness and hardness values from load-displacement data. The basic assumption of the Oliver and Pharr analysis is that the vertical displacement of the contact periphery can be described by models for indentation of a flat elastic body by a rigid tip of geometry. According to this method, the unloading portion of the load-displacement curve fits the power law function, as given in Eq. (7.1).

$$P = \alpha \left(h - h_f \right)^m \tag{7.1}$$

where h = any depth of penetration, h_f = unrecoverable or plastic depth, P = indentation load, and α and m are constants. The parameters α, m, and h_f are determined by a least squares fitting procedures. Modulus of the thin film is calculated from the initial unloading slope, which is found by differentiating Eq. (7.1) and evaluating the derivatives at peak load and displacement. In the Olivar and Pharr analysis, the reduced modulus calculated a function of maximum indenter depth. However, the analysis procedure is applicable only for material that behaves in an elastic-plastic manner and does not exhibit any time-dependent behavior or load rate dependence. Several studies have been done on time-dependent (i.e. viscoelastic material) materials by using Olivar and Pharr method. The time dependent effects of the viscoelasticity has been minimized by applying a long holding time after the maximum load and a faster unloading time after end of creep load.

The following Eqs. (7.2, 7.3) are used to measure the reduced elastic modulus and hardness respectively.

$$\frac{1}{E^*} = \frac{1-\nu^2}{E} + \frac{1-\nu_i^2}{E_i} \tag{7.2}$$

where E is Young's modulus of the material, ν is Poisson's ratio of the material, E_i is Young's modulus of the indenter and ν_i is Poisson's ration of the indenter, E^* is the reduced modulus.

$$H = \frac{P_{max}}{A} \tag{7.3}$$

where P_{max} is peak load and A is projected area of contact at peak load. Young's modulus and hardness of mastic materials are already measured using nanoindentation (Tarefder, Zaman, et al. 2010). Nanoindentation is performed on AC and claimed that Young's modulus of mastic materials are less than 3.0 GPa and for aggregate this value is greater than 12.0 GPa. The other study focused only on the loading and unloading part of the test data. In this study, the test is done with loading and then creep and unloading and emphasis are given mostly on the creep indentation part.

Nanoindentation on mastic materials has some additional challenges. The challenge arises due to use of fine aggregates in the AC mix. Fine aggregates are mixed to facilitate the compaction of AC and make thin samples for nanoindentation tests by cutting it using laboratory saw. A schematic of nanoindentation tests are shown in Figure 7.2. Figure 7.2(a) shows the AC sample with fines and fine aggregates; during indentation, indenter might hit to the fine aggregates, which is shown in Figure 7.2(b); Figure 7.2(c) shows

indentation on mastic materials and Figure 7.2(d) shows another limitation of this test that is indenter might hit on micro void. In this study, nanoindentation tests are done on such location that is free from fine aggregates and the test data is carefully analyzed to remove data that shows indentation on micro voids.

7.5 Laboratory Procedures

7.5.1 Sample Preparation

Superpave mixes used with PG 70-22 and fine aggregates are collected from plant. Mixture is compacted into 150 mm (6 in) diameter cylinders by a Superpave Gyratory compactor using 600 KPa (87.02 psi) vertical pressure. The sample is prepared at a target low air voids of 4% to reduce voids in the sample. Using a fine laboratory saw, 6 mm (0.25 in) thick square shape of size 25 mm x 25 mm (1 in x 1 in) slice is prepared for the test. Smooth surface of the cube is very important for nanoindentation experiment. Because the contact area is measured indirectly form the depth of penetration, a rough surface may cause errors in the determination of the area of contact between the indenter and the specimen. Therefore, the square samples are polished by a grinding machine rotating a angular speed of 150 rpm with sequence of SiC paper of decreasing abrasiveness (100, 200, 400, 800, 1000, 1200, and 1400 grit). Only one surface is polished. Finally the specimens are washed in a water bath to remove any remaining dusts. Figure 7.3 shows a sample on stud and substrate. Sample is fixed on substrate and stud with glue. The red box is shown to locate the location of indentation test, which is free from fine aggregates. It should be noted that the indentation on micro voids cannot be avoided.

7.5.2 Nanoindentation Tests

The nanoindenter device, manufactured by MicroMaterials Ltd, at the UNM nano test laboratory is used for indentation. More details on the nanoindentation testing equipment are given in this reference (Tarefder and Faisal 2013a). For this study, Berkovich indenter tip is used since some previous study shows than spherical indenter sticks with the unaged binder. As a result, system compliance can be lost during indentation on asphalt. A Berkovich tip consists of three-sided pyramidal Berkovich tip with a semiangle of 65.27°. It has sharp and well-defined (pyramid defined by face angle 65.3°) tip geometry. In this study, a maximum load of 0.51 mN is applied with an unloading rate of 0.02 mN/sec. A sitting load of 0.01 mN is used for all the samples. A creep time of 200 seconds is applied after reaching the maximum load. This creep time is also known as dwell time (Goodall and Clyne 2006; Sarihan 1994). The viscous effects of the test results are reduced by using a fast unloading rate and applying an extended dwell time. Tarefder and Faisal have shown that a dwell time of 100-200 seconds (long) can minimize the viscous effect of asphalt (Tarefder and Faisal 2013a). Mastic phase of the AC sample is indented at 50 locations to deal with the variability of nanoindentation results, considering the limitations as mentioned earlier, and due to material heterogeneity in the asphalt mastic. Five rows with ten columns are selected for the indentations, each column is separated by 500 micrometer (μm) and each row is separated by 300 micrometer (μm). A 15 micrometer (μm) retraction distance is selected for the test. The test chamber temperature is kept at 26 °C, within a fluctuation of ±0.2 °C. After the test, the temperature corrections are also provided to the analysis.

7.6 Results and Discussions

7.6.1 Force-Depth Relationship

Figure 7.4(a) shows the force-depth curves for dry mastic materials obtained from the nanoindentation tests on mastic materials. Forth indentations are plotted from the fifty indentation test results. Ten indentations are discarded due to fact that the indenter might hit on the micro voids. The force-depth curves are discontinuous or showing negative displacement for those discarded tests. It is observed that the force-depth curves widely ranges with displacement from 52.96 nm to 6392.30 nm for same load of 0.51 mN. The average displacement is 3222.63 nm. This wide variation is due to the heterogeneous behavior of mastic materials and these variations are expected. Also, as mentioned earlier, indenter might hit either fines or the asphalt binder. Though, all the indentations showed plastic depth after unloading. In addition, no negative slope is observed at the unloading curve, this means 200 sec holding time is appropriate to overcome the viscous effects of mastic materials. Due to this wide range of deformation, it would be practical to get an average value of the indentation depths.

Figure 7.4(b) shows the force-depth relationships for wet mastic materials. Forty indentations are plotted. The number of indentations is kept forty to compare with the indentations on dry mastic materials. It should be noted that, unlike the dry indentation, the loading and unloading curves for the wets mastic shows “noises”. In previous studies, this noise is also observed for indentation on wet mastic materials. Despite these noises, elastic modulus of mastic materials are determined from the tests data. There are several reasons that could cause these noises: when mastic samples are conditioned using

AASHTO T283 standards, the top surface might have eroded and roughened; when indenter hits those eroded surface then the irregular force-depth showed; also the eroded surface has more micro voids then the dry surface and could effects on the indentation results. In addition, when the fine aggregates and fines absorbed water, it increase it volume and the surface texture roughens, these also cause irregular force-depth relationships. To consider this limitation, the creep test data seems appropriate to study the viscoelastic nature of mastic materials.

For wet mastic materials, the minimum depth measured at the beginning of the creep load is 66.40 nm and the maximum depth measured is 4673.72 nm. The average depth is 2370.06 nm. It is seen that the minimum depth measured under wet condition is 25.38% higher than the dry condition but the maximum depth measured in the wet condition is 36.77% lower than the dry condition. Also the average depth measured in the wet condition is 26.46% lower comparing to the dry condition. The results indicate that the wet condition shows less indentation while average indentation depth is considered. This suggests that due to moisture conditioning, the surface stiffness is increases for wet mastic materials.

7.6.2 Creep Behavior

Figure 7.5 shows the creep behavior of mastic materials. The hold time is 200 sec for all indentations. Fourth creep indentations for dry mastic materials are plotted in Figure 7.5(a) and the normalized forty indentations are plotted in Figure 7.5(b). Creep data shows both linear and nonlinear depth increase with time. Again, the linear depth increase might be due to the fact that, indenter hits on the fines and the nonlinear depth

increase caused by when indenter hits on the binder. Since fines mixed with binder and while indenter hits fine and pressed downward, underneath the fines there are both binder and more fines and when indenter hits binder, underneath the binder there are fines or binder. So for mastic materials we have to consider combine effects of binder and fines. For this reason, to keep both linear and nonlinear creep behavior, the average depth is considered. This average plot is further analyzed.

Figure 7.5(c) shows the creep behavior of the wet mastic materials and 5(d) shows the normalized creep behavior for the forty indentation data. Creep data shows less disturbance compare to the loading and unloading curve. It should be noted that, all the forty data shows depth increases linearly. This indicates, wet mastic shows more elastic behavior compare to the dry mastic. Though, the indentation depth is lower than the dry mastic materials. Moisture makes the top of the mastic rough and hard to penetrate.

Figure 7.6(a) and (b) shows the average of the normalized creep indentation depth data. The maximum average indentation depth is 980.96 nm for dry mastic materials and 792.10 nm for wet mastic materials. The average indentation depth is 23.84% higher for dry mastic comparing to the wet mastic materials.

7.6.3 Contact Area of Indenter

The contact area for the Berkovich tip can be measured using the following equations (Lu et al. 2003),

$$A = 24.37h^2 + 197.0h - 675.3\sqrt{h} \tag{7.4}$$

where *A* is in nm square and *h* is in nm. Figure 7.7 shows the contact area measured for the wet and dry mastic materials. The normalized average depth is used to measure the contact area. The maximum contact area is 23,623,127 nm square for dry mastic and 15,427,267 nm square for wet mastic materials. Since the indentation depth is higher for dry mastic materials, the contact area of the indenter is also higher. The contact area is 34.69% higher for the dry mastic compare to the wet mastic.

7.6.4 Viscoelastic Mechanical Model

Viscoelastic model can be expressed using several mechanical modes such as Maxwell, Kelvin, and Burgers model. Figure 7.8(a) and (b) shows representations of Burgers model, which is a combination of Maxwell and Kelvin models. Figure 7.8(c) and (d) shows Maxwell model. It has been mentioned that, Burgers model best represents the viscoelastic materials (Huang 2004). The mechanical Burgers model and Maxwell model for the nanoindentation tests can be represented by the following Eq. (7.5) and (7.6) (Fischer-Cripps 2004):

$$h^2(t) = \frac{\pi}{2} P_0 \cot\alpha \left[\frac{1}{E_1} + \frac{t}{E_1 \tau_1} + \frac{1}{E_2}\left(1 - e^{-\frac{t}{\tau_2}}\right) \right] \tag{7.5}$$

$$h^2(t) = \frac{\pi}{2} P_0 \cot\alpha \left[\frac{1}{E_1} + \frac{t}{E_1 \tau_1} \right] \tag{7.6}$$

where *h* is the displacement due to applied load on a material, P_0 is the indentation load, α includes half angle of Berkovich indenter, *E* is the elastic modulus, , *t* is time, τ_1 is relaxation time, and τ_2 is retardation time. Relaxation time is defined as the time required for the stress reduces to 36.8% of the original value. On the other hand, retardation time

is defined as the time to reach 63.2% of the total retarded strain. The total strain of the materials has three components, an instantaneous elastic strain, a viscous strain, and a retarded elastic strain as shown in Fig 7.8(b). For the known value of h, P_0 and t, from the indentation test, the values of E_1, E_2, τ_1, and τ_2 can be obtained from the simplified Eq. (7.7).

$$h^2(t) = A_1 + A_2 t + A_3\left(1 - e^{-\frac{t}{\tau_2}}\right) \tag{7.7}$$

where $A_1 = \frac{\pi}{2} P_0 \cot\alpha \frac{1}{E_1}$, $A_2 = \frac{\pi}{2} P_0 \cot\alpha \frac{1}{E_1 \tau_1}$, and $A_3 = \frac{\pi}{2} P_0 \cot\alpha \frac{1}{E_2}$.

On the other hand, there is no retarded strain shown in the Maxwell model. The linear increase in viscosity is observed in the Maxwell model. The Maxwell model and Burger model is selected in this study since the viscoelastic behavior for dry mastic materials follows Burger model trend and wet mastic materials follow Maxwell model trends. For the known value of h, P_0 and t, from the indentation test, the values of E_1 and τ_1 can be obtained from the simplified Eq. (7.8).

$$h^2(t) = A_1 + A_2 t \tag{7.8}$$

where $A_1 = \frac{\pi}{2} P_0 \cot\alpha \frac{1}{E_1}$ and $A_2 = \frac{\pi}{2} P_0 \cot\alpha \frac{1}{E_1 \tau_1}$.

In this study, Eq. (7.5) and (7.6) is fitted with the Fig 7.8(b) and 8(d), respectively, to find A_1, A_2, and A_3. A nonlinear curve fitting algorithm is used in MATLAB to optimize those parameters.

Figure 7.9(a) shows the optimized Burgers model with the laboratory test results. The optimized values are: E_1=0.158 GPa, E_2=0.286 GPa, τ_1=144.85 sec, and τ_2 = 30.86 sec. Using the Burgers model parameters, Creep compliance, *J(t)* of the dry mastic materials are determined from the following Eq. (7.9).

$$J(t) = \frac{1}{E_1} + \frac{t}{E_1\tau_1} + \frac{1}{E_2}\left(1 - e^{-\frac{t}{\tau_2}}\right) \tag{7.9}$$

The Creep compliance plot is shown in Figure 7.9(b). This is also known as contact creep compliance.

Figure 7.9(c) shows the optimized Maxwell model with the laboratory test results. The optimized values are: E_1=0.491 GPa and τ_1=64.31 sec. Using the Maxwell model parameters, creep compliance, *J(t)* of the wet mastic materials are determined form the following Eq. (7.10).

$$J(t) = \frac{1}{E_1} + \frac{t}{E_1\tau_1} \tag{7.10}$$

It should be noticed that the Maxwell model does not fit well with the wet mastic indentation data. Though, the *R*-square value is 0.986 for this fit. The *h*-square value seems concave shape and increases nonlinearly with time. For this reason modified Maxwell models are considered to fit the wet indentation data. Eq. 7.11 considered power *m* as a nonlinear response. Two models are selected since this is unknown which model best fit with the laboratory results. The modified Maxwell models are as below:

$$h^2(t) = \frac{\pi}{2} P_0 \cot\alpha \left[\frac{1}{E_1} + \frac{t^m}{E_1\tau_1^m}\right] \tag{7.11}$$

Figure 7.10(a) shows the fitting of modified Maxwell model with the laboratory test data. The modified E_1= 0.408 GPa , τ_1=95.55 sec, and m= 1.256. The curve is fitted with the R-square value of 0.9996.

Modified Maxwell model indicates increase in depth and creep compliance with time. This suggests that, if dry and wet creep compliance compared then at some time the wet creep compliance would cross the dry creep compliance and keep increasing. This means at certain depth the Elastic modulus is lower than that is measured at the top of mastic materials. The top of mastic materials showing high modulus value due to roughness and aging effects but at certain depth, moisture reduces the stiffness of mastic materials. Previous studies shows that, wet mastic materials have lower Young's modulus value compare to the dry mastic materials (Kasthurirangan Gopalakrishnan, Broj Birgisson, Peter Taylor 2011). The previous study is conducted only comparing the Young's modulus measured from the unloading part of nanoindentation. However, the creep indentation shows different results from the conventional nanoindentation results. Since the surface is rough and shows stiffer nature, so creep duration longer than 200 sec is necessary to test on wet mastic materials.

Figure 7.11 shows the extension of creep time up to 2000 sec. Figure 7.11(a) shows the increase in depth while the creep time is extended and Figure 7.11(b) shows the increase in creep compliance with extended creep time. From the figures it could be seen that at 1252 sec creep holding time, the depth measured for wet mastic materials is higher than the depth measured for the dry mastic materials and the corresponding depth is 4303.68 nm.

7.6.5 Viscous Depth

Viscous Depth is measured for dry and wet mastic materials. For dry mastic, viscous depth is measured by taking a slope as shown in Figure 7.8 (b) at 200 sec. Retarded depth can be measured from the slope and the viscous depth can be found by deducting retarded depth from the total depth. Figure 7.12 shows the viscous depth for both dry and wet mastic materials. It has been observed that, viscous depth under wet condition is higher comparing to the dry condition. At 200 second, the viscous depth for dry mastic material is 518.81 nm and for wet mastic material the depth is 554.89 nm. Wet mastic material shows higher viscous depth comparing to the dry mastic material. This indicates that, viscous strain is also higher for wet mastic material compare to the dry mastic material. Viscous materials follow the following stress-strain relationship,

$$\sigma = 2\mu\dot{\varepsilon} \tag{7.12}$$

where σ is applied stress, μ is viscosity, and $\dot{\varepsilon}$ is strain rate. For a viscous material, viscosity is decreases while viscous strain is increases and vice versa. Thus, wet mastic material shows less viscous effects compare to the dry mastic materials.

7.7 Conclusions

Nanoindentation tests are done to understand the contact creep behaviors and to develop viscoelastic mechanical models for dry and wet mastic materials in AC. The findings are concluded below:

1. Dry mastic follows Burgers viscoelastic mechanical model and wet mastic follows modified Maxwell viscoelastic mechanical model.

2. Wet mastic material is less viscous compare to the dry mastic material. Also wet mastic material does not show retarded strain.

3. Surface of wet mastic materials are stiffer due to the erosion and ageing, and change in volume in mastic materials. Beneath the surface the wet mastic is softer compare to the dry mastic materials. More than 4000 nm depth wet mastic materials are affected by the conditioning effects. If indenter could penetrate more than 4000 nm, it is more likely to have softer mastic materials beneath these hard and stiffer surface materials.

4. The creep holding time of 200 sec is suitable for dry mastic materials but the wet mastic materials required longer creep holding time to penetrate more than 4000 nm and according to this study the holding time higher than 1200 sec would be appropriate.

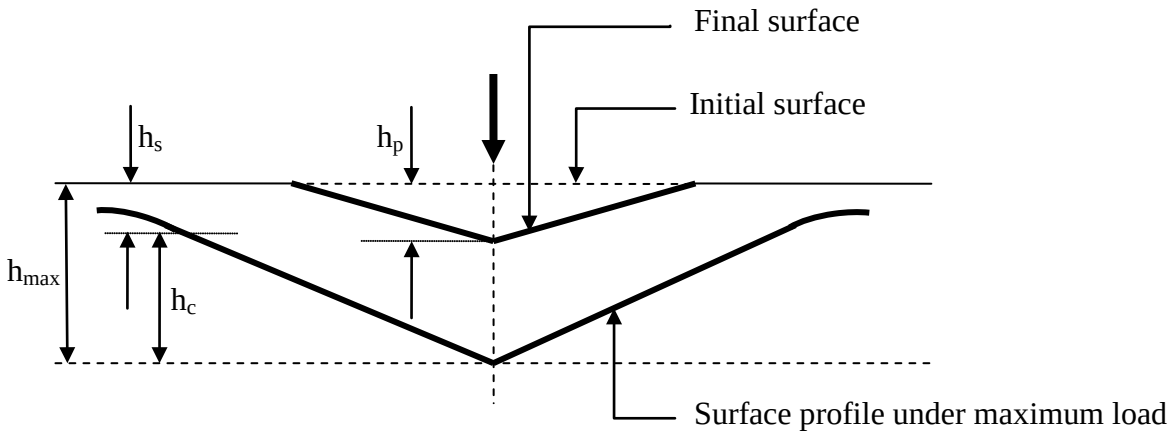

(a) Indentation process

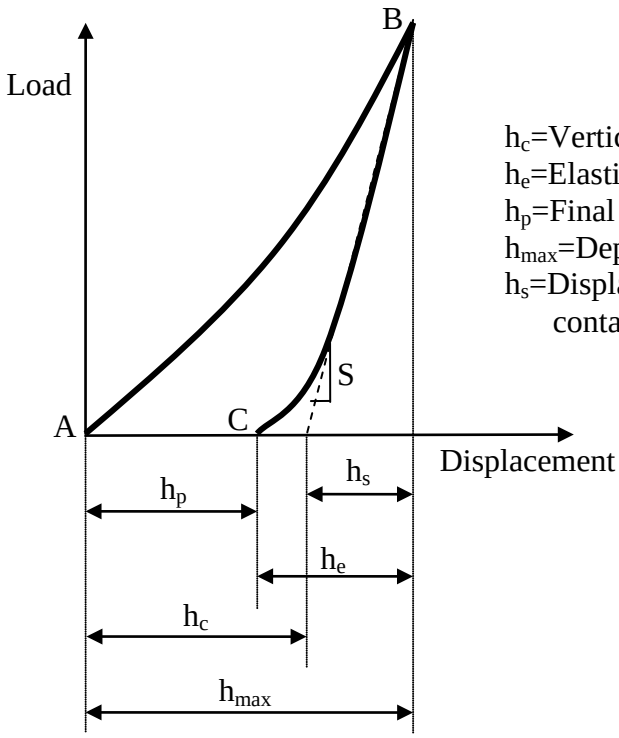

h_c=Vertical depth along which contact is made
h_e=Elastic depth recovery during unloading
h_p=Final depth after unloading
h_{max}=Depth at maximum load
h_s=Displacement of the surface at the perimeter of the contact

(b) Load-displacement curve

Figure 7.1 Schematic diagram of indentation test

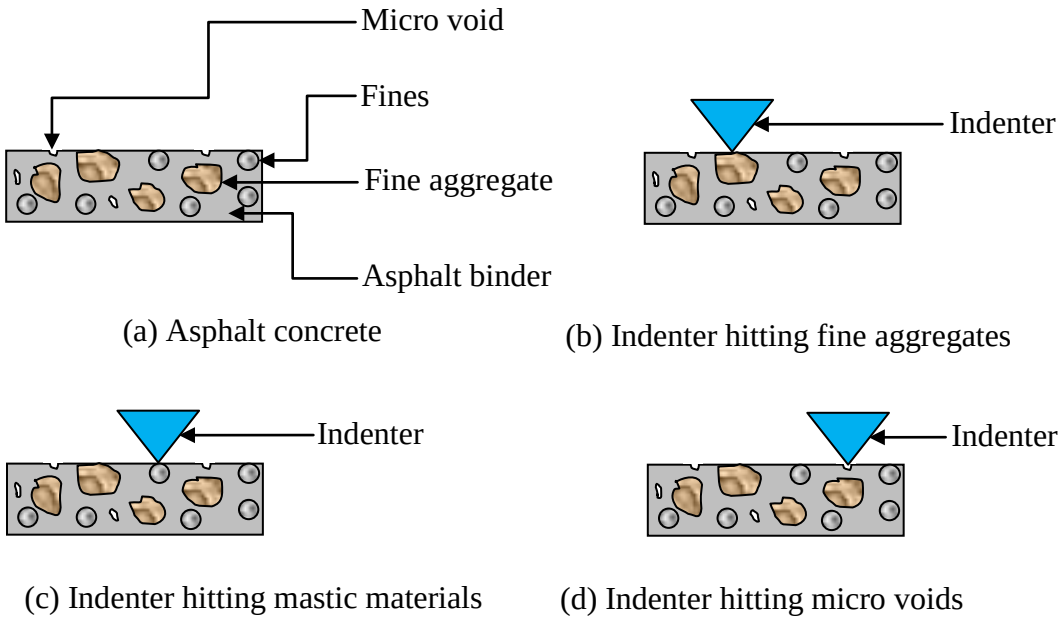

(a) Asphalt concrete

(b) Indenter hitting fine aggregates

(c) Indenter hitting mastic materials

(d) Indenter hitting micro voids

Figure 7.2 Schematic diagram of nanoindentation on mastic materials

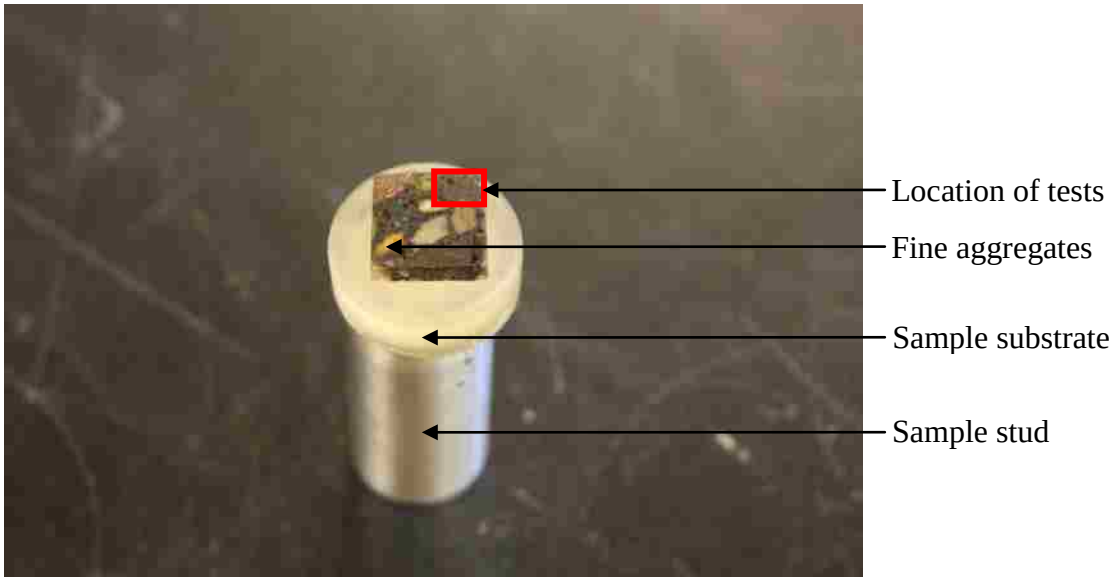

Figure 7.3 Laboratory sample for nanoindentation tests

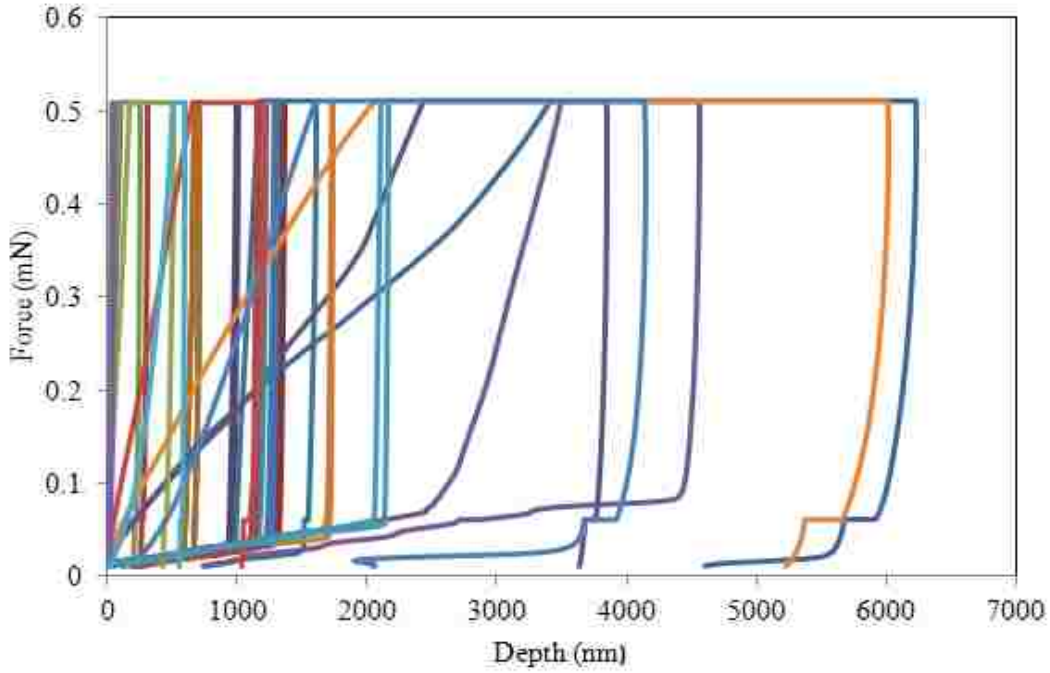

(a) Dry

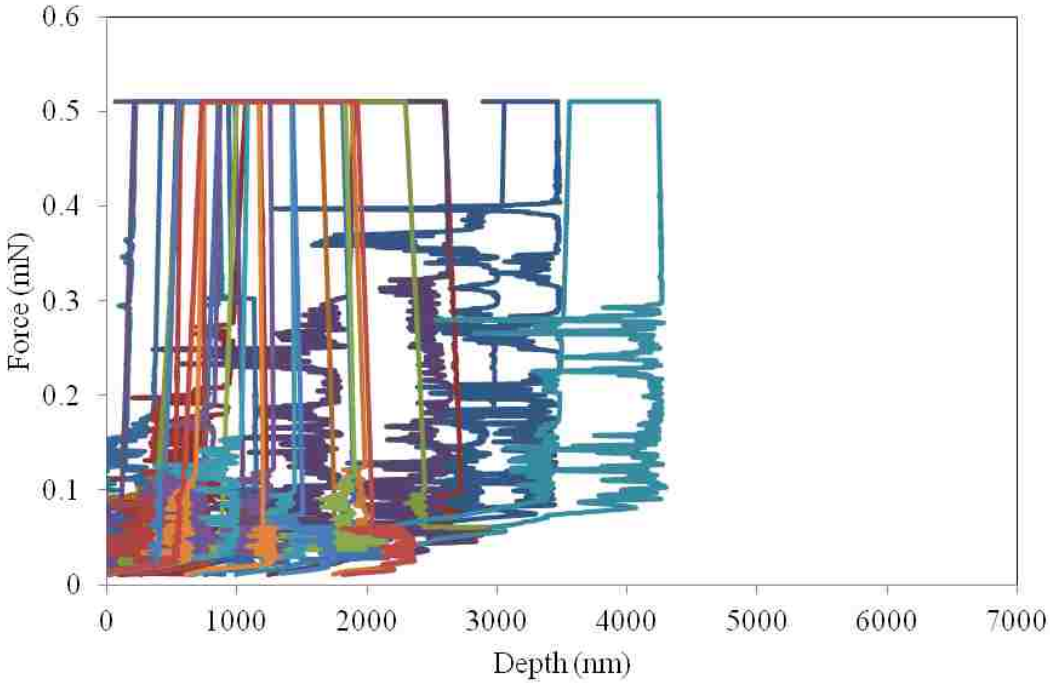

(b) Wet

Figure 7.4 Force-depth relationships derived from nanoindentation test

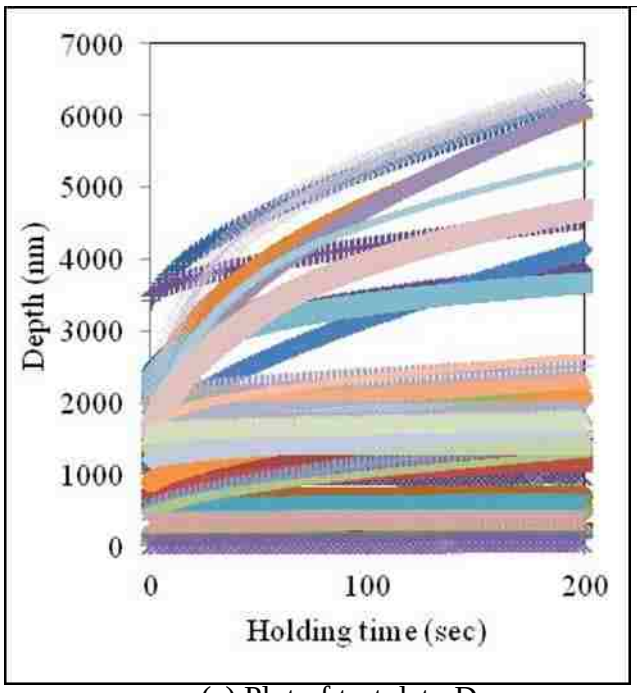

(a) Plot of test data-Dry

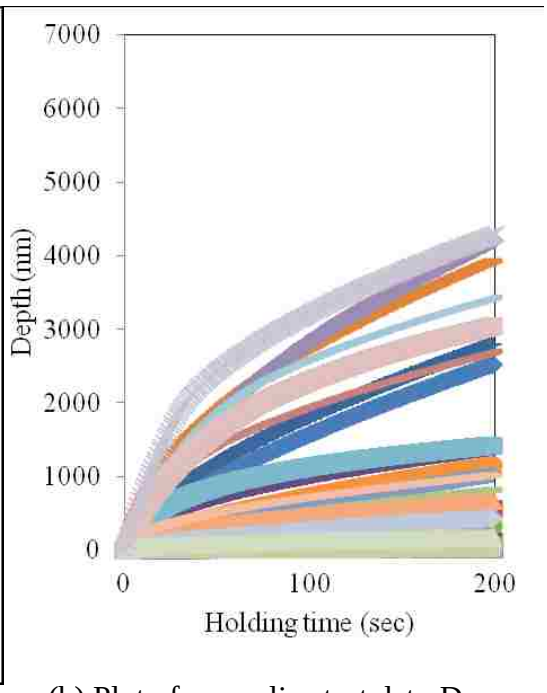

(b) Plot of normalize test data-Dry

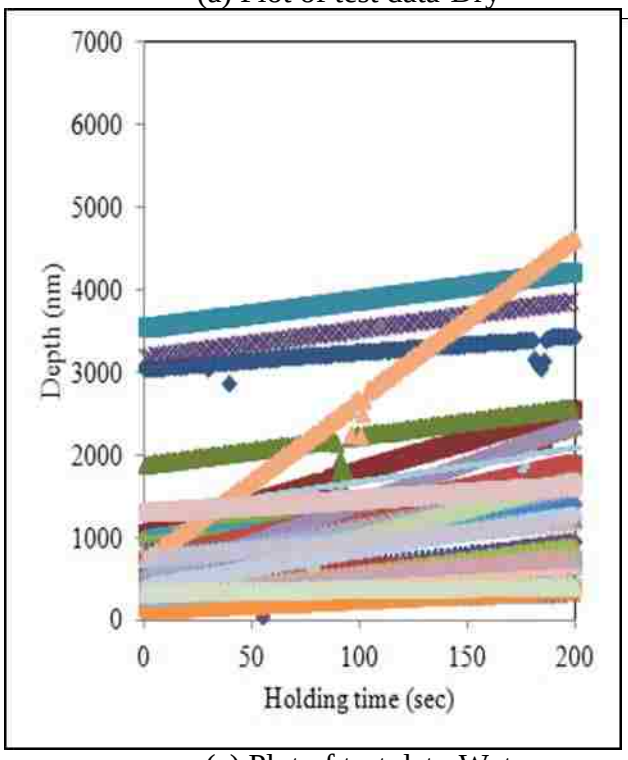

(c) Plot of test data-Wet

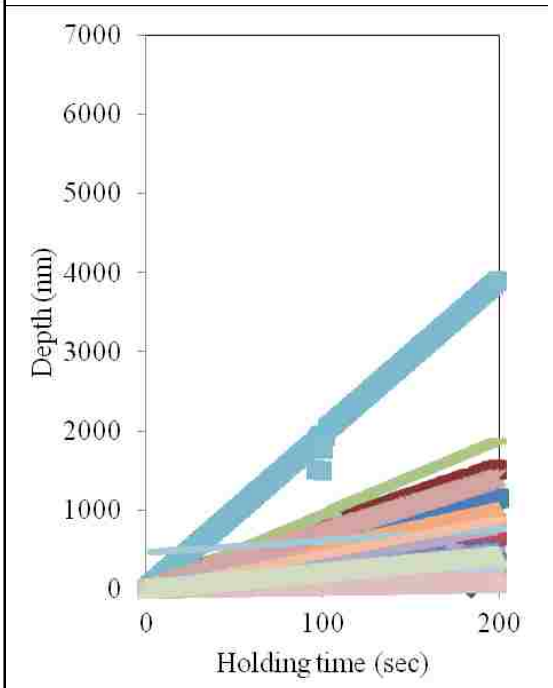

(d) Plot of normalized test data-Wet

Figure 7.5 Creep behaviors of mastic materials under nanoindentation tests

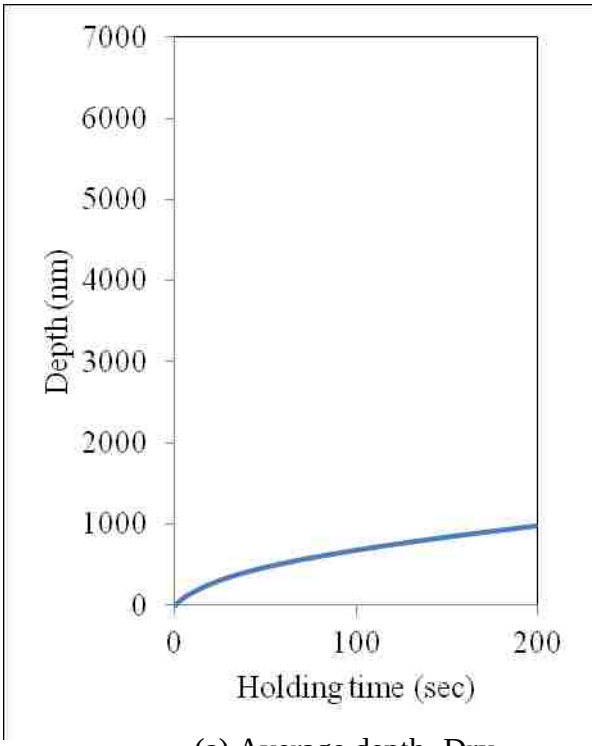

(a) Average depth -Dry

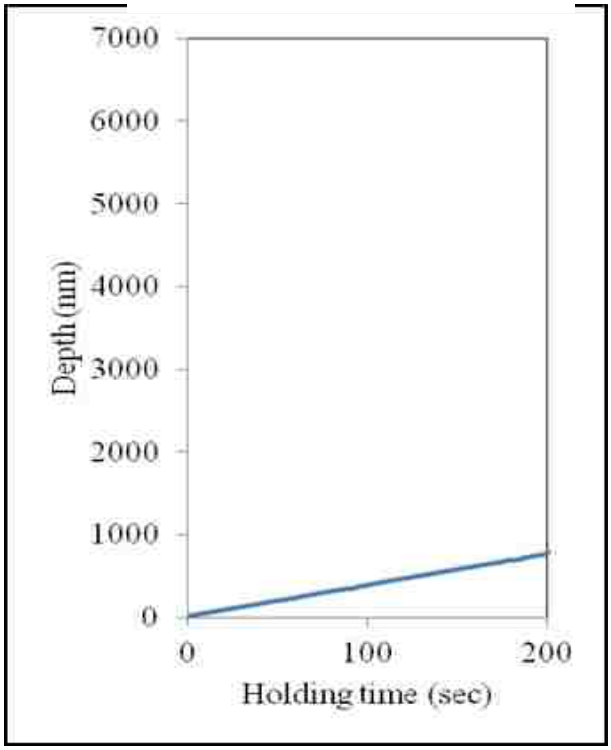

(b) Average depth -Wet

Figure 7.6 Averages of creep indentations

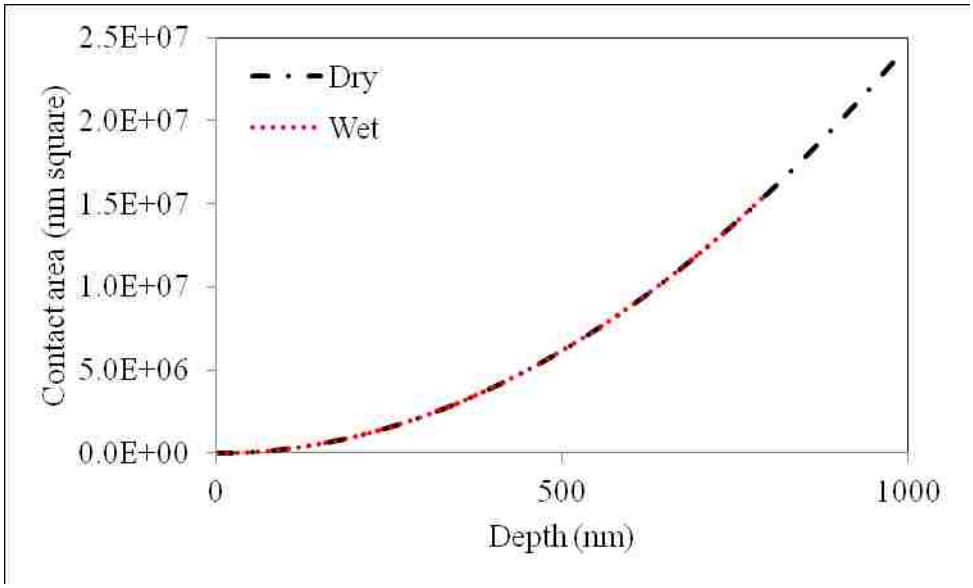

Figure 7.7 Measured contact area

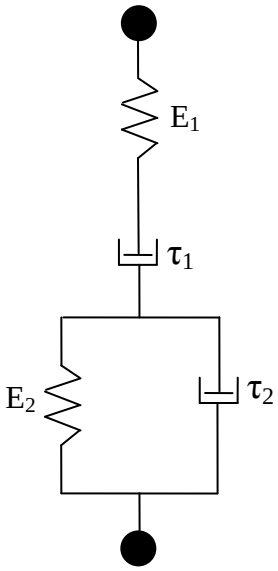

(a) Four elements Burgers spring and dashpot representation of viscoelastic material

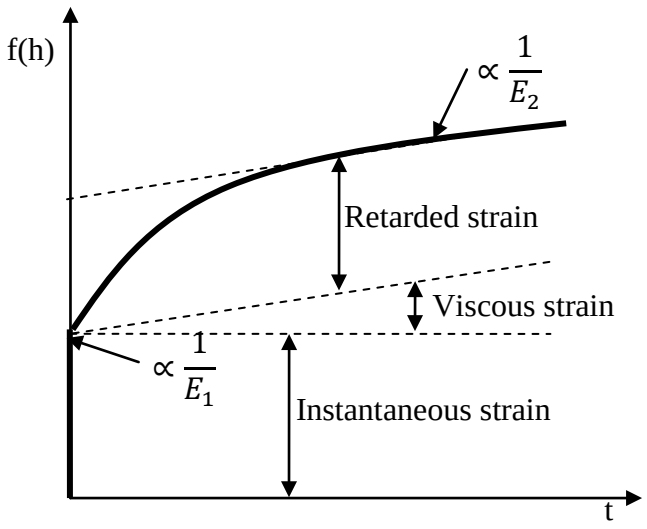

(b) Displacement response for steep increase in load for Burgers model

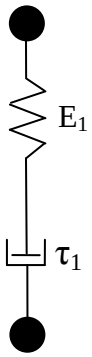

(c) Two elements Maxwell spring and dashpot representation of viscoelastic

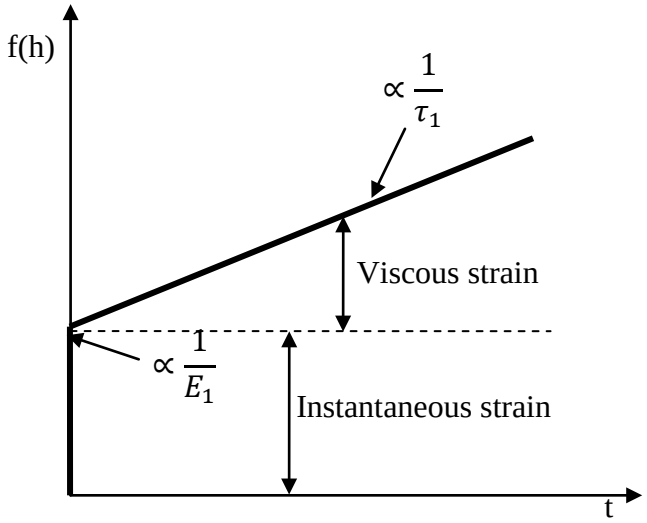

(d) Displacement response for steep increase in load for Maxwell model

Figure 7.8 Mechanical models of viscoelastic materials

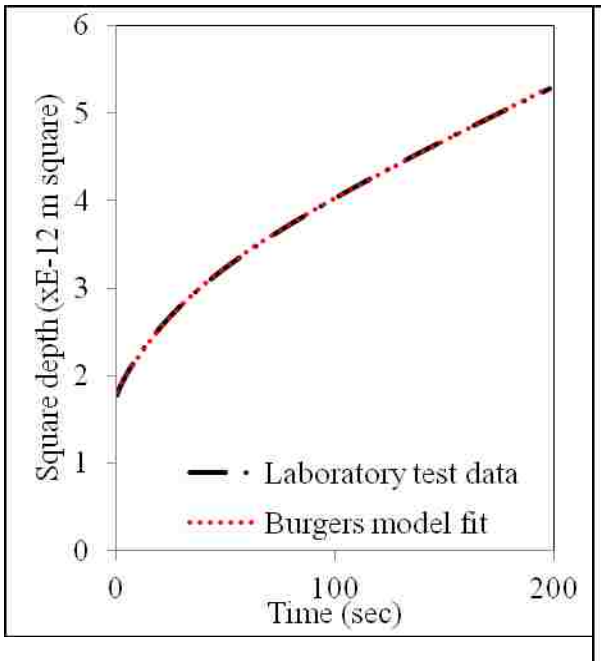

(a) Optimization of creep test data-Dry

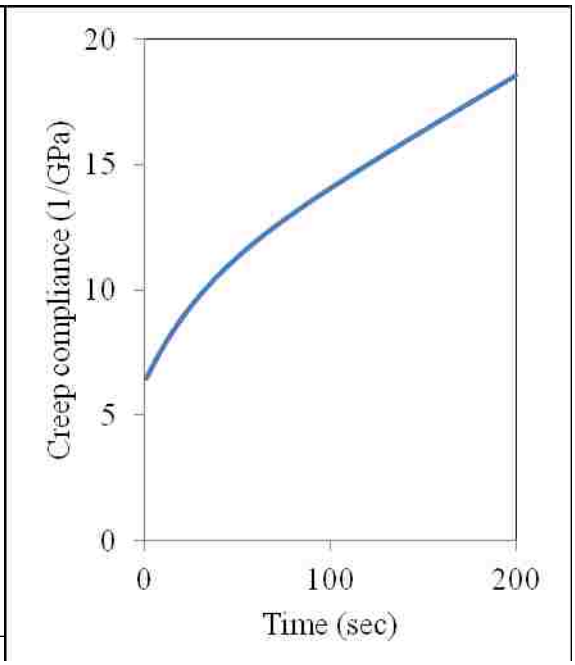

(b) Contact creep compliance-Dry

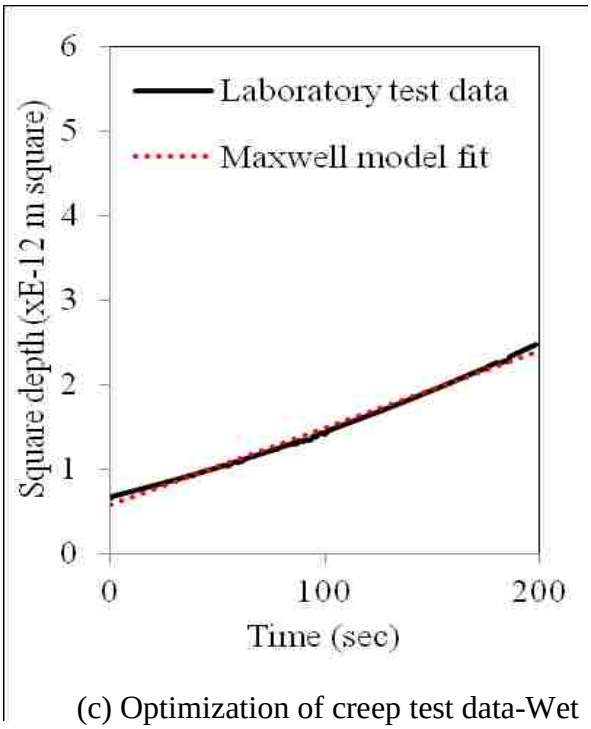

(c) Optimization of creep test data-Wet

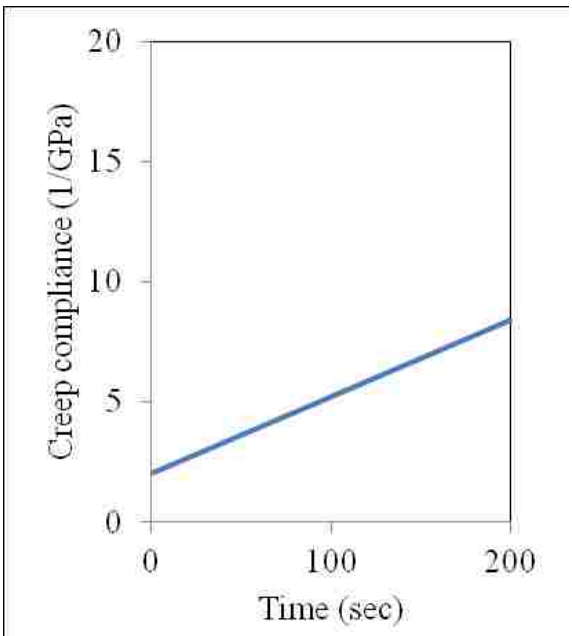

(d) Contact creep compliance-Wet

Figure 7.9 Mechanical models of mastic materials

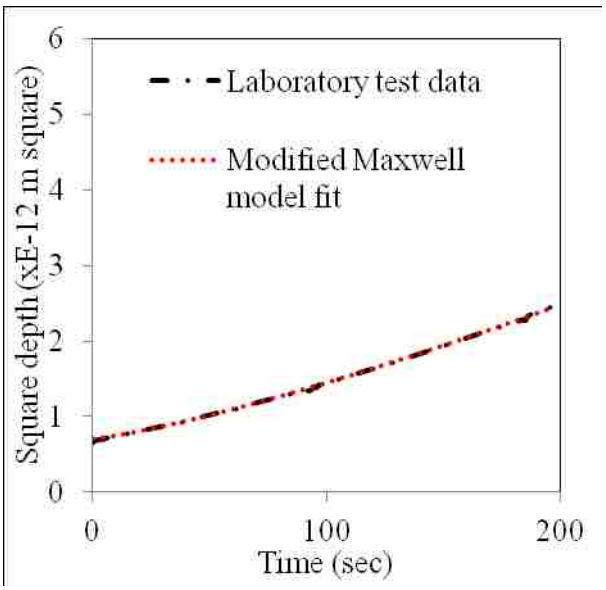

(a) Optimization of creep test data-Wet

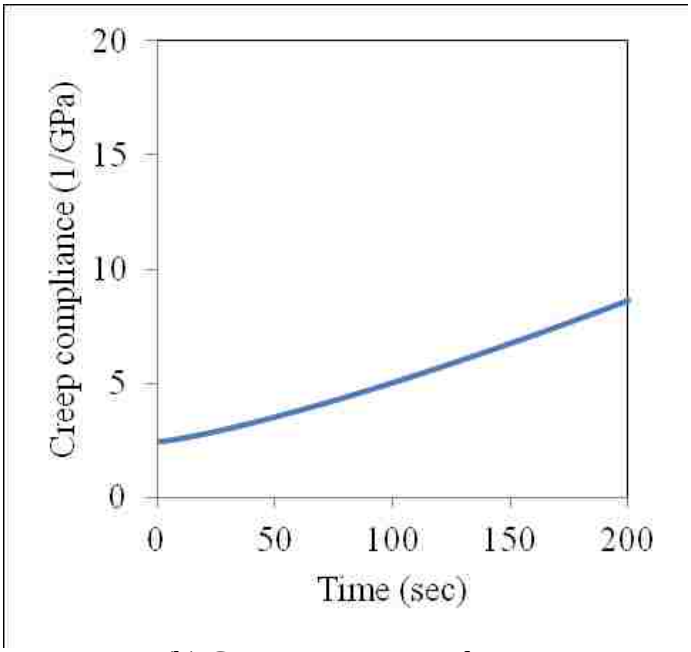

(b) Contact creep compliance-Wet

Figure 7.10 Modified mechanical model for wet matrix materials

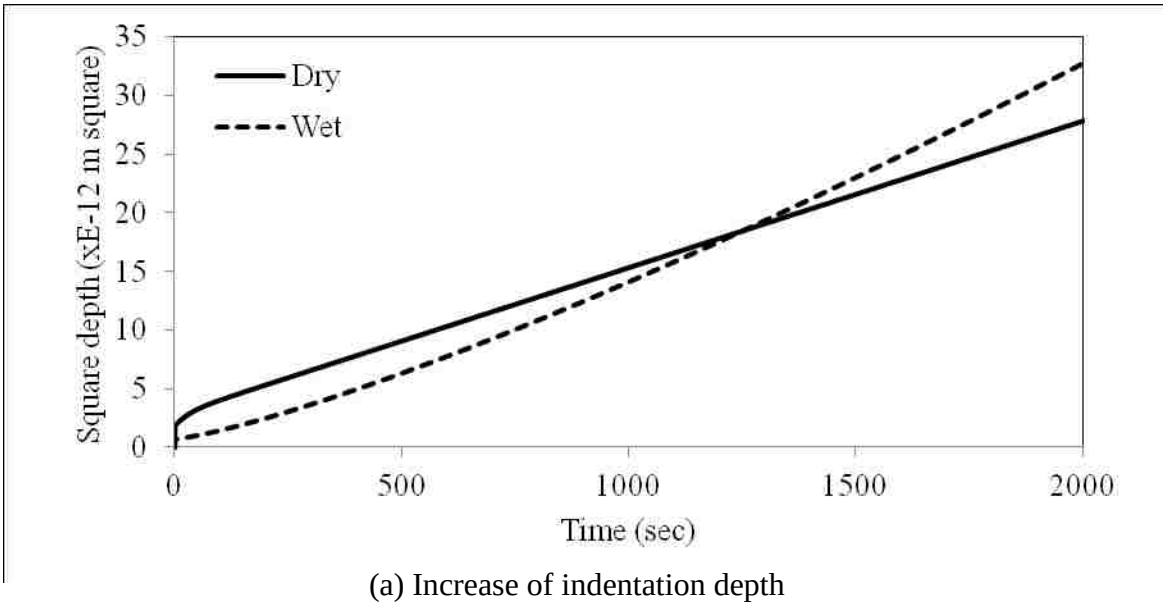

(a) Increase of indentation depth

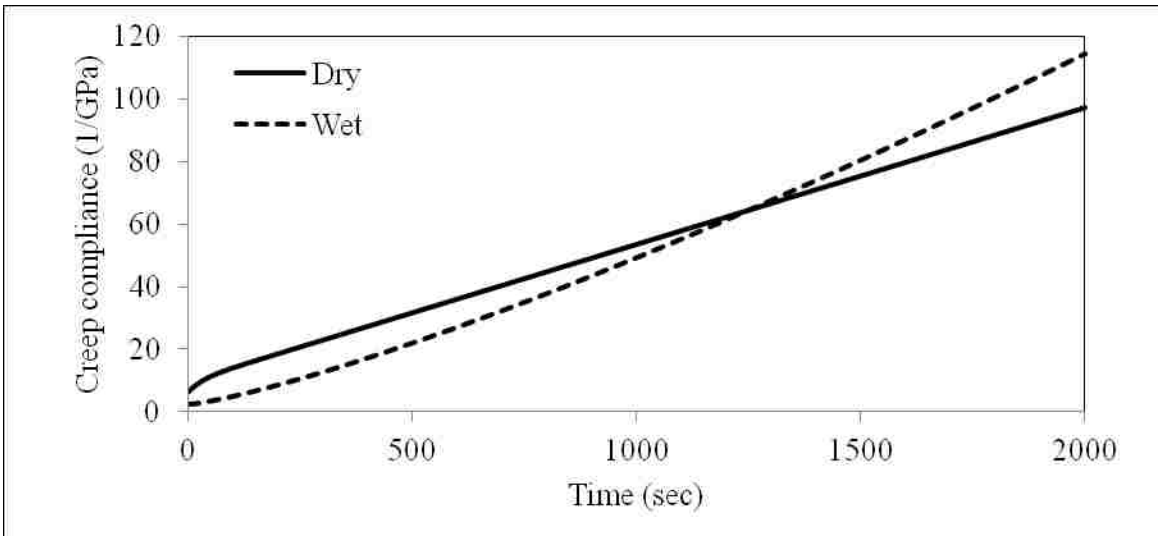

(b) Increase of creep compliance

Figure 7.11 Creep due to extended holding time

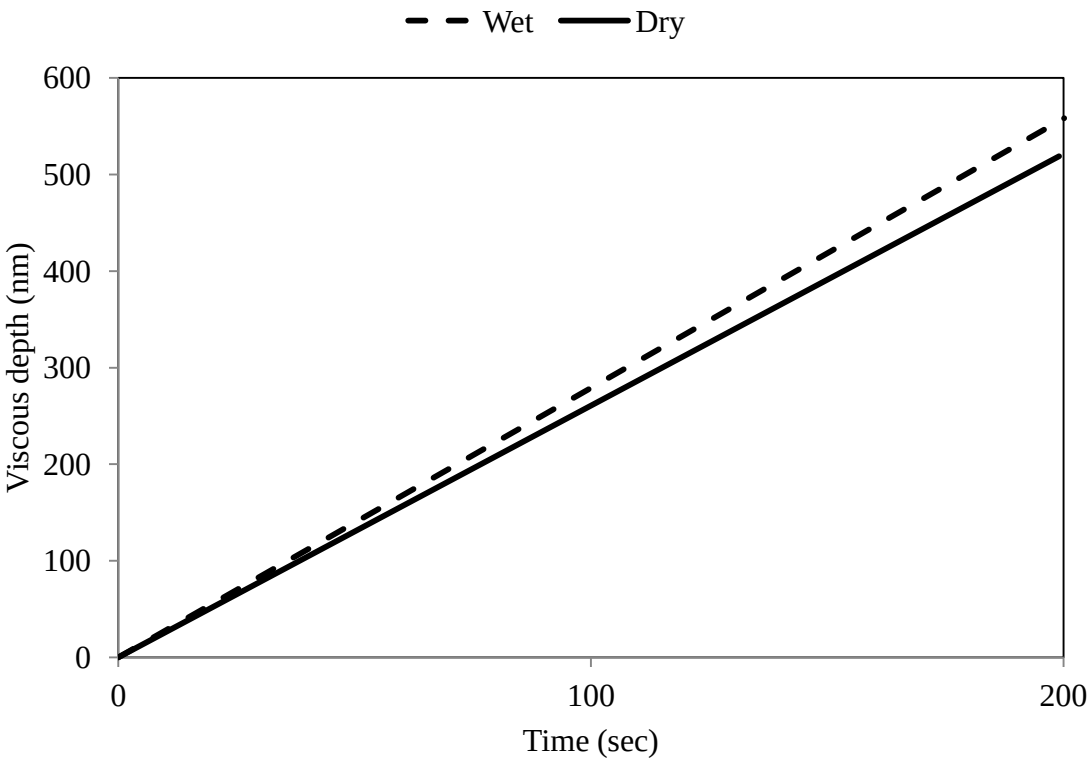

Figure 7.12 Measured viscous depth under dry and wet conditions

CHAPTER 8

CONCLUSIONS AND RECOMMENDATIONS

8.1 General

This chapter summarizes the findings of this work and recommends possible future studies. In this study, mastic and matrix materials are considered as elastic material for Finite Element Modeling (FEM). The geometry of the FEM model is assumed to be spherical to represent aggregate particle surrounded by mastic or matrix materials. Each of the mastic, matrix, and aggregate are considered as homogeneous materials at a macroscale in the FEM. Based on these assumptions, the following conclusions can be made.

8.2 Conclusions

8.2.1 Damage at Mastic-Aggregate Interface

The asphalt mastic-aggregate interface damage is quantified using FEM and traction separation law. Model parameters are determined from laboratory pull-off and strength testing of mastic materials. Model geometry is defined by a two dimensionally idealized aggregate particle surrounded by mastic materials to study adhesive damage. Moisture damage is quantified through contact stress, load magnitude to damage initiation, and de-bonding. The specific findings of this model are:

1. The contact stress due to applied deformation load is significantly higher in dry conditioned mastic-aggregate interface than in the wet conditioned mastic-

aggregate interface for all load magnitudes and patterns. Lower contact stresses are one of the reasons for higher mastic-aggregate interface damage that occurs in wet conditioned samples.

2. FEM model shows that damage initiates and progresses mostly on the upper half of the mastic-aggregate interfaces. In wet conditioned samples, surface damage initiates at applied deformation load of 0.00508 mm (0.002 in), whereas damage initiates at 0.508 mm (0.02 in) deformation load in dry conditioned samples. Dry mastic being stiffer than wet mastic, carries higher applied deformation and shows smaller mastic-aggregate interface damage. Softer wet mastic material is unable to carry smaller applied deformation and exhibits higher interface damage.

3. De-bonding, measured by separation between mastic and aggregate surfaces, in wet samples is significantly higher than that in dry sample. About 6.8% (% perimeter) interface de-bonding occurs in dry sample. On the other hand, about 49.1% interface de-bonding occurs in wet conditioned sample. De-bonding occurs due to lower contact stresses at the interface regions. De-bonding between mastic and aggregate is one of the main reasons for premature permanent failure of AC pavement under wet condition.

8.2.2 Damage in Matrix Materials

To study cohesive and adhesive damage, a hypothetical model aggregate is coated with the matrix material and the damage inside is identified. Damage at the vicinity of matrix and between matrix-aggregate interfaces is termed as cohesive damage. On the other hand, damage near the matrix-aggregate interface is defined as adhesive damage.

1. The outer exposed surface of the matrix shows significant cohesive damages. Cohesive damage is higher under wet conditioning than dry conditioning. Matrix materials near the interface region show significant adhesive damage. Adhesive damage is higher in wet conditioned sample than in dry conditioned sample.
2. Based on the damage contour plots, cohesive damage initiates at the top of matrix and then damage propagates towards the bottom of matrix and matrix-aggregate interface, where it initiates adhesive damage. Adhesive damage is significantly higher under the wet conditioning and for the rectangular pattern loading. Therefore, adhesive damage is critical for degradation of AC.
3. The interface region is weakest considering the whole domain of FEM model. The weakest interface is a reason for higher adhesive damage in AC. Therefore, the commonly used additives used to prevent moisture damage in the interface region, such as hydrated lime, are needed to be evaluated more to understand their roles at the interface between aggregate and matrix material.
4. Only cohesive damage is observed in thick matrix but both cohesive and adhesive damages are observed in thin matrix. Higher matrix thicknesses improve deformation carrying capacity and transfer less stresses to the interface, so no adhesive damage occurs near interface. Therefore, an optimum asphalt content should be determined that reduces adhesive damage at the interface by providing thicker matrix coating on the coarse aggregate. Also pre-coated aggregate might reduce adhesive damage and more studies are required in this area.
5. The worst damage scenario observed for thin matrix is when a deformation loads magnitude of 1.27 mm (0.057 in.) is applied. About 16.67% and 30.30% matrix

materials exhibit adhesive and cohesive damages, respectively, in wet conditioned samples. Matrix materials exhibit 13.75% adhesive damage and 15.85% cohesive damage in dry sample.

8.2.3 Damage at Matrix-Aggregate Interface

Instead of mastic and matrix materials, an attempt is made to evaluate the damage behavior of AC under dry and wet conditions. AC is defined by aggregate coated with matrix materials. FEM modeling is used to simulate behavior considering damage in the matrix materials and at the matrix-aggregate interface. The models considered are, one with dry matrix with dry aggregate, the second with wet matrix with dry aggregate, and the third with wet matrix with wet aggregate. Results are summarized below:

1. Damage occurs in the matrix materials due to shear stress reaching its capacity before normal stress reached its allowable limit. Slipping occurs at the end of the loading zone when vertical deformation is applied on the spherical shape FEM model. In addition, shear stress is smaller in wet matrix compared to that in dry matrix. Moisture causes higher damage in the wet matrix materials than in dry matrix. Moisture caused 62.80% more damage in the wet matrix compared to that in the dry matrix.
2. Damage occurs at the matrix-aggregate interface due to shear contact stress when it reaches its ultimate stress measured from lab testing. Interfacial de-bonding occurs at damaged locations. Interface de-bonding is higher in wet matrix than that in dry matrix. Moisture causes 17.45% more de-bonding in wet matrix at the interface regions compared to that in dry matrix.

3. Moist aggregate has least influence on damage at the matrix-aggregate interface. De-bonding region is same for dry aggregate compared to that in wet aggregate surrounded by wet matrix. The maximum shear contact stress is 1.51% higher in wet aggregate than that in dry aggregate.

8.2.4 Damage of Mastic Films

Direct pull-off and shear tests were conducted on the mastic film under three Relative Humidity (RH%) conditions also known as vapor conditioning. Mastic films are created in between two square shape aggregate plates. Laboratory RH% conditions are established by three aqueous solutions of salts. After conditioning the samples at different vapor concentrations, for tension test, one aggregate plate is fixed at the base while the other is pulled out; for shear test, one aggregate is fixed at the base and the other is forced to slide on the film. The conclusions of the study are:

1. Normal pull-off – Mastic films show flexible or ductile behavior at high RH% conditioning and brittle behavior at low RH% conditioning while normal pull-off strength is measured.
2. Shear pull-off – The flexible or ductile nature of mastic films at high RH% influences shear pull-off strength by showing higher shear pull-off strength.
3. Strength degradation – Increase in elasticity at high RH% conditioning causes a decrease in viscosity in mastic films. Decrease in viscosity of mastic materials might cause binding inefficiency between aggregates. Binding inefficiency causes damage in AC.

8.2.5 Nanoindentation on Mastic Materials

Nanoindentation tests are conducted to understand the contact creep behaviors and to develop viscoelastic mechanical models for dry and wet mastic materials in AC. The findings are summarized below:

1. Dry mastic follows the Burgers model and wet mastic follows the Maxwell or modified Maxwell viscoelastic mechanical model.
2. Wet mastic material is less viscous compared to the dry mastic material. Also wet mastic material does not show retarded strain.

8.3 Summary

Based on the above conclusions and considering the assumptions, the following summaries are outlined for this study:

1. Moisture-induced adhesive damage in AC can be defined as separation between asphalt binder and aggregates due to bonding inefficiency caused by reduction of viscosity resulting from moisture effects.
2. Moisture-induced cohesive damage in AC can be defined as softening of the asphalt binder due to microscopic bonding inefficiency caused by reduction of viscosity resulting from moisture effects.
3. Under mechanical loading and moisture-induced conditions, cohesive and adhesive damage initiates in AC by softening of mastic and matrix materials and separation between mastic or matrix aggregate interface, respectively. Cohesive damage progressed as adhesive damage at the mastic-aggregate or matrix-

aggregate interface and continues progressing as both cohesive and adhesive damage until complete failure occurs.

8.4 Recommendations for Future Studies

It is observed that viscous effect decreases in AC due to moisture-induced conditions. AC is a visco-elastic-plastic material and bonding inside the AC is due to the viscous effects of asphalt binders. Binding inefficiency will occur due to reductions in viscous effects caused by moisture. It is necessary to understand how the viscosity of the binder can be restored using admixtures. Engineers use hydrated lime to reduce moisture-induced damage in AC pavements. Hydrated lime increases viscosity in asphalt binder and restores bonding efficiency between binder and aggregates. In addition, hydrated lime hardens the AC resulting in a reduction of both adhesive and cohesive damage. More studies need to be done on asphalt binder using several admixtures to see the changes in viscous effects.

REFERENCES

AASHTO Standard T283 (2007). Resistance of compacted hot mix asphalt (HMA) to moisture induced damage, *Standard Specifications for Transportation Materials and Methods of Sampling and Testing, 27th Edition*, Capitol Street, WA.

ABAQUS 6.9.EF/CAE Documentations, (2009), Simulia Inc.

Abu Al-Rub, R. K., Darabi, M. K., Masad, E. a., and Little, D. N. (2011). "A Unified Continuum Damage Mechanics Model for Predicting the Mechanical Response of Asphalt Mixtures and Pavements." *International Journal of Roads and Airports*, 1(1), 68–84.

Abu Al-Rub, R. K., Masad, E. A., and Graham, M. A. (2010). *Physically Based Model for Predicting the Susceptibility of Asphalt Pavements to Moisture-Induced Damage*. College Station, Texas.

Abu Al-Rub, R. K., You, T., Masad, E. A., and Little, D. N. (2011). "Mesomechanical Modeling of the Thermo-Viscoelastic, Thermo-Viscoplastic, and Thermo-Viscodamage Response of Asphalt Concrete." *International Journal of Advances in Engineering Sciences and Applied Mathematics*, 3(1-4), 14–33.

Allen, R. G., Little, D. N., Bhasin, A., and Lytton, R. L. (2013). "Identification of the Composite Relaxation Modulus of Asphalt Binder Using AFM Nanoindentation." *Journal of Materials in Civil Engineering, ASCE*, 25(4), 530–539.

Allix, O., and Hild, F. (2002). *Continuum Damage Mechanics of Materials and Structures*. Elsevier, New York.

Arambula, E., Caro, S., and Masad, E. (2010). "Experimental Measurement and Numerical Simulation of Water Vapor Diffusion through Asphalt Pavement Materials." *Journal of Materials in Civil Engineering, ASCE*, 22(6), 588–598.

ASTM Designation No. D4541-09 Standard Test Method for Pull-Off Strength of Coatings Using Portable Adhesion Testers. (2009).

ASTM Designation No. E104-02 Standard Practice for Maintaining Constant Relative Humidity by Means of Aqueous Solutions. (2012).

Azari, H. (2010). *NCHRP Web-Only Document 166: Precision Estimates of AASHTO T283: Resistance of Compacted Hot Mix Asphalt (HMA) to Moisture-Induced Damage*.

Ban, H., Kim, Y.-R., and Pinto, I. (2011). "Integrated Experimental-Numerical Approach for Estimating Material-Specific Moisture Damage Characteristics of Binder-Aggregate Interface." *Transportation Research Record: Journal of the Transportation Research Board*, 2209, 9–17.

Bhasin, A., Masad, E., Little, D., and Lytton, R. (2006). "Limits on Adhesive Bond Energy for Improved Resistance of Hot-Mix Asphalt to Moisture Damage." *Transportation Research Record: Journal of the Transportation Research Board*, 1970, 3–13.

Birgisson, B., Roque, R., and Page, G. C. (2003). “Evaluation of Water Damage Using Hot Mix Asphalt Fracture Mechanics.” *Journal of the Association of Asphalt Paving Technologists*, 72, 424–462.

Birgisson, B., Reynaldo R., Gale C. P., and Jianlin W. (2007). “Development of New Moisture-Conditioning Procedure for Hot-Mix Asphalt.” *Transportation Research Record: Journal of Transportation Research Board*, 2001, 46-55.

Blab, R., and Harvey, J. T. (2002). "Modeling measured 3D tire contact stresses in a viscoelastic FE pavement model." *International Journal of Geomechanics*, 2(3), 271–290.

Bonora, N. (1999). "Identification and Measurement of Ductile Damage Parameters." *Journal of Strain Analysis*, 34(6), 463-477.

Caro, S., Masad, E., Bhasin, A., and Little, D. (2010a). “Coupled Micromechanical Model of Moisture-Induced Damage in Asphalt Mixtures.” *Journal of Materials in Civil Engineering, ASCE*, 22(4), 380–389.

Caro, S., Masad, E., Bhasin, A., and Little, D. (2010b). “Micromechanical Modeling of the Influence of Material Properties on Moisture-Induced Damage in Asphalt Mixtures.” *Construction and Building Materials*, Elsevier Ltd, 24, 1184–1192.

Caro, S., Masad, E., Bhasin, A., and Little, D. N. (2008). “Moisture Susceptability of Asphalt Mixtures, part 1: Mechanisms.” *International Journal of Pavement Engineering*, 9(2), 81–98.

Cheng, D., Little, D. N., Lytton, R. L., and Holtse, J. C. (2002). “Use of Surface Free Energy Properties of Asphalt–Aggregate System to Predict Damage Potential.” *Presented at Annual Meeting of the Association of Asphalt Paving Technologists*, March.

Cheng, D., Little, D. N., Lytton, R. L., and Holste, J. C. (2003). “Moisture Damage Evaluation of Asphalt Mixtures by Considering Both Moisture Diffusion and Repeated-Load Conditions.” *Transportation Research Record: Journal of the Transportation Research Board*, 1832, 42–49.

Copeland, A. R. (2007). “Influenct of Moisture on Bond Strength of Asphalt-Aggregate Systems.” Vanderbilt University.

Crank, J. (1956). *The Mathematics of Diffusion*, Oxford at the Clarendon Press.

Dai, Q., and You, Z. (2007). “Prediction of Creep Stiffness of Asphalt Mixture with Micromechanical Finite-Element and Discrete-Element Models.” *Journal of Engineering Mechanics, ASCE*, 133(2), 163–173.

Degrieck, J., and Van Paepegem, W. (2001). “Fatigue Damage Modeling of Fibre-Reinforced Composite Materials: Review.” *Applied Mechanics Reviews*, 54(4), 279.

Desai, C. S. (2007). "Unified DSC Constitutive Model for Pavement Materials with Numerical Implementation." *International Journal of Geomechanics*, ASCE, 7(1), 83-101.

Desai, C. S., (2001). *Mechanics of Materials and Interfaces: The Disturb State Concept*. CRC Press, Boca Raton.

Fakhari Tehrani, F., Absi, J., Allou, F., and Petit, C. (2013). "Heterogeneous Numerical Modeling of Asphalt Concrete through use of a Biphasic Approach: Porous matrix/inclusions." *Computational Materials Science*, Elsevier B.V., 69, 186–196.

Fischer-Cripps, A. C. (2004). "A Simple Phenomenological Approach to Nanoindentation Creep." *Materials Science and Engineering: A*, 385(1-2), 74–82.

Fromm, H. J. (1974). "The Mechanisms of Asphalt Stripping from Aggregate Surfaces." *Journal of the Association of Asphalt Paving Technologists*, 43, 191–223.

Goodall, R., and Clyne, T. W. (2006). "A Critical Appraisal of the Extraction of Creep Parameters from Nanoindentation Data Obtained at Room Temperature." *Acta Materialia*, 54(20), 5489–5499.

Graf, P. E. (1986). "Factors Affecting Moisture Susceptibility of Asphalt Concrete Mixes." *Journal of the Association of Asphalt Paving Technologists*, 55, 175–212.

Gubler, R., Partl, M. N., Canestrari, F., and Grilli, A. (2005). "Influence of Water and Temperature on Mechanical Properties of Selected Asphalt Pavements." *Materials and Structures*, 38(279), 523–532.

Gupta, S., Carrillo, F., Balooch, M., Pruitt, L., and Puttlitz, C. (2011). "Simulated Soft Tissue Nanoindentation: A Finite Element Study." *Journal of Materials Research*, 20(08), 1979–1994.

Hao P., and Hachiya Y. (2003). "Moisture Susceptibility of Asphalt Mixture and Effectiveness of Anti-Stripping Additive." *Journal of Materials, Concrete Structure and Pavement*, 61(746), 265-273.

Hodzic, A., Kalyanasundaram, S., Kim, J. K., Lowe, A. E., and Stachurski, Z. H. (2001). "Application of Nano-Indentation , Nano-Scratch and Single Fibre Tests in Investigation of Interphases in Composite Materials." *Micron*, 32, 765–775.

Hossain, M. I., and Tarefder, R. A. (2013). "Effects of Moisture in Asphalt Concrete." *Basic Research Journal of Engineering Innovation*, 1(1), 16–25.

Hossain, M. I., and Tarefder, R. A. (2013a). "Determining Damage Effects on Asphalt Concrete Composites." *International Journal of Civil and Structural Engineering*, 3(4), 692–703.

Hossain, M. I., and Tarefder, R. A. (2013b). "Quantifying Moisture Damage at Mastic–Aggregate Interface." *International Journal of Pavement Engineering*, 1–16.

Hossain, M., and Tarefder, R. (2013). "Numerical Computation of Coupled Adhesive and Cohesive Damages in Asphalt Concrete." *International Journal of Pavement Research and Technology*, 6(4), 261–268.

Huang, Y. H. (2004). *Pavement Analysis and Design*. Pearson Prentice Hall, Upper Saddle River, NJ.

Inman, D. J., Farrar, C. R., Junior, V. L., and Junior, V. S. (2005). *Damage Prognosis for Aerospace, Civil and Mechanical Systems*. John Wiley & Sons, Ltd.

Kachanov, L. M. (1986). *Introduction to Continuum Damage Mechanics*. Kluwer Academic Publisher, Dordrecht.

Kasthurirangan Gopalakrishnan, Broj Birgisson, Peter Taylor, N. O. A.-O. (Ed.). (2011). *Nano-technology in Civil Infrastructure: A Paradigm Shift*. Springer, Berlin.

Khalid, H. A., and Monney, O. K. (2009). "Moisture Damage Potential of Cold Asphalt." *International Journal of Pavement Engineering*, 10(5), 311–318.

Kim, Y., Allen, D. H., and Little, D. N. (2005). "Damage-Induced Modeling of Asphalt Mixtures through Computational Micromechanics and Cohesive Zone Fracture." *Journal of Materials in Civil Engineering, ASCE*, 17(5), 477–484.

Kim, Y., and Little, D. N. (2004). "Linear Viscoelastic Analysis of Asphalt Mastics." *Journal of Materials in Civil Engineering, ASCE*, 16(2), 122–132.

Kim, Y., Little, D. N., and Lytton, R. L. (2004). "Effect of Moisture Damage on Material Properties and Fatigue Resistance of Asphalt Mixtures." *Transportation Research Record: Journal of the Transportation Research Board*, 1891, 48–54.

Kim, Y.-R., Souza, F. V., and Teixeira, J. E. S. L. (2012). "A Two-Way Coupled Multiscale Model for Predicting Damage-Associated Performance of Asphaltic Roadways." *Computational Mechanics*.

Krajcinovic, D. (1996). *Damage Mechanics*, Elsevier.

Krajcinovic, D. (2002). *Essential Damage Mechanics-Bridging the Scales, Continuum Damage Mechanics of Materials and Structures*, Elsevier.

Kringos, N., and Scarpas, A. (2005). “Raveling of Asphalt Mixes due to Water Damage: Computational Identification and Controlling Parameters.” *Transportation Research Record: Journal of Transportation Research Board*, Vol. 1929, 79-87.

Kringos, N., and Scarpas, A., (2008). "Physical and Mechanical Moisture Susceptibility of Asphalt Mixtures." *International Journal of Solids and Structures*, 45, 2671–2685.

Kringos, N., Scarpas A., Kasbergen C., and Salvadurai, P. (2007). “Three Dimensional Elasto-Visco-Plastic Finite Element Model for Combined Physical-Mechanical Moisture Induced Damage in Asphaltic Mixes.” *Journal of Association of Asphalt Paving Technologies*, Vol. 76, 495-524.

Kringos, N., Scarpas, A., and Bondt, A. de. (2008a). “Determination of Moisture Susceptibility of Mastic-Stone Bond Strength and Comparison to Thermodynamical Properties.” *Journal of the Association of Asphalt Paving Technologists*, 77, 435–478.

Kringos, N., Scarpas, A., Copeland, A., and Youtcheff, J. (2008b). “Modeling of Combined Physical-Mechanical Moisture Induced Damage in Asphaltic Mixes, Part 2: Moisture Susceptibility Parameters.” *International Journal of Pavement Engineering*, 9(2), 129–151.

Kringos, N., Scarpas, T., Kasbergen, C., and Selvadurai, P. (2008c). "Modelling of Combined Physical–Mechanical Moisture-Induced Damage in Asphaltic Mixes, Part 1: Governing Processes and Formulations." *International Journal of Pavement Engineering*, 9(2), 115–128.

Kurapati, S. N. V. R. K. (2008). "Elastic-Plastic Indentation Deformation in Homogeneous and Layerd Materials: Finite Element Analysis." University of Kentucky.

Kutay, M. E., Aydilek, A. H., Masad, E., and Harman, T. (2007). "Computational and Experimental Evaluation of Hydraulic Conductivity Anisotropy in Hot-Mix Asphalt." *International Journal of Pavement Engineering*, 8(1), 29–43.

Lemaitre, J. (1996). *A Course on Damage Mechanics*. Springer.

Lemaitre, J., and Desmorat, R. (2005). *Engineering Damage Mechanics: Ductile, Creep, Fatigue and Brittle Failures*. Springer, New York.

Logan, D. L. (2007). *A First Course in the Finite Element Method*, Fourth Edition, Nelson, New Delhi, India.

Lu, H., Wang, B., Ma, J., Huang, G., and Viswanathan, H. (2003). "Measurement of Creep Compliance of Solid Polymers by Nanoindentation." *Mechanics of Time-Dependent Materials*, 7(3/4), 189–207.

Lu, L., and Likos, W. J. (2004). *Unsaturated Soil Mechanics*. John Wiley & Sons, Inc., New Jersey.

Lucas, L. J., Black, T. M., and Jones, D. P. (2007). "Use of Cohesive Elements in Fatigue Analysis." *2007 ASME Pressure Vessels and Piping Division Conference*, ASME, San Antonio, Texas, 13–25.

Masad, E., Somadevan, N., Bahia, H., and Kose, S., (2001). "Modeling and Experimental Measurements of Strain Distribution in Asphalt Mixes." *Journal of Transportation Engineering, ASCE*, 127(6), 477-485.

Minster, J., and Micka, M. (2012). "Numerical Simulation of an Indentation Process for Defining the Viscoelastic Characteristics of Time-Dependent Materials." *Journal of Materials Science and Engineering*, 2(1), 81–89.

Mohamed, E. H. H. (1993). "Debonding Location in Asphalt Concrete Associated with Moisture Damage." *Journal of Materials in Civil Engineering, ASCE*, 5(4), 497–509.

Moraes, R., Velasquez, R., and Bahia, H. U. (2011). "Measuring the Effect of Moisture on Asphalt-Aggregate Bond with the Bitumen Bond Strength Test." *Transportation Research Record: Journal of the Transportation Research Board*, 2209, 70–81.

Nadkarni, A. A., Kaloush, K. E., Zeiada, W. A., and Biligiri, K. P. (2009). "Using Dynamic Modulus Test to Evaluate Moisture Susceptibility of Asphalt Mixtures." *Transportation Research Record: Journal of the Transportation Research Board*, 2127, 29–35.

Oliver, W. C., and Pharr, G. M. (1992). “An Improved Technique for Determining Hardness and Elastic Modulus Using Load and Displacement Sensing Indentation Experiments.” *Journal of Materials Research*, 7(6), 1562–1583.

Ossa, E. A., Deshpande, V. S., and Cebon, D. (2005). “Spherical indentation behaviour of bitumen.” *Acta Materialia*, 53(11), 3103–3113.

Park, S. W., Kim, Y. R., and Schapery, R. A. (1996). “A Viscoelastic Continuum Damage Model and its Application to Uniaxial Behavior of Asphalt Concrete.” *Mechanics of Materials*, 24(4), 241–255.

Roque, R., Koh, C., Chen, Y., Sun, X., and Lopp, G. (2009). *Introduction of Fracture Resistance to the Design and Evaluation of Open Graded Friction Courses in Florida*. Tallahassee, FL.

Saanouni, K. (2001). *Numerical Modeling in Damage Mechanics*. Hermes Science Publication, Paris.

Saad, B., Mitri, H., and Poorooshasb, H. (2005). "Three-Dimensional Dynamic Analysis of Flexible Conventional Pavement Foundation." *Journal of Transportation Engineering*, 131(6), 460–469.

Sadd, M. H., Dai, Q. L., Parameswaran, V., and Shukla, A., (2003). “Simulation of Asphalt Materials using Finite Element Micromechanical Model with Damage Mechanics.” *Transportation Research Record: Journal of Transportation Research Board*, Vol. 1832, 86-95.

Santi, P. M., Holschen, J. E., and Stephenson, R. W. (2000). "Improving Elastic Modulus Measurements for Rock Based on Geology." *Enviornmental and Engineering Geoscience*, 6(4), 333–346.

Sarihan, V. (1994). "Energy Based Methodology for Damage and Life Prediction of Solder Joints Under Thermal Cycling." *IEEE Transactions on Components, Packaging, and Manufacturing Technology: Part B*, 17(4), 626–631.

Scarpas, A., Blaauwendraad, J., AlKhoury, R., and vanGurp, C., (1997). "Experimental Calibration of a Viscoplastic-Fracturing Computational Model" *8th International Conference on Computational Methods and Experimental Measurements*, Greece.

Schilde, C., and Kwade, A. (2012). "Measurement of the Micromechanical Properties of Nanostructured Aggregates via Nanoindentation." *Journal of Materials Research*, 27(04), 672–684.

Schuh, C. A. (2006). "Nanoindentation Studies of Materials." *Materialstoday*, 9(5), 32–40.

Shah, B. D. (2003). "Evaluation of Moisture Damage within Asphalt Concrete Mixes." Texas A&M University.

Shashidhar, N., and Shenoy, A. (2002). "On Using Micromechanical Models to Describe Dynamic Mechanical Behavior of Asphalt Mastics." *Mechanics of Materials*, 34(10), 657–669.

Solaimanian, M., Tahmoressi, J. M., and Tandon, V. (2003). "Test Method to Predict Moisture Sensitivity of Hot-Mix Asphalt Pavements." *Moisture Sensitivity of Asphalt Pavement: A National Seminar*, Transportation Research Board of the National Academics.

Spinel, S. C. (2009). "A Coupled Micromechanical Model of Moisture-Induced Damage in Asphalt Mixture: Formulation and Applications." Texas A&M University.

Suaris, W., Ouyang, C., and Fernando, V. M. (1990). "Damage Model for Cyclic Loading of Concrete." *Journal of Engineering Mechanics, ASCE*, 116(5), 1020–1035.

Talreja, R. (1994). "Damage Characterization by Internal Variables." *Damage Mechanics of Composite Materials*, 53-78.

Tarefder, R. A., and Faisal, H. (2013a). "Effects of Dwell Time and Loading Rate on the Nanoindentation Behavior of Asphaltic Materials." *Journal of Nanomechanics and Micromechanics, ASCE*, 3(2), 17–23.

Tarefder, R. A., and Faisal, H. M. (2013b). "Modeling Nanoindentation Creep Behavior of Asphalt Binder." *Advances in Civil Engineering Materials, ASTM*, 2(1), 418–440.

Tarefder, R. A., Kias, E. M., and Stormont, J. C. (2009). "Evaluating Parameters for Characterization of Cracking in Asphalt Concrete." *Journal of Testing and Evaluation, ASTM*, 37(6), 1–11.

Tarefder, R. A., Yousefi, S. S., and Kias, E. (2010). “Factors that Affect the Rheological Properties of Asphalt Matrix.” *Pavement and Materials: Testing and Modeling in Multiple Length Scales, ASCE*, Special Pu(1), 121–133.

Tarefder, R. A. and Arifuzzaman, M. (2011). "A Study of Moisture Damage in Plastomeric Polymer Modified Asphalt Binder Using Functionalized AFM Tips." *Journal of Systemics*, Cybernetics and Informatics, 9(5), 1-12.

Tarefder, R. A., and Arifuzzaman, M. (2010). "Nanoscale Evaluation of Moisture Damage in Polymer Modified Asphalts." *Journal of Materials in Civil Engineering, ASCE*, Vol. 22(7), 714-725.

Tarefder, R. A., Zaman, A. M., and Uddin, W. (2010). “Determining Hardness and Elastic Modulus of Asphalt by Nanoindentation.” *International Journal of Geomechanics, ASCE*, 10(3), 106–116.

Tarefder, R. A. and Yousefi, S. S. (2012)."Laboratory Evaluation of Moisture Damage in Asphalt." *Canadian Journal of Civil Engineering*, 39(1), 104-115.

Tarefder, R., and Faisal, H. (2013). “Nanoindenthation Characterization of Asphalt Concrete Aging.” *Journal of Nanomechanics and Micromechanics, ASCE*.

Tong, Y., Luo, R., and Lytton, R. L. (2013). “Modeling Water Vapor Diffusion in Pavement and Its Influence on Fatigue Crack Growth of Fine Aggregate Mixture.” *Transportation Research Record: Journal of the Transportation Research Board*.

Ugural, A.C. (1991). *Mechanics of Materials*, McGraw-Hill, Inc.

Vallejo, M. J., and Tarefder, R. A. (2011). “Predicting Failure Behavior of Polymeric Composites Using a Unified Constitutive Model.” *Journal of Mechanics*, 27(03), 379–388.

Voyiadjis, G. Z., and Allen, D. H. (1996). *Damage and Interfacial Debonding in Composites*. Elsevier, New York.

Voyiadjis, G. Z., Ju, J.-W., and Chaboche, J.-L. (1998). *Damage Mechanics in Engineering Materials*. Elsevier, Oxford.

Wang, L. (2011). *Mechanics of Asphalt Microstructure and Micromechanics*. McGrawHill.

Wasiuddin, N. M., Saltibus, N. E., and Mohammad, L. N. (2011). “Novel Moisture-Conditioning Method for Adhesive Failure of Hot- and Warm-Mix Asphalt Binders.” *Transportation Research Record: Journal of the Transportation Research Board*, 2208, 108–117.

West, R. C., Zhang, J., and Cooley, A. (2004). *Evaluation of the Asphalt Pavement Analyzer for Moisture Sensitivity Testing*.

Wu, Z., Baker, T. A., Ovaert, T. C., and Niebur, G. L. (2012). “The Effect of Holding Time on Nanoindentation MEasurements of Creep Bone.” *Journal of Biomechanics*, 44(6), 1066–1072.

Y. Richard Kim. (2009). *Modeling of Asphalt Concrete*. (McGrawHill, ed.), ASCE Press.

Y. Richard Kim, Baek, C., Underwood, B. S., Subramanian, V., Guddati, M. N., and Lee, K. (2008). “Application of Viscoelastic Continuum Damage Model Based Finite Element Analysis to Predict the Fatigue Performance of Asphalt Pavements.” *KSCE Journal of Civil Engineering*, 12(2), 109–120.

You, T., Abu Al-Rub, R. K., Darabi, M. K., Masad, E. A., and Little, D. N. (2012). “Three-Dimensional Microstructural Modeling of Asphalt Concrete Using a Unified Viscoelastic–Viscoplastic–Viscodamage Model.” *Construction and Building Materials*, Elsevier Ltd, 28, 531–548.

Zaghloul, S. M., and White, T. D. (1993). "Use of Three-Dimensional Dynamic Finite Element Program for Analysis of Flexible Pavement." *Transportation Research Record*, 1388, 60–69.

Zhu, X., Huang, Z., Yang, Z., and Chen, W. (2010). “Micromechanics-Based Analysis for Predicting Asphalt Concrete Modulus.” *Journal of Zhejiang University SCIENCE A*, 11(6), 415–424.

APPENDIX A

International Journal of Pavement Engineering
Publication details, including instructions for authors and subscription information:
http://www.tandfonline.com/loi/gpav20

Quantifying moisture damage at mastic-aggregate interface

Mohammad I. Hossain [a] & Rafiqul A. Tarefder [a]
[a] Department of Civil Engineering , University of New Mexico , 210 University Blvd NE, Albuquerque , NM , 87106 , USA
Published online: 27 Jun 2013.

To cite this article: Mohammad I. Hossain & Rafiqul A. Tarefder (2013): Quantifying moisture damage at mastic-aggregate interface, International Journal of Pavement Engineering, DOI:10.1080/10298436.2013.812212

To link to this article: http://dx.doi.org/10.1080/10298436.2013.812212

International Journal of Pavement Engineering, 2013
http://dx.doi.org/10.1080/10298436.2013.812212

Taylor & Francis
Taylor & Francis Group

Quantifying moisture damage at mastic–aggregate interface

Mohammad I. Hossain* and Rafiqul A. Tarefder[1]

Department of Civil Engineering, University of New Mexico, 210 University Blvd NE, Albuquerque, NM 87106, USA

(Received 7 December 2012; final version received 3 June 2013)

This study quantifies moisture damage at the asphalt mastic–aggregate interfaces using finite element method modelling technique in ABAQUS. A model aggregate surrounded by a layer of mastic is subjected to static loads of varying magnitudes and patterns. Using dynamic shear and elastic moduli of wet and dry mastic and aggregate as model inputs, moisture-induced damage is quantified through parameters such as contact stresses at interface, load to initiate damage and de-bonding at the interface. Results show that contact stresses are significantly higher in dry samples than wet samples. It is revealed that damage initiates at a smaller magnitude of deformation (0.0508 mm) in the wet sample than that (0.508 mm) in the dry sample. That is, a stiffer dry sample carries more loads and deforms less before damage initiation than a softer wet sample. In addition, approximately 6.8% interface de-bonding occurs in the dry sample, whereas 49.1% de-bonding occurs in the wet sample.

Keywords: moisture damage; mastic; interface; asphalt concrete; finite element method

Introduction

Moisture causes damage in asphalt concrete. This damage can be classified into two main categories: adhesive and cohesive damage. Adhesive damage is the separation between the aggregate and asphalt binder at the interface locations. Adhesion damage is also known as stripping or de-bonding. On the other hand, cohesive damage is stiffness degradation within the asphalt materials (Mohamed 1993, Hao and Hachiya 2003, Tarefder and Yousefi 2012). When aggregate is mixed with hot asphalt, asphalt binder makes a coating around the aggregate surface. The coating is made up of asphalt combined with fine particles. The combination of asphalt and fine particles that passes through #200 sieves is called mastic. Figure 1 shows generalised phenomena of adhesive and cohesive damage in asphalt. Figure 1(a) shows the aggregate coated with mastic. Figure 1(b) shows that the mastic coating on some portions is worn out, which resembles cohesive damage. Figure 1(b) also shows that there is no mastic at some aggregate surface locations, which resembles adhesive damage. The weakening of mastic–aggregate interfaces (i.e. adhesive damage) under dry and wet conditions is modelled in this study.

In the past, a number of researchers have studied asphalt damage using finite element method (FEM). Most of the FEM study considers a pavement section and subjected to traffic loading condition (Kim *et al.* 2008, Desai 2009). However, very few of them address how damage initiates in the asphalt components such as matrix, mastic and aggregate interface. For example, Kim (2009) developed visco-elastic–plastic continuum damage (VEPCD) under tension and compression loading of asphalt concrete. However, VEPCD model is unable to differentiate the adhesive and cohesive damage at mastic–aggregate interfaces and within the material itself. Desai (2001) has developed a disturbed state concept (DSC) model to predict damage in asphalt concrete. Although DSC was used to quantify damage as a disturbance, DSC model has never been used to predict the degradation stiffness at the mastic–aggregate interface. Recently, Kringos *et al.* (2008b) and Kringos and Scarpas (2008) have conducted FEM study considering mastic–aggregate interface. These studies determined moisture damage due to diffusion through mastic and aggregates. Mainly, stress variations within the materials due to selected diffusion rate of moisture were observed in their studies; however, they are not directly related to the quantification of damage at the mastic–aggregate interface.

Objective and scope

The main objective of this study was to quantify moisture-induced damage at the mastic–aggregate interface in terms of contact stresses at the interface, load magnitude to initiate damage and de-bonding. The interface strength and stiffness are determined from laboratory testing of dry- and wet-conditioned samples. The stiffness (i.e. modulus of elasticity) of the aggregate is obtained from the literature. The shear modulus of mastic is determined by a dynamic shear rheometer (DSR) test in the laboratory.

*Corresponding author. Email: mhossain@unm.edu

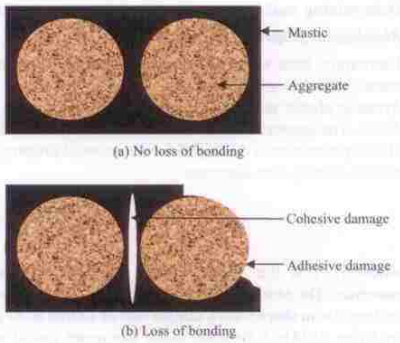

Figure 1. Schematic diagram of adhesive and cohesive damages in aggregates and mastic.

Shear and elastic modulus are used to define a surface-based traction–separation damage law readily available in ABAQUS. The damage at asphalt–aggregate interfaces is simulated using FEM.

Concept of damage

Different definitions of damage have been introduced based on constitutive behaviour of materials. According to Krajcinovic (1996), a material is said to be damaged if (i) some of the bonds connecting the parts of its microstructure are missing, (ii) the bond between the molecules within the materials is ruptured, (iii) the molecular chain in a polymer is broken or (iv) the adhesion between two materials is lost. The classical damage models are based on micro voids extension and coalescences concepts; they are also known as porosity-based models (Bonora 1999). The continuum damage models are based on reduction in strength due to breakdown of molecules or changes in molecular structures (Lemaitre and Desmorat 2005).

The degradation of strength at the interfaces of mastic and aggregate is the primary indication of moisture damage in asphalt (Bhasin *et al.* 2006, Kringos *et al.* 2008b, Caro *et al.* 2010, Tarefder and Arifuzzaman 2011, Tarefder and Yousefi 2012). This phenomenon is characterised using traction–separation damage law in this study. For a mastic–aggregate assembly, the traction forces are generated by the physical–chemical–mechanical interaction between the mastic and aggregate. Generally, the interaction strength is smaller than the material strength itself. Interactions between two materials could fail even before the material fails by degradation of its own stiffness due to various reasons such as loading magnitudes and environmental conditions. On the other hand, separation is the opening between the two surfaces, which were previously in contact with each other.

To facilitate an easier understanding of traction–separation damage law, the authors have created a schematic plot in Figure 2 following the description in the technical manual of ABAQUS software (2009). The two surface layers in Figure 2 can be considered to be attached to each other with some glue-like material. If a normal force is applied on the surface, a traction force develops between the interfaces of these two surfaces. The developed traction force is resisted by the interlocking of two surfaces generated from the glue-like material. As the magnitude of the applied normal force increases, the two surfaces tend to separate from each other due to increased traction force. Under the increment of traction force, the separation between the two surfaces increases until the force reached its ultimate strength at point B. The slope of line AB, as shown in Figure 2, is known as the interface stiffness and termed as *K*. After point B, the separation between the two surfaces increases as the load-carrying capacity decreases. Point B is known as damage initiation phenomenon, which means there is a separation between

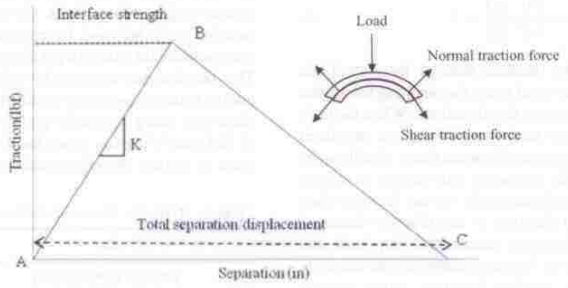

Figure 2. Schematic of traction–separation damage law.

the two surfaces that will not recover. Beyond point B to point C, the phenomenon is known as damage evolution or progression. At the damage progression region, the separation between two surfaces increases, eventually leading to a surface failure.

The following linear traction–separation law is used in this study:

$$t = K\delta, \tag{1}$$

$$\begin{Bmatrix} t_1 \\ t_2 \\ t_3 \end{Bmatrix} = \begin{bmatrix} K_{11} & K_{12} & K_{13} \\ K_{21} & K_{22} & K_{23} \\ K_{31} & K_{32} & K_{33} \end{bmatrix} \begin{Bmatrix} \delta_1 \\ \delta_2 \\ \delta_3 \end{Bmatrix}. \tag{2}$$

In Equation (2), t_1, t_2 and t_3 are the three components of force on a surface in three orthogonal directions, Ks are the stiffness coefficients and δ_1, δ_2 and δ_3 are three displacement components due to the respective forces. The diagonal terms are for three orthogonal directions, and the off-diagonal terms are for coupled directions. In this study, only two-dimensional idealisation is made, and therefore the off-diagonal components are not considered. The FEM model is developed considering stiffness in two directions: one is normal to the surface and the other is along the surface. The resulting equation of the traction–separation is shown below:

$$\begin{Bmatrix} t_1 \\ t_2 \\ 0 \end{Bmatrix} = \begin{bmatrix} K_{11} & 0 & 0 \\ 0 & K_{22} & 0 \\ 0 & 0 & 0 \end{bmatrix} \begin{Bmatrix} \delta_1 \\ \delta_2 \\ 0 \end{Bmatrix}. \tag{3}$$

Damage can be initiated either normal to the surface or along the tangential direction of the surface. The ratio between the force or load[2] and the interface strength is measured along the normal to the surface and tangential direction (i.e. shear direction) of the surface. The maximum ratio indicates the damage initiation at a particular direction and is presented in as follows:

$$\max\left\{\frac{t_1}{t_1^0}, \frac{t_2}{t_2^0}\right\} = 1, \tag{4}$$

where t_1^0 and t_2^0 are the interface strength for normal and shear directions. Here, $t_1$and t_2 are the resulting forces due to applied load in the respective directions. When the ratio becomes one, the bond state between the two interfaces breaks down and a gap occurs between them, which can be predicted by FEM. The maximum ratio cannot be greater than one. According to Equation (4), for any location when the ratio is one, that location is identified as damaged location. Damaged location cannot take any load and damage progresses upon further loading. In this research, the mastic–aggregate interface locations, where damage initiates under dry and wet conditions, are studied.

Determining model parameters by laboratory testing

Rheological properties of mastic

Laboratory tests were performed to determine dynamic shear modulus of mastic material and converted to dynamic elastic modulus using Equation (5) (Kim *et al.* 2010). The converted dynamic elastic modulus is used as elastic parameters in ABAQUS for the material property of mastic coating over aggregate.

$$|E^*| = 2.5|G^*|, \tag{5}$$

where $|G^*|$ is the dynamic shear modulus of mastic materials. The samples that were tested for G* value were rectangular in shape with a sample size of 12 mm (0.47 in.) by 6 mm (0.24 in.). Bending beam rheometer mould was used to prepare the rectangular solid samples. These samples were tested in shear torsion using a research grade DSR that has dynamic mechanical analyser capability. A total of six samples were prepared; three samples were tested under dry condition and three samples were tested for wet condition. The mastic samples were compacted in three layers using small round-headed tamping rod. The average theoretical maximum specific (G_{mm}) gravity for the sample was 2.319, and the percent air voids of the samples were 11.5 ± 1.0. It was hard to compact a small size mastic sample to smaller air voids (say, 7%) without crushing some particles. For this reason, higher (i.e. 11.5%) air voids were chosen for rheological testing of mastic materials. The wet condition was prepared following AASHTO T283. The laboratory test was carried out at 22°C and 1 Hz frequency. A strain rate of 0.007% was applied on the rectangular shape sample. The modulus values are given in Table 1. The modulus value is taken as average of three test results under dry and wet conditions.

Damage model parameters

Laboratory aggregate pull-off tests under both dry and wet conditions were carried out to measure the stiffness of mastic–aggregate interfaces. For tensile pull-off tests, the samples were prepared by compacting mastic materials into moisture tin with a target air voids ratios of 4 ± 0.5%. This requirement was met by calculating the amount of matrix material necessary to fill the bottom of the direct shear box using a specific gravity equal to 38.673 g/in.^{3} (2.360 g/cm^3) leaving room for 4 ± 0.5% air voids. The mass of mastic material needed to meet the void ratio

Table 1. Dynamic shear and elastic modulus of mastic.

	Dry	Wet
$\|G^*\|$	2.0 MPa (290.075 psi)	0.74 MPa (108,778 psi)
$\|E^*\|$	5.0 MPa (725,188 psi)	1.87 MPa (271,945 psi)

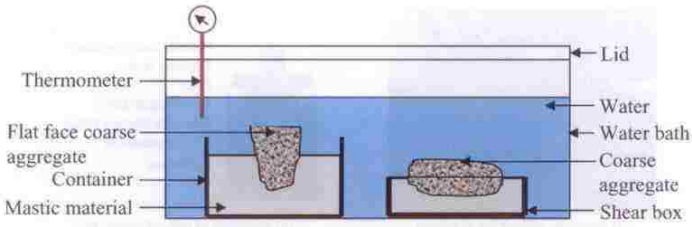

Figure 3. Schematic of sample moisture conditioning for pull-off tests.

requirement was found to be 205.34 g. A coated aggregate was cut into half and the flat face was exposed and the other end was embedded into mastic up to the half of the aggregate. The mastic material was compacted in three lifts by hand using a metal tamp. Prior to the final tamping of the top most lift, the fractured face of asphalt-coated aggregate was pressed against mastic so as to ensure contact between the mastic material and the aggregate face.

The wet condition was prepared following AASHTO T 283 method before conducting the pull-off test. A coarse aggregate embedded inside mastic material was moisture conditioned. According to AASHTO T 283 procedure, the aggregate embedded in mastic sample was subjected to vacuum saturation for 10 min. After vacuum, the sample was plastic wrapped and kept in freezing condition for 16 h. After removing from the freezer, the sample was emerged into water bath for 24 h with a constant water temperature of 140°F. After 24 h, the sample was emerged into water bath at room temperature for 10 min before the pull-off tests. A schematic diagram of moisture conditioning is added in Figure 3 which shows that the sample emerged into controlled hot water bath. While conditioning, water diffuses through the mastic, aggregate and mastic–aggregate interface. In field, mastic–aggregate interface can be affected by moisture diffusion through mastic material to aggregate or though aggregate to mastic material (Kringos *et al.* 2008a). In reality, when water diffuses through mastic material and infiltrates into interface and saturate aggregate, then the mastic, aggregate and mastic–aggregate interface degraded its strength. In this study, only the strength degradation of mastic and mastic–aggregate interface due to moisture is considered; the strength degradation for aggregate is not considered.

Pictures taken at the laboratory are shown in Figure 4. Two schematic drawings are shown in Figure 4(b),(d) to clarify the loading setup under tension and shear, respectively. For tensile pull-off test, the flat end was fixed with the loading frame with glue, and the bottom of the mastic material container was also fixed with the base. The sample was then loaded in tension at a rate of 1.27 mm/min (0.05 in./min). Two samples were prepared: one sample was kept dry and other was wet-conditioned before test.

Aggregate pull-off tests were also performed under direct shear load. The mastic material samples were prepared in a similar fashion except the materials that were prepared in the shear box of the direct shear testing equipment. The dimension of the shear box is 177.8 mm (7 in.) length, 139.7 mm (5.5 in.) wide and 50.8 mm (2 in.) deep. The hot mastic materials were compacted in two lifts into the bottom half of the shear box. Just before the final compaction of the top layer, a coated and fractured face of the hot aggregate was pressed onto the surface of the top lift, and the compaction to the required volume was then completed to ensure proper contact between the aggregate and the mastic. One sample was left in a dry condition, and the other is conditioned following AASTHTO T 283 standard. The top of the shear box was placed on the bottom of the shear box, and the apparatus was placed into the direct shear machine. The set screws in the shear box were removed, and the height of the top of the shear box was raised so that no mastic material impedes the shearing of the aggregate. The sample was then loaded in shear at a rate of 1.27 mm/min (0.05 in./min).

The load–displacement graphs due to aggregate pull-off in tension under dry and wet conditions are shown in Figure 5. As expected, the tensile strength of aggregate pull-off is higher under dry condition than under wet condition. The load–displacement curves due to shear pull-off under dry and wet conditions are shown in Figure 6. Under wet conditions, as shown in the dotted line, the initial load–displacement curve has lower values and then it increases rapidly. Unlike the tension pull-off test, the aggregate was not glued to the loading frame for shear pull-off tests. For this reason, the load–displacement curve shows wavy and discontinuous phenomena under dry and wet conditions for direct shear test. Also, the ultimate load under wet condition is higher than the dry condition. The phenomena can be explained based on a previous study, where it was observed that the roughness of aggregate and mastic surfaces increase due to moisture actions (Tarefder and Arifuzzaman 2010). In direct shear

(a) Aggregate pull-off due to tension

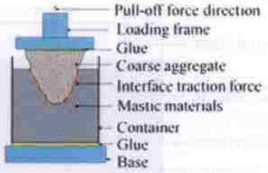

(b) Schematic of pull-off tension test

(c) Aggregate pull-off due to shear

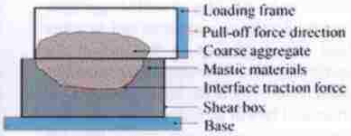

(d) Schematic of pull-off shear test

Figure 4. Laboratory measurement of interface strength.

tests, when a shear force is applied on the aggregate, friction force develops at the mastic–aggregate interface. The interlocking between the rough aggregate surface and the mastic material needs to overcome by applied shear force. Due to higher surface roughness at the moisture-conditioned aggregate, the load-carrying capacity of mastic–aggregate interface increases under wet condition comparing to dry condition requires higher ultimate load to fail at the interface. In tensile pull-off, the aggregate comes out of the mastic material while applying tensile force and the phenomena of increased surface roughness due to moisture conditioning is not a significant issue, since rough surfaces are not encountered by any lateral force or vertical compression load.

The stiffness of mastic–aggregate interface due to tension and shear is determined by measuring the slope of the curve before peak load, also known as secant modulus. The secant modulus is determined by measuring the slope of tangent connecting origin with 50% of maximum strength (Santi *et al.* 2000). The tangent lines for determining secant modulus are shown in the graphs of Figures 5 and 6. The measured sustained loads and stiffness for both tension and shear under both dry and wet conditions are given in Table 2. Both tensile and shear interface stiffness are higher under dry conditions than under wet conditions.

The displacements at ultimate strength and failure strength were recorded. The displacement at ultimate

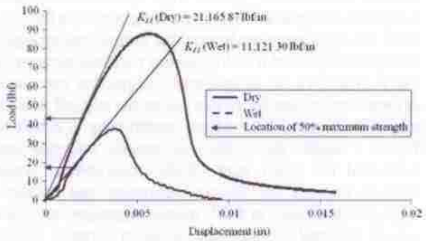

Figure 5. Load versus displacement curve in tension with secant modulus.

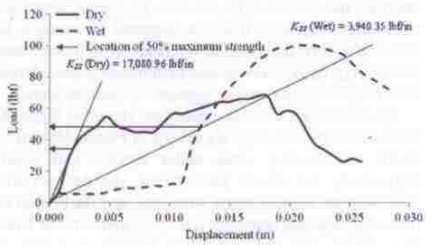

Figure 6. Load versus displacement curve in shear with secant modulus.

Table 2. Ultimate strength and interface stiffness under dry and wet conditions.

	Ultimate strength in tension	Ultimate strength in shear	Interface stiffness in tension (K_{11})	Interface stiffness in shear (K_{22})
Dry	391.67 N (88.05 lbf)	302.50 N (68.00 lbf)	3.68 N/mm (21,165.87 lbf/in.)	2.98 N/mm (17,080.96 lbf/in.)
Wet	167.21 N (37.59 lbf)	489.30 N (110.00 lbf)	1.93 N/mm (11,121.30 lbf/in.)	0.53 N/mm (3940.35 lbf/in.)

strength is 0.139 mm (0.0055 in.) for tensile pull-off and 0.119 mm (0.0047 in.) for shear pull-off and 0.096 mm (0.0038 in.) for tensile pull-off and 0.533 mm (0.0210 in.) for shear pull-off under dry and wet conditions, respectively. The displacement at failure strength is 0.402 mm (0.0158 in.) for tensile pull-off and 0.660 mm (0.026 in.) for shear pull-off and 0.244 mm (0.0096 in.) for tensile pull-off and 0.686 mm (0.027 in.) for shear pull-off under dry and wet conditions, respectively.

Interface modelling techniques

Two methods are available in ABAQUS for surface damage simulations: cohesive element approach and cohesive surface approach. In the cohesive element approach, two objects are connected with cohesive elements in between them, and in cohesive surface approach, the surfaces of the two objects are connected and make a single interface. For cohesive element approach, the stiffness degradations of materials are considered. On the other hand, for cohesive surface approach, the stiffness degradation of interface (interaction of two surfaces) is considered. For cohesive element approach, the stress–strain distribution and the modulus of connecting material and fracture energy, which is the area under the stress–strain curve, are the essential requirements. For cohesive surface approach, the modulus of materials is necessary, but the strength and stiffness of the interfaces (interaction of two surfaces) are essential for damage simulations. Also, the interface separation is required to simulate the damage evolutions. For example, if two metal plates are lap joined by adhesive materials such as glue and the damage of that adhesive material needs to be investigated, then the proper way of simulation is to model the adhesive material with cohesive elements. For this particular research, there is no additional adhesive material between mastic and aggregate. Mastic works as an adhesive material on aggregates, and the purpose of simulation is not determining the damage of mastic. The damage at the interface is the point of interest. In addition, the laboratory tests were conducted to predict the mastic–aggregate interface damage rather than damage of the mastic itself. For this reason, the cohesive surface approach is considered as the mastic–aggregate interface in the FEM model. An aggregate coated with mastic material is considered to evaluate damage at the mastic–aggregate interface. The inner surface of the mastic material and the outer surface of aggregate are considered as mastic–aggregate interface in the FEM model.

Finite element model developments

ABAQUS/CAE version 6.9-EF1 (2009) is employed for conducting FEM analysis. Only one circular shape aggregate is considered in this model. The radius of the aggregate is 19.05 mm (0.75 in.). A 0.254 mm (0.01 in. ≈ 300 μm) mastic thickness is considered. Previously, Kringos *et al.* (2008a, 2008b) considered a 300 μm of mastic thickness in her model. The inner side of mastic and outer side of aggregate is restrained in both horizontal and vertical directions at four points to overcome the rigid body movements. For compacted dense pavement, the aggregate might move sidewise due to shear force from tire and move vertically or rotate around its axis. The left- and right-hinged supports prevent the lateral rigid body motion, and the top and bottom hinges prevent the vertical and rotational movements. The boundary conditions are limited to four locations based on the assumption that damage occurs near the boundary condition due to high stress concentration. It is assumed that no damage occurred inside the aggregate. Generalised shape, boundary conditions and loading state are shown in Figure 7. A portion of the finite element model that is simulated is shown in Figure 7. The finite element model shows a combination of both triangular and rectangular elements. The model is generated as a two-dimensional continuum homogeneous structure. The model is developed with plane stress continuum three- and four-noded linear quadrilateral elements.

The mastic and aggregate are considered as elastic materials. The elasticity of mastic is assigned according to Table 1 with a Poisson's ratio of 0.30 under dry and wet conditions. In a previous study, Kringos *et al.* (2007) considered 0.30 Poisson's ratio of mastic materials. Despite visco-elastic–plastic behaviour of mastic materials, several studies assumed mastic material as elastic material for simplification of FEM simulation; this trend is followed in this study. It has been mentioned that AC behaves viscoelastically at a higher temperature and elastically at a lower temperature (Zhu *et al.* 2010). Also at low temperatures, the stiffness of an asphalt binder becomes close to the stiffness of a filler material, that is,

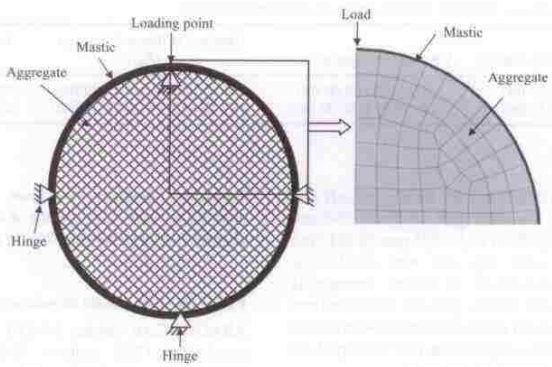

Figure 7. A generalised diagram of aggregate and mastic with boundary conditions, loading and a portion of the FEM.

fine particles passing #200 sieves (Shashidhar and Shenoy 2002). In addition, Tarefder *et al.* (2010) have shown that a wet mastic shows a very small phase angle, which indicates that wet mastic material can be assumed to behave elastically rather than visco-elastically at ambient temperatures. The elasticity value of aggregate is assumed as 48.3 GPa (7,000,000 psi) with Poisson's ratio of 0.20 (Roque *et al.* 2009). The damage evolution is assumed as linear, and an elastic displacement value has been given for controlling the damage initiations. From the pull-off tests data, the displacement at ultimate force is considered as elastic displacement, and the displacement at failure force is considered as total displacement. Between tensile pull-off and shear pull-off test, the smaller displacement between these two is selected as critical displacement and assigned as elastic displacement in the FEM model. The damage stabilisation is given as 1E − 05, which is a very small value required for analysis purpose. The FEM model that accounts softening and stiffness degradation shows severe convergence issue. The small value of damage stabilisation parameter will overcome this issue.

Real pavement experiences cyclic tire pressure that comes from traffic. The monotonically increasing static loading condition does not show the actual degradation of materials. For this reason, the FEM is simulated with three different patterns loads. The loading pattern resembles one cycle of dynamic tire pressure. The three different load patterns are shown in Figure 8. The load patterns are named triangle, sawtooth and rectangle. The triangular pattern represents a very high speed car, the sawtooth pattern represents a moderate-to-low speed car and the rectangular pattern represents a car that is stationary for a while and suddenly moves from its stationary position, also known as a stop and go situation. Several studies were carried out with cyclic loading on asphalt concrete pavements (Zaghloul and White 1993, Blab and Harvey 2002, Saad *et al.* 2005). Three different types of load magnitudes are used in this study. Three displacement loads of values 0.00508 mm (0.0002 in.), 0.0508 mm (0.002 in.) and 0.508 mm (0.02 in.) are applied as peak amplitudes. Huang (2004) showed that in two-layer pavement systems with 0.483 MPa (70 psi) dual tire loads applied over 152.4 mm (6 in.) asphalt concrete of 689.48 MPa (100,000 psi) elastic modulus, the maximum vertical deflection is 0.6858 mm (0.027 in.) under one tire at the bottom of the asphalt concrete. The assumption of

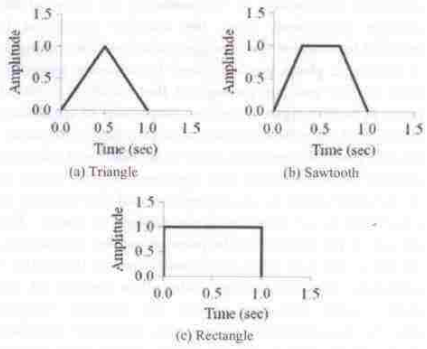

Figure 8. The load patterns.

maximum vertical deformation load of 0.508 mm (0.02 in.) seems appropriate for these simulations.

Results and discussions

Contact stresses at the interface

Contact stresses are generated at the surface between the mastic and aggregate. At every element of the surface, the resulting stresses are divided into normal and shear contact stresses. The contour of contact stresses along the surface can be shown using FEM. Variations of contact stresses under dry and wet conditions are investigated for different load patterns. The rectangular pattern causes higher normal and shear contact stresses under both dry and wet conditions. For the case of the rectangular pattern, the load is applied with its maximum amplitude for a longer time compared to the triangular and sawtooth patterns. The normal and shear contact stresses due to rectangle pattern load under dry and wet conditions are shown in Figure 9. The locations of maximum positive and negative normal contact stresses are shown in Figure 9(a),(b). The locations of maximum positive and negative shear contact stresses are shown in Figure 9(c),(d). For normal contact stress, positive value represents tensile stress and negative value represents compressive stress. In the case of shear stress, counter-clockwise from the element centre is positive. Higher intensity of normal contact stresses is close to the supports and loading point. Maximum tensile contact stresses are located at the two right and left support conditions. For shear contact stresses, the positive and negative stresses are on either side of the support. The locations of maximum shear contact stresses are not the same for dry and wet conditions. Figure 10 shows the variations of the maximum positive contact stresses of 0.00508 mm (0.0002 in.) vertical deformation under dry and wet conditions for all load patterns. From Figure 10, it could be observed that for all load patterns, dry conditions give both higher normal and shear contact stresses than wet conditions. The presence of moisture in mastic develops reasonably lower normal contact stresses and significantly lower shear contact stresses at the interface locations. Low contact stresses at the interfaces could be one of the reasons for having higher adhesive damage at moist mastic–aggregate interfaces. It should be noticed that the shear

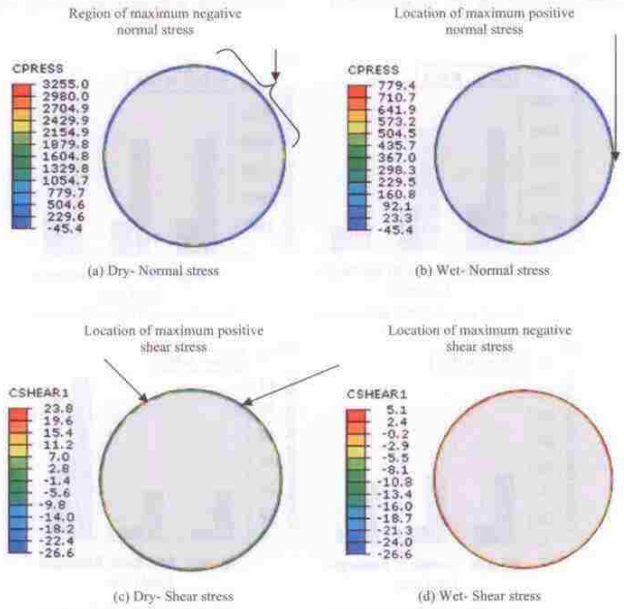

Figure 9. Contact stresses due to 0.0508 mm (0.002 in.) vertical deformation under rectangular load (CPRESS means contact pressure and CSHEAR1 means contact shear 1).

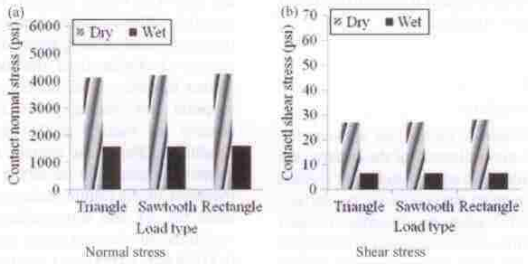

Figure 10. Contact stresses due to 0.00508 mm (0.0002 in.) vertical deformation for three load patterns.

strength is higher under wet conditions than under dry conditions, but secant modulus or interface stiffness is higher under dry conditions than under wet conditions. For this reason, interface contact stress affected due to stiffness of interface rather strength of interface.

Effects of loading

The contact stress variations due to three load patterns and two load magnitudes are compared and presented. Normal and shear contact stresses for 0.0508 mm (0.002 in.) and 0.508 mm (0.02 in.) deformation load under dry and wet conditions are presented in Figure 11. Contact stress variations for 0.00508 mm (0.0002 in.) vertical deformation load have been presented in Figure 10. There are no significant differences of normal and shear contact stresses under dry and wet conditions for triangular and sawtooth patterns load due to incremental deformations from 0.00508 mm (0.0002 in.) to 0.0508 mm (0.002 in.) to 0.508 mm (0.02 in.). Mastic is taking most of the applied deformation and the load-carrying capacity of mastic–

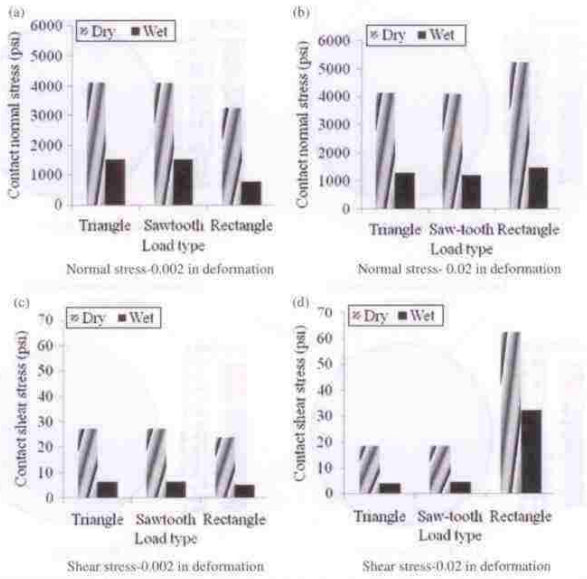

Figure 11. Contact stresses due to vertical deformation loading for three load patterns.

aggregate interface does not increase significantly. The major differences have been observed although vertical deformation increases from 0.0508 (0.002 in.) to 0.508 mm (0.02 in.) under rectangular pattern load. For rectangular pattern load, although vertical deformation increases from 0.0508 mm (0.002 in.) to 0.508 mm (0.02 in.), the normal contact stresses increase about 61% under dry conditions and approximately 90% under wet conditions. In addition, while comparing the shear contact stresses due to vertical deformation increments from 0.0508 mm (0.002 in.) to 0.508 mm (0.02 in.) for the rectangular pattern load, the shear contact stresses under both dry and wet conditions increase by about 163% and 537%, respectively. Normal contact stresses under dry conditions are two to four times higher than the wet conditions for all three load patterns. Shear contact stresses under dry conditions are around two to five times higher than wet conditions. Wet conditions show higher adhesive damage than dry conditions due to lower contact stresses for all three load patterns.

Resistance to moisture-induced damage

According to AASHTO T 283 standard, the ratio of strength of wet and dry samples is a common measure for resistance of compacted asphalt mixtures to moisture-induced damage. The ratio is known as tensile strength ratio (TSR). Indirect tensile strength is developed within the sample by applying direct compression load. The standard indicates that the lower the ratio, the higher the damage in the samples. In other words, the lower the ratio, the sample has a lower resistance to moisture. Laboratory investigations for wet condition samples are completed following AASHTO T283 standard. Although there are some differences between T 283 test and this study, instead of tensile strengths, the contact stresses are compared in this study, also T 283 is carried out with ramp loading, and this study considers three load patterns. In these mastic–aggregate interface damage simulation models, from Figure 9, it is observed that under vertical deformation load, the maximum contact tensile stresses are developed at the left and right supports. This resembles the T283 standard's indirect tension development in the samples. In addition, the loading phenomenon is similar to the T283 standard. The contact stress ratios under wet and dry conditions are given in Table 3. The variations of the ratios are also plotted in Figure 12 for normal contact stresses and shear contact stresses. It can be observed that for the triangular load pattern the maximum ratio under normal contact stress is 0.39 for 0.0508 mm (0.0002 in.) deformation load. For the rectangle pattern load, the minimum ratio under normal contact stress is 0.24 for 0.508 mm (0.002 in.) deformation load. Similar to normal contact stress, decrease in ratio is also observed for shear contact stresses under all pattern loads. Shear contact stress ratio is smaller than normal contact stress ratio except for rectangular pattern load for 0.508 mm (0.02 in.) deformation. The general trend is that normal and shear contact stress ratio is decreased for deformation load increment except in the rectangular pattern. Under rectangular pattern, contact stresses under wet condition and dry conditions increase significantly compared with the triangular and sawtooth patterns. For this reason, the ratio is also high under the rectangular pattern compared with the other two load patterns. Detailed investigations are necessary to see how contact stresses are varying at the

Table 3. Ratio of wet and dry contact stresses.

Load pattern	Deformation magnitudes (in.)	Wet/dry	
		Normal	Shear
Triangular	0.0002	0.39	0.24
	0.002	0.37	0.23
	0.02	0.31	0.23
Sawtooth	0.0002	0.38	0.23
	0.002	0.37	0.23
	0.02	0.29	0.24
Rectangular	0.0002	0.38	0.23
	0.002	0.24	0.21
	0.02	0.28	0.52

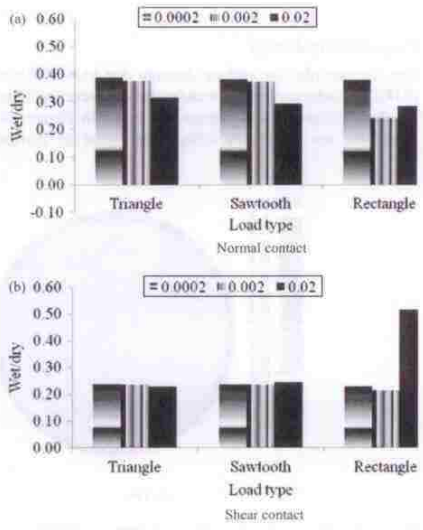

Figure 12. Ratio of wet and dry contact stresses.

mastic–aggregate interface under deformation. In addition, if T 283 test could be carried out with different load patterns, the comparison between TSR and the ration of wet to dry contact stresses would be more meaningful.

Damage analysis

Location of maximum damage

Damage is also termed as scalar degradation of stiffness, which is a dimensionless quantity, and varies from zero to one. Zero represents no degradation of stiffness and one represents complete degradation of stiffness. The location between zero and one is sensitive to damage and will become damaged upon increment of loading. In the following discussions, surface damage and interface damage are used interchangeably. The location of damage can be identified by observing the contour images of damage initiation criteria. For rectangular pattern loads, the damage initiation criteria of 0.0508 mm (0.002 in.) deformation loads under dry and wet conditions are plotted in Figure 13. Damage initiates near the location of applied boundary conditions and progresses along the surfaces. Initially, there are 13 locations where the maximum damage occurs under wet conditions and 8 damaged locations under dry conditions. Wet conditions show higher damage locations than dry conditions. The higher the deformation load, the higher the damage locations on the interfaces.

Progression of damage

The contour plot for surface damage due to 0.0508 mm (0.002 in.) deformation loads under dry and wet conditions for three different load patterns is shown in Figure 14. There are no significant differences found in surface damage contours between 0.00508 (0.0002 in.) and 0.508 mm (0.002 in.) deformation loads under both dry and wet conditions. According to Figure 14, the wet conditions show a considerable amount of damage near the supports for rectangular load pattern. The stiffness degradations are about 0.4, 0.4 and 0.9 for triangular, sawtooth and rectangular pattern loads, respectively, under dry conditions. The maximum surface damage value is 1.0, which is calculated from the ratio of surface strength and applied load at the node or element. For this reason, under dry conditions for all three load patterns, the surface damage has not reached its limiting value, or, there is still some stiffness left to the nodes under dry conditions. It should be noticed that initiation of damage are near the supports, which means the damage initiation is based on boundary locations for this analysis. The extent of the surface damage under wet conditions is more than under dry conditions. Under wet conditions, eight damage initiation points show a stiffness degradation of 1.0, which means there is no stiffness left in those particular nodes or elements. Under wet conditions, damage has been initiated for low (0.002 in.) vertical deformation loads. Damage contours between triangular and sawtooth under wet conditions do not clearly differentiate, but they can differentiate between sawtooth and rectangle pattern loads.

The contour plot for surface damage due to 0.508 mm (0.02 in.) deformation loading under dry and wet conditions for three different load patterns is shown in Figure 15. Damage contour shows clear differences in dry and wet conditions for all three load patterns in Figure 15. Under both dry and wet conditions for all three loading patterns, several locations of interfaces are exposed to damage. For triangular load pattern under dry conditions, two new locations and under wet conditions, three new locations are exposed to damage. For sawtooth load

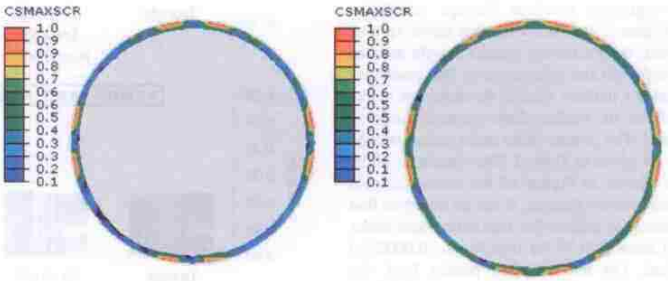

(a) Dry (b) Wet

Figure 13. Damage locations due to 0.0508 mm (0.002 in.) vertical deformation under rectangular load (CSMAXSCR is maximum traction damage initiation criteria for cohesive surfaces).

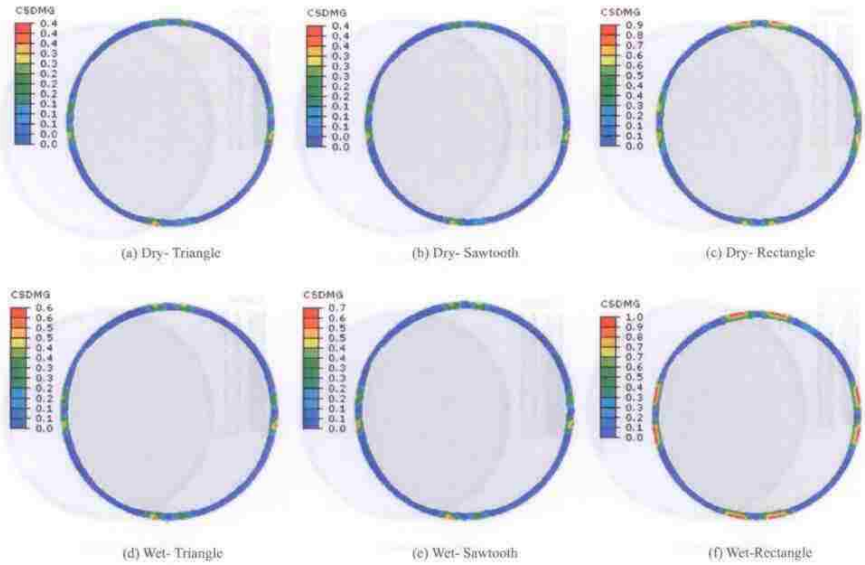

Figure 14. Contour of surface damage due to 0.0508 mm (0.002 in.) vertical deformation load (CSDMG is scalar stiffness degradation for cohesive surfaces).

pattern under dry conditions, three new locations and under wet conditions, four new locations are exposed to damage. For rectangular load pattern under wet conditions, the upper portion of the interfaces shows as entirely damaged. Under dry conditions for rectangle load patterns, the upper portion shows nearly complete damage. The extent of damage increased for all previously exposed eight locations. The upper portion of interfaces shows more surface damage than the lower portion of the interfaces for all load patterns. The loaded region at upper portion of mastic–aggregate interface carries more load than the lower interface region. For this reason, the load-carrying capacity of the upper portion of the mastic–aggregate increases and reaches the strength and caused damage.

The numerical values of damage under dry and wet conditions due to three different deformation load magnitudes for a particular nodal point are shown in Figure 16. Node A is chosen and the position of the node is also shown in Figure 16. This node is very critical as it is near the applied deformation location and more sensitive to damage. Node A is not exactly under the loaded region and not at the stress intensity region that caused due to boundary condition. Also node A shows clear progression of damage under different load patterns and magnitudes. Under dry conditions and three different load patterns, the variations of damage are shown. As the deformation increases, the slope of the curve becomes steeper. Also damage magnitude increases as loading time and magnitude increase. Similar phenomena observed under wet conditions. For higher load magnitudes, the wet interfaces initiate damage earlier than dry interfaces.

Interface de-bonding due to damage

Contact interface status

The bond state under dry and wet conditions for rectangular load pattern due to 0.0508 mm (0.002 in.) deformation loading is shown in Figure 17. The contour value 1.0 means bonded and 0.0 means de-bonded between the two surfaces. For 0.0508 mm (0.002 in.) deformation loads under dry conditions, there is no de-bonded region. On the other hand, under wet conditions, some particular locations show de-bonding between mastic and aggregate. The locations where the de-bonding occurs have surface damage values equal to 1.0. If we compare Figures 14 and 17, under dry conditions the surface damage does not exceed 1.0, indicating that the interfaces of mastic and aggregate are bonded. The similar

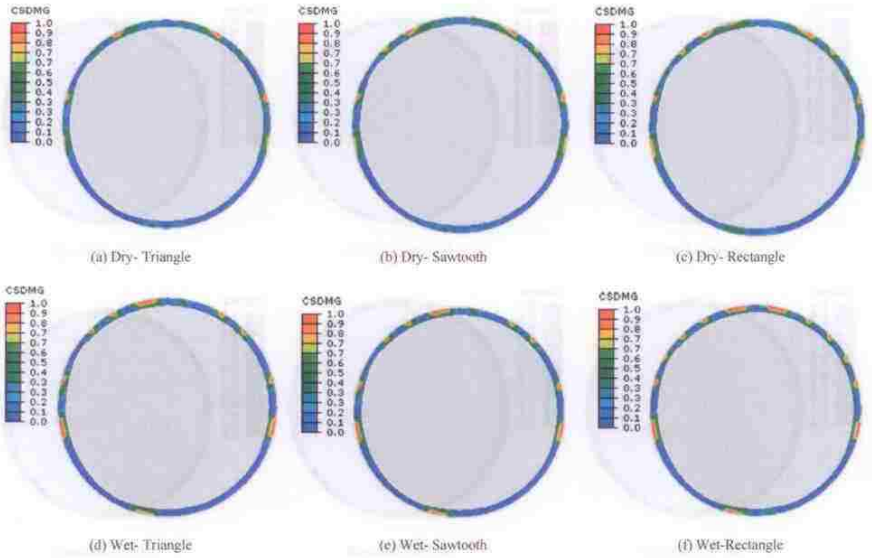

Figure 15. Contour of surface damage due to 0.508 mm (0.02 in.) vertical deformation load (CSDMG is scalar stiffness degradation for cohesive surfaces).

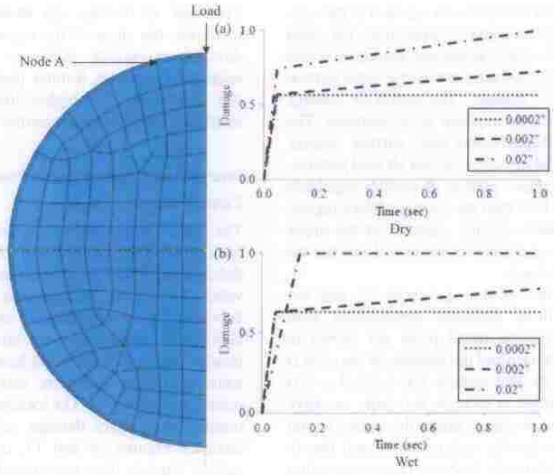

Figure 16. Damage at node A due to vertical deformation load.

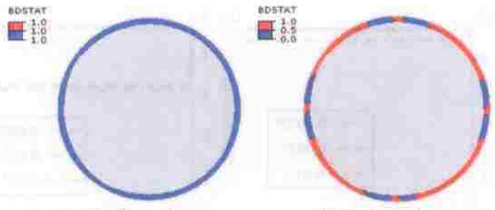

(a) Dry- Rectangle (b) Wet-Rectangle

Figure 17. Interface bonding due to 0.0508 mm (0.002 in.) vertical deformation load (BDSTAT is bond state).

scenario is also observed for 0.0508 mm (0.0002 in.) deformation loading and similar loading patterns. It is clear that bondage between mastic and aggregate depends on the interface damage and the phenomena are critical under wet conditions.

The bond state under dry and wet conditions for three different load patterns due to 0.508 mm (0.02 in.) deformation loading is shown in Figure 18. As the deformation increases from 0.0508 mm (0.002 in.) to 0.508 mm (0.02 in.), the bonding status under dry conditions changes and under wet conditions becomes worse. Figure 18 shows that under dry conditions, we have initiation of de-bonding that begins from the upper portion of the interfaces. Under wet conditions, the rectangular pattern load shows severe bond damage. For triangular load pattern under dry conditions, there are three de-bonded locations, and under wet conditions there are nine de-bonded locations. Similar numbers of damaged locations are observed for sawtooth load patterns under dry and wet conditions. For rectangle load pattern under both dry and wet conditions, there are 3 and 12 de-bonded locations, respectively. The de-bonding locations are

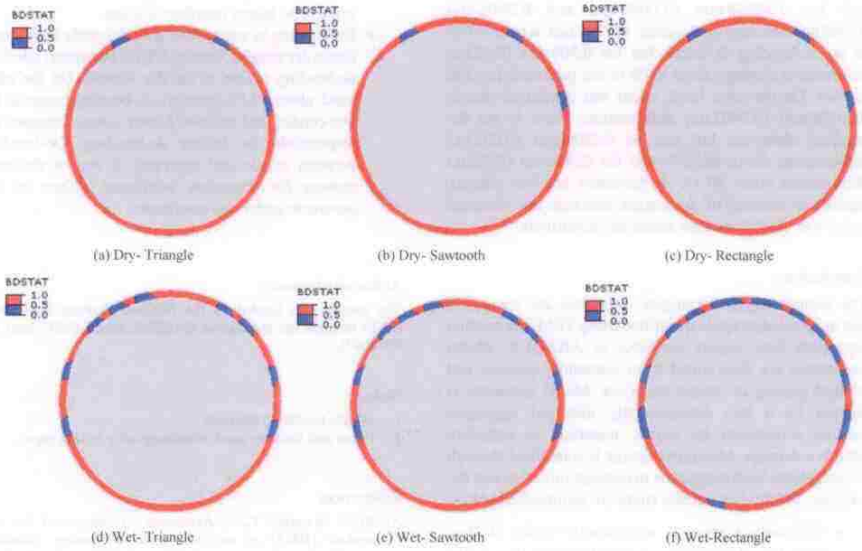

(a) Dry- Triangle (b) Dry- Sawtooth (c) Dry- Rectangle

(d) Wet- Triangle (e) Wet- Sawtooth (f) Wet-Rectangle

Figure 18. Interface bonding due to 0.508 mm (0.02 in.) vertical deformation load (BDSTAT is bond state).

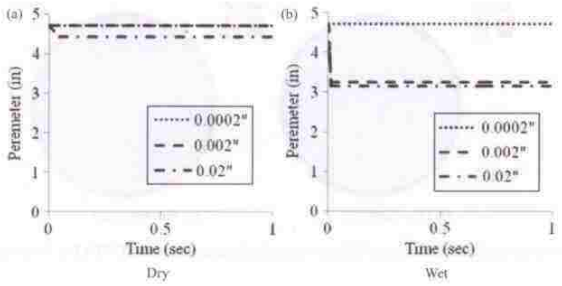

Figure 19. Contact perimeter between mastic and aggregate under rectangular load.

dominated at the upper portion of the surfaces. It has been previously observed that the damage locations are also extended over the upper portion of the interfaces.

Quantification of de-bonded surfaces

The bond status can be explained by determining the contact perimeter between mastic and aggregate. Before loading, the bonded contact perimeter is measured as 119.63 mm (4.71 in.). The contact perimeter, after applying the deformation load, can be computed for rectangular pattern and is shown in Figure 19. Under dry conditions and for 0.00508 mm (0.0002 in.) and 0.0508 mm (0.002 in.) deformation loading, the contact area is intact or no de-bonding is found, but for 0.508 mm (0.02 in.) deformation loading, about 6.8% of the perimeter has lost contact. On the other hand, under wet conditions due to 0.00508 mm (0.0002 in.) deformation, there is no de-bonding observed, but due to 0.0508 mm (0.002 in.) deformation, about 44.92% and for 0.508 mm (0.02 in.) deformation about 49.1% of perimeter has lost contact. Significant amount of de-bonded interface are observed under wet conditions than under dry conditions.

Conclusions

The asphalt mastic–aggregate interfaces are simulated, and interface damage is quantified using FEM and traction separation law, readily available in ABAQUS. Model parameters are determined from laboratory pull-off and strength testing of mastic materials. Model geometry is defined by a two dimensionally idealised aggregate particle surrounded by mastic materials to represent adhesive damage. Moisture damage is quantified through contact stress, load magnitude to damage initiation and de-bonding. The findings of this study are summarised below.

- The contact stress is significantly higher in dry-conditioned mastic–aggregate interface than in the wet-conditioned interface for all load magnitudes and patterns. Lower contact stresses are one of the reasons for higher mastic–aggregate interface damage under wet condition.
- It is shown that damage initiates and progresses mostly on the upper half of the mastic–aggregate interface. In wet-conditioned samples, surface damage initiates at 0.00508 mm (0.002 in.) deformation, whereas damage initiates at 0.508 mm (0.02 in.) deformation in dry condition. Stiffer dry mastic material carries higher applied deformation and shows lower mastic–aggregate interface damage. Softer mastic material is unable to carry smaller applied deformation and exposed to higher interface damage.
- De-bonding in wet sample is significantly higher than that in dry sample. About 6.8% (% perimeter) interface de-bonding occurs in the dry sample. On the other hand, about 49.1% interface de-bonding occurs in the wet-conditioned sample. Lower contact stresses are responsible for higher de-bonding. De-bonding between mastic and aggregate is one of the main reasons for premature permanent failure of AC pavement under wet conditions.

Acknowledgement

The project was funded by the National Science Foundation (NSF) through the prestigious CAREER award (NSF grant no. 0644047).

Notes

1. Email: tarefder@unm.edu
2. Force and load are used interchangeably in this paper.

References

AASHTO Standard T283, *Resistance of compacted hot mix asphalt (HMA) to moisture induced damage. Standard specifications for transportation materials and methods of sampling and testing*. 27th Ed Vancouver, WA: AASHTO.

ABAQUS/CAE User's Manual, Dassault Systems, 2009. Version 6.9-EF1.

Blab, R. and Harvey, J.T., 2002. Modeling measured 3D tire contact stresses in a viscoelastic FE pavement model. *International Journal of Geomechanics*, 2 (3), 271–290.

Bhasin, A., *et al.*, 2006. Limits on adhesive bond energy for improved resistance of hot-mix asphalt to moisture damage. *Transportation Research Record: Journal of the Transportation Research Board*, (1970), 3–13.

Bonora, N., 1999. Identification and measurement of ductile damage parameters. *Journal of Strain Analysis*, 34 (6), 463–477.

Caro, S., *et al.*, 2010. Coupled micromechanical model of moisture-induced damage in asphalt mixtures. *Journal of Materials in Civil Engineering, ASCE*, 22 (4), 380–389.

Desai, C.S., 2001. *Mechanics of materials and interfaces: the disturb state concept*. Boca Raton, FL: CRC Press.

Desai, C.S., 2009. Unified disturb state constitutive modelling of asphalt concrete. *In*: Y.R. Kim, ed. *Modeling of asphalt concrete*. New York: McGraw-Hill, 205–228.

Hao, P. and Hachiya, Y., 2003. Moisture susceptibility of asphalt mixture and effectiveness of anti-stripping additive. *Journal of Materials, Concrete Structure and Pavement*, 61 (746), 265–273.

Huang, Y.H., 2004. *Pavement analysis and design*. 2nd Ed Upper Saddle River, NJ: Prentice Hall.

Kim, Y.R., *et al.*, 2008. Application of viscoelastic continuum damage model based finite element analysis to predict the fatigue performance of asphalt pavements. *KSCE Journal of Civil Engineering*, 12 (2), 109–120.

Kim, Y.R., 2009. *Modeling of asphalt concrete*. New York: McGraw-Hill.

Kim, J., Lee, H.S., and Kim, N., 2010. Determination of shear and bulk moduli of viscoelastic solids from the indirect tension creep test. *Journal of Engineering Mechanics, ASCE*, 136 (9), 1067–1075.

Krajcinovic, D., 1996. *Damage mechanics*. New York: Elsevier.

Kringos, H., Scarpas, A., and Kasbergen, C., 2007. Three dimensional elasto-visco-plastic finite element model for combined physical–mechanical moisture induced damage in asphaltic mixes. *Journal of the Association of Pavement Engineering*, 76, 495–524.

Kringos, N. and Scarpas, A., 2008. Physical and mechanical moisture susceptibility of asphalt mixtures. *International Journal of Solids and Structures*, 45, 2671–2685.

Kringos, N., *et al.*, 2008a. Modeling of combined physical–mechanical moisture-induced damage in asphaltic mixes part-1: governing processes and formulations. *International Journal of Pavement Engineering*, 9 (2), 115–128.

Kringos, N., *et al.*, 2008b. Modeling of combined physical–mechanical moisture-induced damage in asphaltic mixes part-2: moisture susceptibility parameters. *International Journal of Pavement Engineering*, 9 (2), 129–151.

Lemaitre, J. and Desmorat, R., 2005. *Engineering damage mechanics: ductile, creep, fatigue and brittle failure*. Dordrecht: Springer.

Mohamed, E.H.H., 1993. Debonding location in asphalt concrete associated with moisture damage. *Journal of Materials in Civil Engineering*, 5 (4), 497–509.

Roque, R., *et al.*, 2009. *Introduction of fracture resistance to the design and evaluation of open graded friction courses in Florida*. Final Report, Florida Department of Transportation.

Saad, B., Mitri, H., and Poorooshasb, H., 2005. Three-dimensional dynamic analysis of flexible conventional pavement foundation. *Journal of Transportation Engineering*, 131 (6), 460–469.

Santi, P.M., Holschen, J.E., and Stephenson, R.W., 2000. Improved elastic modulus measurement for rock based on geology. *Environmental & Engineering Geoscience*, 6 (4), 333–346.

Shashidhar, N. and Shenoy, A., 2002. On using micromechanical models to describe dynamic mechanical behaviour of asphalt mastics. *Mechanics of Materials*, 34, 657–669.

Tarefder, R.A. and Arifuzzaman, M., 2010. Nanoindentation study on moisture damage in asphalt concrete. *In*: *Proceedings of 8th international transportation specialty conference*, June 9–12, Winnipeg, Canada. Quebec, Canada: Canadian Society for Civil Engineering (CSCE), 1578–1587.

Tarefder, R.A., Yousefi, S.S., and Kias, E., 2010. *Factors that affect the rheological properties of asphalt matrix. Pavement and materials: testing and modelling in multi length scales, ASCE special publication*. Virginia, USA: American Society of Civil Engineers (ASCE), 121–133.

Tarefder, R.A. and Arifuzzaman, M., 2011. A study of moisture damage in plastomeric polymer modified asphalt binder using functionalized AFM tips. *Journal of Systemics, Cybernetics and Informatics*, 9 (5), 1–12.

Tarefder, R.A. and Yousefi, S.S., 2012. Laboratory evaluation of moisture damage in asphalt. *Canadian Journal of Civil Engineering*, 39 (1), 104–115.

Zaghloul, S.M. and White, T.D., 1993. Use of three-dimensional dynamic finite element program for analysis of flexible pavement. *Transportation Research Record: Journal of Transportation Research Board*, (1388), 60–69.

Zhu, X., *et al.*, 2010. Micromechanics-based analysis for predicting asphalt concrete modulus. *Journal of Zhejiang University – Science A (Applied Physics & Engineering)*, 11 (6), 415–424.

APPENDIX B

Construction and Building Materials 49 (2013) 536–546

Contents lists available at ScienceDirect

Construction and Building Materials

journal homepage: www.elsevier.com/locate/conbuildmat

Identifying damage in asphalt matrix materials surrounding an aggregate particle

Mohammad I. Hossain *, Rafiqul A. Tarefder [1]

Department of Civil Engineering, The University of New Mexico, USA

HIGHLIGHTS

- Cohesive damage is higher than adhesive damage under both dry and wet conditions.
- Matrix–aggregate interface is the weakest region.
- Cohesive damage propagates towards interface and initiate adhesive damage.
- Thicker matrix on aggregate prevents adhesive damage at the interface.

ARTICLE INFO

Article history:
Received 2 June 2013
Received in revised form 23 August 2013
Accepted 29 August 2013

Keywords:
Damage
Asphalt concrete
Matrix
Finite Element Method
Cohesive
Adhesive

ABSTRACT

In this study, damage in asphalt matrix surrounding an aggregate particle is modeled in ABAQUS, which is commercially available finite element software. Damage is identified by damage location, magnitude, and percentage damaged area in matrix under dry and wet conditions. Normal and shear stiffness of matrix material are determined in the laboratory. Model simulations are run considering thin and thick layers of matrix, two applied deformations considering tire pressure, and three deformation intensity patterns considering application time of the tire pressure. The results indicate that damage initiates at the surface and propagates towards the matrix–aggregate interface. Damage in the wet conditioned samples is higher than those in dry samples, which is expected, because wet samples have lower stiffness and strength than dry samples. In both dry and wet conditions, more damage occurred in the vicinity of the surface (cohesive damage) that in the interface (adhesive damage). Cohesive damage is higher than adhesive damage but matrix–aggregate interface is the weakest region since damage propagates towards interface without causing significant damage inside the matrix other than top surface of matrix. However, thicker matrix prevents adhesive damage by protecting damage progression towards interface. Damage increases while deformation magnitude and application time increases. The worst damage scenario observed for thin matrix with 1.27 mm (0.057 in.) deformation and for rectangular pattern; about 16.67% matrix–aggregate interface and 30.30% of the vicinity of surface area are damaged under wet condition.

1. Introduction

Asphalt Concrete (AC) can be defined as asphalt coated coarse aggregate particles surrounded by mastic and matrix materials. Mastic is a mixture of fines (materials passing #200 sieve) and asphalt binders. Matrix is a mixture of asphalt binder with fine aggregates passing through a #4 (4.75 mm) sieve and retained on a #200 sieve [1–4]. Damage due to moisture in AC occurs mostly in the mastic or matrix or interface of the materials [5]. Most researchers agree that damage due to moisture inside an aggregate particle is limited. Rather, most of the moisture damage occurs in mastic and matrix materials. This study focuses only on the matrix damage due to moisture.

Cohesive and adhesive damage are two major reasons of AC damage [6–10]. The phenomena of adhesive and cohesive damage are shown schematically in Fig. 1. Fig. 1a shows a fresh sample of AC, which is not subjected to any damage. Fig. 1b shows loss of bonding within the asphalt binder or mastic or matrix (cohesive)

Abbreviations: AC, Asphalt Concrete; FEM, Finite Element Method; VEPCD, Visco-Elastic–Plastic Continuum Damage; DSC, Disturb State Concept; MAXSCRT, Maximum Stress Criteria; SDEG, Strength Degradation.

* Corresponding author. Address: Centennial Engineering Building, Room-2009, University of New Mexico, 210 University Blvd. NE, Albuquerque, NM 87106, USA. Tel.: +1 505 550 6264; fax: +1 505 277 1988.

E-mail addresses: mhossain@unm.edu (M.I. Hossain), tarefder@unm.edu (R.A. Tarefder).

[1] Address: Centennial Engineering Building, Room-3054, 210 University Blvd. NE, Albuquerque, NM 87106, USA. Tel.: +1 505 277 6083; fax: +1 505 277 1988.

0950-0618/$ - see front matter © 2013 Elsevier Ltd. All rights reserved.
http://dx.doi.org/10.1016/j.conbuildmat.2013.08.083

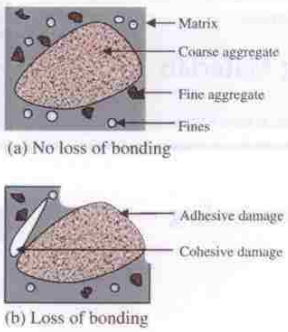

Fig. 1. Schematic of adhesive and cohesive damage in AC.

and at the matrix–aggregate or mastic–aggregate interface (adhesive). Few studies are considered in the past to understand the evolution and progression of matrix damage under dry and wet conditions [1,3,11].

Damage initiates at molecular scale but it is clearly visible at mesoscale, a full scale pavement. Although the previous studies show the severity of damage due to moisture condition but this study is done to understand how damage initiates in matrix materials (cohesive damage) and then move towards matrix aggregate interface (adhesive damage) and quantify this damage for a small scale considering variability of AC. It is believed that, the understanding of damage in small scale will help to improve the mix design procedure, select appropriate construction materials, application of additives, better material design to prevent damage and many more. In this study, damage in a system of aggregate coated by matrix, considered as small scale AC, is studied. Total damage is characterized as cohesive and adhesive damage as described in Fig. 1. To identify initiation and location of damage, the damage is evaluated using damage evaluation criteria defined by maximum nominal stress criteria. Maximum stress criteria is defined as, damage initiates within a material when it reaches to maximum strength under loading condition [12–15].

1.1. Objectives

The objectives of this research work are,

(1) Identify damage and categorize it into the adhesive and cohesive damage in matrix material of AC under dry and wet conditions.
(2) Evaluate the effects of moisture in adhesive and cohesive damage initiation and propagation.
(3) Quantification of adhesive and cohesive damage in the matrix materials.

1.2. Methodology

Maximum stress criteria is used to determine adhesive and cohesive damage by applying Finite Element Method (FEM) modeling. Commercial software ABAQUS is used as a tool of FEM. Laboratory tests are performed on matrix material under dry and wet conditions to determine the FEM damage model inputs. The initiation and progression of the adhesive and cohesive damage of matrix coated an aggregate particles are evaluated and quantified considering two different matrix thicknesses, two deformation magnitudes representing tire pressure on AC, and three deformation intensity patterns representing deformation application time of tire pressure on AC.

1.3. Damage modeling of AC

Concept of damage mechanics is introduced in early 1920 but a major breakthrough is occurred in late 1950 by Kachanov [16]. Damage in material due to environmental degradation such as presence of moisture and damage in concrete materials due to non-homogeneous material is introduced [17]. It is mentioned that geo-materials and polymers changes their mechanical properties under the influence of environment even in the absence of stress. Also concrete like materials have weak mechanical resistant due to non-homogeneity.

Damage in AC is studied for decades. In early 1990, damage in visco-elastic materials in terms of accumulated viscous strain is described [18]. Later on, visco-elastic damage model is applied on AC [19]. This model is modified and a Visco-Elastic–Plastic Continuum Damage (VEPCD) model is developed to study initiation and accumulation of micro-cracking due to material damage and to study damage progression [20]. FEM is implemented using VEPCD and simulation of damage growth due to accumulation of viscous strain under fatigue loading is performed [21]. According to authors knowledge, VEPCD does not identified cohesive and adhesive damage in AC. Desai defined disturbance as a damage to measure the translation, rotation and micro-structural changes within AC materials [20]. Desai's Disturb State Constitutive (DSC) model is not used to characterize stiffness degradation of matrix or disturbance in mastic or matrix due to moisture.

Several Finite Element Method (FEM) based damage models are developed to characterize linear viscoelastic and visco-elastic-plastic materials [22–24]. Most of the models used VEPCD or modified VEPCD with user defined constitutive equation implemented in FEM model for full scale pavement or cylindrical core specimens. Damage due to accumulation of visco-elastic and visco-plastic strain is shown for different temperature under loading conditions. Also, maximum stress criteria is implemented as cohesive zone modeling for predicting multi-scale damage model by FEM [25]. An aggregate surrounded by asphalt is considered as small scale and a full scale AC pavement consists of several aggregates is considered as large scale model. Average stress and strain in the FEM models are computed and compared for both undamaged and damaged conditions. Cohesive zone model is also implemented by FEM for cylindrical AC sample [26]. Only stress and strain relationships are computed for different strain rates.

Many studies are done to identify damage under dry and wet conditions in AC [10,27–32]. Most of the studies evaluate damage in AC by laboratory measurements. Even though both laboratory investigations and FEM model studies are agreed with the concept of adhesive and cohesive damage but very few of them able to identified and evaluated those damage into FEM models. Most of the studies emphasized on the total damage of AC. Also, none of them has able to include and evaluate both adhesive and cohesive damage in a single FEM model. In addition, very few studies conducted FEM analysis under both dry and wet conditions. Initiation, progression, and quantification of the adhesive and cohesive damage using maximum stress criteria in matrix under wet and dry conditions are not performed yet.

1.4. Damage law for cohesive elements

Cohesive element damage law is used in this study to define matrix damage. Cohesive law is defined by a monotonically increasing traction-separation load up to a critical point followed by a monotonically decreasing load or softening curve [33]. The

critical point or highest point or load is known as the damage initiation point. The elastic behavior is defined by an elastic constitutive matrix that relates to the nominal stress and nominal stain in the interface elements. Nominal stress is defined by the force component divided by the element area at each integration point. Nominal strain is the separation divided by the original thickness at each integration point. The nominal stress vector, σ, consists of three traction components σ_n acting to the pure normal direction, σ_s acting toward the first shear direction and σ_t acting toward second shear direction. The stress tensor σ can be express in terms of stiffness E and strain ε

$$\sigma = \begin{Bmatrix} \sigma_n \\ \sigma_s \\ \sigma_t \end{Bmatrix} = \begin{bmatrix} E_{nn} & E_{ns} & E_{nt} \\ E_{ns} & E_{ss} & E_{st} \\ E_{nt} & E_{st} & E_{tt} \end{bmatrix} \begin{Bmatrix} \varepsilon_n \\ \varepsilon_s \\ \varepsilon_t \end{Bmatrix} = E\varepsilon \quad (1)$$

where E_{nn} is the stiffness in the pure normal mode, E_{ss} is the stiffness in the first shear direction and E_{tt} is the stiffness in the second shear direction.

1.5. Damage initiation criteria

Damage is assumed to initiate when the maximum nominal stress ratio reaches a value of one. The maximum nominal stress ratio is defined by the following equation:

$$\max\left\{\frac{\langle\sigma_n\rangle}{\sigma_n^0}, \frac{\sigma_s}{\sigma_s^0}, \frac{\sigma_t}{\sigma_t^0}\right\} = 1 \quad (2)$$

where ε_n^0 is the nominal strength toward the normal direction, ε_s^0 is the nominal shear strength toward the first direction and ε_t^0 is the nominal shear strength toward the second direction measured in the laboratory. In this study, only compressive strength and shear strength to the first direction of the matrix are measured in the laboratory. Also, two dimensional FEM model is considered for identifying damage. For this reason the second shear strength parameter is not required and Eq. (2) becomes,

$$\max\left\{\frac{\langle\sigma_n\rangle}{\sigma_n^0}, \frac{\sigma_s}{\sigma_s^0}\right\} = 1 \quad (3)$$

The tests are done under both dry and wet conditions. The symbol $\langle\rangle$ is known as Macaulay bracket. Macaulay brackets are used to signify that a pure compressive deformation or stress state does not initiate damage. It should be noted that, maximum strain ratio can also be computed by Eq. (4), which is similar to Eq. (2). The maximum strain ratio can be expressed as,

$$\max\left\{\frac{\langle\varepsilon_n\rangle}{\varepsilon_n^0}, \frac{\varepsilon_s}{\varepsilon_s^0}, \frac{\varepsilon_t}{\varepsilon_t^0}\right\} = 1 \quad (4)$$

where ε_n^0 is the maximum nominal compressive strain of matrix, ε_s^0 is the maximum nominal shear strain toward the first direction and ε_t^0 is the maximum nominal shear strain toward the second direction measured in the laboratory. This equation is not used for this study.

2. Materials and methods

2.1. Sample preparation

Asphalt mix is collected from a local plant in cooperation with the New Mexico Department of Transportation (NMDOT). The loose mix is separated by sieving. Loose mix passing through number 16 sieve (1.19 mm) and retained on number 200 sieve (0.074 mm) is collected as matrix material. Cylindrical samples of height 69.85 mm (2.75 in.) and 35.31 mm (1.39 in.) diameter are compacted to a target void ratio of 4.0 ± 0.5%. For wet conditioning, samples are soaked before testing for 48-h under water at room temperature and subjected to a vacuum pressure of 30 mm Hg for half an hour.

2.2. Compression and shear test

Three dry and three wet cylindrical matrix samples are uniaxially loaded to failure under strain-controlled mode [34,35]. A loading rate of 1.27 mm/min (0.5 in./min) is used. Also three dry and three wet samples are compacted in a shear box and subjected to shear failure with a loading rate of 1.27 mm/min. Average of three samples' results from compression and shear tests are summarized in Table 1. Stiffness E-value is determined by measuring the slope of secant modulus. Secant modulus is defined as slope connecting origin to 50% of maximum strength of material [36]. Several studies used and recommended secant modulus to calculate elastic modulus of asphalt concrete [37–39]. Ultimate strength of matrix materials obtained from compression and shear tests are also listed in Table 1 [34,35]. It can be seen that E-values of dry sample are higher than those of wet samples, which is expected, but there is an exception, E-value of wet sample under compression is found to be smaller than the E-value in shear. In a previous study, it is observed that, aggregate surface roughness increases after moisture conditioning [40]. This increased surface roughness might cause the material stiffer than the dry material. Unlike compressive test, the shear test is confined into shear box and might causes additional stiffness.

2.3. FEM model development

The FEM model is developed using ABAQUS/CAE 6.9-EF1, commercially available software. A two-dimensional idealization of a circular aggregate surrounded by a layer of matrix material is considered. Obviously, it can be argued that the circular aggregate is not a true representation of aggregate particles reside in an AC. Similar argument can be made on the size of the aggregate particle. Also other studies use circular shape aggregate to predict moisture-induced damage [3,11]. The fact is the shape and size of aggregate particle varies a lot in asphalt concrete. Therefore a study that would consider the effects of the size and shape on the outcomes, that is asphalt cohesion and adhesion, can itself be complex but doable. For simplicity, the model considered for this study is one quarter of a circular coarse aggregate surrounded by a layer of matrix material, as shown in Fig. 2. This suffices the purpose of this study. The radius of the aggregate is assumed to be 19.05 mm (0.75 in.) based on the nominal maximum size (25.4 mm or 1.0 in.) of the mix aggregate collect from the plant. Since matrix thickness varies in asphalt concrete, two thicknesses of matrix layers (0.508 and 1.27 mm) are considered. The size of the selected fine aggregate is ranges from 1.19 mm to 0.074 mm. The thickness of matrix is chosen such that the fine aggregates itself have sufficiently coated with asphalt binder to make a homogeneous matrix material.

Though AC has been considered to be visco-elastic–plastic material, matrix is assumed to behave elastically following the

Table 1
Laboratory test results under dry and wet conditions.

Test type	Ultimate strength	E-value
Dry		
Compression	2.61 MPa (379 psi)	192.72 MPa (27,952 psi)
Shear	0.81 MPa (118 psi)	147.64 MPa (21,413 psi)
Wet		
Compression	2.02 MPa (293 psi)	129.44 MPa (18,773 psi)
Shear	0.56 MPa (81 psi)	139.10 MPa (20,174 psi)

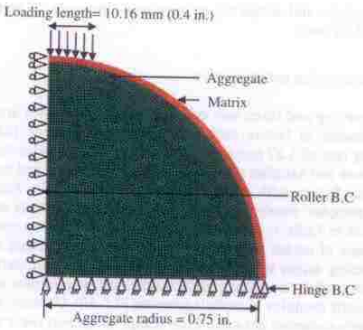

Fig. 2. Aggregate-matrix FEM model geometry.

behavior observed in other studies. It is mentioned that AC behaves elastically at low temperature and visco-elastically at high temperature [41]. Also the stiffness of binder is close to stiffness of filler at lower temperature [42]. In addition, the phase angle and rut factor for wet AC material is small comparing to dry AC material and wet AC material considered behaves elastically [43]. *E*-value of limestone aggregate is well established in literature, therefore laboratory tests are not conducted on aggregate. The *E*-value of aggregate used in this study is 48.26 GPa (7,000,000 psi) and the Poisson's ratio is 0.20 [44].

The loading and the shape of the FEM model are symmetrical to the vertical axis. The model is restrained for vertical and horizontal movement at the bottom, but only horizontal movement is restrained on the sides. Four noded linear quadrilateral cohesive elements are used to define the matrix. Linear elements are used since quadratic elements are not available for assigning axi-symmetric cohesive element in ABAQUS. Three and four noded linear quadrilateral plane stress elements are used to define the aggregate. Combinations of both three and four noded elements are required due to the circular shape of the aggregate. In ABAQUS, maximum stress criteria required maximum stress in both vertical and shear directions according to Eq. (2). Since the model is two-dimensional, data from one shear direction is sufficient as per Eq. (3). The interface between matrix and aggregate is defined as cohesive interaction. The bottom of matrix surface and top of aggregate surface are selected to make an interface. FEM model should have interface interaction behavior while model consists of two different materials and in contact.

In the FEM model, instead of applying a load, a specified deformation is applied and stresses are calculated using Eq. (1) and used to determine damage according to the Eq. (3). Deformation magnitudes of 0.72 mm (0.0285 in.) and 1.45 mm (0.057 in.) are applied on the FEM model. The magnitude of the deformation is calculated based on a standard duel tandem wheel on a pavement. It is observed that a dual tandem wheel of total 889.64 kN (200,000 lb) load produces a 1.45 mm (0.057 in.) deformation in a 203.02 mm (8 in.) thick AC. Therefore 1.45 mm value of the deformation is considered. Also, half of this 1.45 mm is considered. The selected deformation is the extreme deformation that a pavement can experience since the weight of the dual tandem is for the landing gear of an aircraft. Also an aggregate coated with matrix material located at the top surface of pavement might experiences that amount of deformation. This deformation is considered to observe the extreme scenario of damage in AC. The deformation load is applied on 10.16 mm (0.4 in.) length of matrix. Usually, Indirect tensile strength of asphalt concrete wheel is determined by subjecting an asphalt concrete sample diametrically though a 20.32–25.4 mm (0.8–1.0 in.) loading strip. Since the model is axi-symmetric, deformation load is applied over 10.16 mm (0.4 in.) length.

Traffic load on the roadway pavement is dynamic and cyclic. The shape of the dynamic load varies and really depends on the tire foot-print and speed of the vehicle. For example, dynamic modulus of asphalt concrete is determined using sinusoidal loading for using in the new mechanistic-empirical pavement design procedure. In this study the FEM model is simulated using three deformations intensity shapes or patterns namely, triangle, sawtooth and rectangle [45]. In each case, only one cycle of dynamic deformation is applied. These three deformation patterns are shown in Fig. 3. In this study the deformation intensity pattern used to see how damage initiates and progressed into matrix while the deformation applied with highest intensity for a very short time (i.e. triangular patter) or the deformation applied with highest intensity for the entire analysis period (i.e. rectangular patter) and in between of those two (i.e. sawtooth pattern).

The deformation is applied on the FEM model by following three load intensity patterns shown in Fig. 4 and according to the function described in Table 2. According to Table 2, i stands for intensity magnitude and t stands for time in second. For an example, for triangular pattern, at $t = 0$, 0.072 mm deformation multiply with intensity magnitude $i = 0$, so total zero deformation is applied at $t = 0$; then at $t = 0.05$, 0.072 mm deformation multiply with intensity magnitude $i = 1.0$, so total 0.072 mm deformation is applied at $t = 0.5$; then at $t = 0.10$, 0.072 mm deformation multiply with intensity magnitude $i = 0$, so total zero deformation is applied at end of the cycle. If the time increment and corresponding magnitude in the cycle is needed for the ABAQUS solver then it calculated automatically by linear interpolation.

The analysis matrix is shown in Table 3. Total twenty-four FEM simulations are run according to Table 3.

3. Results

The damage locations near the top surface of the matrix and/or in between the top surface and matrix–aggregate interface are named as cohesive damage. The damage locations at the bottom of matrix and/or near the matrix–aggregate interface are named as adhesive damage. The matrix layer with a thickness of 0.508 mm (0.02 in.) is termed as thin matrix and 1.27 mm (0.05 in.) is termed as thick matrix in the subsequent sections.

3.1. Damage magnitudes

Damage magnitudes are identified using Maximum Stress Criteria (MAXSCRT) contours. MAXSCRT contour is a plot of the ratio of stress computed by the FEM model due to applied deformation over ultimate stress or strength measured in the laboratory as described in Eq. (3). Upon applied deformation and using Eq. (1), for each integration point of an element, the normal and shear stresses are calculated; the calculated normal and shear stresses are normalized by using Eq. (3) for two dimensional FEM model; the maximum normalized value between the two ratios are the critical normalized value and showed as MAXSCRT value in the contour diagram. MAXSCRT is a unit less value since it is a ratio of two stresses. The maximum value of MAXSCRT is 1.0. When MAXSCRT value is 1.0 for an element than that particular element is known as damaged element for the whole domain. When MAXSCRT value is less than 1.0 for an element, the element is not damaged yet but will or might damaged upon increase of load magnitude or increase of duration of load or decrease in material thickness. The two deformations are used to see the changes in damage initiation

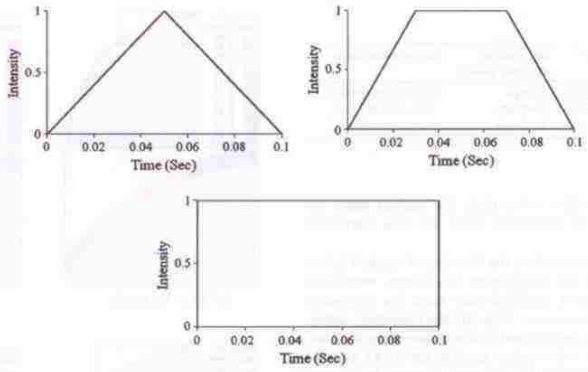

Fig. 3. Deformation intensity patterns used for FEM modeling.

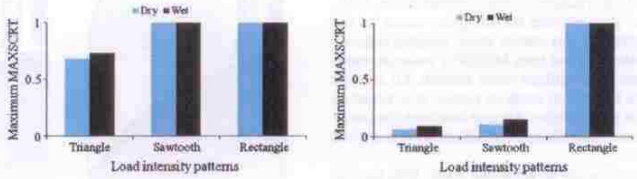

(a) Thin matrix (b) Thick matrix

(i) 0.72 mm (0.0285 in.) deformation

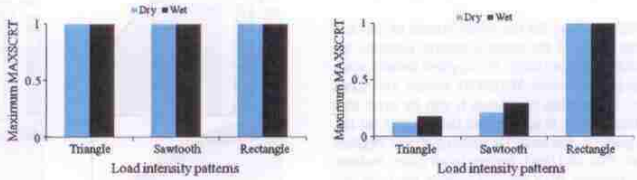

(c) Thin matrix (d) Thick matrix

(ii) 1.45 mm (0.057 in.) deformation

Fig. 4. Maximum values of Maximum Stress Criteria (MAXSCRT) for three intensity patterns under dry and wet conditions for thin and thick matrix.

Table 2
Deformation intensity patterns and functions specify in ABAQUS.

Triangle	Sawtooth	Rectangle
$i = 0$ at $t = 0$	$i = 0$ at $t = 0$	$i = 0$ at $t = 0$
$i = 1.0$ at $t = 0.05$	$i = 1.0$ at $t = 0.03$	$i = 1.0$ at $t = 0.0000001$
$i = 0$ at $t = 0.10$	$i = 1.0$ at $t = 0.07$	$i = 1.0$ at $t = 0.0999999$
	$i = 0$ at $t = 0.10$	$i = 0$ at $t = 0.10$

and progression due to increase of deformation magnitudes; three load patterns are used to see the changes in damage initiation and progression due to changes of duration of applied deformation; thin and thick matrix are used to see the change in damage magnitude due to change in thickness.

According to Table 1, the E-value for normal direction is higher for dry samples than wet samples, so, for same deformation and using Eq. (1), the normal stress under dry condition is higher than wet condition. On the other hand, the maximum normal stress is also significantly higher under dry condition than wet condition, so, the normalized value calculated using Eq. (2) for dry condition might lower than wet condition. If E-value for shear directions are considered, the dry sample has lower E-value than wet sample, so, for the same deformation or strain and using Eq. (1), the shear stress is lower under dry condition than wet condition. Furthermore, the maximum shear stress is significantly higher under dry condition than wet condition, so, the normalized value calculated using Eq. (2) for dry condition might lower than wet condition. While comparing the normalized normal and shear stresses under

Table 3
FEM model analysis matrix.

Condition	Matrix thickness	Deformation intensity pattern	Deformation value
Dry	0.508 mm (0.02 in.)	Triangle	0.72 mm (0.0285 in.)
Wet	1.27 mm (0.05 in.)	Sawtooth	1.45 m (0.057 in.)
		Rectangle	

dry or wet condition, ABAQUS solver picks the highest value between two and shows as MAXSCRT value for that particular condition.

In addition to deformation value, the duration of applied deformation is also important for progression of damage. Maximum deformation is applied for a specified time step. For triangular pattern, deformation increases over time and the maximum deformation applied for almost zero second or instantaneously, for sawtooth pattern, maximum deformation applied for 0.04 s and for rectangular pattern, maximum deformation applied for almost 0.0999998 s. Damage inside the material is higher when deformation is applied for longer time. The reason behind, when damage initiates due to applied deformation in some elements (i.e. MAXSCRT value is 1.0), that element does not carry any stress for the rest of the analysis period. For this reason, stress carrying capacity increase for adjacent elements and their MAXSCRT value increases over time and damaged if normalized value exceeds 1.0 and the process continues until the end of analysis period. It is expected that rectangular pattern shows higher damage locations than sawtooth or triangular pattern since the applied deformation is applied for longer time period.

Moreover, thickness of matrix on aggregate might help prevent damage inside the matrix material. Thicker matrix provides higher stress carrying capacity since more area of matrix is taking stresses. Thick matrix will carry higher deformation and distribute stresses evenly into the larger area to reduce damage than thin matrix.

The maximum MAXSCRT values for the whole model of wet and dry samples are plotted in Fig. 4 for three intensity patterns for 0.72 mm (0.0285 in.) and 1.45 mm (0.057 in.) applied deformation on thin and thick matrix. Maximum MAXSCRT values are taken from the contour plots. Comparing Fig. 4a–d, it can be seen that MAXSCRT values for thick matrix is lower than thin matrix for triangular and sawtooth pattern. Rectangular pattern shows highest MAXSCRT value for both thin and thick matrix in all cases. Indeed, thicker matrix is less damaged than thinner matrix for both dry and wet conditions and proved that thicker matrix sustain more deformation than thinner matrix. On the other hand comparing Fig. 4a and c, and Fig. 5b and d, it can be seen that maximum MAXSCRT value increases due to increase of applied deformation. Also wet samples show higher maximum MAXSCRT value than dry samples and prove that wet samples are more damage prone than dry samples. Reasons for showing higher MAXSCRT value under wet condition comparing to dry condition is explained in the following sections. Also maximum MAXSCRT value increases when load intensity pattern changes from triangular to sawtooth to rectangle. This supports the argument that, duration of applied deformation influences damage in the matrix and more damaged locations are exposed inside the matrix material.

In Fig. 4a, the maximum MAXSCRT value is about 0.68 under dry conditions and 0.73 under the wet conditions for the triangle pattern. Since for the triangular loading, the MAXSCRT value is less than 1.0, so no element is damaged. The MAXSCRT value in some elements reaches the maximum value of 1.0 under both dry and wet conditions for sawtooth and rectangular patterns. So for both sawtooth and rectangular patterns there are damaged elements.

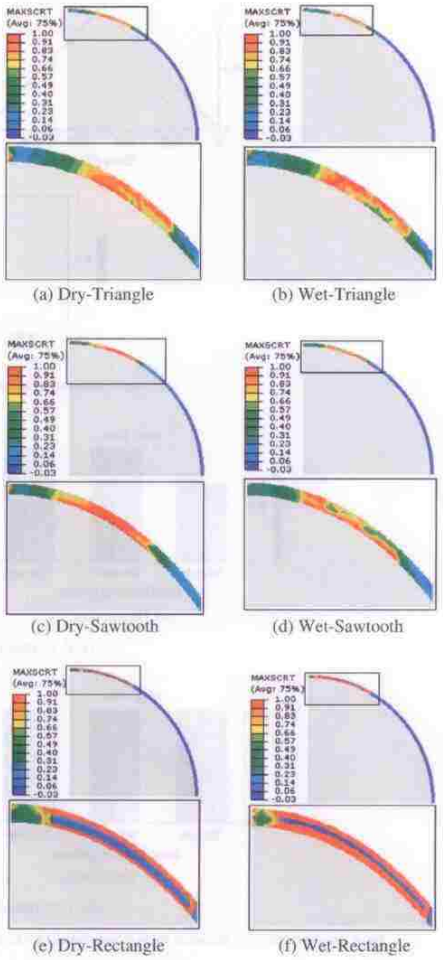

Fig. 5. Maximum Stress Criteria (MAXSCRT) under dry and wet conditions for 1.45 mm (0.057 in.) deformation and for thin matrix.

According to Fig. 4b, the maximum MAXSCRT value is about 0.06 under the dry condition and 0.09 under the wet condition for triangular pattern; the maximum MAXSCRT value is about 0.11 under dry condition and 0.15 under wet condition for sawtooth pattern. In Fig. 4c, the maximum value of MAXSCRT is 1.0 for all three load patterns; means, both dry and wet samples shows damage. In Fig. 4d, the maximum value of MAXSCRT is about 0.13 under dry condition and about 0.18 under wet condition is about 0.18 for the triangular pattern; the maximum MAXSCRT value is about 0.21 under the dry condition and 0.30 under the wet condition for sawtooth load pattern; the maximum value reaches to 1.0 for rectangular pattern under both dry and wet conditions.

3.2. Damage contours

The advantage of the FEM model is the contour plots of the output variables. Figs. 5 and 6 are plotted for MAXSCRT to identify the distribution of damage in the matrix material for the 1.45 mm (0.057 in.) deformation and for the thin and thick matrix respectively. Contour plots for the 1.45 mm (0.057 in.) deformation are presented because according to Fig. 4, 1.45 mm (0.057 in.) deformation shows higher damage in the matrix material. One zoomed in section is shown for each loading pattern so that the contour of damage can be seen clearly. The color of contours ranges from blue[2] to red; blue means small damage and red means large damage. Comparing Fig. 5 with Fig. 6, there are more red color regions for thin matrix than thick matrix, since thin matrix have higher damaged locations than thick matrix. Most importantly both adhesive and cohesive damage are occurred in dry and wet conditioned samples for thin matrix but mostly cohesive damage observed for thick matrix. Surely, thick matrix is stronger than thin matrix and carries more deformation before damage.

It is difficult to quantify damage in matrix and identified it to adhesive and cohesive damage under the triangular pattern for thin matrix by only observing and comparing Fig. 5a and b. Similar scenario is also true for Fig. 5c and d under the sawtooth pattern for thin matrix. For the rectangular pattern, cohesive damage at the top of matrix and adhesive damage at the bottom of matrix and near the interface are clearly shown in Fig. 5e and f for the thin matrix. Both dry and wet samples show cohesive and adhesive damage but wet sample shows more damage at the bottom of the matrix. Damage initiates under the deformation loading zone and at the top of the matrix. Most of the elements at the top of matrix damaged just after applying deformation. After initiating damage at the top of the matrix, it progresses towards the bottom of the matrix and near the interface region since interface region is weakest in the whole domain. Damage progressed towards the bottom of the matrix and continues progression until every element near interface region exposed to damage; when no element is capable of taking any stress at the interface region, than the damage progressed to the second bottom layer since those elements are the weaker in the domain. It is clear that matrix material near interface region is the weakest and prone to damage under both dry and wet conditions for the thin matrix. In addition, the strength and stiffness under dry condition is higher than under wet condition; for this reason, dry condition sustain more deformation and carry more stress than wet condition at the bottom of the matrix and shows less damage. The elements near to the left side boundary conditions do not show significant damage because according to Eq. (3) pure compressive stress will not cause any damage in the matrix. Indeed those elements are under pure compressive stress.

Fig. 6 presents MAXSCRT for 0.057 in. deformation load for the thick matrix. According to Fig. 6a and b the maximum MAXSCRT value is 0.13 and 0.18 for the triangular pattern under the dry and wet conditions respectively. In Fig. 6c and d, the maximum MAXSCRT value is 0.21 and 0.30 for the sawtooth pattern under the dry and wet conditions respectively. The MAXSCRT value less than 1.0 means no element exposed to damage but will damage with changes in deformation duration time or higher deformation magnitude. Fig. 6e and f shows the maximum MAXSCRT value 1.0 for the top elements, means cohesive damage occurred for the rectangular pattern. It should be noticed that the minimum value of MAXSCRT are showing zero but this is not zero rather very small; the values are showing zero since the MAXSCRT values are rounded up to two decimal points. The Triangular and sawtooth patterns do not show damage but they definitely shows the path of the stress flow from top the surface to the bottom surface of matrix. This stress flow and path from the top to bottom of matrix is not clearly visible for thin matrix as shown in Fig. 5. Damage progresses from the top of matrix layer to the bottom of matrix layer following the stress path as show in Fig. 6a–d. The locations of the maximum MAXSCRT for both triangular and sawtooth patterns are on the surface and near 10.16 mm (0.4 in.) from the left support. The region shows the stress concentration at the top of the matrix and perpendicular stress path from the top of the matrix to the

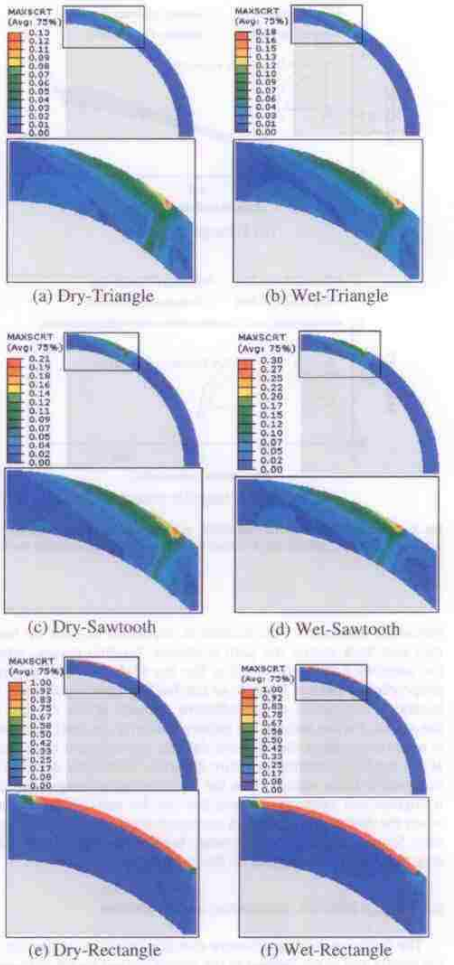

Fig. 6. Maximum Stress Criteria (MAXSCRT) under dry and wet conditions for 1.45 mm (0.057 in.) deformation and for thick matrix.

[2] For interpretation of color in Figs. 5 and 6, the reader is referred to the web version of this article.

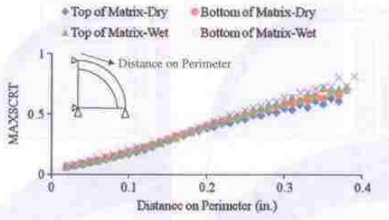

(a) Triangular pattern

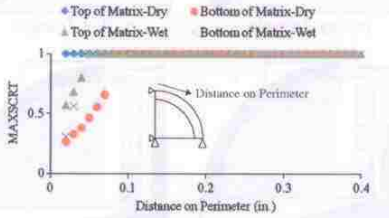

(b) Rectangular pattern

Fig. 7. Maximum Stress Criteria (MAXSCRT) in the matrix measured from the left side boundary conditions for the 0.72 mm (0.0285 in.) deformation and for the thin matrix.

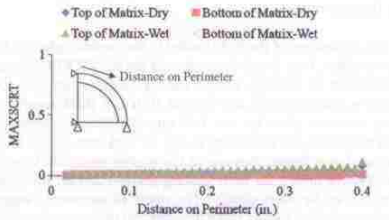

(a) Triangular pattern

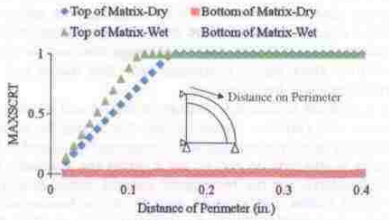

(b) Rectangular pattern

Fig. 8. Maximum Stress Criteria (MAXSCRT) in the matrix measured from the left side boundary conditions for the 0.72 mm (0.0285 in.) deformation and for the thick matrix.

bottom of the matrix. This location is important because for both thin and thick matrix the path is similar. For thin matrix, when the cohesive damage occurred at the top of the matrix than this perpendicular path at the end of the loading zone is followed to initiate and progress of the adhesive damage at the bottom of the matrix. For the rectangular pattern in the Fig. 6e and f, this path is not present, since the cohesive damage initiates and dominates at the top of the matrix for entire duration. This stress concentration path is more visible when the deformation is ramped up like triangular and sawtooth pattern but not for rectangular pattern when the deformation jumps to maximum intensity in a very short time. Stress distributed evenly when load increase gradually with step time like the triangular or the sawtooth pattern.

3.3. Damage initiation, distribution, and progression

The Cohesive and the adhesive damage variations at the top of the matrix and at the bottom of the matrix are not clearly differentiable in the contour diagrams as presented in Figs. 5 and 6. For this reason, the variations of MAXSCRT magnitude are presented in Fig. 7 for the triangular and the rectangular patterns under dry and wet conditions for the 0.72 mm (0.0285 in.) deformation and for thin matrix. Fig. 8 presents the MAXSCRT variation for thick matrix under dry and conditions. The *x*-axis is the distance measured from the left side boundary conditions on the top and the bottom of the matrix perimeter. The *x*-axis is taken up to 10.13 mm (0.4 in.), because the applied deformation is up to 10.13 mm (0.40 in.) on the top of the matrix. Also, from the contour diagrams, it is observed that damage initiates at about 10.13 mm (0.4 in.) distance on the perimeter. The *y*-axis presents the MAXSCRT values for the corresponding elements. Only triangular and rectangular patterns are selected, since triangular pattern shows MAXSCRT value less than 1.0 and rectangular pattern shows highest number of elements exposed to damage for both thin and thick matrix. The first elements at both top and bottom locations are not considered in the graphs, since the elements are horizontally restrained only at the left side and it is assumed that these elements might influenced by boundary conditions and will not provide accurate MAXSCRT values.

According to Fig. 7a and b, it is observed that MAXSCRT value increases gradually for the triangular pattern and abruptly for the rectangular pattern while distance increases. This phenomenon proves that, cohesive damage initiates rapidly while deformation magnitudes increases abruptly. The significance of Fig. 7a is, under both dry and wet conditions, elements at the bottom location shows higher MAXSCRT value than top location. This means, cohesive damage initiates at the top of the matrix but interface of the two materials influences the initiation and propagation of adhesive damage at the bottom of the matrix elements. Clearly, interface between the two materials influences to initiate adhesive damage at the bottom of the matrix and interface is the weakest region in the whole domain. According to Fig. 7b, for the rectangular pattern, MAXSCRT at the bottom of the matrix is higher under wet conditions than dry conditions. Again, lower stiffness and strength causes higher damage under wet condition than dry condition. Also more elements at the bottom of the matrix reach to the MAXSCRT value 1.0 under wet conditions than dry conditions but all the elements at the top of the matrix reach to MAXSCRT value 1.0 under dry conditions. However this scenario is not true for the thick matrix as explained in the next sections.

The MAXSCRT value is low at both top and bottom of the matrix according to Fig. 8a. Cohesive damage at top of the matrix under the wet condition is higher than the dry condition. The scale of the MAXSCRT is kept same for both cases to see the magnitude variations for triangular and rectangular patterns. As seen in Fig. 8b, more locations are exposed to cohesive damage under wet condition than dry condition. MAXSCRT value at the bottom

of the matrix is very low so the adhesive damage is not initiated yet. Clearly thick matrix helps to prevent adhesive damage but not cohesive damage for both lower and higher deformations. This also proves that cohesive damage initiates and progresses due to applied deformation magnitudes and intensity patterns but adhesive damage initiates and progresses due to weak interface between the two elements. Also, the wet condition shows higher cohesive and adhesive damage due to lower stiffness and strength comparing dry condition.

3.4. Strength degradation of damaged elements

It is defined that, when the MAXSCRT value reaches to 1.0 for an element, that element is considered as damaged and unable to carry any stress upon deformation. This phenomenon is called Strength Degradation (SDEG) for that particular element. The SDEG of a material is a scalar value varies from zero to one but only clearly visible in the FEM model when the value is one. Progression of damage can also be clearly observed by plotting SDEG of the matrix material. Fig. 9 shows the SDEG value for the rectangular pattern load under dry and wet conditions. The major similarity between the MAXSCRT contour and the SDEG contour is that, SDEG contour only shows 1.0 where MAXSCRT value is also 1.0. The SDEG contour helps to differentiate and identify cohesive and adhesive damage clearly and later on based on SDEG contour, quantifications of the adhesive and cohesive damage are performed. Explanations of initiation and progression of damage are given in the previous sections.

In Fig. 9 the SDEG are presented for thin matrix and for both 0.72 mm (0.0285 in.) and 1.45 mm (0.057 in.) deformation load. The red color indicates strength degradation in the matrix elements and the blue color indicates no degradation of strength in the matrix elements. Cohesive damage observed for the 0.72 mm (0.0285 in.) deformation load under the dry condition as shown in Fig. 9a. Both cohesive and adhesive damage observed for the 0.72 mm (0.0285 in.) deformation load under the wet condition as shown in Fig. 9b. Both cohesive and adhesive damage observed for the 1.45 mm deformation load under dry and wet conditions, but cohesive damage is significantly higher under wet condition as shown in Fig. 9d. Dry sample shows cohesive damage under 0.72 mm (0.0285 in.) deformation but exposed to both cohesive and adhesive damage under 1.45 mm (0.057 in.) deformation. Wet sample shows both cohesive and adhesive damage under 0.72 mm (0.0285 in.) deformation but adhesive damage extends under 1.45 mm (0.057 in.) deformation.

Fig. 10 shows SDEG for the thick matrix for the rectangular pattern and for both 0.72 mm (0.0285 in.) and 1.45 mm (0.057 in.) deformation load. Damage due to the rectangle intensity pattern is presented because MAXSCRT value due to the triangular and sawtooth patterns are relatively small. One zoomed in section at damaged location is presented for each condition to visualize the SDEG contour plots more clearly. Damage initiation and propagation is observed in the thick matrix. The SDEG value ranges from 0.0 to 1.0 for all cases. It is observed that damage initiations are similar between thin and thick matrix. Maximum cohesive damage is observed at the surface of matrix and at the end of loading zone for both dry and wet conditions and for two different deformation magnitudes. Thick matrix shows cohesive damage and no adhesive damage is observed for any intensity pattern and deformation, since thicker matrix sustains more deformation than thinner matrix and transfer less stresses to the weaker interface region. It is also observed that damage is more under the wet conditions than the dry conditions since wet matrix has lower strength and stiffness than dry matrix. In addition, cohesive damage propagates on top of both dry and wet conditions as deformation increases from 0.72 mm (0.0285 in.) to 1.45 mm (0.057 in.). More elements

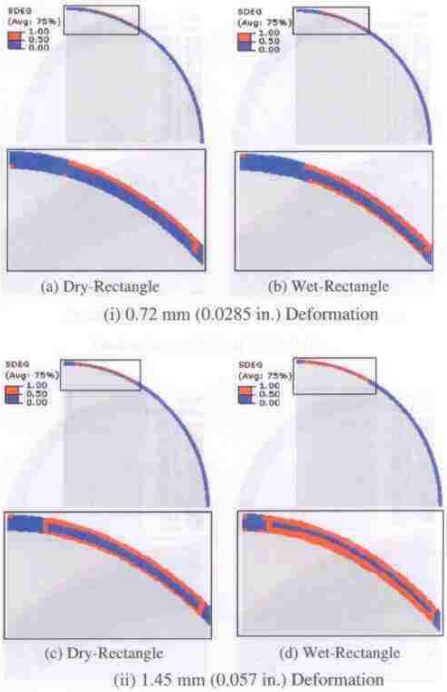

Fig. 9. Strength Degradation (SDEG) of matrix under dry and wet conditions for 1.45 mm (0.057 in.) deformation and for thin matrix.

at the top of the matrix reached to MAXSCRT value 1.0 when deformation value increases.

3.5. Quantifying damaged areas in thin and thick matrix

The MAXSCRT contour provides locations of damaged and undamaged matrix elements; the SDEG contour provides specific location of damaged matrix. In order to measure severity of damage under the dry and the wet condition it is necessary to quantify damage and separate it into the adhesive and cohesive damage. The damaged areas are quantified by measuring the matrix area that is exposed to cohesive and adhesive damage. The SDEG contour plots are selected to quantify adhesive and cohesive damage. The area of single element for both thin and thick matrix is 0.065 square mm (0.0001 square in.). Number of damaged elements are counted and multiplied by the area of the element to determine damaged area. Total undamaged area of thin matrix is 15.48 square mm (0.024 square in.) and thick matrix is 39.35 square mm (0.061 square in.). It can be noted that thin matrix is divided into 4 equal layers of which top three layers are used in the cohesive damage calculations and the bottom single layer that interfaces with aggregate surface is considered for the adhesive damaged area calculation. The percentages of damaged to undamaged areas are calculated. It is observed that cohesive damage initiate at the top layer of matrix and then progress at the bot-

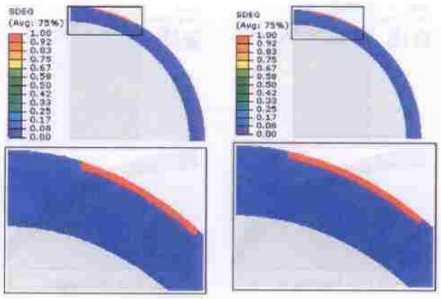

(a) Dry-Rectangle (b) Wet-Rectangle

(i) 0.0285 in. Deformation load

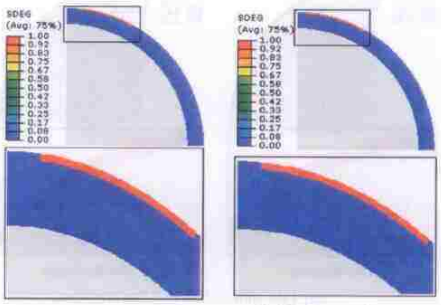

(c) Dry-Rectangle (d) Wet-Rectangle

(ii) 0.057 in. Deformation load

Fig. 10. Strength Degradation (SDEG) in the thick matrix under dry and wet conditions.

tom of matrix and initiates adhesive damage and keep progressing from the bottom of matrix as cohesive damage into the matrix.

A summary of adhesive and cohesive damaged matrix area are given in Table 4. According to the table total 13.3% of the matrix area is damaged under dry condition; among this 12.47% area shows cohesive damage and 0.83% dry matrix area shows adhesive damage. 29.6% of the matrix area is damaged under wet condition; among this 19.18% area shows cohesive damage and 10.42% area shows adhesive damage. When deformation increases from 0.72 mm (0.0285 in.) to 1.45 mm (0.057 in.), then total 29.60% of matrix area is damaged under dry condition; among this 15.85% area shows cohesive damage and 13.75% area shows adhesive damage. On the other hand, total 46.15% of matrix area damaged under wet conditions; among that 30.30% area shows cohesive damage but 16.67% area shows adhesive damage. Thick matrix shows significantly low cohesive damage than thin matrix and no adhesive damaged area is observed. Total 4.1% area is cohesive damaged under dry condition, while 4.8% is damaged under wet condition. When deformation increases, 5.6% of matrix area shows cohesive damage comparing to 6.1% area under wet condition. Adhesive damage increases significantly under the dry and wet conditions while deformation increases from 0.72 mm (0.0285 in.) to 1.45 mm (0.057 in.). For thin matrix and higher deformation, both adhesive and cohesive damage seem vulnerable; on the other hand, cohesive damage is sensitive to both lower magnitude loads.

4. Conclusions

Based on the above results the following conclusions are done.

(1) Top surface of the matrix showed cohesive damage and cohesive damage is higher under wet condition than dry condition. Matrix material near the interface region shows adhesive damage and adhesive damage is higher under wet condition than dry condition. Adhesive damage is the driving factor for pavement degradation and measure needs to be taken to reduce adhesive damage as well as cohesive damage in AC.

(2) Upon deformation, cohesive damage initiates at the top of matrix and then damage propagates towards the bottom of matrix and matrix-aggregate interface and initiates adhesive damage. Adhesive damage is significantly higher under the wet condition and for the rectangular pattern. This finding also supports the previous conclusion regarding adhesive damage, which is critical for ultimate degradation of AC.

(3) Interface region is weakest considering the whole domain. The weakest interface is also a reason for higher adhesive damage in AC. The commonly used additives used to prevent moisture damage in AC, such as lime, are needed to evaluate more to strengthen the interface between aggregate and matrix material.

(4) Only cohesive damage is observed in thick matrix but both cohesive and adhesive damage are observed in thin matrix. Higher matrix thickness improved deformation carrying capacity and transferred less stresses to the interface, so no adhesive damage near interface. In general, interface between the two materials need to be improved to reduce the adhesive damage and improve the overall performance of AC. An optimum asphalt content should be determined that will reduce adhesive damage at the interface by providing thicker matrix coating on coarse aggregate. Also pre-coated aggregate might reduce adhesive damage and more studies are required in this area.

(5) The worst damage scenario observed for thin matrix with 1.27 mm (0.057 in.) deformation; about 16.67% and 30.30% matrix exhibits adhesive and cohesive damage respectively

Table 4
Adhesive and cohesive damaged matrix area for rectangular intensity pattern load.

Deformation magnitude	Damage type	Thin matrix		Thick matrix	
		Dry (%)	Wet (%)	Dry (%)	Wet (%)
0.508 mm (0.0285 in.)	Cohesive damage	12.47	19.18	4.1	4.8
	Adhesive damage	0.83	10.42	–	–
1.27 mm (0.057 in.)	Cohesive damage	15.85	30.30	5.6	6.1
	Adhesive damage	13.75	16.67	–	–

under wet condition. On the other hand, 13.75% and 15.85% matrix material exhibits adhesive and cohesive damage respectively under dry condition.

Acknowledgement

The project is funded by the National Science Foundation (NSF) through the prestigious CAREER program via NSF Grant No. 0644047.

References

[1] Abu Al-Rub RK, Masad EA, Graham MA. Physically based model for predicting the susceptibility of asphalt pavements to moisture-induced damage. College Station, Texas; 2010.
[2] Shah BD. Evaluation of moisture damage within asphalt concrete mixes. Texas A&M University; 2003.
[3] Kringos N, Scarpas T, Kasbergen C, Selvadurai P. Modelling of combined physical–mechanical moisture-induced damage in asphaltic mixes, part 1: governing processes and formulations. Int J Pavement Eng 2008;9:115–28.
[4] Caro S, Masad E, Bhasin A, Little D. Coupled micromechanical model of moisture-induced damage in asphalt mixtures. J Mater Civ Eng, ASCE 2010;22:380–9.
[5] Tarefder RA, Kias EM, Stormont JC. Evaluating parameters for characterization of cracking in asphalt concrete. J Test Eval, ASTM 2009;37:1–11.
[6] Cheng D, Little DN, Lytton RL, Holste JC. Moisture damage evaluation of asphalt mixtures by considering both moisture diffusion and repeated-load conditions. Transport Res Rec: J Transport Res Board 2003;1832:42–9.
[7] Khalid HA, Monney OK. Moisture damage potential of cold asphalt. Int J Pavement Eng 2009;10:311–8.
[8] Wasiuddin NM, Saltibus NE, Mohammad LN. Novel moisture-conditioning method for adhesive failure of hot- and warm-mix asphalt binders. Transport Res Rec: J Transport Res Board 2011;2208:108–17.
[9] Kutay ME, Aydilek AH, Masad E, Harman T. Computational and experimental evaluation of hydraulic conductivity anisotropy in hot-mix asphalt. Int J Pavement Eng 2007;8:29–43.
[10] Spinel SC. A coupled micromechanical model of moisture-induced damage in asphalt mixture: formulation and applications. Texas A&M University; 2009.
[11] Kringos N, Scarpas A, Copeland A, Youtcheff J. Modeling of combined physical–mechanical moisture induced damage in asphaltic mixes, part 2: moisture susceptibility parameters. Int J Pavement Eng 2008;9:129–51.
[12] Inman DJ, Farrar CR, Junior VL, Junior VS. Damage prognosis for aerospace, civil and mechanical systems. John Wiley & Sons, Ltd.; 2005.
[13] Suaris W, Ouyang C, Fernando VM. Damage model for cyclic loading of concrete. J Eng Mech, ASCE 1990;116:1020–35.
[14] Saanouni K. Numerical modeling in damage mechanics. Paris: Hermes Science Publication; 2001.
[15] Allix O, Hild F. Continuum damage mechanics of materials and structures. New York: Elsevier; 2002.
[16] Lemaitre J. A course on damage mechanics. 2nd ed. Springer; 1996.
[17] Kachanov LM. Introduction to continuum damage mechanics. Dordrecht: Kluwer Academic Publisher; 1986.
[18] Lemaitre J, Desmorat R. Engineering damage mechanics: ductile, creep, fatigue and brittle failures. New York: Springer; 2005.
[19] Park SW, Kim YR, Schapery RA. A viscoelastic continuum damage model and its application to uniaxial behavior of asphalt concrete. Mech Mater 1996;24:241–55.
[20] Richard Kim Y. Modeling of asphalt concrete. ASCE Press; 2009.
[21] Richard Kim Y, Baek C, Underwood BS, Subramanian V, Guddati MN, Lee K. Application of viscoelastic continuum damage model based finite element analysis to predict the fatigue performance of asphalt pavements. KSCE J Civ Eng 2008;12:109–20.
[22] Abu Al-Rub RK, Darabi MK, Masad EA, Little DN. A unified continuum damage mechanics model for predicting the mechanical response of asphalt mixtures and pavements. Int J Roads Airports 2011;1:68–84.
[23] You T, Abu Al-Rub RK, Darabi MK, Masad EA, Little DN. Three-dimensional microstructural modeling of asphalt concrete using a unified viscoelastic–viscoplastic–viscodamage model. Constr Build Mater 2012;28:531–48.
[24] Abu Al-Rub RK, You T, Masad EA, Little DN. Mesomechanical modeling of the thermo-viscoelastic, thermo-viscoplastic, and thermo-viscodamage response of asphalt concrete. Int J Adv Eng Sci Appl Math 2011;3:14–33.
[25] Kim Y-R, Souza FV, Teixeira JESL. A two-way coupled multiscale model for predicting damage-associated performance of asphaltic roadways. Comput Mech 2012;9:90.
[26] Kim Y, Allen DH, Little DN. Damage-induced modeling of asphalt mixtures through computational micromechanics and cohesive zone fracture. J Mater Civ Eng, ASCE 2005;17:477–84.
[27] Bhasin A, Masad E, Little D, Lytton R. Limits on adhesive bond energy for improved resistance of hot-mix asphalt to moisture damage. Transport Res Rec: J Transport Res Board 2006;1970:3–13.
[28] Kringos N, Scarpas A, de Bondt A. Determination of moisture susceptibility of mastic–stone bond strength and comparison to thermodynamical properties. J Assoc Asphalt Paving Technol 2008;77:435–78.
[29] Birgisson B, Roque R, Page GC. Evaluation of water damage using hot mix asphalt fracture mechanics. J Assoc Asphalt Paving Technol 2003;72:424–62.
[30] Ban H, Kim Y-R, Pinto I. Integrated experimental-numerical approach for estimating material-specific moisture damage characteristics of binder–aggregate interface. Transport Res Rec: J Transport Res Board 2011;2209:9–17.
[31] Tarefder RA, Zaman AM. Nanoscale evaluation of moisture damage in polymer modified asphalts. J Mater Civ Eng, ASCE 2010;22:714–25.
[32] Fromm HJ. The mechanisms of asphalt stripping from aggregate surfaces. J Assoc Asphalt Paving Technol 1974;43:191–223.
[33] Lucas LJ, Black TM, Jones DP. Use of cohesive elements in fatigue analysis. 2007 ASME pressure vessels and piping division conference, San Antonio, Texas: ASME; 2007. p. 13–25.
[34] Hossain MI, Tarefder RA. Determining damage effects on asphalt concrete composites. Int J Civ Struct Eng 2013;3:692–703.
[35] Hossain MI, Tarefder RA. Effects of moisture in asphalt concrete. Basic Res J Eng Innovation 2013;1:16–25.
[36] Santi PM, Holschen JE, Stephenson RW. Improving elastic modulus measurements for rock based on geology. Environ Eng Geosci 2000;6:333–46.
[37] Wang L. Mechanics of asphalt microstructure and micromechanics. McGrawHill; 2011.
[38] Voyiadjis GZ, Allen DH. Damage and interfacial debonding in composites. New York: Elsevier; 1996.
[39] Degrieck J, Van Paepegem W. Fatigue damage modeling of fibre-reinforced composite materials: review. Appl Mech Rev 2001;54:279.
[40] Kasthurirangan Gopalakrishnan, Broj Birgisson, Peter Taylor NOA-O, editor. Nano-technology in civil infrastructure: a paradigm shift. Berlin: Springer; 2011.
[41] Zhu X, Huang Z, Yang Z, Chen W. Micromechanics-based analysis for predicting asphalt concrete modulus. J Zhejiang Univ Sci A 2010;11:415–24.
[42] Shashidhar N, Shenoy A. On using micromechanical models to describe dynamic mechanical behavior of asphalt mastics. Mech Mater 2002;34:657–69.
[43] Tarefder RA, Yousefi SS, Kias E. Factors that affect the rheological properties of asphalt matrix. Pavement and materials: testing and modeling in multiple length scales, ASCE; 2010 [Special Pu:121–33].
[44] Roque R, Koh C, Chen Y, Sun X, Lopp G. Introduction of fracture resistance to the design and evaluation of open graded friction courses in Florida. Tallahassee, FL; 2009.
[45] Hossain MI, Tarefder RA. Quantifying moisture damage at mastic–aggregate interface. Int J Pavement Eng 2013:1–16.